CHARACTERISATION OF THE UNSTEADY WAKE OF A SQUARE-BACK ROAD VEHICLE

By Giancarlo Pavia

Doctoral Thesis

Submitted in partial fulfilment of the requirements for the award of
Doctor of Philosophy of Loughborough University

April 2019

Abstract

Square-back shapes are popular in the automotive market for their high level of practicality. These geometries, however, are usually characterised by high aerodynamic drag and their wake flow dynamics present many aspects, such as the coexistence of long- and short-time unsteady modes, whose full comprehension is still far from being achieved. The present work aims to provide some contributions to this field.

An extensive experimental campaign consisting of balance, pressure tapping, particle image velocimetry and single point velocity measurements has been carried out in order to characterise the dynamic behaviour of the wake developing downstream of a simplified square-back geometry. Tests have been performed considering the Windsor body, at a Reynolds number (based on the model height) of $Re_H = 7.7 \times 10^5$.

New insights on how the long-time instability develops are provided. The instability is shown to stem from the mutual interactions between the four shear layers bounding the wake rather than being the result of the state of perturbation of a single shear layer. Changes in the level of interaction between two or more shear layers are also reported to affect the short-time unsteady modes.

A drag reduction is reported every time the symmetry of the wake is restored, as a consequence of the increased amount of reverse flow impinging on the base of the model. This seems to be true regardless of the configuration considered (with or without wheels) and the type of optimisation strategy adopted, although it does not necessarily imply the complete suppression of the long-time instability. In fact, a certain level of ‘mobility’ in the flow reversal seems to be inevitable every time the symmetry of the wake is restored.

Several elements that can alter this behaviour are also identified. A change in the curvature of at least one of the four shear layers is shown to increase the frequency of the switches between bi-stable states, until eventually the long-time instability disappears replaced by low frequency flapping or swinging motions. Such changes can be triggered by applying perturbations on either a ‘global’ scale or a more ‘local’ scale.

Overall, the results presented in this work help to ‘bridge the gap’ between simplified geometries and more realistic automotive shapes, as far as the characterisation of the time averaged and main unsteady features of the wake is concerned, and provide insights that may allow in the future the design of more effective flow control systems for drag reduction.

Acknowledgements

First and foremost, I would like to express my gratitude to Professor Martin Passmore for having given me the opportunity to work on this subjected and his continuous support and supervision throughout the course of my PhD.

Thanks are extended to my second supervisor, Dr. Adrian Spencer, to Dr. Jeff Howell, for all the precious advices given during these four years, and to Dr. Simon Tuplin, for the help provided during the design and commissioning of the test rig.

This work could not have been possible without the financial support of Loughborough University and Jaguar Land Rover. I would like to extend my gratitude to Adrian Gaylard for having believed in the project since day one.

Thanks are also due to all the technical staff working in the AAE Department, for their continuous support. In particular, I would like to thank Nigel Lines, Andrew Horsey and David Cooper for their excellent work in manufacturing the models and keeping the test facility always in optimal conditions.

Thanks must also go to all people working in the SM 202 office, for having contributed to create a nice work environment, and to my fellow colleagues of the Applied Aerodynamics Group. In particular I would like to thank Dr. Anna-Kristina Perry and Dr. Mathew Almond for having shared their valuable experimental expertise with me, and to Max Varney, Graham Hodgson and Matthew Ward for the help provided during the setup of the experiments.

I cannot forget to say thank you to Rhian Watt, for the precious help provided when dealing with administrative matters.

Finally, thanks go to my parents for having raised me and given me the opportunity to follow my dreams, and to my sister for having made home feel much closer than it actually was.

List of Publications

Part of the work reported in this thesis has been published in the following:

- Pavia, G., Passmore, M., and Varney, M. (2019) “Low-frequency wake dynamics for a square-back vehicle with side trailing edge tapers.” Journal of Wind Engineering and Industrial Aerodynamics, 184 (2019):417-435.
- Pavia, G., Passmore, M., and Sardu, C. (2018) “Evolution of the bi-stable wake of a square-back automotive shape.” Experiments in Fluids, 59.1(2018):20.
- Pavia, G., and Passmore, M. (2017) “Characterisation of Wake Bi-stability for a Square-Back Geometry with Rotating Wheels.” FKFS Conference. Springer, Cham, 2017.
- Perry, A.-K., Pavia, G., and Passmore, M. (2016b). “Influence of short rear end tapers on the wake of a simplified square-back vehicle: wake topology and rear drag.” Experiments in Fluids, 57.11(2016):169.
- Pavia, G., Passmore, M., and Gaylard, A., “Influence of Short Rear End Tapers on the Unsteady Base Pressure of a Simplified Ground Vehicle.” SAE Technical Paper 2016-01-1590, 2016, doi:10.4271/2016-01-1590.

and presented at:

- “12^{th} International Conference on Vehicle Aerodynamics 2018”, Birmingham (UK), $16^{th}-17^{th}$ October 2018.
- “Aerovehicles 3 - Third International Conference in numerical and experimental aerodynamics of road vehicles and trains”, Milan (Italy), $13^{th}-15^{th}$ June 2018.
- 11^{th} FKFS conference in “Progress in Vehicle Aerodynamics and Thermal Management”, Stuttgart (Germany), $26^{th}-27^{th}$ September 2017.
- Meeting of the “Special Interest Group in Ground Vehicle Aerodynamics”, Loughborough University (UK), $25^{th}-26^{th}$ May 2017.
- “2016 SAE World Congress”, Detroit (Michigan), $12^{th}-14^{th}$ April 2016.

Table of contents

List of figures

List of tables

‘When I meet God, I am going to ask him
two questions:
Why relativity? And why turbulence?
I really believe he will have an answer for
the first.’

WERNER HEISENBERG

Chapter 1

Introduction

As the pressure exerted by the public opinion on car manufacturers to produce cleaner than ever vehicles keeps increasing, the need to reduce aerodynamic drag become more and more stringent. From an aerodynamic point of view, passenger cars are essentially three-dimensional semi-bluff bodies moving close to the ground (Carr, 1971). Wake dynamics are commonly recognised to affect noticeably the aerodynamic forces acting on such bodies. Indeed, achieving a better understanding of these dynamics may unlock new possibilities in terms of flow control strategies for drag reduction. The present work aims to give a contribution to this field. The unsteady behaviour of the wake of a simplified square-back vehicle, the Windsor body, is investigated, together with its sensitivity to small perturbations. The impact of wheels, in either stationary or rotating conditions, on the same dynamics is also assessed. The work is experimental, consisting of balance, pressure tapping, particle image velocimetry and single point velocity measurements carried out at a Reynolds number (based on the model height) of $Re_H = 7.7 \times 10^5$.

In this chapter, the flow around generic bluff bodies in two- and three-dimensional domains is characterised, with a particular emphasis on wake dynamics (§1.1). A review of the most relevant literature in the field of road vehicle aerodynamics is then presented in §1.2, where the aerodynamic forces acting on a car are also identified. The main time averaged and unsteady features of the wakes generated by simplified square-back shapes are outlined in §1.3. Great emphasis is placed on the characterisation of the properties of bi-stable wakes and their sensitivity to small perturbations in the fluid domain. The level of complexity is gradually increased by adding a rear slant to the model and considering the effects produced by either stationary or rotating wheels. A short summary on the latest advancements in the field of passive and active flow control systems is also provided. Particular attention is paid to trailing edge tapering and control strategies aiming to either suppress the long-time wake dynamics or minimise the detrimental effects of the aerodynamic interactions between the wheels and the main body. The objectives of the thesis are then outlined in §1.4, where an overview of the structure of the present manuscript is also provided.

1.1 Bluff body aerodynamics

The aerodynamics of a generic ‘bluff body’ is characterised by the presence of a large region of separated flow, responsible for most of the drag. As the boundary layer detaches from the body, concentrated vorticity is introduced into the wake, leading to the formation of mixing layers between the undisturbed flow in the freestream region (where $V \simeq V_\infty$) and the flow trapped in the wake (where $V < V_\infty$).

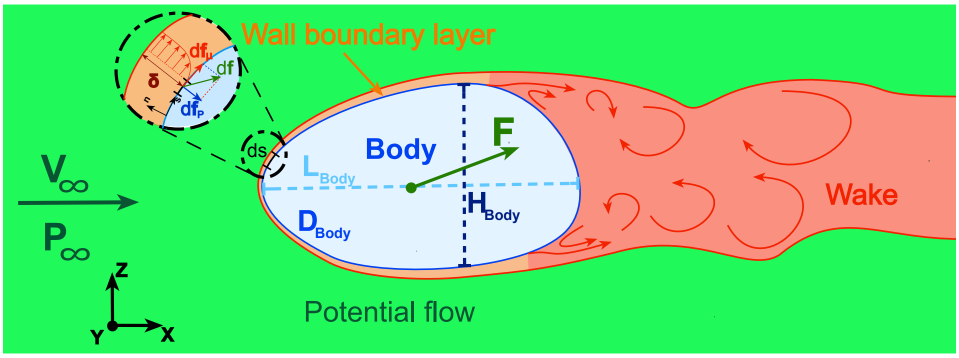

Figure 1.1: Schematic representation of the flow field around a generic bluff body.

The behaviour of the fluid around such a body can be described by using the Navier-Stokes equations which, for an incompressible flow in absence of external forces and including the action of the gravity into the pressure term (see Batchelor (2000)), can be written as:

$$\nabla \cdot \mathbf{V} = 0, \tag{1.1}$$

for the continuity equation, and

$$\rho \left(\frac{d\mathbf{V}}{dt} + \mathbf{V} \cdot \nabla \mathbf{V} \right) = -\nabla p + \mu \nabla^2 \mathbf{V}, \tag{1.2}$$

for the momentum equation. In Eq. 1.2, $\mathbf{V} = \{u, v, w\}$ is the velocity vector, ρ the fluid density, p is the (modified) pressure term (Batchelor, 2000) and μ the dynamic viscosity, while the symbols ∇ and ∇^2 denote respectively the Gradient operator ($\nabla = \partial_x \mathbf{i} + \partial_y \mathbf{j} + \partial_z \mathbf{k}$) and the Laplacian operator ($\nabla^2 = \partial^2_{xx} \mathbf{i} + \partial^2_{yy} \mathbf{j} + \partial^2_{zz} \mathbf{k}$). A non-dimensional form of equations 1.1 and 1.2 can be written after having defined non-dimensional coordinates $x^* = x/H_{Body}$, a normalised velocity $V^* = V/V_\infty$ and a non-dimensional time $t^* = tV_\infty/H_{Body}$, yielding

$$\nabla^* \cdot \mathbf{V}^* = 0 \tag{1.3}$$

for the mass conservation and

$$\frac{d\mathbf{V}^*}{dt^*} + \mathbf{V}^* \cdot \nabla \mathbf{V}^* = -\nabla^* p^* + \frac{1}{Re} \nabla^2 \mathbf{V}^*, \tag{1.4}$$

for the momentum equation. H_{Body} and V_∞ denote respectively a characteristic length of the body and the value of the freestream velocity. In Eq. 1.4, p^* is the normalised pressure, expressed as:

$$p^* = \frac{p}{\rho {V_\infty}^2}, \tag{1.5}$$

while *Re* is the *Reynolds number*, defined as:

$$Re = \frac{\rho V_\infty H_{Body}}{\mu} = \frac{V_\infty H_{Body}}{\nu}, \tag{1.6}$$

where $\nu = \frac{\mu}{\rho}$ is the kinematic viscosity. Another non-dimensional parameter that is often used used is the *Strouhal number*, expressed as:

$$St = f^* = \frac{1}{t^*} = \frac{H_{Body}}{t V_\infty}. \tag{1.7}$$

Applying the Reynolds decomposition ($\mathbf{V}^* = \overline{\mathbf{V}}^* + \mathbf{V}^{*\prime}$) and averaging over time, Eq. 1.4 becomes:

$$\overline{V}_j^* \frac{\partial \overline{V}_i^*}{\partial x_j^*} = -\frac{\partial \overline{p}^*}{\partial x_j^*} + \frac{1}{Re} \frac{\partial^2 \overline{V}_j^*}{\partial x_i^* \partial x_j^*} + \frac{\partial T_{ij}^*}{\partial x_j^*}, \tag{1.8}$$

where the terms $T_{ij}^* = \overline{-{V^*}_i' {V^*}_j'}$ denote the Reynolds stresses (Pope, 2000).

When the Reynolds number is high (as in the case of ground vehicles, for which $Re >> 10^4$) the viscous actions, described by the second term on the right-hand side of Eq. 1.8, can be neglected. In these conditions the motion of fluid particles is characterised by irregular and incoherent paths. The inertial effects (expressed by the numerator of equation 1.6) are dominant and Eq. 1.8 can be simplified as:

$$\overline{V}_j^* \frac{\partial \overline{V}_i^*}{\partial x_j^*} - \frac{\partial T_{ij}^*}{\partial x_j^*} \approx -\frac{\partial \overline{p}^*}{\partial x_j^*}, \tag{1.9}$$

suggesting that the motion of the fluid around the body is dictated mainly by pressure gradients. A pressure gradient in the streamwise direction is associated with a variation of the fluid momentum while a transverse pressure gradient is linked to the curvature of fluid trajectories. For such high Reynolds number, three different regions can be identified in the fluid domain around the body: the potential flow region, the wall boundary layer and the wake (see Fig. 1.1).

1.1.1 Potential flow

The potential flow region consists of the whole fluid domain apart from the boundary layer around the body and its wake. In this zone the flow can be considered inviscid and irrotational ($\nabla^* \times \mathbf{V}^* = \boldsymbol{\Omega}^* = 0$, with $\boldsymbol{\Omega}^*$ denoting the vorticity). In these conditions, a potential Φ can be defined for the velocity, in such a way that $\mathbf{u}^* = \nabla^* \Phi$. Along each streamline, pressure and velocity satisfy Bernoulli's equation:

$$p_0{}^* = \frac{1}{2}|\mathbf{V}^*|^2 + p^* = const., \tag{1.10}$$

with $p_0{}^*$ denoting to the total pressure. A stream surface can be also used to define a solid interface. The inviscid theory has allowed to obtain analytical solutions for flows around 2D shapes, such as wing profiles (Anderson, 2009), but it is less suited to study the flow field around bluff bodies because the inviscid hypothesis is not sustainable close to the walls of the geometry and inside its wake.

1.1.2 Wall boundary layer

The boundary layer region is defined around the surface of the body (D_{Body} in Fig. 1.1), where $\mathbf{V}^* = \mathbf{0}$ due to the boundary conditions of no-slip and impermeability. For simplification, the main properties of the boundary layer are usually described using a 2D view of a stationary flow, with a characteristic length δ. A small element ds of the body surface D_{Body} is considered and a local coordinate system $(\mathbf{s}, \mathbf{n})$ is defined, with $\mathbf{s}$ and $\mathbf{n}$ respectively tangent and perpendicular to the considered surface and $\mathbf{n}$ oriented inside the fluid domain (see Fig. 1.1). v_s and v_n are the velocity components in this local frame of reference. Starting from the velocity of the fluid outside the boundary layer $\overline{V}_{s\infty} = \overline{V}_{s(n=\delta)}$, the boundary layer thickness δ_{99} is then defined as the distance along $\mathbf{n}$ between the body surface and the point where $\overline{V}_s = 0.99\overline{V}_{s\infty}$. Depending on its regime, the boundary layer evolves along the surface due to viscous or turbulent diffusion. In absence of streamwise pressure gradients, the growth rate follows the relations $d\delta/ds \sim Re_\delta^{-1/2}$ in the laminar regime and $d\delta/ds \sim Re_\delta^{-1/5}$ in the turbulent case (Anderson, 2009). Under boundary layer assumptions ($\overline{V}_n << \overline{V}_s$ and $\partial/\partial n >> \partial/\partial s$), when a large Reynolds number is considered ($Re_\delta = V_{s\infty}\delta/\nu >> 1$), Eq. 1.8 becomes

$$\frac{\partial \overline{p}^*}{\partial n^*} + \frac{\partial \overline{V_n'^{*2}}}{\partial n^*} = 0, \tag{1.11}$$

along $\mathbf{n}$, and

$$-\frac{\partial \overline{p}^*}{\partial s^*} + \frac{1}{Re_\delta}\frac{\partial^2 \overline{V}_s{}^*}{\partial n^{*2}} + \frac{\partial(\overline{-V_s'^* V_n'^*})}{\partial n^*} = 0, \tag{1.12}$$

along $\mathbf{s}$.

Eq. 1.11 integrated along $\mathbf{n}$ direction gives $p^* + \overline{V}_n'^{*2} = const.$ across the boundary layer. This means that the pressure on the body is equal to the pressure in the potential flow region, since $\overline{V_n'^{*2}} = 0$ on the body surface D_{Body}. Eq. 1.12, instead, shows that the pressure gradient $\partial p^*/\partial s^*$ along the direction $\mathbf{s}$ tangent to the body surface affects both the curvature of the velocity profile and the Reynolds stresses in the region close to the wall. An adverse pressure gradient in this direction ($\partial \overline{p}^*/\partial s^* > 0$) makes the boundary layer thicker and more turbulent while, on the contrary, a favourable pressure gradient ($\partial \overline{p}^*/\partial s^* < 0$) makes the boundary layer thinner, reducing its turbulent activity. A strong pressure gradient along **s** can also induce a change in the sign of $\overline{V}_s^*$, triggering the separation of the flow from the surface of the body or promoting its reattachment. Points of separation and reattachment are defined as the positions s^* for which:

$$\left.\frac{\partial \overline{V}_s{}^*}{\partial n^*}\right|_{n^*=0} = 0. \tag{1.13}$$

Flow separation can be triggered by a strong and localised pressure gradient, as for example in the presence of a sharp edge on the body surface, or can be a consequence of a progressive slow down of the flow, resulting in a more ‘gentle’ adverse pressure gradient. In the former case a fixed point of separation is seen, whereas in the latter case points of separation tend to change their position over time.

1.1.3 Wake

The wake region extends downstream of the body, where the vorticity $\mathbf{\Omega}^*$, initially concentrated in the boundary layer, is convected past the separation point. In this zone, the flow is out of the viscous influence of the wall so that the inviscid hypothesis is still sustainable at high Reynolds numbers. However, the potential theory is no longer applicable, as the flow field is not irrotational. In this region, the vorticity distribution can be used to deduce the velocity field and its dynamics affect noticeably the behaviour of the flow (Saffman, 1992). By taking the curl of Eq. 1.4 and considering that $\nabla \times \nabla p^* = 0$ for flows with constant density, the *vorticity equation* is obtained:

$$\frac{d\mathbf{\Omega}^*}{dt^*} + \mathbf{V}^* \cdot \nabla \mathbf{\Omega}^* = \mathbf{\Omega}^* \cdot \nabla \mathbf{V}^* + \frac{1}{Re} \nabla^2 \mathbf{\Omega}^*. \tag{1.14}$$

The first term on the right-hand side of Eq. 1.14 refers to the *vortex-line stretching* (Pope, 2000). It is linked to the increase in magnitude of Ω^* due to the strain rate produced by the velocity gradients and, in the case of three dimensional flows, represents a dominant effect in the generation and maintenance of turbulence. The second term on the right-hand side of Eq. 1.14 is a *diffusion-like* term and describes the spread of vorticity from points where it is high to those where it is low. As in the case of the diffusivity term in Eq. 1.4, this term tends to zero for high Reynolds numbers.

Strictly connected to vorticity is *circulation*, which is usually used for quantifying the strength of a generic vortex tube. It is defined as the line integral of the velocity around a closed simply connected curve $\partial S^*_{\Gamma^*}$ bounding any cross section of the tube, or alternatively (applying Stokes’ theorem) as the surface integral of the vorticity passing through the surface $S^*_{\Gamma^*}$ bounded by the same curve:

$$\Gamma^* = \int_{\partial S^*_{\Gamma^*}} \mathbf{V}^* d\mathbf{s}^*_{\Gamma^*} = \int_{S^*_{\Gamma^*}} \mathbf{\Omega}^* \cdot \mathbf{n}^*_{\Gamma^*} dS^*_{\Gamma^*}. \tag{1.15}$$

In a turbulent flow, such as the wake developing downstream of a bluff body at high Reynolds number, vortical structures of different sizes are seen to coexist. The bigger vortical structures tend to decay in ever-smaller eddies until disappearing due to viscosity, in such a way that, as stated by Richardson (1922), *"Big whirls have little whirls, / Which feed on their velocity / And little whirls have lesser whirls, / and so on to viscosity / - in the molecular sense"*. As pointed out by Kolmogorov (1941), this break-up process is responsible for transferring energy from the larger scales, where Re is too high for the viscous actions to dominate over the inertial forces, to the smaller scales, until the value of the Reynolds number Re_E related to the size of the eddies is small enough for the dissipation to be effective. The scale at which the dissipation of turbulence takes place (assuming that the flow is locally homogeneous, isotropic and in a condition of statistical equilibrium) is called *Kolmogorov microscale* and is defined as:

$$\eta = \left(\frac{\nu^3}{\epsilon}\right)^{1/4}, \tag{1.16}$$

where ϵ refers to the energy dissipation rate:

$$\epsilon \sim \frac{u_{E_0}^3}{l_{E_0}}. \tag{1.17}$$

In Eq. 1.17, l_{E0} (also known as *integral lengthscale*) denotes the lengthscale of the largest eddies in the flow field, associated with the lowest wave numbers κ (with $\kappa = 2\pi/l_E$). u_{E_0} refers to the velocity of the same vortical structures. It is derived from the total kinetic energy and it is usually expressed as $u_{E_0} = \overline{(V'^2)}^{1/2}$, where V' refers to the fluctuating part of the velocity field. For length scales much smaller than the integral length scale an *equilibrium range* can be defined. In this range the energy spectrum E_s depends only on the nature of the small-scale flow regardless on how much energy is present at the larger scales, so that $E = E(\kappa, \epsilon, \nu)$. Within this range two different subranges can be defined. In the first subrange (known as *inertial subrange*), the effects of viscosity can be still neglected and the shape of the energy spectrum $E_s(\kappa)$ can be predicted using the *Kolmogorov's $\kappa^{-5/3}$ law* (derived from dimensional analysis):

$$E_s(\kappa) = C\epsilon^{2/3}\kappa^{-5/3}, \tag{1.18}$$

where $\eta^{-1} << \kappa << l_{E_0}^{-1}$ and C indicates the *Kolmogorov constant*; experimental evidence suggests $C = 1.5$ (Pope, 2000). For the second subrange (*viscous subrange*) the dimensional analysis does not provide a solution. A more general model for the energy-spectrum function, valid in the whole equilibrium range (for $\kappa >> l_{E_0}^{-1}$), can be defined as:

$$E_s(\kappa) = C\epsilon^{2/3}\kappa^{-5/3} f_\eta(\kappa\eta), \tag{1.19}$$

where $f_\eta(\kappa\eta)$ refers to a generic non-dimensional function of the type

$$f_\eta(\kappa\eta) = \exp\{-\beta\{[(\kappa\eta)^4 + c_\eta^4]^{1/4} - c_\eta\}\}, \tag{1.20}$$

with β and c_η positive constants (Pope, 2000).

1.1.4 Aerodynamic forces

The global forces **F** that a fluid exerts on a body can be estimated by integrating, over the wetted area, the local force **df** that the fluid applies on the elementary surface ds:

$$\mathbf{F} = \int\int_{Body} \mathbf{df} ds; \tag{1.21}$$

The local fluid force **df** can be decomposed as a sum of a pressure term $\mathbf{df_p}$, orthogonal to the body elementary surface,

$$\mathbf{df_p} = -pds\mathbf{n} \tag{1.22}$$

and a viscous term $\mathbf{df}_\mu$, parallel to the same surface,

$$\mathbf{df}_\mu = \mu\left(\frac{\partial u_s}{\partial n}\mathbf{s_x} + \frac{\partial v_s}{\partial n}\mathbf{s_y}\right), \tag{1.23}$$

where all the quantities are evaluated at $n = 0$.
Aerodynamic forces are usually expressed by means of normalised coefficients, defined as

$$\mathbf{C_{fi}} = \frac{F_i}{\frac{1}{2}\rho {V_\infty}^2 S_{Body}}, \tag{1.24}$$

where $i \in \{x, y, z\}$ and S_{Body} represents the area of a characteristic section of the body (usually the body's cross-section in the case of bluff bodies).

For a generic bluff body, at null yaw and pitch angles the drag is by far the most important aerodynamic force. Total drag is the sum of the pressure force, caused by the difference between the high pressure exerted on the front part of the body and the low pressure acting over the rearward facing surfaces, and the friction forces, applied over the tangential surfaces. In the case of bluff bodies, the first contribution is much higher than the second one and presents, especially in the case of a body with rounded trailing edges, a high sensitivity to the Reynolds number, as pointed out by Roshko (1993) for a circular cylinder (Fig. 1.4). The pressure drag consists of two different elements, namely the *forebody drag* (referring to the front part of the body) and the *afterbody* (defined as the portion of the body lying inside the separated wake). The latter contribution is determined by the suction acting over the model's rearward facing surfaces and usually prevails over the former.

1.1.5 Planar free shear layers

The time averaged and unsteady features of the wake are direct consequences of the characteristics of the free shear layers originating from the interaction between the 'high' velocity free-stream flow bounding the wake and the 'low' velocity flow 'trapped' in the so called 'dead-water region' (Schuetz, 2016). Planar shear layers are a classical examples of planar mixing layers. An extensive description of this type of flows can be found in Pope (2000). A classical example of such flows is the layer that originates when two parallel streams of different velocities (V_a and V_b, with $V_a > V_b$) come together downstream of a thin splitter plate, oriented in the same direction (Fig. 1.2a). In these conditions, the characteristic convective velocity $\overline{V_c} = (\overline{V_a} + \overline{V_b})/2$ and the characteristic velocity difference $\overline{V_d} = (\overline{V_a} - \overline{V_b})/2$ can be defined, together with the characteristic width of the layer $\delta_m(x) = y_{0.9}(x) - y_{0.1}(x)$, where $y_{m_{0.9}}(x)$ and $y_{m_{0.1}}(x)$ represents respectively the points where $\overline{V_{0.1}} = \overline{V_b} + 0.1\overline{V_d}$ and $\overline{V_{0.9}} = \overline{V_b} + 0.9\overline{V_d}$. For $\overline{V_b} = 0$ there are several experiments that suggest that the mixing layer is self-similar (Champagne et al (1976), Wygnanski and Fiedler (1970)). As pointed out in Townsend (1980), the necessary conditions for self-similarity are the linear growth of the layer and the independence of the mean velocity and turbulent profiles from the streamwise position x, when scaled using δ_m and $\overline{V_d}$ as reference quantities.

The spreading rate of the flow, as it is convected downstream, can be calculated from

$$\frac{d\delta_m}{dx} \approx S_{\delta_m} \frac{\overline{V_d}}{\overline{\overline{V_c}}}, \tag{1.25}$$

where S_{δ_m} is a spreading parameter, whose values have been found to range between $S_{\delta_m} \approx 0.06$ and $S_{\delta_m} \approx 0.11$ (Dimotakis, 1991), depending mainly on the state of the flow as it leaves the splitter plate.

A high level of unsteadiness characterises the shear layers, as velocity fluctuations are generated in these regions by turbulent phenomena and vorticity dynamics. At moderate Reynolds numbers, the velocity difference across the shear layer leads to the formation of 'vortical lumps' of concentrated vorticity (Winant and Browand, 1974). This represents a classical example of Kelvin-Helmholtz instability. As neighbouring vortices interact, a pairing process occurs, triggered by slight imperfections in the vortex spacing and strength (Fig. 1.2b). In this way, larger coherent structures are formed. The repetition of this process, as the distance from the splitter plate increases, leads to the growth of the turbulent mixing layer. Similar structures are also seen at higher Reynolds number (fully turbulent shear layer), as shown by the schilleren images captured by Brown and Roshko (1974) (Fig. 1.2c). In these conditions, the characteristic frequency of the rolling up of the larger structures decreases moving downstream of the origin of the velocity discontinuity (Hussain and Zaman, 1985) and finer-scale structures also become visible.

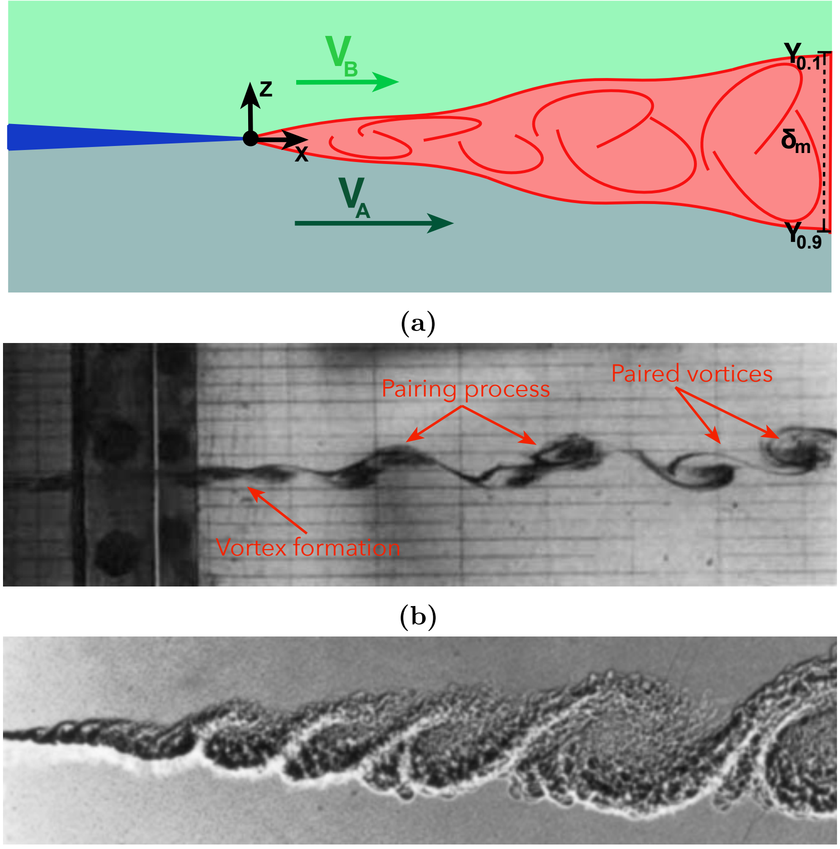

(a)

(b)

(c)

Figure 1.2: **a** schematic illustration of a mixing layer. **b** visualisation of vortex pairing process (picture from Winant and Browand (1974)). **c** example of turbulent mixing layer (picture from Brown and Roshko (1974)).

The growth rate of Kelvin-Helmholtz instabilities can be altered by the presence of centrifugal forces, as in the case of curved free shear layers. As pointed out by Liou (1994), centrifugal forces are seen to stabilise the flow in the case of a curved mixing layer with the fast stream located outside of the slow stream. In these conditions, the spatial growth rate of the instabilities tends to decrease as the curvature of the shear layer increases. Centrifugal forces have been reported instead to promote the occurrence of instabilities in the case of curved shear layers with a velocity profile characterised by the presence of an outer low-speed stream interacting with an inner high-speed stream. In these conditions, both the frequency range and the growth rates of the unstable modes are seen to increase with the curvature of the mixing layers.

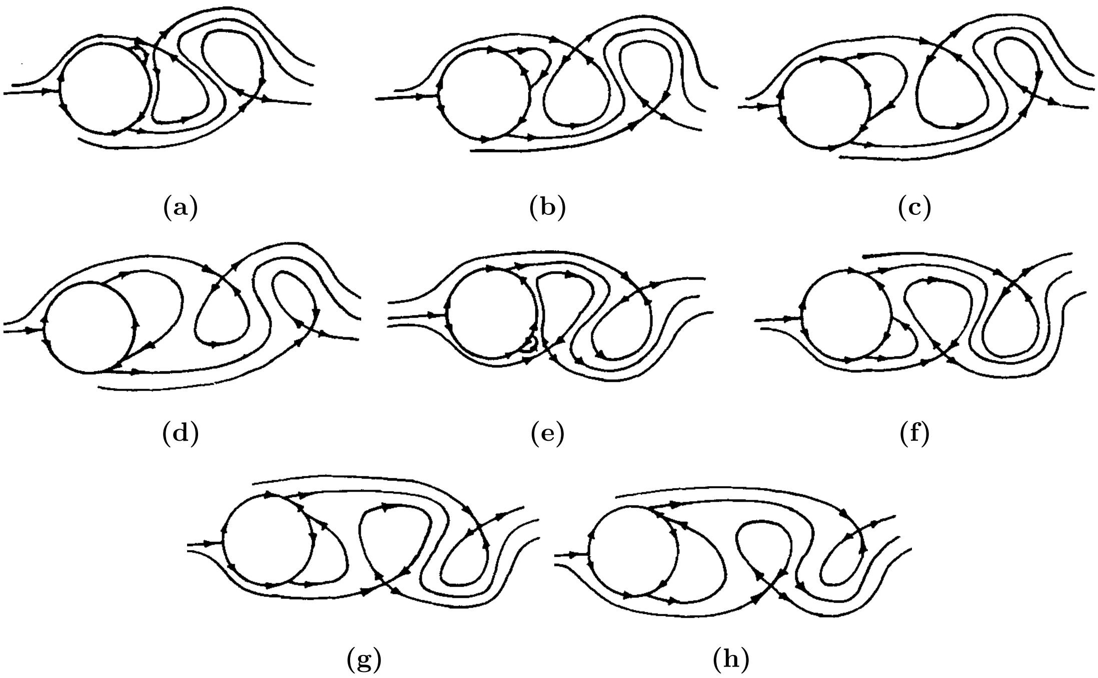
(a) (b) (c) (d) (e) (f) (g) (h)

Figure 1.3: Simplified model of vortex shedding past a 2D cylinder. Sketches from Perry et al (1982).

1.1.6 Wakes of 2D geometries

The wake of two-dimensional bluff bodies has been shown to develop a self-similar behaviour in the far field (about 30 lengths downstream of the body), where it becomes independent to the inlet conditions (Pope, 2000). Near-wake topology and base pressure depend instead on the shape of body considered, since they are the result of the interactions between the shear layers developing in the proximity of the separation points. The nature of these interactions depends mainly on the values of the Reynolds number Re_H and the kinematic viscosity ν. In the case of a circular cylinder, for $Re_D \approx 47$ (with $D \equiv H_{Body}$ in Eq. 1.6), an absolute instability described as a *Hopf bifurcation* occurs (Provansal et al, 1987). The equilibrium between the reverse flow trapped in the core of the wake and the flow entrained by the mixing layers is broken and vortex shedding starts to become visible. As described by Gerrard (1966), the shear layer separating from one side of the cylinder rolls up into a vortex, fed by the circulation from the same shear layer, until the vortex becomes strong enough to interact with the opposite shear layer across the wake. At this point, the accumulation of oppositely-signed vorticity cuts off further supply of circulation to the vortex, which as a result ceases to increase in strength and is convected (*shed*) downstream, allowing the formation of a new vortical structure on the opposite side. A periodic process, known as *von Kármán vortex street*, is established, and a reduction in the length of the time averaged recirculation bubble is seen. A more accurate description of the shedding cycle was proposed by Perry et al (1982), based on the evolution of the saddle points on the body contour. As shown in Fig. 1.3a and Fig. 1.3e, three saddles points can be seen on the afterbody (two saddles located at the separation points and a third saddle corresponding to an instantaneous attachment point). A 'separatrix' streamline joins one of the separation saddles with the reattachment point, defining a closed region delimiting the growth of the vortex. As the vortex develops, this region expands (Fig. 1.3b - 1.3c and Fig. 1.3f - 1.3g). The shedding of the vortex indeed occurs when the attachment saddle, during its motion across the base, reaches the separation point opposite to the one it stems from (Fig. 1.3d and 1.3h). At this point, the two joining saddles disappear from the body surface replaced by a new saddle point in the wake, the feeding of vorticity is interrupted and the vortex is convected downstream (1.3a and Fig. 1.3e).

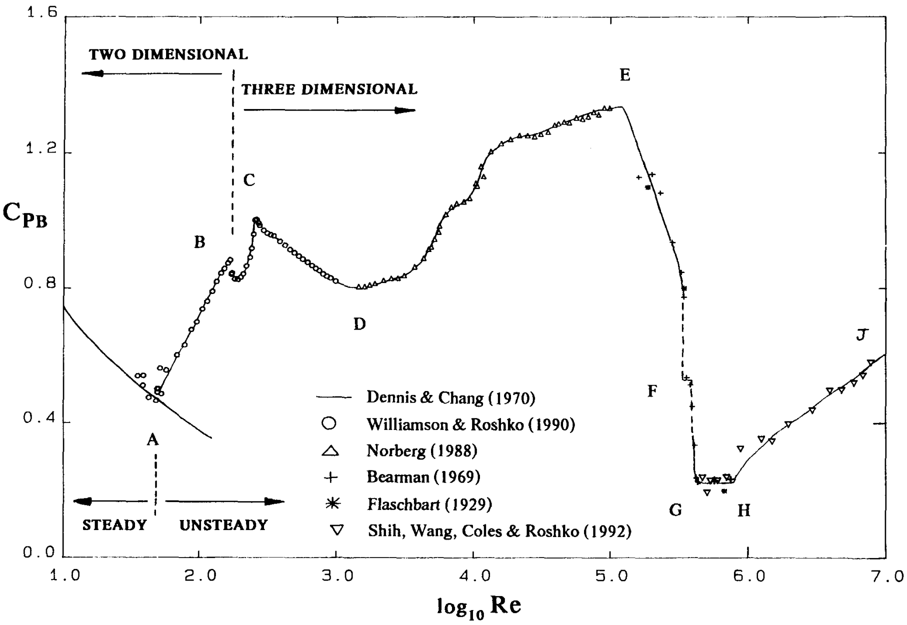

Figure 1.4: Plot of base pressure coefficient for a generic bluff body over a large range of Reynolds numbers. Picture from Roshko (1993).

Von Kármán vortices are sources of low pressure in the wake, which in turn affects the aerodynamic forces exerted on the body, and are responsible for between 35% and 55% of the Reynolds stresses measured in the wake downstream of circular cylinders (Cantwell and Coles, 1983). Indeed, a strong correlation between mixing layer activity, vortex formation, recirculation length and drag can be seen. As pointed out by Roshko (1954), for a given body, a decrease in the shedding frequency is usually accompanied by an increase in the *formation length* (defined by the position of the point downstream of the body where the level of velocity fluctuations is higher), which in turn yields a dampening of the Reynolds stresses and reduction of the base suction (Bearman (1965), Parezanović and Cadot (2012)).

As the Reynolds number increases, three dimensional features become visible, even in the case of nominally two-dimensional conditions (as described in Roshko (1993) and Williamson

(1996)). Laminar vortices are shed up to $Re_D \approx 190$ (regime **A-B** in Fig. 1.4). As the wake instabilities are amplified, the Reynolds stresses in the near-wake region increase whilst the formation length is reduced, yielding an increase in the base suction. Under these conditions, oblique shedding has been reported in some experiments, with different patterns depending on the configuration of end plates considered. For $190 \lesssim Re_D \lesssim 260$ (regime **B-C** in Fig. 1.4), the laminar periodic wake undergoes a transition to turbulence while the base suction continues to increase. New three-dimensional phenomena can be seen in this regime, in the form of vortex loops, streamwise vortex pairs and vortex dislocations. In the range $260 \lesssim Re_D \lesssim 10^3$ (regime **C-D** in Fig. 1.4), the $3D$ streamwise vortical structures become increasingly disordered, with a reduction in the two-dimensional Reynolds stresses and an increase of the formation length. As a result, the base suction, after having reached a peak at $Re_D \approx 260$ starts to decrease. An opposite trend is seen for $10^3 \lesssim Re_D \lesssim 2 \cdot 10^5$ (regime **D-E** in Fig. 1.4), following the development of the Kelvin-Helmholtz instability at the shear layers bounding the wake. Vortices are generated in the shear layer at a frequency of $St \approx Re^{3/2}$ (Bloor, 1964). The turbulent transition point has been reported to move upstream as Re increases. For $2 \cdot 10^5 \lesssim Re_D \lesssim 5 \cdot 10^5$ (regime **E-F-G** in Fig. 1.4) the so called *critical transition* occurs. The formation of a separation-reattachment bubble energises the boundary layer delaying its separation, resulting in a reduced wake and lower base suction. The symmetry in the flow field is lost at $Re_D \approx 3.5 \cdot 10^5$ (point **F** in Fig. 1.4) where the separation-reattachment bubble appears only on one side of the body and shows a bi-stable behaviour (Bearman (1969), Schewe (1983) and Lehmkuhl et al (2014)). The symmetry is restored in the *supercritical regime* (regime **G-H** in Fig. 1.4). A further increase of the Reynolds number ($Re_D \gtrsim 6 \cdot 10^5$, regime **H-J** in Fig. 1.4)) leads to the motion of the turbulent transition point further upstream until, for values of high enough Re, the boundary layer on the surface of the cylinder becomes turbulent prior to separation. In these conditions, separation occurs further upstream, yielding higher base drag and, although the wake is fully turbulent, periodic vortex shedding is still visible (Roshko, 1961).

In the case of bluff bodies with sharp trailing edges the dependence with Re is much weaker, although additional parameters start to play a role. For non-circular geometries, the vortex shedding frequency has been shown to be affected by the ratio between the longitudinal and transverse dimensions as well as the value of the incidence angle between the body and the onset flow (see for example Okajima (1982), Knisely (1990), Norberg (1993), Huang et al (2010) and Schewe (2013)). In these cases, an asymmetric vortex shedding is seen for values of the incidence angle greater than zero, as the points of separation located at the windward and leeward sides of the body move to different locations. Combining changes in the angle of incidence with variations of the afterbody shapes, Luo et al (1994) reached the conclusion that when the separated shear layers are curved inwards by the presence of a tapered surface, they tend to interact more quickly resulting in a more rapid vortex shedding and hence a higher Strouhal number. Asymmetric vortex shedding has been shown to occur also when the cylinder is placed in proximity to a wall. As described in the work of Shi et al (2010) for a square cylinder tested at $Re_H = 2.25 \cdot 10^3$, vortex shedding becomes weaker as the body is moved close to the wall, although the characteristic frequency of the shedding tends to increase slightly (Kim et al, 2003). Vortex shedding disappears for a gap less than 20% of the body height, replaced by a large and stable separation bubble forming close to the base. The value of the critical gap at which vortex shedding disappears is not constant but depends on Re (Bhattacharyya and Maiti, 2004).

1.1.7 Wakes of 3D geometries

When three dimensional bodies are considered, vortex shedding is still present, although it is significantly weakened by three dimensional effects. In these conditions, streamwise vortices can be seen in the wake (Bearman, 1997). These vortices can originate in the forebody region and interact with both the flow around the body and the near-wake (Martinuzzi et al, 1993). The flow field is heavily affected by the body's width-to-height ratio W/H (with W and H indicating respectively the spanwise and transverse dimensions). Martinuzzi et al (1993), for instance, showed that the middle region of the wake developing downstream of a prismatic body, immersed in a fully turbulent channel flow, was nominally 2D for $W/H > 6$, whereas 3D interactions between the wake and the horseshoe vortex forming upstream of the body could not be neglected for $W/H < 4$. Norberg (1994) reported a bi-modal behaviour when testing a circular cylinder with $W/D < 7$ (with $D \equiv H$), attached to circular endplates with a diameter $D_{EP} = 10D$ and $Re_D \approx 2 \cdot 10^3$. In these conditions, the flow was seen to switch between a regular vortex shedding and an 'irregular' state.

This review will focus on bodies with $W/H \approx 1$ since they are the most relevant to the topic discussed in the present thesis. The simplest geometries with such property are the bodies of revolution.

The flow behind an axisymmetric body is usually dominated by a global instability, which plays an important role in the laminar-turbulent transition of the wake. As shown by Bohorquez et al (2011) and Bury and Jardin (2012), at low Reynolds numbers the wake of a bluff body with a blunt base undergoes two successive bifurcations from an axisymmetric steady state. The first is a steady bifurcation with an azimuthal wavenumber $|m| = 1$, characterised by a double threaded wake structure. In these conditions the flow is no longer axisymmetric but it is still steady and preserves a reflectional symmetry around a fixed plane passing trough the axis of the body. As the Reynolds number is increased, a Hopf bifurcation with $m = \pm 1$ occurs, leading to the formation of an unsteady flow field dominated by the shedding of alternating hairpin-like vortices, each composed by two streamwise legs connected downstream by a cross-flow section. Nevertheless, the flow still preserves a reflectional symmetry due to the eccentricity of the vortex shedding. Bury and Jardin (2012) demonstrated that the values of Re_D at which these bifurcations occur depend on the ratio between the length of the body and its diameter (L/D). For a body with $L/D = 7$, the first regime was observed at $450 < Re_D < 590$ (Fig. 1.5a) whilst the second regime occurred for $Re_D > 590$ (Fig. 1.5b). For higher values of Re_D, a chaotic regime was reported (Fig. 1.5c). In this regime, the reflectional symmetry is broken, although a reflectional symmetry plane still exists in an instantaneous sense. The plane of the shedding, in fact, is reoriented randomly and intermittently over a very long time scale. A second mode, with a characteristic frequency lower than the natural shedding frequency, was also identified by the same authors and linked to the fluctuations seen in the drag values.

Similar regimes have been observed over the years for the wakes of other axisymmetric bodies, such as spheres and circular flat discs (Kiya et al, 2001), although with some differences. Fabre et al (2008) pointed out the existence of two additional vortex shedding modes for the wake behind a flat disc. The first mode, dubbed *reflectional symmetry breaking* mode was reported to be characterised by the twisting of the main vortical structures around the body's axis of revolution. It was seen to originate from the steady symmetric state, following a Hopf bifurcation at $Re_D = 123$ and it was proven to be unstable, using linear stability analysis. A second mode was found at $Re_D \simeq 140$ and described as a *standing wave* mode. Similar modes were also found by Auguste et al (2010) for the wake behind a disc with $L/D = 1/3$.

The effects of the bifurcating oscillatory modes seen in the laminar regime persist at high Reynolds numbers, resulting in the shedding of large coherent structures. In the case of a disc, the near-wake dynamics have been shown to be dominated by the action of antisymmetric modes with $m = \pm 1$ and a constant shedding frequency (Fuchs et al, 1979). In addition, hairpin vortices are shed from the disc for $Re_D > 10^3$; the angle of the shedding, however, changes irregularly

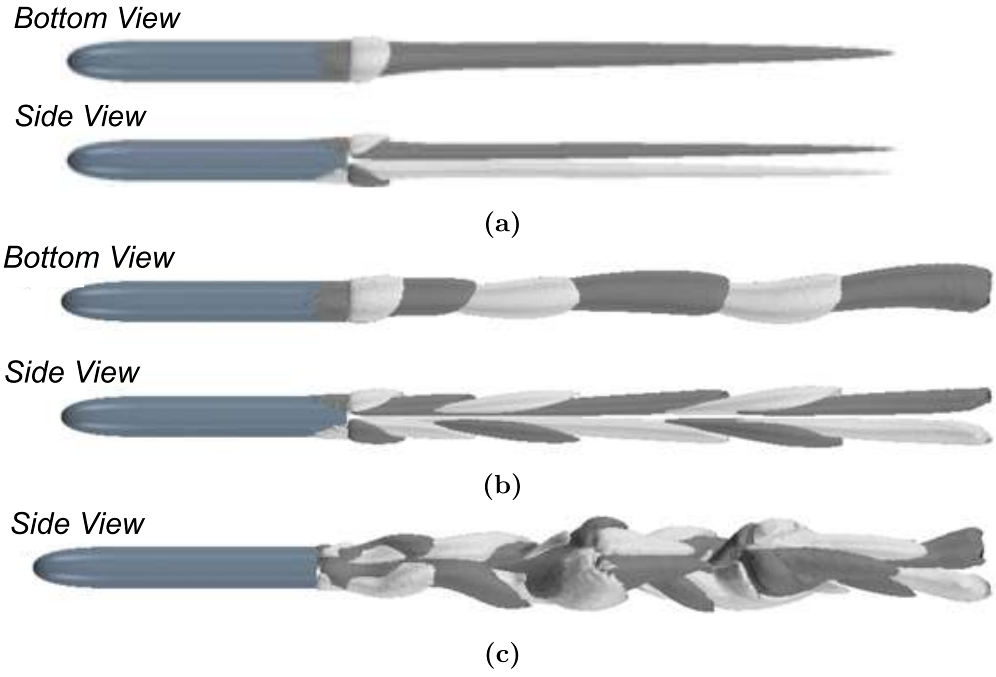

Figure 1.5: Iso-contours of normalised streamwise vorticity $= \Omega^* D/V_\infty$ obtained at $Re_D = 550$ **(a)**, $Re_D = 700$ **(b)** and $Re_D = 900$ **(c)**. Plots from Bury and Jardin (2012).

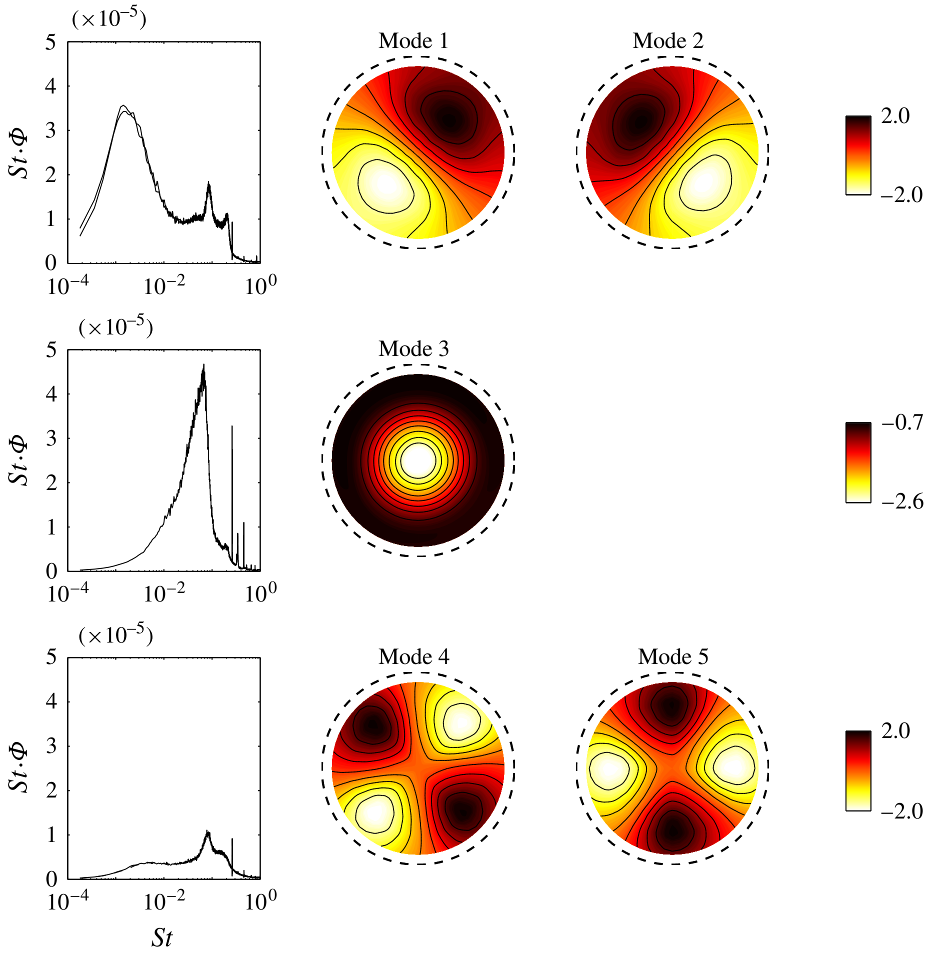

Figure 1.6: First five POD modes extracted from the fluctuating part of the pressure dataset recorded over the base of an axisymmetric bluff body with $L/D = 6.48$, tested at $Re_D = \simeq 2 \cdot 10^5$. Plots from Rigas et al (2014).

from cycle to cycle, as pointed out by Miau et al (1997). For the same geometry, a second mode with $m = 0$ was observed by Berger et al (1990). This mode, known as *'pumping mode'*, was described to be the result of the alternate expansion and shrinkage of the separation bubble, with a characteristic frequency of $St_D = 0.05$. An unsteady vortex shedding with $St_D \simeq 0.2$, reminiscent of the $m\pm = 1$ symmetry-breaking laminar instabilities, was found by Rigas et al (2014) to be the most energetic structure in the wake downstream of an axisymmetric bluff body with $L/D = 6.48$, tested at $Re_D = \simeq 2 \cdot 10^5$. Applying proper orthogonal decomposition (POD, see §2.4.1) to a set of pressure data recorded over the base (see Fig. 1.6), it was shown that the shedding is asymmetric and rotates randomly around the body's axis of revolution at a frequency of $St_D \simeq 0.002$. The reflectional symmetry, however, was reported to be still visible when a rotating reference frame was considered. As a result, two distinct time scales were identified for the evolution of the flow, a short-time scale at $T_s \simeq 5D/V_\infty$, associated with the vortex shedding, and a long-time scale at $T_l \simeq 5 \cdot 10^2 D/V_\infty$, referring to the rotation of the reflectional symmetry plane of the shedding mode. In the frequency range corresponding to the short-time scale, three distinct peaks were isolated. The first peak at $St_D \approx 0.06$ was linked to the pumping motion (Berger et al, 1990), since it was found to be mostly evident for the 3^{rd} POD mode, showing an $m = 0$ symmetry. A second peak at $St_D \approx 0.20$ was linked to the vortex shedding. This peak was found in the frequency spectra associated with the first pair of POD modes, characterised by an $m = \pm 1$ symmetry. Between these two frequencies, a third peak was also isolated at $St_D \approx 0.10$. This last peak was inferred to be a sub-harmonic of the main shedding mode, since its presence was seen in the spectra of both the first pair and the second pair of POD modes, with the latter pair showing a $m = \pm 2$ symmetry (see Fig. 1.6). Rigas et al (2015) have then showed that the long-time and short-time dynamics can be modelled using a nonlinear two-dimensional Langevin equation (Lemons and Gythiel, 1997) consisting of a deterministic part, describing the symmetry breaking modes occurring at the laminar and transitional regimes, and a stochastic term, accounting for the turbulent fluctuations of the large scale structures. Most recently, the findings of Rigas et al (2014) have been confirmed by the results of the cross-planar time-resolved PIV acquisitions carried out by Gentile et al (2016). In this case, an axisymmetric body with $L/D = 5$ was tested at $Re_D = 6.7 \cdot 10^4$ performing stereoscopic PIV at different azimuthal planes, located downstream of the model base. The application of snapshot POD (see §2.5.3) to the fluctuating part of the velocity vector showed the existence of the same anti-symmetric mode with $m = \pm 1$. This mode was found to be responsible of the long-time erratic motion of the reverse flow in the region close to separation, whereas more downstream it was linked to the fluctuations originating from the shear layer. A second mode pair with $m = \pm 2$, representing the wake ovalisation, was also identified, together with an axisymmetric mode with $m = 0$ (visible only close to the base) describing the streamwise pulsation of the reverse flow region. For the same axisymmetric blunt body with $L/D = 5$, Gentile et al (2017) pointed out that a variation of the model's pitch angle as small as $0.2°$ is enough to suppress the low-frequency large scale dynamics. In these conditions, the centroid of the backflow region was found to be displaced from the model axis and constrained to move around the off-centre position visible in the time averaged field. A similar level of sensitivity of the time averaged wake topology had been previously reported in the case of small variations of the model's yaw angle (Wolf and Stumpf, 2014). The very low frequency mode has been shown to be highly sensitive also to perturbations of the boundary layer before separation as well as alterations of the turbulent shear layer bounding the wake. A similar effect to that produced by a small variation in the angle of the onset flow, with the selection one stable asymmetric state, was reported by Grandemange et al (2012b) perturbing the wake behind an axisymmetric bluff body with an $m = 1$ disturbance, represented by a control cylinder. In the same study, the number of preferred positions of the wake was seen to increase to two when a perturbation with an azimuthal wave number of $m = 2$ was applied (in the form of a pair of wings attached to the main body, upstream of the line of separation), resulting in a bi-stable behaviour. Similar results were also obtained in the case of a sphere (Grandemange et al, 2014a). Nevertheless, the considerations made in §1.1.6, about the link between base pressure and mean recirculation length as well as the connection between recirculation length and location of the incipient shear layer instability, still hold, as pointed out by the findings of Mariotti and Buresti (2013) and Mariotti et al (2015).

Similarly rich dynamics have been reported in the case of non-axisymmetric bodies. The simplest example of such geometries is an elliptic disc set normal to the free-stream flow. A body with such a shape was studied by Kiya and Abe (1999) at $Re = 2 \cdot 10^4$. They reported the existence of two distinct components of the velocity fluctuations in the wake. The fluctuation associated with the higher frequency was found to be centred around the minor axis of the body and was linked to the alternate shedding of hairpin-like vortices. The second (lower) frequency, on the other hand, was mostly evident along the major axis and was associated with a meandering motion of the wake. When the distance between the shear layers was reduced, by decreasing the aspect ratio W/H, an increase in the values of the frequency peaks associated with these dynamics was observed. A low-frequency amplitude modulation of the velocity fluctuations along both axis was also reported and it was described as the result of the alternate enlargement and shrinkage of the wake along the two axis, in contrast with the description of the pumping motion provided by Berger et al (1990), where the longitudinal motion of the wake appeared to be in phase over the entire base of the disc. Similar trends were found when the elliptical plates where swapped with rectangular plates. The fluctuations seen around the major axis were reported to eventually disappear for $W/H \gtrsim 40$; a this point the normalised frequency of the fluctuations around the minor axis was found to tend to the value of the 2D plate.

As seen in the case of the vortex shedding past 2D or axisymmetric bodies, the flapping motions around the body's axes of symmetry are reminiscent of the unsteady global instabilities occurring at low Reynolds number, as shown by the linear stability analysis performed by Marquet and Larsson (2015) at $40 \lesssim Re_H \lesssim 120$, for $1 \leq W/H \leq 6$. In this case, a Hopf bifurcation corresponding to an unsteady global mode breaking the top/bottom symmetry was found for $2.5 \leq W/H \leq 6$, whilst a second Hopf bifurcation breaking the left-right symmetry was identified for $2 \leq W/H \leq 2.5$. For lower aspect ratios ($1 \leq W/H \leq 2$), a steady symmetry breaking global mode, similar to that previously described for axisymmetric bodies, was also identified. This mode was indeed found to be responsible of the long-time stochastic dynamic behaviour described by Cadot (2016) for the wake of a rectangular plate with $W/H \approx 1$, tested at $Re_H = 2.64 \cdot 10^5$. In this study, a multi-stable behaviour with some similarities with that described by Rigas et al (2014) in the case of an axisymmetric body, was documented and its contribution to the loads acting on the plate was shown to be much greater than that of the vertical flapping associated with vortex shedding (at least for $W/H > 1/6$).

Similar dynamics have been described in the case of prismatic bodies with $L > W$. A long time bi-stable behaviour was documented by Herry et al (2011), studying the wake

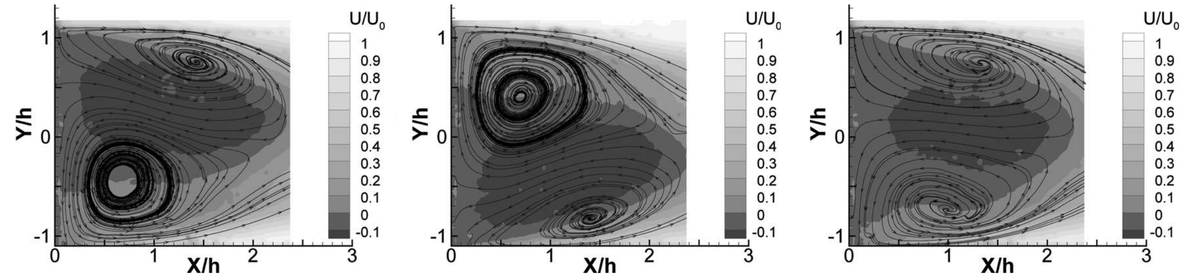

(a) *L State* **(b)** *R State* **(c)** Time averaged field

Figure 1.7: 2D horizontal PIV fields from Herry et al (2011): **a** *L State*, **b** *R State*, **c** time averaged field.

developing downstream of the upper portion of a 3D double backward facing step tested at $5 \cdot 10^3 \leq Re_H \leq 8 \cdot 10^4$ (with H referring to the height of the first step). Two different solutions, corresponding to two lateral symmetry breaking configurations were found around 0° yaw. Each configuration, when analysed using a horizontal 2D PIV plane centred with the first step, showed the existence of two different vortical structures: a big circular vortex acting close to the base of the step, on one side, and a smaller elliptical vortex forming further downstream close to the side shear layer, on the opposite side (Fig. 1.7a and 1.7b). The time averaged wake topology (Fig. 1.7c) was indeed found to be the result of a linear combination between these two states. The preferential selection of one of the two solutions for small variations of the yaw angle was also noticed. Most recently, a similar bi-stable behaviour has been described for other prismatic bodies, such as the square-back Ahmed model (Ahmed et al, 1984). A review of the literature concerning the characterisation of the flow field around this geometry as well as other simplified vehicle shapes is presented in §1.2.2.

1.2 Vehicle aerodynamics

Despite the more than a century history of the automotive industry, vehicle aerodynamics is still a relatively young subject. The first cars, because of the low speeds that they could reach, were no more than simple coaches with internal combustion engines replacing the horses. The interest towards aerodynamic concepts, initially developed by the aeronautical industry, begun to grow in the period between the two world wars, when the major car companies of that era started to develop more streamlined cars in their pursuit of new speed records. However, aerodynamics was still considered a ‘niche’ subject, mainly confined to the racing world. The drag reductions achieved in those years on mass production cars were in fact essentially byproducts of improvements in body construction techniques or new styling trends. Only with the oil crisis of the 1970’s, did car manufacturers recognise aerodynamics as a valuable ally in their quest for new means for lowering the fuel consumption of their fleets.

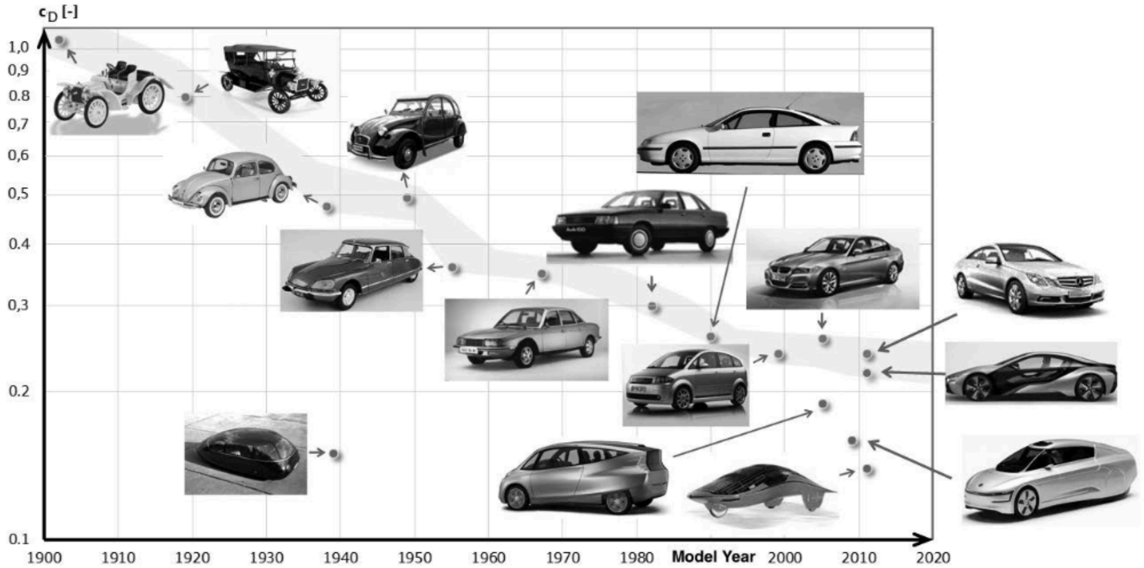

Figure 1.8: Drag trend throughout the automotive history. Plot from Schuetz (2016).

As a consequence, air drag started to decrease very quickly, although after a few years the improvement rate slowed down until reaching an asymptotic value ($C_D \approx 0.30$) between the 1990's and first decade of the 21^{st} century (Fig. 1.8). This 'barrier' has been broken only in the last few years, pushed by the growing environmental awareness as well as the need to meet ever stricter regulations in terms of CO_2 emissions (EC-No-443/2009, 2010).

Different strategies have been adopted to lower fuel consumption, including powertrain and tyres optimisation, vehicle electrification and weight reduction. These measures, however, tend to focus on reducing the power required to accelerate or move the vehicle at low speeds. At higher (constant) speeds, a significant reduction of the fuel consumption can be achieved only by cutting the aerodynamic losses. For a car travelling at $180\,kph$ (or $50\,m/s$), for example, a 20% reduction of the aerodynamic drag alone can result in a fuel saving of $1.5l/100\,km$, accompanied with an increase in the maximum speed achievable and better performances in terms of acceleration and drivability (Schuetz, 2016).

The lower drag figures recorded in the last few years have been achieved mainly by optimising the way air flows around the wheels and underneath the car, adopting better strategies for the management of cooling flows and enhancing pressure recovery at the afterbody.

1.2.1 Aerodynamic forces acting on a vehicle

As air flows around its body, the vehicle experiences more than just drag. The resultant aerodynamic force has components in all six degrees of freedom (3 forces and 3 moments as

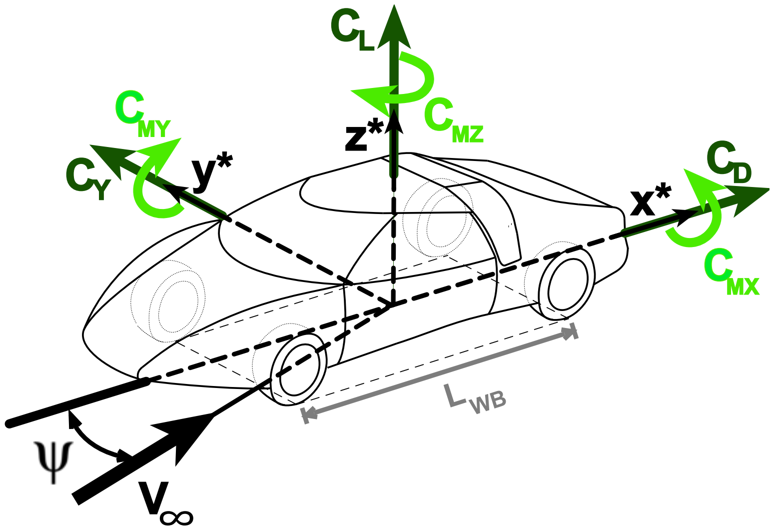

Figure 1.9: Aerodynamic forces and moments acting on a vehicle. Figure based on SAE (2010).

shown in Fig. 1.9). As can be seen by rewriting Eq. 1.24 in the form

$$F_i = \frac{1}{2}\rho V_\infty^2 S_{Body} C_{fi}, \tag{1.26}$$

the magnitude of of each component is proportional to the squared velocity V_∞ and varies in a linear fashion with the air density ρ, the vehicle frontal area S_{Body} and the force coefficient C_f; with the latter depending on the particular shape considered (§1.1.4). In the case of aerodynamic moments, a third length must be considered. For automotive geometries, it is usually represented by the vehicle wheelbase L_{WB}.

Similarly to the SAE reference system, the component of the aerodynamic force are defined as follows: drag **D** is aligned with the longitudinal body axis **x** and positive backwards; lift **L** acts along the vertical direction **z** and is positive upwards; side force **S** is aligned with the body's transverse axis and it is positive when pointing towards the right-hand-side of the model. Three components of the aerodynamic moment can also be identified, namely the rolling moment **MX** (aligned with **x**, positive clockwise), the pitching moment **MY** (aligned with **y**, positive counterclockwise) and the yawing moment **MZ** (aligned with **z**, positive clockwise). For the sake of simplicity, only the related coefficients will be considered in the present work.

Traditionally, automotive engineers distinguish between the vehicle behaviour in still air (*handling*) and in the presence of crosswind (*crosswind sensitivity*). In the first case, the flow approaching the vehicle is considered symmetric about the vehicle's longitudinal plane of symmetry. In such conditions, drag C_D, lift C_L and pitching moment C_{MY} are the only aerodynamic components acting on the car. Generally, the vertical force on a bluff body close to the ground is positive, in the sense that it tends to lift the vehicle. The consequent decrease in the load acting on the tyres, reduces the maximum lateral force that each tyre can generate, resulting ultimately in a degradation of the car handling performances. The dynamic behaviour of the vehicle, on the other hand, is mostly influenced by the pitching moment, linked to the lift distribution between the front and rear axles. Changes in the load distribution between the two axles can lead to noticeable variations of the steering properties of the vehicle. At high speed, reducing the values of rear axle lift has been found to significantly improve the steering feeling. When crosswind is present, a side force C_Y is produced, together with yawing C_{MZ} and rolling C_{MX} moments. At the same time, drag and lift are altered too. Side force and the yawing moment, however, are generally assumed to be the only components to produce important effects on the vehicle dynamics. The yawing moment, in particular, is often used to provide a first indication of the vehicle's crosswind sensitivity. Sometimes, the handling qualities of a vehicle can also be altered by unsteady aerodynamic features, difficult to identify in the time averaged flow field, as documented in Kawakami et al (2015).

1.2.1.1 Aerodynamic drag

In normal conditions (at zero degree yaw and no gusts), drag is by far the strongest aerodynamic force experienced by a passenger car. The most relevant contribution to the drag experienced by the vehicle is the so called 'pressure drag'. This element represent between 80% and 90% of the drag experienced by the entire vehicle (Schuetz, 2016). Friction resistance, on the other hand, is less relevant.

Strictly linked to drag is the presence of large streamwise trailing vortices that originate in different regions of the car's body and interact with the wake. From a fluid-dynamic point of

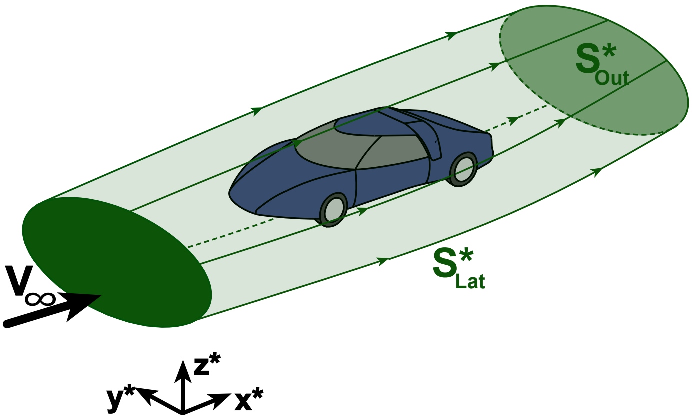

Figure 1.10: Stream tube around the model. S^*_{In}, S^*_{Lat} and S^*_{Out} denote respectively the inlet surface, the lateral surface and the outlet surface bounding the control volume. All surfaces have been normalised considering the square of the model height H_{Body} as reference.

view, the wind-axis drag (equivalent to the body-axis drag at null yaw angle) can be determined by applying the streamwise momentum equation to a large control volume containing the vehicle (Fig. 1.10). Bearing this in mind, Onorato et al (1984) rewrote the momentum equation 1.4 in a form that expresses C_D in terms of three integrals across the stream tube containing the body:

$$C_D S^*_{Body} = 2\int_{S^*_{Out}} (p^*_{0,In} - p^*_{0,Out})\, dS^* - \int_{S^*_{Out}} (1-u^*)^2\, dS^* + \int_{S^*_{Out}} (v^{*2} + w^{*2})\, dS^*, \tag{1.27}$$

where S^* denotes non dimensional surfaces (normalised considering the square of the model height H_{Body}) while $p^*_{0,In}$ and $p^*_{0,Out}$ refer to the values of the non dimensional total pressure at the inlet and the outlet of the control volume defined in Fig. 1.10 (having normalised p_0 according to Eq. 1.5). The first term in the Eq. 1.27 describes the difference in stagnation pressure between the inlet and the outlet; the second term quantifies the longitudinal velocity deficit (associated with the development of transverse vortices at the base of the vehicle) while the third term represents the so called *'vortex drag'*.

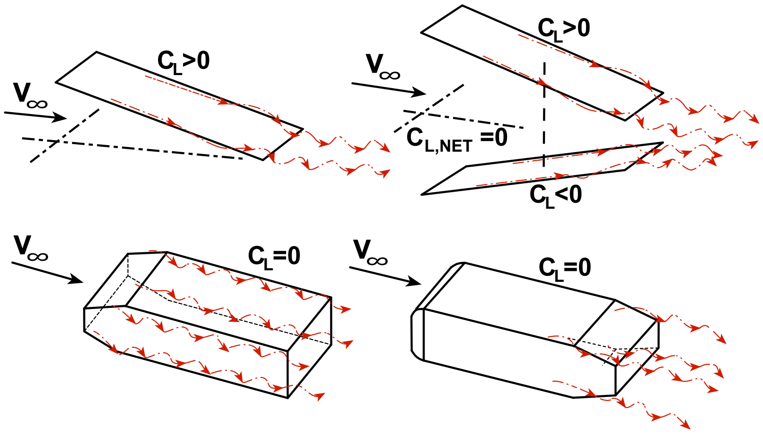

Figure 1.11: Schematic examples of longitudinal streamwise vortices generated by lifting and non-lifting bodies. Picture from Hucho and Sovran (1993).

Contrary to the case of finite-span wings, vortex drag contributes to the overall drag even when $C_{L,NET} = 0$, with $C_{L,NET}$ indicating the net lift (see Fig. 1.11). This can be ascribed to the fact that, as pointed out by Morelli (1983) and Howell and Le Good (2004), lift is a function of the sum of the strengths Γ^*_i of different vortex pairs

$$C_L = C_L\left(\sum \Gamma^*\right), \tag{1.28}$$

with $\sum \Gamma^* = \Gamma^*_1 - \Gamma^*_2 + \Gamma^*_3$, whereas drag is a function of the *overall* vortex strength, independent on the sign of the rotation

$$C_D = C_D\left(2\sum \mid \Gamma^* \mid\right), \tag{1.29}$$

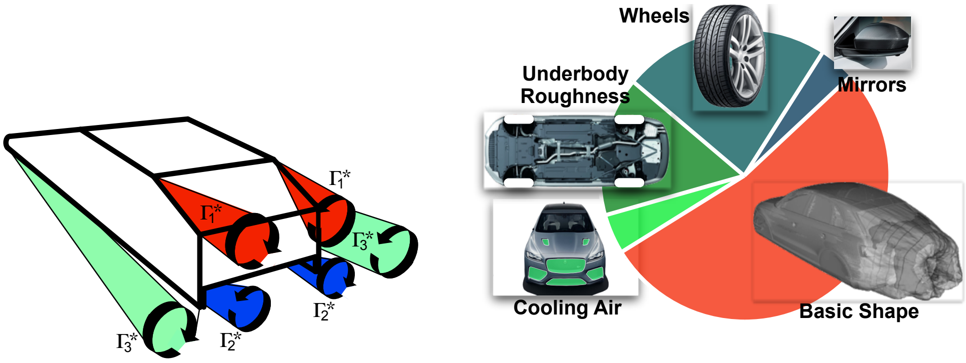

(a) (b)

Figure 1.12: **a** schematic representation of trailing vortices developing downstream of a simplified vehicle (sketch from Howell and Le Good (2004)). **b** drag breakdown usually adopted by car aerodynamicists (based on Schuetz (2016)).

where $\sum |\Gamma^*| = \Gamma_1^* + \Gamma_2^* + \Gamma_3^*$ (see Fig. 1.12a). Vortex drag has been found to account for $\approx 30\%$ of the total aerodynamic drag experienced by fastback cars (Fig. 1.14). This value has been reported to drop to $\approx 10\%$ in the case of estate cars (Ahmed, 1981).

A more practical approach for car aerodynamicists is to split the drag in different contributions depending on their origin. According to this classification, as can be seen in the pie chart reported in Fig. 1.12b, most of the drag ($\approx 55\%$ of the overall drag) is originated by the basic shape of the vehicle itself, consisting of the vehicles's outer shell with no wheels or cooling systems and with filled wheel wells and a smooth underbody. This also justifies the use of simplified geometries for ground vehicle aerodynamic investigations, as discussed in §1.2.2. The second highest contribution to the overall drag is represented by the wheels and the way they interact with the main body flow. Elements contributing to the overall drag are also the cooling system, underbody roughness and add-on parts such as mirrors, antennas, etc.

1.2.2 Simplified automotive geometries

In vehicle aerodynamics the use of simplified reference models is quite common. These models are usually simplified reduced-scale bluff bodies that preserve the main aerodynamic features of real cars. They have been used over the years mainly for validation and research purposes, allowing light to be shed on some fundamental aspects of the flow behaviour around ground vehicles. Examples of such models are the Ahmed model 1.13a, the Windsor body 1.13b, the Davis model 1.13c and SAE geometry 1.13d.

The Ahmed body was employed for the first time by Ahmed et al (1984) with the aim of investigating the effect of the backlight angle on the dramatic increase in drag experienced by early hatchback cars (see §1.3.5.1). It is a box shaped model with rounded front edges to delay the flow separation along the lateral surfaces and sharp edges around the rear face. For its particular shape it is well suited to represent the flow field around MPVs and vans

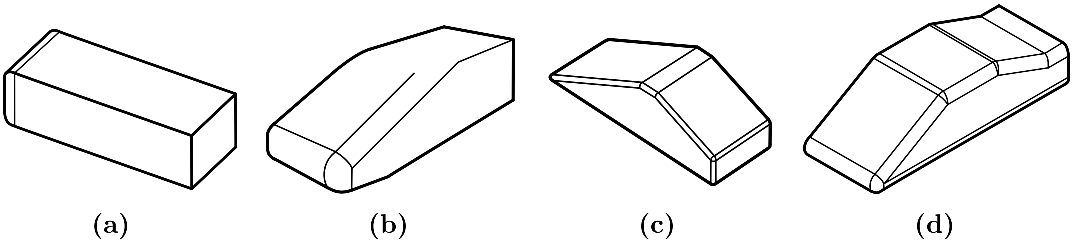

Figure 1.13: Schematic representation of the most commonly used simplified models: **a** Ahmed model, **b** Windsor body, **c** Davis model, **d** SAE geometry.

(Grandemange, 2013).

The Windsor body was developed by Rover in the 1980's and it has been used since then in several research activities, focusing mostly on fundamental aspects of car Aerodynamics. The model preserves the dimensions and aspect ratio of the Ahmed body, but features a slanted front-end more representative of passenger cars. Applications of such geometry can be found in Littlewood (2013) and Perry (2016b).

The SAE model was proposed in SAE (1997) and used for the first time by Cogotti (1998) in a parametric study focusing on the effects of ground simulation on wind tunnel testing. Over the years it has found application in several research activities, focusing mostly on the validation of numerical simulations (Ishima et al, 2011).

Quite popular among researchers is also the Davis model, introduced by Davis (1982). It is a 10^{th} scale model with interchangeable front- and rear-ends and a diffuser. Most recently it has been used in crosswind and unsteady aerodynamics studies (Fuller and Passmore (2013) and Forbes (2017)).

All the models mentioned above are highly simplified and lack many features present on production cars. In order to overcome these limitations and provide some insights into series development, the Technische Universität München, in cooperation with Audi AG® and BMW Group® have proposed a new more realistic model, known as the *DrivAer* model (Fig. 1.14). This model is representative of a typical medium-size vehicle and includes rotating wheels, three interchangeable top rear-ends and two different underbodies, allowing to test the most common passenger car configurations. So far, it has been successfully used both for experimental

Figure 1.14: Schematic representation of the DrivAer model. Pictures from Heft et al (2012).

(Strangfeld et al (2013) and Wieser et al (2014)) and numerical investigations (Ashton and Revell, 2015). Nevertheless, its high level of detail (with features such as door handles, side mirrors and and engine compartment) is not needed in the case of more fundamental research.

1.3 Wake topology and dynamics

The topology and the size of the wake behind a vehicle, and the related pressure losses, are strictly determined by the vehicle shape, especially in the base region (Fig. 1.15). The present work focuses on the square-back configuration, typical of estate cars, SUVs and commercial vehicles. An in depth description of the topology of the wakes developing behind fastback and notchback cars can be found in Baden Fuller (2012) and Wood (2015).

1.3.1 Square-back geometry

The time averaged topology of the wake of a square-back vehicle is commonly described as a ring vortex (Fig. 1.16a), as reported in Krajnovic and Davidson (2003), Rouméas et al (2009a) and Perry et al (2016). This structure results from the pressure drop at the model base. The topology of the ring vortex is altered in the presence of slanted surfaces (Ahmed et al (1984) and Howell (1993)), ground effect (Wang et al (2013) and Pellerin et al (2016)) and wheels (Wood et al, 2015). In all cases, however, the dynamics of such wakes is characterised by a level of complexity similar to that seen in §1.1.7 for other 3D shapes.

Using a square-back model similar to that of Ahmed et al (1984) with a width-to-height ratio of 1, Duell and George (1999) observed the existence of a periodic pumping mode of the wake caused by the interaction between the upper and lower parts of the ring vortex (Fig. 1.16b), similar to that seen in §1.1.7 in the case of axisymmetric bodies. This mode was shown to trigger periodic fluctuations of the base pressure, with a model height based Strouhal number of $St_H = 0.069$. Similar results were obtained by Khalighi et al (2001) and Khalighi et al (2012), performing experimental and numerical investigations using a different square-back geometry with an aspect ratio W/H of 1.4. The same mode was also found by Al-Garni et al (2004)

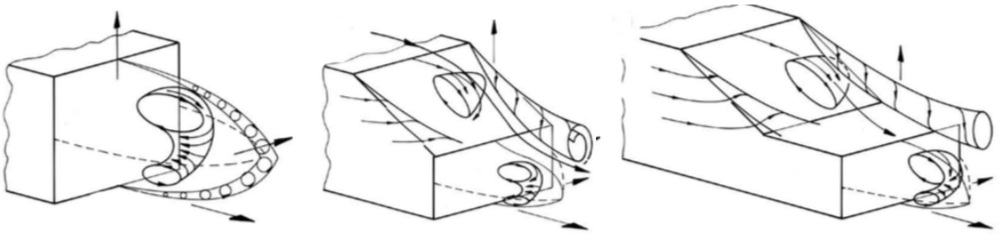
(a) (b) (c)

Figure 1.15: Schematic representation of the wake topology behind **a** square-back, **b** fastback and **c** notchback geometries. Sketches from Schuetz (2016).

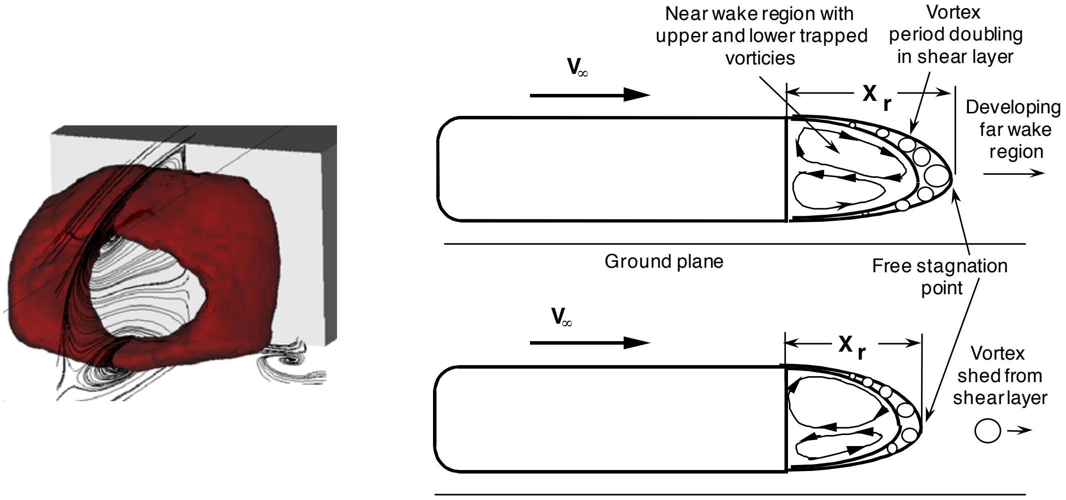

(a) (b)

Figure 1.16: **a** time averaged topology of the near-wake developing downstream of a simplified square-back body, from Rouméas et al (2009a) (iso-surface drawn considering the total pressure loss coefficient C_{p_l}, with $C_{p_l} = 1.17$). **b** schematic representation of the pumping mode behind a square based Ahmed body (sketch from Duell and George (1999)).

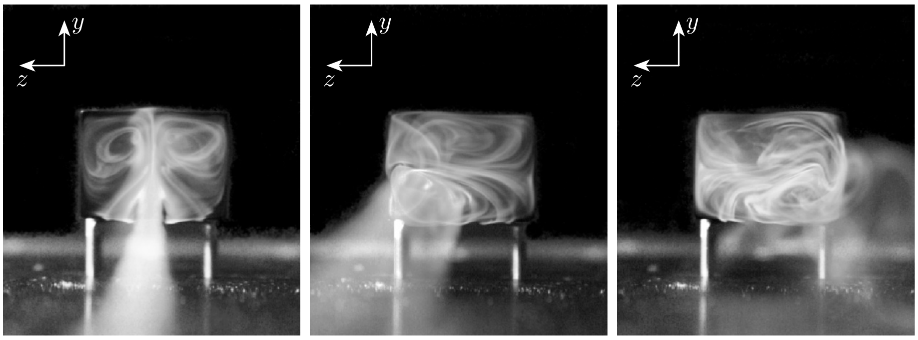

(a) (b) (c)

Figure 1.17: Flow visualisations of the wake developing behind an Ahmed body at **a** $Re_H = 310$, **b** $Re_H = 365$ and **c** $Re_H = 415$. Pictures from Grandemange et al (2012a).

during an experimental campaign aiming to characterise the main features of the wake of a simplified SUV model.

For the wake behind a simpler geometry (a $26mm$ high Ahmed body tested in a low speed hydrodynamic facility) Grandemange et al (2012a) reported the existence of a permanent reflectional symmetry breaking state (Fig. 1.17). A first bifurcation from the trivial symmetric state (Fig. 1.17a) to a steady reflectional symmetry breaking state (Fig. 1.17b) was observed at a model height based Reynolds number Re_H of 340. The reflectional symmetry breaking state was reported to become unsteady after a second bifurcation at $Re_H = 410$ (Fig. 1.17c), resulting in a bi-stable behaviour that has subsequently been demonstrated at Reynolds

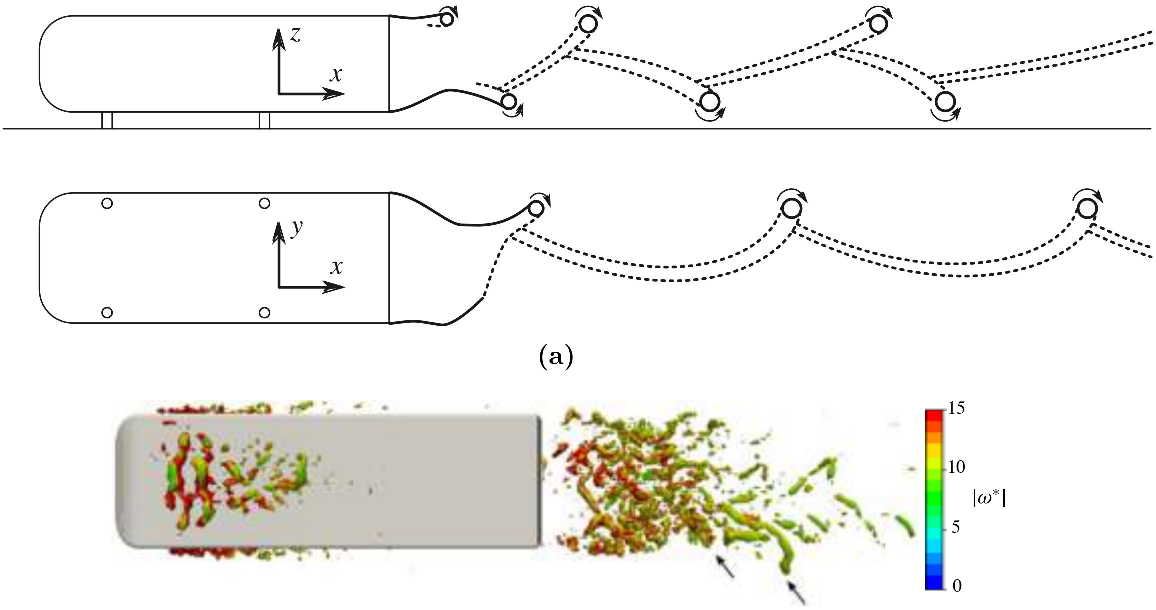

(a)

(b)

Figure 1.18: **a** schematic representation of the short time scale modes for the wake behind a square-back Ahmed body; sketch from Grandemange et al (2013b). **b** wake visualisation of the Q-criterion ($Q^* = 22$) coloured by the magnitude of the normalised vorticity; the arrows indicate vortex loops shed from side shear layer (see Lucas et al (2017)).

numbers up to 10^7 (Grandemange et al, 2015). A similar trend has been recently identified in the LES simulations carried out by Evstafyeva et al (2017). The bi-stable behaviour was further characterised by Grandemange et al (2013b), testing an Ahmed body in a 3/4 open jet wind tunnel at $Re_H = 9.2 \times 10^4$. In these conditions, it was found that the characteristic time between switches can be estimated as $T_l \sim 10^3 H/V_\infty$, where V_∞ is the free-stream velocity. The succession of reflectional symmetry breaking states was initially thought to behave like a stationary Markov chain, although more recent findings from Varon et al (2017a) suggest that this low-frequency dynamic may be considered as a weak chaotic process with two attractors. In Grandemange et al (2013b) it is also shown that this long period motion yields an unsteady side force, that was inferred to be responsible for part of the drag. This conclusion has later found confirmation in the IDDES simulations performed by Lei et al (2017) considering the same geometry. Grandemange et al (2013b) reported also the existence of a shorter time scale $T_s \sim 5H/V_\infty$. This scale was attributed to weak coherent oscillations of the wake in the vertical and lateral directions, caused by the interactions of top-bottom and lateral shear layers (Fig. 1.18a). These oscillations have been subsequently shown to be linked to the shedding of vortex loops (Fig. 1.18b), as pointed out in Lucas et al (2017). The two distinct time scales (T_l and T_s) present strong similarities with those reported in §1.1.7, in the case of axisymmetric bodies.

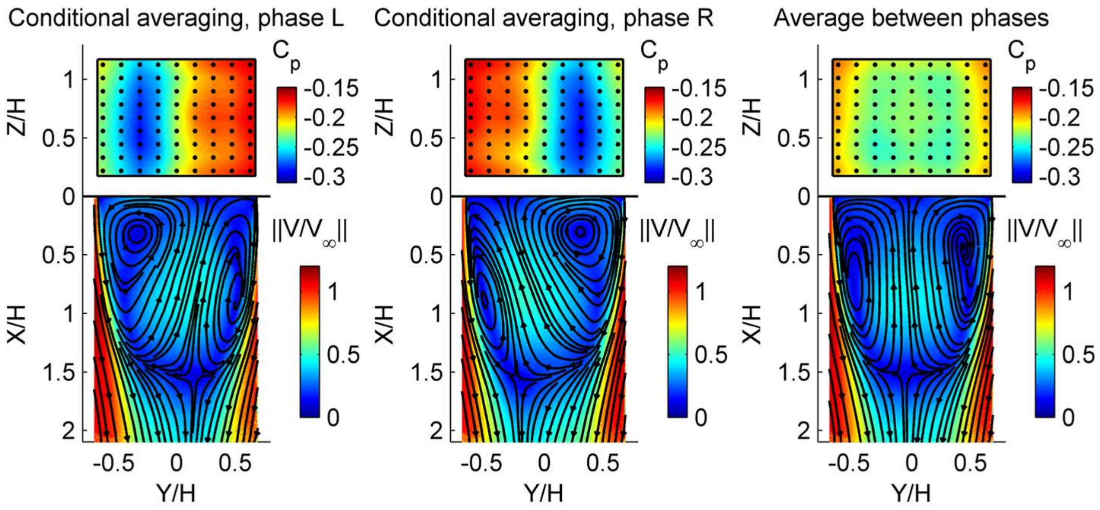

(a) (b) (c)

Figure 1.19: Visualisations of the two bi-stable states by means of base pressure tappings and horizontal 2D PIV: **a** *L State*, **b** *R State*, **c** average of the two states. Plots from Volpe et al (2015).

Evidence of the existence of the pumping mode was not found by Grandemange et al (2013b). However, the existence of this mode was later confirmed by Volpe et al (2015), performing wind tunnel tests using the same geometry but at higher Reynolds numbers ($Re_H = 5.1 \cdot 10^5$ and $Re_H = 7.7 \cdot 10^5$). In this study, the existence of a bi-stable behaviour was also reported, together with the other two short-time scale modes. The wake pumping, with a normalised frequency of $St_H = 0.08$, was found to be predominant in the shear layer of the recirculation bubble whilst the other two modes, with $St_H = 0.13$ and $St_H = 0.19$, were found to be more visible downstream of the wake closure. Furthermore, the wake topology associated with each bi-stable mode was reconstructed using spatial conditional averaging of multiple planes of 2D-2C PIV data as well as base pressure tappings. The results suggested the existence of a deformed toroidal structure for each state (Fig. 1.20a), with lower pressure developing in the region of the model base closer to the circular vortex seen from the horizontal 2D PIV plane (Fig. 1.19a and 1.19b). This was reported to cause the development of a horizontal pressure gradient that was seen to disappear only when the lateral symmetry was restored, by combining for example the two states together (Fig. 1.20a), in agreement with the previous findings of Grandemange et al (2013b). The sensitivity of bi-stability to small variations of the yaw angle Ψ was also investigated; when a value of $\Psi = 0.4°$ was imposed, a 70% predominance of one of the two reflectional symmetry breaking states was encountered, matching the results obtained by Herry et al (2011) for a 3D backward facing step (§1.1.7).

The time dependent structure of the bi-stable states was further investigated by Evrard et al (2016), who proposed a horseshoe vortex structure (Fig. 1.20b) for each state. According to the same authors, it is the temporal average of these asymmetric structures that results in the toroidal vortex that is traditionally reported in vehicle aerodynamics. This speculation, however, did not find confirmation in the results of the numerical simulations carried out by Lucas et al (2017) considering the same model. In this case, the topology of the symmetry breaking state was visualised using pressure iso-surfaces, revealing the existence of a deformed torus with no connections with the streamwise vortices forming outside of the rear recirculation (Fig. 1.20c). Nevertheless, it is worth highlighting the fact that the use of pressure iso-surfaces as a mean of isolating vortical structures, although very easy to implement in a numerical simulation, usually leads to a loss of detail in the resolution of the vortical structures, since, as stated by Jeong and Hussain (1995), *'pressure is inherently of a larger scale than vorticity'*.

Focusing on the effects of base aspect ratio on the bi-stable mode, Grandemange et al (2013a) showed a bi-stable motion of the wake in the lateral direction for $W > H$ and in the vertical direction when $H > W$, further highlighting the existence of strong analogies between this phenomenon and the multi-stable behaviour described for axisymmetric bodies (§1.1.7). An *'interfering region'*, where the vertical and lateral reflectional symmetry breaking modes may coexist, was in fact isolated for $0.77 \lesssim W/H \lesssim 1.30$ at a non dimensional ground clearance $C^* > 0.08$, where $C^* = h/H$, with h referring to the distance between the bottom flat surface of the model and the ground. Within this range, it was postulated that instabilities from both the shortest and the largest side may occur, although the limit case expected for $W/H = 1$ was not observed in the experiment, arguably due to the presence of residual asymmetries in the experimental setup (such as the four pins used to hold the model in place) that triggered the selection of the vertical symmetry breaking mode as soon as $W/H < 1.05 \pm 0.05$. The link between the wall-normal pressure gradient and the long-time wake dynamics was further investigated by Barros et al (2017), considering an Ahmed body with $W/H \approx 1.18$ and a ground clearance of $C^* \approx 0.17$, tested at at $Re_H = 3 \cdot 10^5$. Different passive devices (including horizontally or

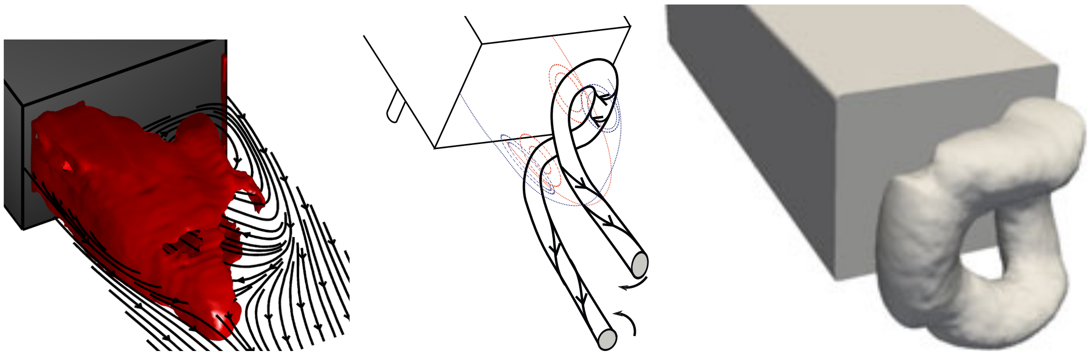
(a) **(b)** **(c)**

Figure 1.20: Proposed topologies for the reflectional symmetry breaking state: **a** velocity iso-surface for $V/V_\infty = 0.1$ (Volpe et al, 2015), **b** sketch based on 2D mid-horizontal and mid-vertical PIV planes (Evrard et al, 2016), **c** iso-surface of mean pressure coefficient $C_p = -0.320$ (Lucas et al, 2017).

vertically aligned cylinders with different diameters and turbulence grids with different mesh sizes) were used to perturb the flow passing underneath the model before separation. The results showed that the restoration of the flow symmetry along a plane normal to the ground was always accompanied with the occurrence of a bi-stable motion of the wake in the spanwise direction, revealing the existence of a bifurcation scenario where the flow switches between a wall-normal asymmetric recirculation and a bi-stable spanwise configuration. During the transition between these two scenarios, meandering motions of the wake between asymmetric wall-normal and spanwise states were also described, although without the presence of a perfect bimodal distribution (Fig. 1.21). These conclusions agree with the trends reported by Perry (2016b), investigating the effects produced on the bi-stable mode by high aspect ratio tapers applied to the top and bottom trailing edges of a square-back Windsor body (§1.3.5.1). In these conditions, a progressive reduction of T_l was seen as the symmetry of the wake along the mid-vertical plane was progressively worsened, by either increasing the upwash or downwash. No information, however, was provided about either the magnitude of the reductions of T_l or its impact on the aerodynamic forces exerted on the model.

In Grandemange et al (2013a) when a configuration with $W/H = 0.75$ was tested at different values of the ground clearance C^*, a bi-stable behaviour was seen only for $C^* = 0.10$ and $0.50 \leq C^* \leq 1.00$, whereas a stable state, asymmetric in the vertical direction, was reported for $0.1 < C^* < 0.5$, with $\partial C_p/\partial z^* < 0$ over the model base. The same asymmetry can be seen in the base pressure data collected by Cabitza (2014) considering a prismatic model with $W/H = 0.86$ tested at a ground clearance of $C^* = 0.56$. In that case, the author speculated that the cause of the asymmetry was to be found in the proximity of the model with the ground. Nevertheless, when the shear layers were perturbed using synthetic jets and the sensitivity of the system to different forcing frequencies and amplitudes was tested, a bi-stable behaviour was seen along both vertical and spanwise directions. Interestingly, the control strategy yielding the lowest drag was found to stabilise the wake in a non symmetric configuration, aligned with one of the two diagonals of the base (§1.3.5.2). Similar results in terms of time averaged base pressure distribution were reported by Perry (2016b), testing a square-back model at $C^* \approx 0.2$, with $W/H \approx 1$ and a leading edge radius of $r/W \approx 0.10$ (Fig. 1.22a). It is clear from this case that the time averaged velocity field along the model centreline (Fig. 1.22b) presents strong similarities with the two lateral symmetry breaking states shown in Fig. 1.19a and 1.19b, featuring a circular vortex acting close to the base (responsible of the low pressure area visible on the upper half of Fig. 1.22a) and an elliptical vortical structure forming along the bottom shear layer, in proximity to the wake closure. Perry (2016b) reported also the appearance of a bi-stable motion, mostly along the y^* direction, when the boundary layer developing along the lateral surfaces of the model was perturbed by changing the ride height ($0.13 \lesssim C^* \lesssim 0.33$) and/or altering the shape of the model front-end considering different leading edge radii ($0.10 \lesssim r/W \lesssim 0.26$). A comparable topology was reported by Van Raemdonck and Van Tooren (2008), for a prismatic model with $W/H = 0.74$ tested at $C^* = 0.14$, with a

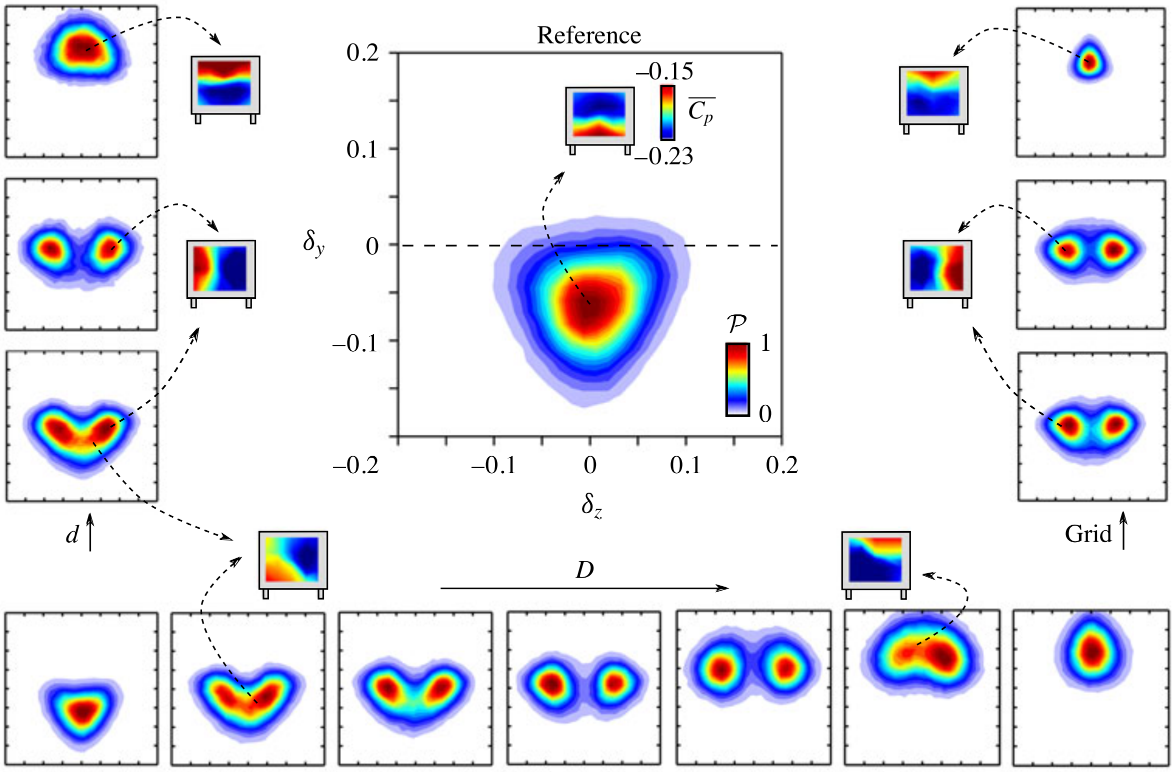

Figure 1.21: Diagram of normalised probability distribution $P(\delta_y, \delta_z)$ of pressure gradients for perturbed wakes (based on experimental measurements). Reference flow presented at the centre of the picture. The arrows indicate increasing (non dimensional) size of the perturbation applied to the model underbody: $d = 0.020, 0.027, 0.054$ for the circular cylinder spanning the entire width of the model; $D = 0.027, 0.067, 0.084, 0.10, 0.17, 0.20, 0.24$ for the vertical cylinder mounted in the symmetry plane; grid with coarse, medium and fine mesh. Plot from Barros et al (2017).

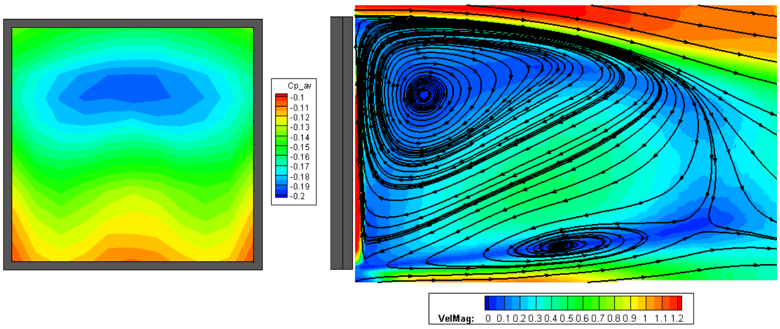

(a) **(b)**

Figure 1.22: Time-averaged base pressure distribution **a** and velocity field **b** at $y^* = 0$ for an Ahmed body with $W/H \approx 1$ and a front edge radius of $r/W \approx 0.10$, tested with a ground clearance of $C^* \approx 0.20$. Plots from Perry (2016b).

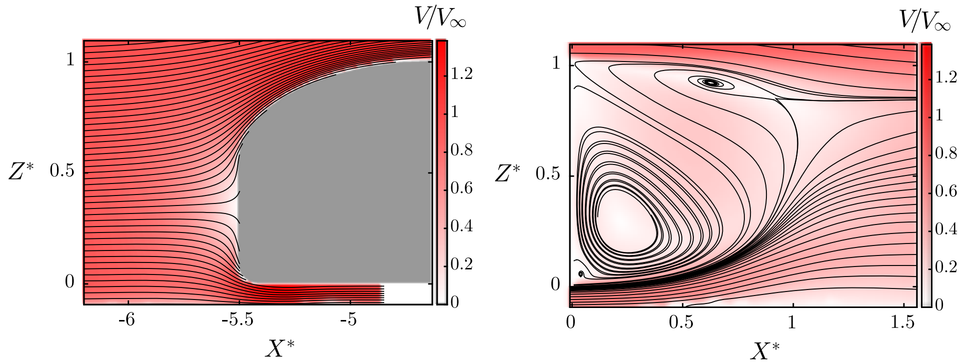

(a) **(b)**

Figure 1.23: Time averaged velocity field at $y^* = 0$ from McArthur et al (2016): **a** front-end of the model, **b** rear-end of the model.

length-to-height ratio ($L/H = 4.70$) closer to that of the model employed by Cabitza (2014) ($L/H = 5.61$) than that used in Perry (2016b) ($L/H = 2.22$). However, no information was provided on the wake dynamics. A certain level of asymmetry in the vertical direction had been previously reported for the wake behind an Ahmed body with $W/H = 1$ by Krajnovic and Davidson (2003), performing the LES simulations. The asymmetry, however, was found to almost disappear when the level of refinement of the mesh was increased, further suggesting the existence of a strong relationship between the boundary layer development and the wake's size and topology. A stable vertical asymmetry can also be seen in the experimental results collected by McArthur et al (2016). In this case, although the model employed had strong similarities with that considered by Van Raemdonck and Van Tooren (2008) ($W/H = 0.74$, $C^* = 0.14$, $L/H = 5.49$), the topology of the wake along the model centreline was shown to be a mirror image of that described in the previous cases (Fig. 1.23b). One explanation for this may be found in the different shape of the model front-end (Fig. 1.23a), featuring an upper leading edge with a radius ($r/W = 2.35$) almost 20 times larger than radii used for the side and lower leading edges ($r/W = 0.12$). Nevertheless, the short-time wake dynamics described in Volpe et al (2015) were still recognisable, with a pumping motion occurring at $St_H \approx 0.08$ (limited to the upper portion of the wake) and a lateral flapping seen at $St_H \approx 0.17$. For a similar geometry, Castelain et al (2018), reported a switch from an upwash dominated stable wake to a downwash dominated stable wake when the underbody blockage was increased from $\approx 0\%$ to $\approx 90\%$.

Traces of bi-stable dynamics on a more realistic geometry were found by Grandemange et al (2015), considering an Ahmed body scaled to a full size small car, tested at $Re_H = 2.5 \times 10^6$ and equipped with four rotating wheels. The presence of a lateral bi-stable motion was inferred from the large fluctuations seen in the side force signal, recorded at $10Hz$ for $40s$, for values of the yaw angle Ψ ranging between $-0.5°$ and $+0.5°$. In the same range, the drag was seen to remain constant. The dependency between C_D and Ψ was then confirmed by Bonnavion et al (2017a), assessing the presence of bi-stability in the wake behind a commercially available light van. A bi-stable regime between two different positions of the reverse flow impinging on the base was reported when the model was at yaw. In this case, however, the reflectional symmetry breaking mode was found to have an effect mainly on the vertical component of the aerodynamic force, since the model height was greater than the width, in agreement with the conclusions drawn in Grandemange et al (2013a). In all these studies, however, the values considered for the free stream turbulence intensity TI^* (with $TI^* = \sqrt{\overline{(u^{*\prime}(t))^2}} \cdot 100$) did not exceed 0.4% (Bonnavion et al, 2017a). This is one order of magnitude lower than that suggested by the data measured in on-road conditions (Watkins and Saunders (1995), Newnham (2007) and Wordley and Saunders (2008)). Additional research in this field is therefore needed.

1.3.2 Rear window inclination

The rear-end of passenger cars is usually quite far from being perfectly squared. In fact, a slanted upper surface appears on the afterbody of many vehicles (usually at the rear window). The length and angle of the slant can vary over a wide range, depending mainly on stylistic choices and functional needs. The introduction of a backlight angle, besides reducing the base area, yields noticeable changes in the time average and dynamic features of the wake, when compared to those seen in §1.3.1 for the square-back case.

A seminal study in this field was carried out by Ahmed et al (1984) using the model that bears his name. In this work, the sensitivity of the wake topology to variations of the rear slant angle ϕ (with $0° \leq \phi \leq 40°$) was investigated, together with its impact on the aerodynamic drag. It was shown that the time averaged structure of the wake is characterised by a pair of horseshoe vortices (whose existence has been recently confirmed by the findings of Venning et al (2015) and Venning et al (2017)) placed one above the other in the separation bubble forming downstream of the base (Fig. 1.24a and Fig. 1.24c). A pair of counter-rotating longitudinal vortices developing from the side edges of the slanted surface was also seen. The strength of all these vortical structures was shown to be strictly linked to the slant angle. As shown in Fig. 1.24b, for $0° < \phi < 12.5°$, the flow remains attached to the slanted surface and separation occurs only at the rear trailing edge. The strength of the transverse vortical structures decreases with ϕ, resulting in a reduction of C_D, until reaching a minimum for $\phi \simeq 12.5°$. For $12.5° < \phi < 30.0°$, flow separates at the front edge of the slant but then quickly reattaches, leading to the formation of a small recirculation bubble. The size of this bubble increases with the slant angle until $\phi = 30°$. For $\phi \approx 30°$, *high-drag* and *low-drag* regimes coexist. In the *high-drag regime*, the separated flow reattaches just before the trailing edge of the slant or reattaches only partially, mixing with the large separated region downstream of the base (Vino et al, 2005); the strength of the streamwise vortices, source of additional drag (§1.2.1.1), reaches a maximum. In the *lower-drag regime*, the recirculation bubble and the longitudinal vortices seen over the top slant disappear, replaced by a fully separated wake, similar to that described in §1.3.1 for the

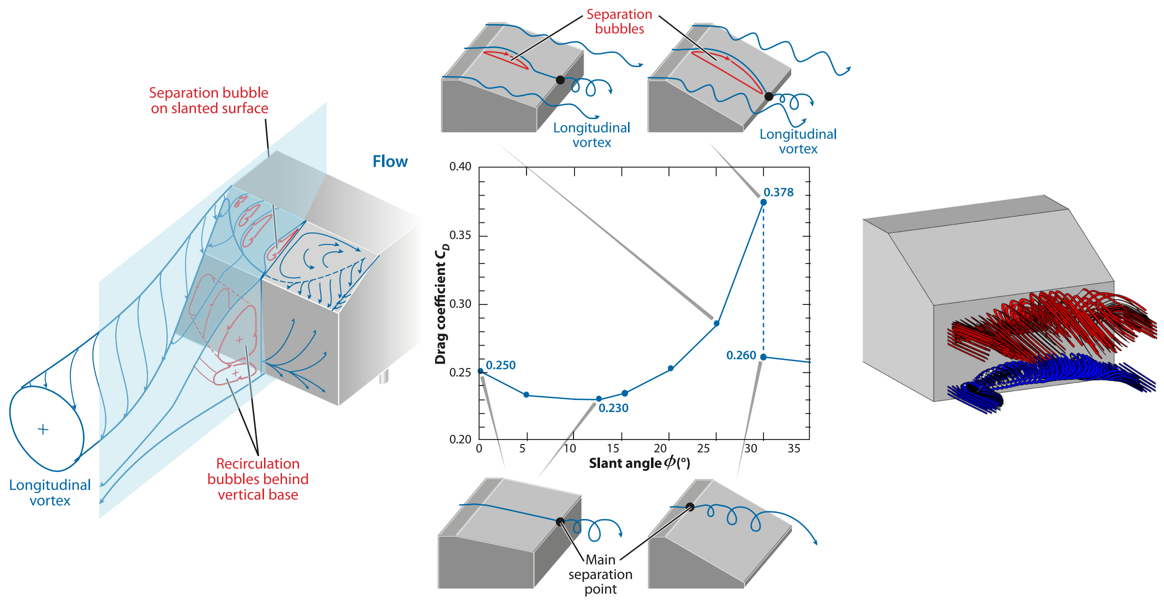

(a) **(b)** **(c)**

Figure 1.24: Aerodynamics of the Ahmed body: **a** time-averaged three-dimensional flow structures in the wake; **b** the drag coefficient C_D versus the slant angle (ϕ). Plots from Choi et al (2014) based on the work of Ahmed et al (1984). **c** time averaged topology proposed by Venning et al (2017) for the wake behind an Ahmed model with a 25° slant.

square-back case. The continuous switching between these two states has been reported to behave like a stochastic process (Kohri et al, 2014) and to have a long-time scale similar to that seen in §1.3.1 for the lateral symmetry breaking mode. It has been shown to disappear for $\phi > 30.0°$, when the *low-drag* configuration becomes the only stable solution (Lienhart and Becker, 2003) .

Although the relationship between C_D and ϕ has been confirmed by several studies over the years, some parameters that can lead to more or less noticeable deviations from the original results of Ahmed et al (1984) have been identified. Performing wind tunnel tests using a Windsor body, Howell (1993) pointed out that rounding the slant leading edge almost eliminates the drag peak at $\phi \approx 30°$, whereas the same peak was reported to reappear, although for much higher values of ϕ, when radii were applied to both front and side edges of the slant. Similar trends were noticed by Thacker et al (2012) and Rossitto et al (2016) considering an Ahmed model with $\phi = 25°$ (see §1.3.5). The back light aspect ratio is another parameter that has been reported to have an impact on $\partial C_D/\partial\phi$, as well as the value of C_D recorded in the minimum-drag case (Howell and Le Good, 2008). In fact, a reduction in c/W (with c denoting the length of the slant) has been associated with a noticeable increase of $C_{D_{min}}$. The model height-to-width ratio has also been reported to produce significant effects on C_D. Venning et al (2015) and Corallo et al (2015) demonstrated that the *'drag crisis'*, seen at $\phi \approx 30°$ in the original experiment of Ahmed et al (1984), can be anticipated at lower slant angles ($\phi \approx 25°$) by increasing the spanwise separation between the rear pillar vortices, until the downwash created by their interaction becomes too weak to promote flow reattachment over the slant. These results have been confirmed more recently by the numerical simulations of Rao et al (2018). In the latter study, the sensitivity of the transitional regime to variations of the yaw angle Ψ was also investigated, considering an Ahmed model with a $35°$ slant. For $|\Psi| \lesssim 12.5°$ only the *low-drag state* was observed. However, when the yaw angle was increased to $|\Psi| = 15.0°$, the *high-drag state* became visible, with flow reattachment over the rear slant aided by the development of strong longitudinal vortices. The simulations succeeded in replicating the trend that had been previously seen in the experimental work of Meile et al (2016), who also showed the existence of a bi-stable switching between the two states for $10° \leq |\Psi| \leq 15°$. The bi-stable mode, however, was not captured in the numerical study. In Meile et al (2016), the bi-stable switching was found to be most pronounced at $\Psi \approx 12.5°$, causing strong variations in the lift and pitching moment (whose sign was reported to change depending on the state selected). Analogous effects were noticed by Bonnavion et al (2017a) for a commercially available hatch-back car featuring a similar backlight angle, when tested at $-8° \leq \Psi \leq -10°$. In these conditions a bi-stable mode, consisting in the alternation between attached and detached flow over the rear slant, was seen for $\Psi \approx 8.6°$ accompanied with noticeable fluctuations of both lift and drag. A lateral symmetry breaking bi-stable mode, similar to that described in §1.3.1 for the square-back case, was instead reported by Varney et al (2017), when the strength of longitudinal vortices developing on either side of the rear upper slant of a simplified generic SUV model was reduced by applying vertical end-plates.

Besides the long-time wake dynamics, additional unsteady features have been identified over the years. In this section the focus is on the *high-drag state*, as the *low-drag state* presents strong similarities with the square-back case already presented in §1.3.1. Up to date, the most complete representation of the quasi-periodic unsteady flow structures characterising this regime is that provided by Zhang et al (2015), testing an Ahmed body with a $25°$ slant at $4.5 \cdot 10^4 \leq Re_{\sqrt{A}} \leq 2.4 \cdot 10^5$ (with A referring to the model cross-sectionl area). In this study, three distinct predominant frequencies were reported in the wake, two of which were isolated on the rear window (Fig. 1.25a). The first mode was found at $0.18 \lesssim St_{\sqrt{A}} \lesssim 0.28$ and linked to the shedding of 3D hairpin vortices from the separation bubble forming at the leading edge of the slant, in agreement with the findings of Krajnovic and Davidson (2005a) and Minguez et al (2008). The continuous release of vortical structures was reported to be the cause of the 'flapping' motion of the rear slant recirculation previously described by Thacker et al (2010). The second unsteady motion was seen at $0.25 \lesssim St_{\sqrt{A}} \lesssim 0.45$ and related to the roll-up of the side shear layers into the discrete vortical structures forming the rear pillar vortices, as pointed out by Sims-Williams et al (2006) (Fig. 1.25b). A strong correlation was found between these two unsteady features and the transverse vortical structures originating from the front-end separation. In the fore-body region, longitudinal vortices, with $St_{\sqrt{A}} \approx 0.14$, were also seen. However, they were reported to disappear for $Re_{\sqrt{A}} > 1 \cdot 10^5$. The third coherent motion

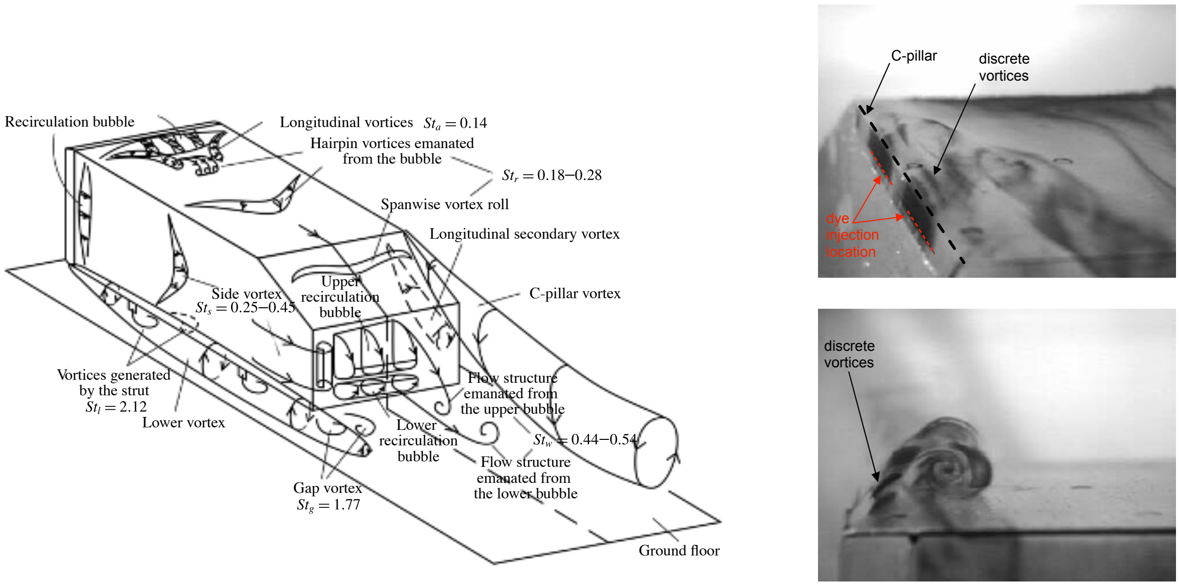

(a) (b)

Figure 1.25: **a** conceptual representation of the flow structures around an Ahmed body with a 25° slant; sketch from Zhang et al (2015), based on instantaneous data. **b** visualisation of the discrete vortices forming periodically at the rear pillar (pictures from Sims-Williams et al (2006)).

isolated in the wake was detected downstream of the model base, for $0.44 \lesssim St_{\sqrt{A}} \lesssim 0.54$. This mode was inferred to be the result of the emanation of coherent structures from the upper and lower recirculation bubbles developing behind the base, confirming the previous findings of Vino et al (2005) and Minguez et al (2008). The process was divided into four different phases, as illustrated in Fig. 1.26. In the first phase, the upper recirculation grows, fed by the flow separating from the upper edge of the base (Fig. 1.26a), until the bubble collapses under its own pressure, drastically reducing its size. As the bubble bursts, weak coherent structures are shed downstream (Fig. 1.26b). After the collapse of the upper recirculation, the bottom recirculation begins to grow, fed by the flow separating from the bottom trailing edge (Fig. 1.26c). As the pressure in the lower bubble rises, exceeding that of the upper recirculation, flow moves from the lower to the upper region of the wake, until the bottom recirculation collapses under its own pressure, releasing coherent structures downstream of the wake closure (Fig. 1.26d). The space left by the lower recirculation is then filled, again, by the upper bubble, which starts to gradually expand in size and rise in pressure, reiterating the process (Fig. 1.26a). A similar frequency ($St_H \approx 0.31$) was reported by Tunay et al (2014), with a maximum located close to the bottom shear layer. Since this was found to be the only frequency visible in the wake for $\phi = 25°$, the existence of a link with the spectral activity found in the slant region was suggested. Nevertheless, when the slant angle was increased at $\phi = 30°$ and $\phi = 35°$,the vortex

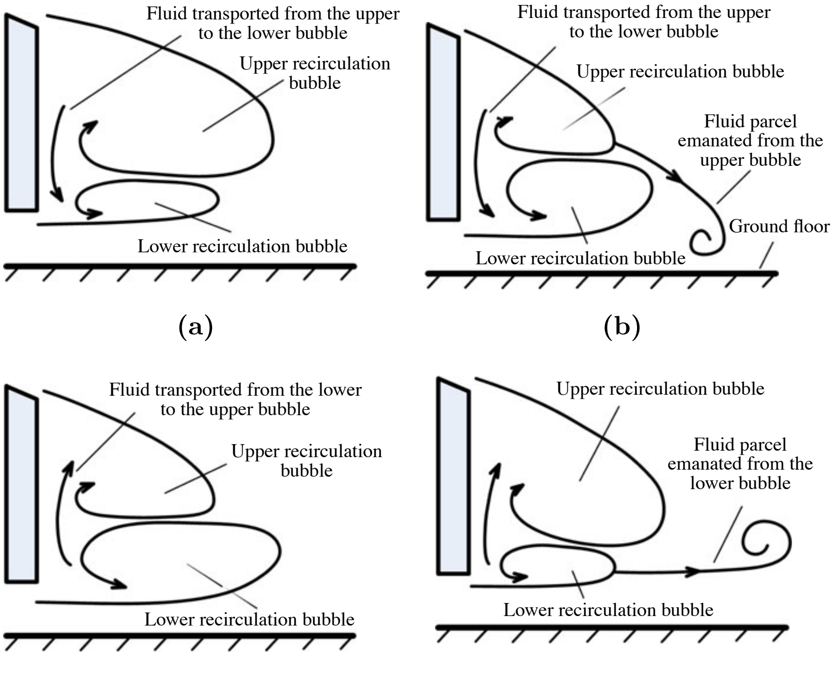

Figure 1.26: Model of the pulsating motion of the two recirculation bubbles. Sketch from Zhang et al (2015).

shedding frequency was seen to decrease respectively at $St_H \approx 0.18$ and $St_H \approx 0.08$. At the same time, a second peak at $St_H \approx 0.22$ was isolated in proximity to the upper shear layer. A lateral flapping motion with similar frequencies was also identified by Tunay et al (2016).

1.3.3 Effect of the ground

The relatively small distance from the ground has been found to produce non-negligible effects on the flow field around cars, albeit to different extents depending on the type of vehicle considered. Ground effect plays a fundamental role in defining the aerodynamic performances of race cars (Katz, 2006). However, it also has an impact on the wakes developing downstream of passenger vehicles. The presence of the ground creates an asymmetry in the flow field, as the flow beneath the body accelerates due to the ground constraint, yielding a reduction in the underbody static pressure which ultimately contributes to the generation of downforce (Cooper et al, 1998). As the ground clearance C^* is reduced, the vertical symmetry seen in time averaged wake behind a square-back geometry (§1.3.1) is lost (Pellerin et al, 2016). The bottom recirculation starts to increase in size at the expenses of the top one. The wake torus is progressively squeezed towards the model base until disappearing for $C^* \approx 0$, replaced by an arch shaped vortex (Martinuzzi et al, 1993).

A variation of the ground clearance also introduces changes to the vortex shedding, as already pointed out in §1.1.6 in the case of 2D geometries. As a model is moved close to the ground, two 'gap vortices' develop at the lower corners of the body (Fig. 1.25a), driven by the pressure difference between the sides and the underbody (Krajnovic and Davidson (2005a), Wang et al (2013)). Considering an Ahmed body with different rear slant angles, Strachan et al (2007) showed that the strength of the gap vortices is somehow linked to that of the rear pillar vortices developing over the rear slant. It was noticed that the formation of stronger rear pillar vortices had the effect to force more flow from the underbody upwards, thus reinforcing the gap vortices. Zhang et al (2015) isolated in the underbody region two different frequency peaks at $St_{\sqrt{A}} \approx 2.12$ and $St_{\sqrt{A}} \approx 1.77$. These coherent motions were related to the vortices shed respectively from the front and rear cylindrical struts connecting the model to the floor. For an Ahmed body with a 25° slant, a change in C^* has been found to yield modifications in the strength of the side vortices as well as the rear pillar vortices (Wang et al, 2013). For a square-back shape, similar variations have been shown to affect also the tendency of the wake to develop a bi-stable behaviour (Perry (2016b), §1.3.1). Grandemange et al (2013a) showed that the bi-stable mode was suppressed when $C^* \lesssim 0.08$, although it was still seen in the lateral direction at $C^* = 0$ (when $W > H$), whilst Cadot et al (2015) pointed out that the minimum value of ground clearance needed to trigger a bi-stable behaviour decreases with increasing Re.

Noticeable variations in the time averaged topology were reported by Makihara et al (2016), for the near-wake developing downstream of a simplified model of a commercially available hatchback car, tested without wheels. In that case, the application a shallow diffuser at the end of a smooth underbody was found to promote a drastic change in the near-wake topology, as a consequence of the increase in the volume-flow rate underneath the car itself. For each case (with and without the bottom taper in place), two different upper body configurations were considered, with either a squared or a slanted upper rear-end. For the squared upper-body case, the wake was seen to switch from a toroidal shape (Fig. 1.27a) to a more elongated structure (Fif. 1.27b) when the diffuser was removed. For the slanted upper-body case, the removal of the bottom taper resulted in the strengthening of the two streamwise vortices forming at either side of the rear bumper (Fig. 1.27c and 1.27d).

Another element that affects the generation of aerodynamic forces around a vehicle is the way ground is simulated. Considering an Ahmed body equipped with adjustable rear upper slant and underbody diffuser, Howell (1994) showed that a moving floor produced, when compared with the stationary ground, higher drag and lower lift for almost all combinations of upper slant angles ϕ_t and diffuser angles ϕ_b. One exception was the case with $\phi_t = 25°$ and $\phi_b = 0°$, for which the moving ground was found to yield a reduction in C_L but no change in C_D. This configuration was object of further investigation in the LES simulations carried out by Krajnovic and Davidson (2005b). In contrast with the experimental results of Howell (1994), the motion of the floor was reported to reduce both drag and lift, respectively by 8% and 16%. Changes in the flow field between the two cases (stationary and moving ground) were seen, in

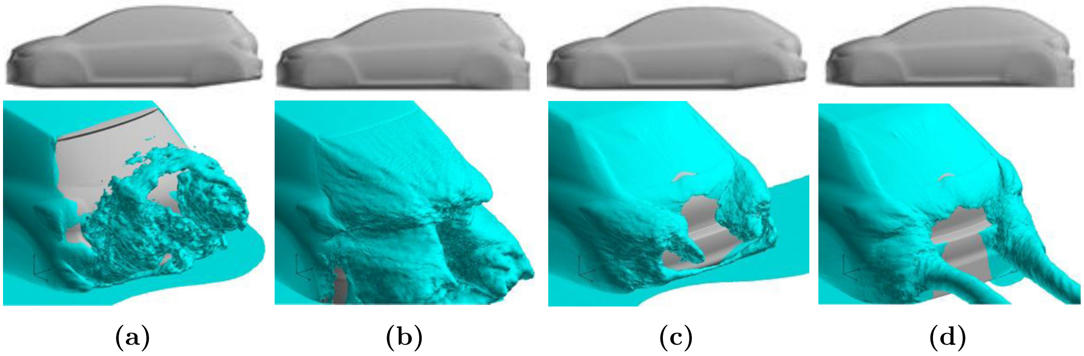

Figure 1.27: Vortical structures developing behind the model of a simplified hatchback car without wheels (Makihara et al, 2016). **a** square-back configuration with a shallow diffuser; **b** square-back configuration with a squared bottom trailing edge; **c** model with a 30° rear slant and a shallow diffuser; **d** model with a 30° rear slant and a squared bottom trailing edge. **a**, **b**, **d** iso-surfaces of $C_{p_0} = -0.12$; **c** iso-surface of $C_{p_0} = -0.02$.

particular close to the floor and in proximity to the rear slant. The motion of the floor was found to alter also the wake dynamics, as suggested by the different shapes obtained for the power spectral density of both lift and drag. One dominant frequency peak indeed was seen in the spectra of C_L and C_D in the moving ground case, as compared to the more scattered spectra reported for the stationary case.

1.3.4 Wheel Aerodynamics

Wheels and wheelhouses produce significant effects on the aerodynamic performances of passenger cars. Their contribution to the overall drag has been estimated between 25% and 40%, depending on the particular shape considered (Wickern et al (1997), Elofsson and Bannister (2002)). Besides their own drag, wheels also strongly interact with the vehicle underbody, further increasing the overall drag. Understanding the flow field around these elements and its interactions with the rest of the car is therefore of paramount importance.

1.3.4.1 Isolated wheel

Although the flow around isolated wheels has been the object of several investigations over the years, the scientific community is still divided on some aspects concerning the topology of the flow developing around a rotating wheel. Fackrell and Harvey (1975) performed the first experimental investigation of an isolated wheel in realistic conditions, considering a rotating wheel in contact with a moving floor at $Re_D = 5.3 \cdot 10^5$. A high pressure region, source of lift (Pirozzoli et al, 2012), was described upstream of the wheel-ground contact patch, together with a lateral jet stream (dubbed *'jetting'*) developing on each side of the same area, resulting in the formation of a pair of small vortices. The presence of a strong suction downstream of the contact patch was also predicted although not proven experimentally. This was done in

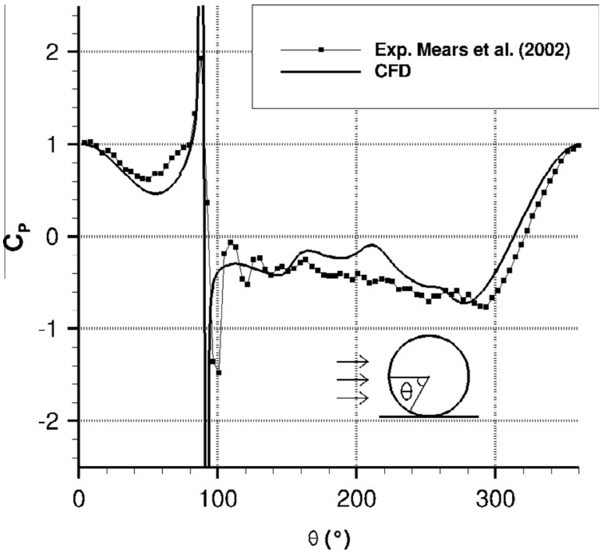

Figure 1.28: C_p distribution along the wheel centreline: comparison between the experimental results from Mears et al (2002) and the numerical data of Croner et al (2013). Plot from Croner et al (2013).

later works, such as the experimental investigations performed by Mears et al (2002) and the numerical simulations carried out by Croner et al (2013), Fig. 1.28.

On the upper surface, Fackrell and Harvey (1975) pointed out that the rotation of the wheel was able to trigger boundary layer separation further upstream compared to the stationary case, as a consequence of the fluid entrained by the moving wall. For the same reason, the point of separation was also seen to move above the wheel surface. Together with the jetting effect, the earlier boundary layer separation was found to alter the topology of the wake developing downstream of the rotating wheel, making it taller and narrower than that seen in the stationary case. This ultimately resulted in a reduction of both drag and lift over the stationary case.

An accurate description of the vortical structures developing in the near-wake region was provided by Saddington et al (2007), performing laser doppler anemometry measurements on a 50% scaled F1 wheel at $Re_D = 6.8 \cdot 10^5$. A region of velocity deficit was seen behind the wheel, with a characteristic inverted 'T' shape (Fig. 1.29a). This region was described to be the result of the interactions between two pairs of counter-rotating vortices, one in the upper half of the wheel and one closer to the ground. The upper vortices appeared to be weaker and to merge with the ground vortices within one diameter downstream of the wheel axis (Fig. 1.29b). These findings partially confirmed the results of previous URANS simulations carried out by McManus and Zhang (2006), which had predicted the presence of a similar pair of counter-rotating vortices forming in the lower near-wake. The simulations however differed from the experiment on the upper region of the wake, where an arch-shaped vortex had been seen (Fig. 1.30a), instead of the pair of counter-rotating vortices reported in Saddington et al (2007). These vortices were later captured by the URANS simulations carried out by Croner et al

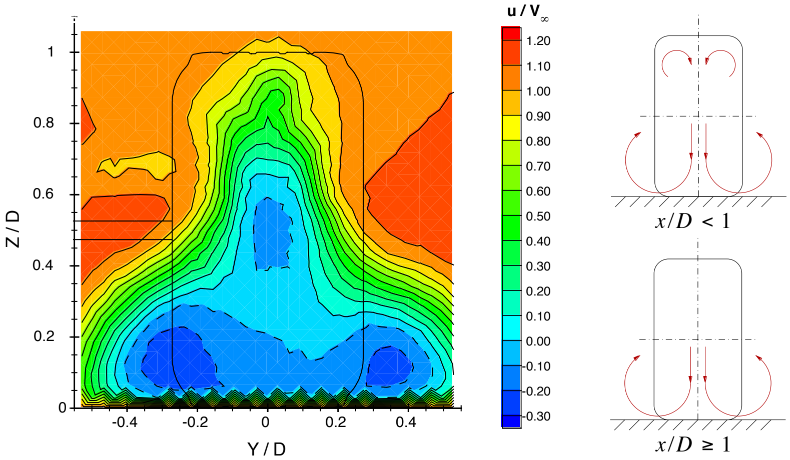

(a) (b)

Figure 1.29: **a** velocity field obtained from the LDA measurements of Saddington et al (2007) at $x/SD = 0.75$; **b** schematic representation of the vortical structures proposed in the same work.

(2013), together with a much smaller arch-shaped vortex developing just downstream of the separation line (Fig. 1.30b). The arch vortex was also isolated in the DES simulations carried out by Dassanayake et al (2012), but was reported to disappear when LES simulations were performed on the same geometry, replaced by hairpin vortices shed from the upper separation (Fig. 1.30c). In the lower portion of the wheel, Croner et al (2013) reported the existence of an unsteady coupling between the jetting vortices and the depression developing downstream of the contact patch. This unsteady behaviour resulted in the shedding of vortical structures at a

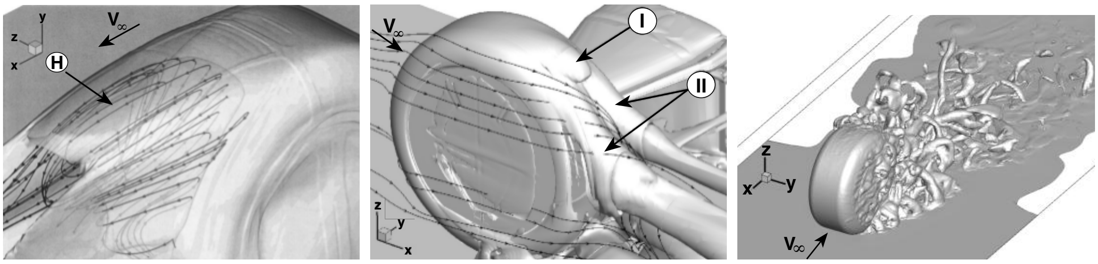

(a) (b) (c)

Figure 1.30: Vortical structures developing on the upper portion of an isolated wheel: **a** arch-shaped vortex **(H)** isolated by the URANS simulations carried out by McManus and Zhang (2006) (velocity streamlines superimposed on the iso-surface of $\Omega D/U_\infty = 3.5$); **b** time averaged flow field from the URANS simulations performed by Croner et al (2013) (velocity streamlines superimposed on the iso-surface of $Q = 1000s^{-1}$, **I** and **II** denote respectively the arch-shaped vortex and the counter-rotating vortex pair); **c** visualisation of the unsteady flow field obtained from LES simulation carried out by Dassanayake et al (2012) (iso-surface of $\Omega = 500\ s^{-1}$).

characteristic frequency of $St_D = 0.717$ (based on the wheel diameter). The same frequency was reported to control the evolution of both drag and lift.

The flow field developing around a wheel can be altered by several elements. For instance, the presence of a negative wheel camber can yield asymmetries in the separated region, with the inverted 'T' shape seen in Fig. 1.29a altered by the weakening of the outboard lower vortex and the strengthening of the inboard lower vortical structure (Knowles et al (2002), Axerio et al (2009), Issakhanian et al (2010)). The symmetry, however, can be restored by suitably changing the through hub flow, as pointed out by Sprot et al (2011). The amount of flow passing trough the rim of the wheel has been shown also to have an effect on the drag exerted on the wheel itself (Mayer and Wiedemann (2007), Vdovin et al (2013)). On the other hand, the absence of through hub flow, combined with the presence of flat side walls and rounded tyre shoulders, may allow the formation of a third pair of longitudinal vortices located between the first two pairs (Diasinos et al, 2015). This third pair of vortices was theorised by Cogotti (1983) and Mercker and Berneburg (1992) but it has never been seen in the experiments (Saddington et al, 2007). Other parameters that have been found to influence the aerodynamic performances of the wheel are: the profile of the tyre (Diasinos et al, 2015) and the way it changes under loading conditions (Sprot et al, 2012), the tyre thread pattern (Leśniewicz et al, 2014) as well as the shape and size of the contact patch (Schnepf et al, 2015).

1.3.4.2 Wheel-vehicle interactions

The interactions between the wheels and the main body of a car play an important role in determining the overall aerodynamic performances of the vehicle. According to Carr (1983), the addition of wheels and wheel-wells to a simplified vehicle may result in a drag increase between 70 and 90 counts ($1\,count = 0.001$) and a lift growth between 230 and 580 counts. For these reasons, over the years this aspect has been object of several research works, carried out considering simplified geometries as well as full scale models.

Apart from altering the flow field around the main body, wheel-car interactions produce changes also to the wheel flow (Krajnovic et al, 2011). The flow approaching the wheel is deflected by the main body outwards, resulting in a yaw angle that moves the separation point over the wheel, thus altering the wheel's wake (Regert and Lajos, 2007). In the case of passenger cars, this flow field is further complicated by the fact that wheels are always placed in wheel housings, whose shape can be reduced to that of a half-cylindrical cavity with its outer side open. The addition of the wheel-arch has been reported to cause the suppression of the upper pair of counter-rotating vortices (Morelli, 2000). Of the vortical structures seen in the isolated case (§1.3.4.1), in fact, only the jetting vortices survive (**L** and **R** in Fig. 1.31). Nevertheless, new structures are seen in the flow field surrounding the wheel. Krajnovic et al (2011), performing LES simulation on the simplified geometry proposed by Fabijanic (1996), reported the formation of three regions of separated flow (**H**, **C** and **S** in Fig. 1.31), the first

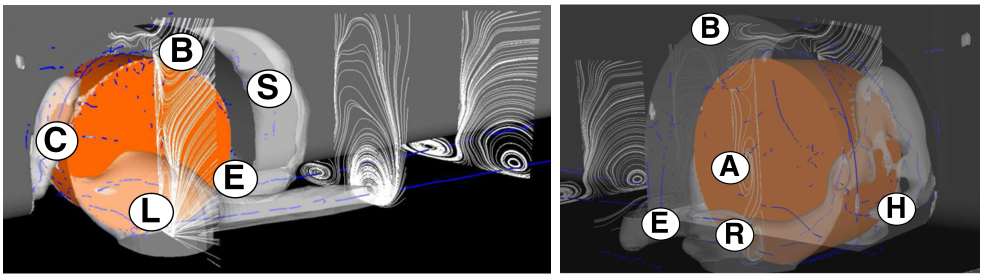

(a) **(b)**

Figure 1.31: Vortical structures developing around a simplified wheel in a wheel-house cavity. Velocity streamlines superimposed on the pressure iso-surface of $p = 1.0116\, bar$: **a** side view; **b** inside view. The letters refers to different vortical structures. Plots from Krajnovic et al (2011) (edited).

of which was found to be originated by the underbody flow separating at front edge of the wheel-arch. The other two recirculations were described as the result of the detachment of the boundary layer over the lateral surface of the main body, occurring upstream and downstream of the wheel-house. Three additional structures were also identified. The first two (**A** and **B** in Fig. 1.31) were ascribed to the motion of flow entering the gap between the wheel and the inner surface of the wheel-house and then moving up over the wheel. The third vortex (**E** in Fig. 1.31) was seen behind the wheel and referred to the motion of flow structures from the inboard side of the wheel to the lateral surface of the main body, downstream of the wheel-house. In addition, it was pointed out that a change in the volume of the wheel-house can alter not only the position and strength of the vortical structures developing around the wheel but also their shedding frequencies. The effects of similar changes on the aerodynamic forces had been previously investigated by Fabijanic (1996), who had identified two parameters, namely the depth of the wheel-house W_{wh} and its radius R_{wh}, driving respectively the changes in lift and drag.

An explanation of the origin of the relationship between R_{wh} and C_D was provided by Thivolle-Cazat and Gilliéron (2006), who observed that changes in the radius of the wheel-arch were able to modify the width of the wake developing downstream of the wheel, interacting with the lateral surface of the main body.

Considering a similar geometry to that used by Fabijanic (1996), Regert and Lajos (2007) pointed out that the flow field in the wheel-house is mainly influenced by the underbody flow entering the wheel-well through the lower opening. Furthermore, the vortices **A** and **B** reported in Fig. 1.31 were found to be affected mostly by the yaw angle of the flow approaching the wheel. A reduction of the flow angularity was reported as the distance between the wheel and the front face of the model was increased.

Similar structures to those presented in Fig. 1.31 were isolated in the flow field around the front wheel of a commercially available passenger car by Wäschle (2007). They can also

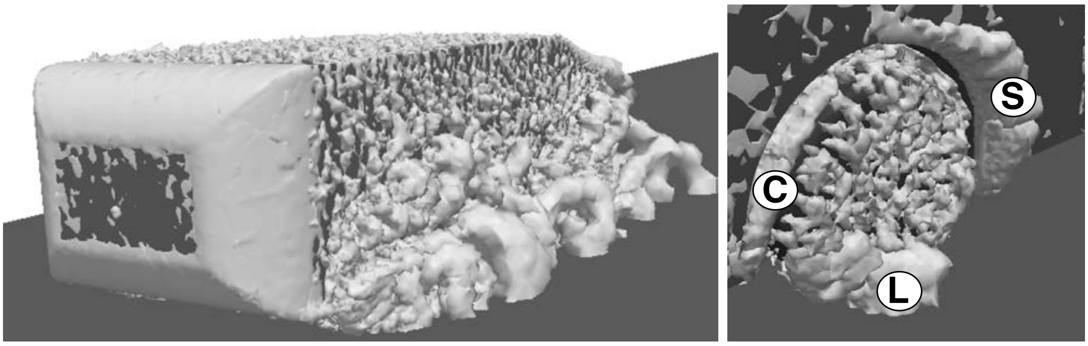

(a) **(b)**

Figure 1.32: Flow field developing around an Ahmed body with a 25° rear slant and rotating wheels: **a** vortical structures developing along the model side (instantaneous iso-surface of $Q^* = 10$); **b** vortical structures developing in proximity to the rear wheel (time averaged iso-surface of $Q^* = 50$). Pictures from Aljure Osorio (2017) (edited).

be seen at the rear wheels, as highlighted by the results of the simulations carried out by Aljure Osorio (2017), considering a modified version of the Ahmed body equipped with rotating wheels (Gulyás et al, 2013). In this case, flow separation was reported on the lateral surface of the main body, both upstream and downstream of the rear wheel-arch (**C** and **S** in Fig. 1.32b). The jetting vortex was also seen close to the ground (**L** in Fig. 1.32b). Nevertheless, these structures were reported to be weaker than those seen at the front-end, due to the shielding of the front wheels. A highly turbulent flow was indeed described at the lower side of the model, as a consequence of the interactions between the vortical structures stemming from front wheels and the flow along the sides of the main body. Because of this, the corner vortices reported by Krajnovic and Davidson (2005a) for the same geometry without wheels (§1.3.2) were no longer visible. All these structures were found to alter the topology of the wake developing downstream of the model, especially close to the lower corners of the base.

The effects of the wheels on the base wake were further investigated by Huminic and Huminic (2017), performing RANS simulations on a similar geometry, but with the rear slant angle increased to 35°. In these conditions, the lower portion of the rear recirculation was reported to be squeezed between two streamwise vortices originating from the upper portion of the rear wheel-arches. In the presence of a squared bottom trailing edge, these structures were found to be deflected towards the ground while moving downstream (Fig. 1.33a). Following the work of Howell (1994), a diffuser, with an extension of about 30% of the model length, was then applied to the model underbody. In these conditions, the size of the wheel vortices was seen to decrease with the diffuser angle ϕ_b (Fig. 1.33b), until a drag minimum was achieved for $\phi_b \approx 6°$. Drag was seen to increase again for larger values of ϕ_b, when the vortices originating from the diffuser itself were found to prevail.

The changes in the base wake topology triggered by the addition of wheels has been documented to directly affect the pressure distribution over the vehicle's rearward facing

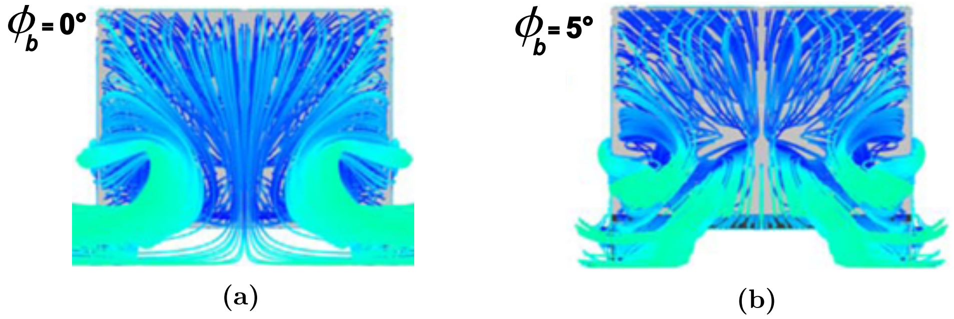

(a) (b)

Figure 1.33: Time averaged velocity stream-ribbons for the wake of an Ahmed body with rotating wheels and a 35° top slant: **a** model with a squared bottom trailing edge; **b** model with a 5° bottom diffuser. Pictures from Huminic and Huminic (2017).

surfaces (Makihara et al, 2016). Wood et al (2015) reported a 28.3% increase in the rear pressure drag $\overline{C}_{D_{Rear}}$ when adding four stationary wheels to a 1/4 scale generic SUV model featuring a 30° bottom slant, no cooling flow and a ground clearance of $C^* = 0.21$. In the same study, wheels were reported to change the way flow separation occurred at the bottom slant too. In the case without wheels, flow was seen to detach from the bottom tapered surface at the model centreline ($y^* = 0$), but it reattached at $y^* = 0.22$ for then separating again closer to the side edges ($y^* > 0.41$). Separation was seen to move in the spanwise direction when wheels were added to the model. In this case, attached flow was indeed documented at $y^* = 0$ whereas regions of separated flow were reported for $y^* > 0.22$. Variations in the rear pressure drag were also seen when changing the model ride height. In particular, a 23% reduction of the ground clearance was found to improve pressure recovery over the model rearward facing surface by 6.7%. On the other hand, a 1.5% increase of $\overline{C}_{D_{Rear}}$ was reported when the ride height was increased by a similar amount (23%) over the nominal case. This trend has been recently confirmed by the measurements of Pitman and Gaylard (2017), considering a commercially available SUV tested in an industrial wind tunnel with rotating wheels and a moving ground.

Besides altering the time averaged wake topology, the addition of wheels may have an effect also on the long-time wake dynamics (§1.3.1), as pointed out by Varney et al (2017). In this study, the same geometry used in Wood et al (2015) was tested, but with the bottom slant replaced by a squared trailing edge. No bi-stable mode was seen for the square-back configuration with wheels. Bi-stability, however, became visible when the vertical symmetry in the base pressure distribution was restored by counteracting the upwash induced by the rear wheels with the downwash created through the combined action of tapering and ventilation of the upper surfaces. No further information, however, was provided on the wake dynamics.

1.3.4.3 Wheel rotation

The effects of the ground, described in §1.3.3, become even more significant when a vehicle with wheels is considered. Over the years, several studies have pointed out the need to reproduce

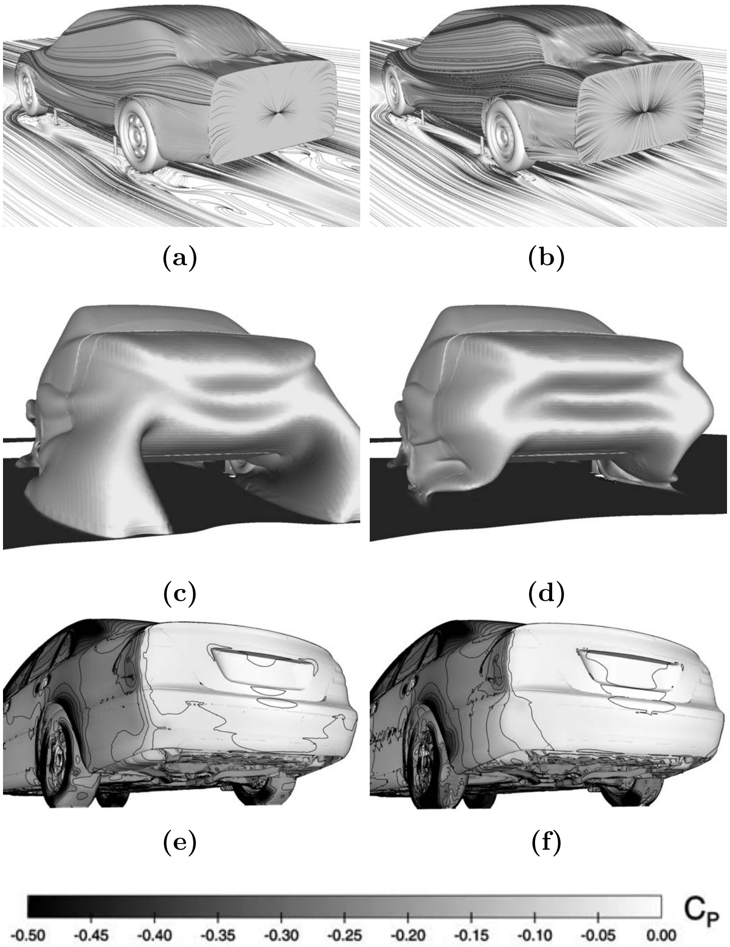

Figure 1.34: Effects produced by rotating wheels on the base wake of notchback cars. **a** and **b**: near wall streamlines for a simplified vehicle with stationary wheels **(a)** and rotating wheels **(b)**. **c** and **d**: iso-surface of normalised total pressure ($C_{p_0} < 0$) for stationary wheels **(c)** and rotating wheels **(d)**. **e** and **f**: pressure maps for a commercially available vehicle with stationary wheels **(e)** and rotating wheels **(f)**. Plots from Wäschle (2007).

realistic rolling conditions in order to perform accurate estimations of the flow field around wheels (Cogotti (1983), Mercker et al (1991)) and its interactions with the rest of the car (Wickern et al, 1997). Testing commercially available vehicles, Wickern and Lindener (2000) saw a decrease in the overall lift when rotating the rear wheels, whereas front wheel rotation was found to increase C_L. Elofsson and Bannister (2002) reported a reduction in C_D when switching from a stationary configuration to a rotating configuration. This was ascribed to a change in the aerodynamic interference between the rear wheels and the vehicle's wake. Front wheel rotation was in fact found to cause a small increase in drag, overcome by the larger reduction in C_D induced by the rotation of the rear wheels. Similar conclusions were drawn by Elofsson and Bannister (2002),who also reported a larger drag improvement for a sedan car when compared to a square-back vehicle. Wäschle (2007) noticed a reduction in C_L under rotating wheel conditions for two different notch-back models. In this case, the lift reduction was found to be a consequence of the narrowing of the wheels' wake triggered by the combined action of wheel rotation and moving ground (Fig. 1.34a and 1.34b). This was reported to lower the pressure inside each wheel-house and increase at the same time the mass flow rate trough the rear diffuser. For the drag, a reduction was reported too. As for the lift, the origin of this reduction was found in the smaller wake developing behind each wheel under rotating conditions, in agreement with the previous findings of Elofsson and Bannister (2002). The narrowing of the wheels' wake was seen to allow a better pressure recovery over the tapered rear bumper as well as the bottom diffuser (Fig. 1.34e and 1.34f), resulting in a more effective 'boat tailing' (see §1.3.5.1). These effects were seen in the case of a mass produced passenger car (Fig. 1.34e and 1.34f) as well as a simplified notchback model (Fig. 1.34c and 1.34d). In the latter case, the differences between stationary and rotating conditions were even more pronounced, as a consequence of the higher mass flow rate passing underneath the vehicle, helped by the absence of elements like the engine compartment or a rough underbody that could dampen the effects of the wheels.

For a similar geometry, Koitrand et al (2014) noticed that the addition of rear wheel rotation promoted non-negligible changes in the unsteady flow field. In these conditions, an increase in the unsteadiness of the vortical structures developing around the rear wheel-arches was seen. On the contrary, a reduction in pressure fluctuations was noticed over the base of the vehicle.

1.3.5 Flow control strategies

The need to reduce drag has led over the past few decades to the development of different flow control strategies. From Eq. 1.27 it is clear that a reduction of aerodynamic drag can be achieved by limiting the loss in total pressure as well as reducing the size and strength of the transverse and longitudinal vortical structures. In order to to achieve these goals, several solutions have been proposed over the years. These can be summarised into two different categories, namely active flow control systems, which require an external power input to work, and passive flow control systems, for which an external power source is not needed. A detailed review on the application of such systems to ground vehicles is presented in Choi et al (2014).

Active systems comprise different solutions such as continuous suction, steady blowing and synthetic jet actuators. These systems have been reported to be particularly effective in controlling the rear window flow separation (§1.3.2). Rouméas et al (2009b), for instance, reported a 17% drag reduction for an Ahmed body featuring a 25° top slant, when the flow separation occurring in proximity to the tapered surface was suppressed by applying continuous suction close to the leading edge of the slant. An even greater decrease in C_D (around 20%) was obtained by Gilliéron and Kourta (2013), applying pulsed jets to an Ahmed body with a rear slant angle of 35°. In the latter case, however, the drag reduction was achieved by increasing

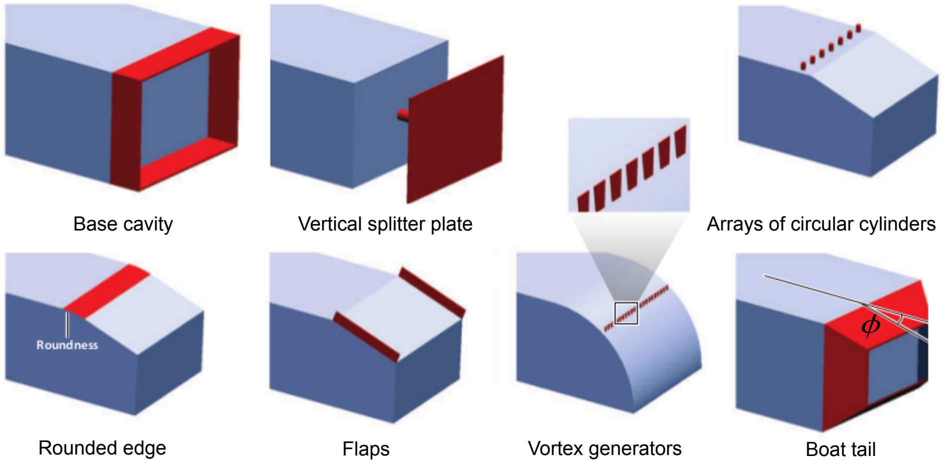

Figure 1.35: Examples of passive drag reduction systems. Drawings from Choi et al (2014).

the size of the separated flow region, as this led to the weakening of the rear pillar vortices described in §1.3.2. Active systems have also found application in the control of 'fully' separated wakes, such as those seen in the case of square-back geometries (§1.3.1). The implementation of these systems, when successful, has been shown to promote changes in the shear layer growth as well as modifications in the curvature of the streamlines in proximity to the model trailing edges (Littlewood and Passmore (2012), Rouméas et al (2009a) and Barros et al (2016)), which ultimately lead to an increase in the gap between the cores of the vortical structures seen in the time averaged flow field and the model base (Bruneau et al, 2010).

From a 'practical' point of view, however, active systems have so far shown limitations difficult to overcome, such as the needs of an external power supply and additional space for installation. These limitations, combined with the high level of noise that these systems generate when in operation, make their implementation on passenger cars unlikely in the foreseable future.

Passive technologies (Fig.1.35), on the other hand, do not require external sources of energy, produce far less noise and are less expensive to install. For these reasons, several studies on the effectiveness of such systems have been carried out over the years. Duell and George (1999) pointed out that an increase of the mean base pressure of up to 11% can be obtained by suppressing the pumping mode (§1.3.1) by adding a rear cavity to an Ahmed body with $W/H = 1$. A similar gain in terms of drag reduction was reported for a more 'conventional' Ahmed body (with $W/H = 1.35$) by Gilliéron and Kourta (2010), altering the formation of the recirculation bubble trough the application of a vertical splitter plate downstream of the model base. Pujals et al (2010) recorded a 10% drag reduction when suppressing flow separation over the slanted surface of an Ahmed body (with $\phi = 25°$) by means of an array of circular cylinders mounted on the roof, slightly ahead of the slant leading edge. Flow reattachment was shown to be triggered by coherent streamwise vortices, generated by the cylindrical protrusions, pushing high momentum flow near the wall. The existence of this mechanism was confirmed by the results of the numerical simulations carried out by Krajnovic (2013). Similar results were reported by Thacker et al (2012) rounding the edge between the roof and the slanted surface of the same model. Evidence of the beneficial effects of afterbody rounding on C_D was found also by Rossitto et al (2016). In this case, a 16% decrease in drag was reported when rounding the slant's leading edge. This result was linked to two concurring processes: the suppression of the separation on the slanted surface and the lengthening of the recirculation developing downstream of the base. No further gain in terms of drag reduction, however, was seen when similar radii were added to the side edges of the slant, as in this case the weakening of the rear pillar vortices was counteracted by an increase of the downwash in the core region of the wake. Beaudoin and Aider (2008) showed that a decrease in C_D can be also obtained by applying flaps to the trailing edges of either the slant or the base of an Ahmed body featuring a top slant with a 30° angle and a cord 30% of the model length L. In particular, it was noticed that the most relevant drag and lift reductions were obtained with flaps mounted on the side edges of the rear slant, as a consequence of the disruption of the longitudinal vortices described in 1.3.2, which led to the development of fully separated flow over the slant. A similar mechanism was found to be the source of the decrease of both C_D and C_L measured by Aider et al (2010) studying the effects of vortex generators installed in proximity to the rear separation line of a modified Ahmed body, with the rear slant replaced by a curved surface. In this case, contrary to their conventional function, the vortex generators were found to trigger early separation, leading to the formation of a large recirculation. In this way, the formation of longitudinal vortices was prevented and a 12% reduction of C_D was achieved.

1.3.5.1 Trailing edge tapering

Boat tailing is considered one of the most effective and practical way to reduce drag in the case of ground vehicles (Choi et al, 2014). This technique is based on the fact that, for a generic bluff body with a blunt trailing edge, the time averaged value of the base pressure is almost constant over the entire base and equal to the pressure outside the boundary layer at the separation line §1.1.2. Just before separation, however, the static pressure is subjected to a sudden decrease under the effect of the convex curvature of the streamlines bounding the wake, as they bend towards the axis of the body. This curvature is responsible for a local increase of the velocity, which in turn yields a drop of C_p (Eq. 2.9) in the region just upstream of the separation line. These effects can be mitigated by creating a slanted lateral surface before the line of separation, obtained through a gradual reduction of the body-cross section. In these conditions, the growth of the boundary layer thickness along the tapered surface leads to a change in the curvature of the streamlines towards a concave shape. A local decrease in the velocity is therefore obtained, resulting in a pressure increase that eventually benefits the entire base (Mariotti et al, 2017). A fundamental parameter for the effectiveness of boat-tailing in

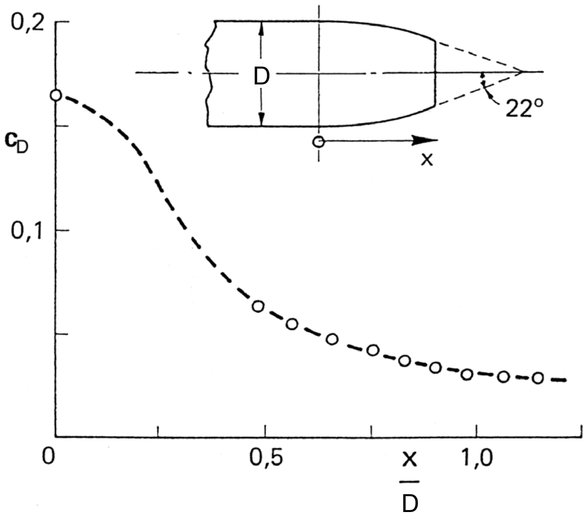

Figure 1.36: Effect of boat tailing on the aerodynamic drag experienced by an axisymmetric body. Plot from Mair (1978).

reducing drag is the slant angle ϕ, which needs to be low enough to prevent boundary layer separation before the base (Yi, 2007). The extension of the tapered surface, on the other hand, can be relatively limited. Indeed, as shown in Fig. 1.36 for an axisymmetric body, C_D initially drops steeply for small increments of x/D but then converges towards an asymptotic value for $x/D > 0.5$. This concept is the driving principle of the 'truncated base' or 'Kamm-back' design widely used in the automotive industry since the middle of the 1930s (Schuetz, 2016).

Over the years several researchers have investigated boat tailing as a means to reduce aerodynamic drag on axisymmetric bluff bodies (Mair, 1978) as well as automotive shapes (Verzicco et al (2002), Khalighi et al (2012)). A noticeable increase in the effectiveness of such systems has been noticed when coupling them with cavities (Balkanyi et al, 2002), although so far this solution has found a real application only on large trucks. The geometric modifications that the implementation of a tapered cavity requires, in fact, are rarely feasible on passenger cars, due to the presence of rather 'stringent' aesthetic and functional constraints.

On the other hand, over the last few years there has been a growing interests of the scientific community towards the effects produced by smaller changes in the shape of the vehicles' trailing edges, since they are more representative of the methodologies followed by car manufacturers to limit the drag of their products. A seminal study in this field was carried out by Littlewood and Passmore (2010), characterising the sensitivity of the wake of a square-back model to the application of high aspect ratio tapers. Small chamfers, with a chord c of approximately 4% of the model length (or 16% of the model height), were applied to the roof trailing edge of a Windsor body. Six different slant angles ϕ, ranging from 0° to from 20° were tested, in 4° increments. A parabolic dependence between C_D and ϕ was reported, reminiscent of that found by Ahmed et al (1984) for bigger slants (§1.3.2). A drag minimum was seen to occur at $\phi = 12°$, resulting in a 4.4% drag reduction over the square-back case. The quadratic dependency between C_D and ϕ was further investigated by Grandemange et al (2013c), applying flaps with a similar chord to the roof and underfloor trailing edges of an Ahmed body. The existence of a linear relationship between C_L and ϕ was seen. This, combined with the aforementioned quadratic dependency seen between C_D and ϕ, led the author to the formulation of a quadratic relationship between drag and lift, which was found to be self-similar for for five different values of the bottom angles. Similar results had previously been reported by Howell and Le Good (2004) considering larger slanted surfaces (with a slope length of about 20% of the model length), for a range of different backlight and diffuser angles. In addition, Grandemange et al (2013c) proposed a second-order polynomial function for describing the link between C_D and the top and bottom flap angles (ϕ_t and ϕ_b), with the presence of a coupling term $\phi_t\phi_b$ highlighting the fact that the minimum drag configuration could be achieved only through the concurrent optimisation of the two flap angles. Similar conclusions were drawn also by Perry et al (2015). In the latter case, the same chamfers used in Littlewood and Passmore (2010) were applied to both horizontal trailing edges of the Windsor body and the aerodynamic forces experienced by model were measured together with the static pressure acting over half of the model base. A good correlation between both C_D and C_L and the base pressure distribution was found. In particular, it was noticed that a variation of either ϕ_t or ϕ_b was able to trigger a non-negligible change in the size of the corresponding lobe of the wake torus. This resulted in a modification of the base pressure distribution which in turn led to a change in the forces experienced by the entire model. The lowest drag value (-5% over the square-back case) was obtained for $\phi_t = 16°$ and $\phi_b = 6°$, corresponding to the highest level of base pressure. Further investigations carried out in Perry (2016b), pointed out that the improvement in pressure recovery over the base could be ascribed to the establishment of a more ‘balanced’ wake structure rather than to the reduction in the size of the recirculation bubble. An even better result in terms of drag reduction was obtained in Perry et al (2015) when the same tapers were applied to the vertical trailing edges of the model, leaving the top and the bottom edges squared. In this case, only configurations featuring the same chamfer angle ϕ_s on the two sides were tested and a 7% decrease in C_D was recorded for $\phi_s = 12°$. The further improvement over the $\phi_t = 16°$, $\phi_b = 6°$ configuration was ascribed to an increase in size of the side lobes of the torus, which led to a more balanced 3D structure of the wake. None of these studies, however, has provided information regarding the effects of such small geometrical modifications on the wake dynamics described in §1.3.1.

1.3.5.2 Suppression of the long-time wake dynamics

Recently researchers have started to focus their attention on the suppression of the very low frequency dynamics of the wake as a way to further reduce drag. For an axisymmetric body Grandemange et al (2012b) reported a 14% decrease in C_D when the flow was perturbed using

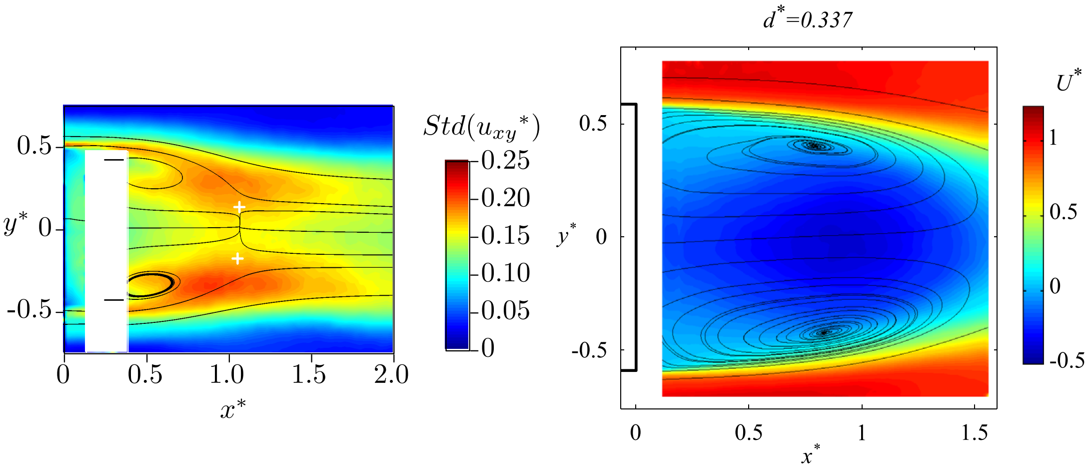

(a) **(b)**

Figure 1.37: Examples of stable symmetric wakes obtained stabilising the wake by means of passive control devices: **a** streamlines superimposed to the colormap of the fluctuating velocities for the wake behind an axisymmetric blunt body controlled with a ring (white collar in the plot) with a diameter of $d_D^* = 0.425$, placed at $x_D^* = 0.15$ downstream of the model base (plot from Grandemange et al (2012b)); **b** streamlines and colormap showing the magnitude of the streamwise component of the velocity for the wake of an Ahmed body featuring a $d/H = 0.337$ deep rear cavity (plot from Evrard et al (2016)).

a disturbance with an azimuthal wave number of $m = 0$ (represented by a ring with an outer diameter $d_D^* = 0.425$ placed at $x_D^* = 0.15$ downstream of the model base), resulting in a stable axisymmetric wake (Fig. 1.37a). Considering an Ahmed body, Grandemange et al (2014b) demonstrated a base drag reduction of between 4% and 9% when the lateral symmetry of the wake was restored by means of a vertical control cylinder positioned at the core of the wake's reverse flow. These results suggest the existence of an unstable branch for the solution of the equations describing the wake dynamics, dubbed reflectional symmetry preserving mode by Cadot et al (2015). Even better results in terms of drag reduction were reported by Evrard et al (2016), applying a cavity to the base of a similar model. In this case, a 18% reduction in the base drag was documented for a cavity depth of $d \approx 0.27H$, resulting in a 9% decrease in the drag experienced by the entire model. The stabilising effect of the cavity (Fig. 1.37b) was modelled using a Langevin equation (Lemons and Gythiel, 1997). The origin of the drag reduction was found to be in the weakening of the vortex system associated with each of the reflectional symmetry breaking states as the cavity depth was increased, until a saturation was reached for a depth $d \gtrsim 0.24H$. Similar trends were seen in the experimental work of Bonnavion et al (2017b) and the numerical simulations performed by Lucas et al (2017), using a lattice Boltzmann solver. In the former study, the effectiveness of a cavity with $d = 0.285$ in reducing base drag was documented even at low ground clearances ($c^* \approx 0.06$), albeit with the selection of a stable vertically asymmetric state rather than the 'fully' symmetric state seen at $c^* \approx 0.12$.

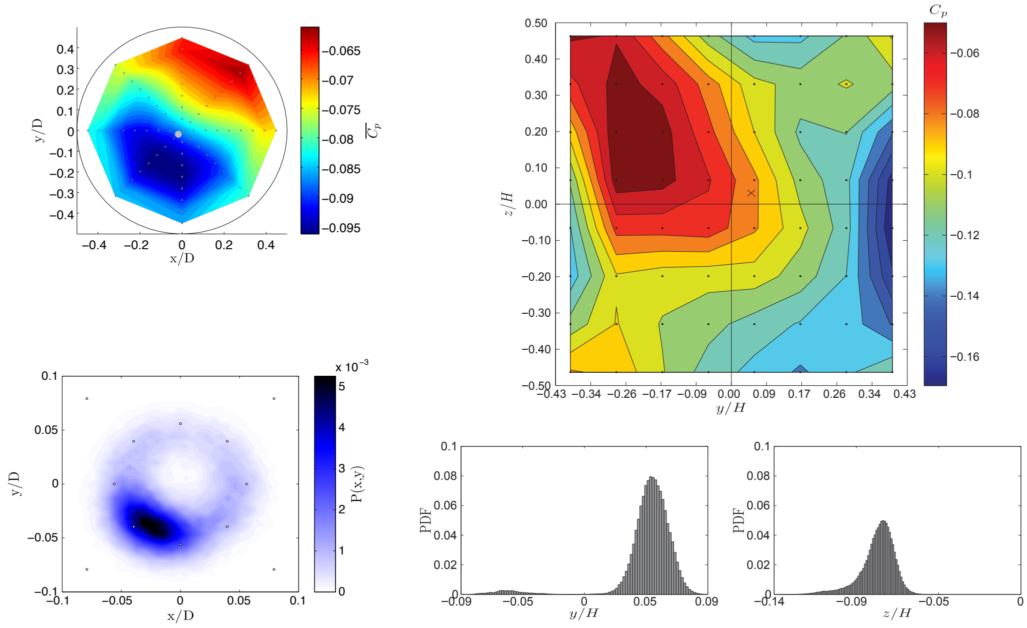

(a) (b)

Figure 1.38: a effects of high-frequency forcing, performed using synthetic jets. on the wake behind an axisymmetric body (Oxlade, 2013): **top** time averaged base pressure map; **bottom** 2D probability density distribution of the centre of pressure. **b** lowest drag configuration obtained by Cabitza (2014) when controlling the wake behind a square-back body with $W/H = 0.86$ using synthetic jets: **top** time averaged base pressure map; **bottom** probability density function distribution of the position of the centre of pressure along y^* and z^*.

In the latter study, base cavities were shown to act as high pass filters, suppressing not only the bi-stable mode but also the lateral flapping motion of the wake. In all these works, however, no information was provided about the effects produced by rear cavities on the pumping mode described in §1.3.1 and §1.3.5.

Active control systems aiming to gain a reduction of C_D through the re-symmetrisation of the wake have been proposed by Evstafyeva et al (2017), Li et al (2016) and Brackston et al (2016). Evstafyeva et al (2017) implemented a closed loop controller into LES simulations performed matching the experiment of Grandemange et al (2012a), at $Re_H = 435$. The re-symmetrisation of the wake resulted in a 33% reduction of the root mean square of the base pressure fluctuations and a 3% reduction of the aerodynamic drag over the unforced case. Li et al (2016) tested a control system consisting of of two lateral slit jets and pressure sensors mounted on the rear surface of an Ahmed body, operating at a higher Reynolds number ($Re_H = 6 \cdot 10^5$). A 2% increase of the base pressure was achieved by stabilising the unstable symmetric state observed during the transition between two reflectional symmetry breaking states. The sensitivity of this last state, dubbed *'transient symmetric state'*, to different control strategies was further investigated by Varon et al (2017b), using tangential blowing along the top trailing edge of a square-back model. It was shown that, depending on the controlled strategy employed, the bimodal wake can be forced into a stable asymmetric or symmetric state or even switch to a new multimodal behaviour. A more efficient actuating system, featuring moving flaps, was tested by Brackston et al (2016). In this case, the feedback control loop was designed using a modelling approach similar to that suggested by Rigas et al (2015). Following this approach, the flow field was modelled using a nonlinear Langevin equation consisting of a deterministic part, describing the evolution of the large-scale structures, and a stochastic term, capturing the effects of the turbulent forcing. In neither case, however, was the drag reduction greater than 2%.

As already pointed out by Lucas et al (2017), the results of these studies seem to suggest that control strategies targeting the wake re-symmetrisation through a perturbation of the outer shear layers are less effective in reducing C_D than perturbations acting directly on the recirculation bubble (such as the control cylinder used by Grandemange et al (2014b) or the base cavity tested by Evrard et al (2016), Bonnavion et al (2017b) and Lucas et al (2017)). Moreover, although there seems to be agreement among researchers on the fact that the suppression of the very low frequency dynamics may be exploited to reduce drag, it is still not clear whether the suppression of this mode should aim at stabilising a symmetric or an asymmetric state. For instance, Oxlade (2013) and Cabitza (2014), controlling the dynamics of the wakes behind an axisymmetric body and a square-back body respectively, using synthetic jets actuated at different frequencies, reported that the configurations featuring the lowest drag were characterised by stable asymmetric wakes, as can be inferred from the pressure maps presented in Fig, 1.38a and Fig. 1.38b. This is in contrast with the results obtained by Grandemange et al (2012b) and Evrard et al (2016) for similar bodies, where the lowest drag configurations were characterised by the presence of stable symmetric wakes.

1.3.5.3 Wheel-flow control

As seen in §1.3.4 wheels are one of the biggest source of aerodynamic drag, due to their interactions with the underbody flow and the base wake. For these reasons, many efforts have been made over the years to control wheels' wakes and minimise their impact on the aerodynamic performances of the entire vehicle.

The potential of the aerodynamic optimisation of the wheel/wheel-house system, as a means to reduce drag locally while improving at the same time the quality of the flow travelling towards the base, is well known in the literature (Wickern et al, 1997). One of the most effective ways to achieve this goal is to reduce the angle of the flow impinging on the wheels, particularly at the front axle. This can be achieved by isolating the wheel-house from the engine compartment (Schuetz, 2016), controlling flow separation at the front bumper (Chaligné et al, 2017) or adding front-wheel deflectors (Sebben, 2004). A beneficial contribution in terms of drag reduction can be also obtained through the ventilation of the wheel cavities. Systems based on this concept, once used on closed-wheel race cars only (Katz, 2006), have found their way in most recent years on mass produced vehicles (Schütz et al, 2016). Further reductions of C_D can be achieved through the optimisation the wheel rim design. Schwarczkopf et al (2009), for instance, showed that the application of an opened rim design at the front wheels of an Ahmed body, in combination with a closed rim design at the rear wheels, led to a relatively large improvement in both drag and lift without the need of adding extra devices to the vehicle. The same arrangement was found to be the most effective in reducing C_D also when adopted on commercially available passenger cars, as pointed out by the investigations of Landström et al (2011b). In this study, it was shown that the application of a fully closed wheel design at the rear axle led to the formation of a significantly smaller wake behind the rear wheels, together with a reduction of the cross flow through the rear wheel-housings. This ultimately resulted in a base pressure increase over the baseline case (featuring an open rim design on all four wheels). On the other hand, covering the front wheels only, resulted in a noticeable growth of the overall C_D, as a consequence of the pressure build-up on the upstream surfaces of front the wheel-arches and the significant widening of the front wheel wakes. The lowest drag value was achieved by combining fully closed rear wheels with partially opened front wheels (with a $30\,mm$ radial cover attached to the outer edge of the rim). Nevertheless, the aerodynamic optimisation of wheels on realistic car geometries does not always lead to a monotonic relationship between base pressure recovery and overall drag, as pointed out by Landström et al (2011a). Optimising the rim design can also yield non-negligible reductions of the ventilation moment created by the rim itself (Vdovin et al, 2013).

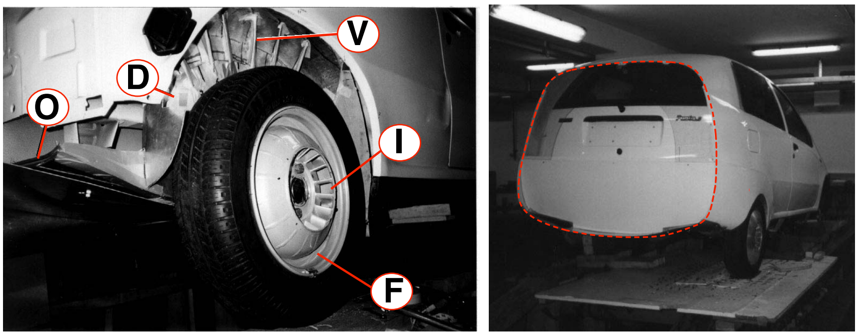

(a) (b)

Figure 1.39: Drag reduction system proposed by Morelli (2000). **a** overview of the system: **F** centrifugal fan; **I** inlet; **V** guide vanes; **D** ducts; **O** base outlet. The dashed red line in Fig. **b** denotes the single line of flow separation at the model base.

A more radical solution to reduce the base drag by exploiting the rotation of the rear wheels was proposed by Morelli (2000), who proposed to fit a centrifugal fan in each of the rear wheels (Fig. 1.39a), with the aim of redirecting flow into purpose built ducts placed inside the wheel-arches (**D** in Fig. 1.39a). The ducts ended in an outlet placed at bottom of the model base (**O** in Fig. 1.39a). The system was based on the idea of shielding the upper part of the wheels' wake, thus restoring the continuity of the boundary layer, in order to allow the creation of a single line of flow separation spanning over the entire perimeter of the base (Fig. 1.39b). When tested, the system yielded a drag reduction of more than 20% over the baseline configuration, but since then it has never found its way into production vehicles, arguably due to its inherent complexity.

1.4 Objectives of the thesis

Although remarkable progress has been made in the last few years in the characterisation of the most relevant dynamic features of the wake of square-back vehicles, there are still questions whose answer has yet to be found. For example, it is still not clear how the switch between symmetry breaking states occurs, and how such an event affects the aerodynamic drag experienced by the entire vehicle. Indeed, the impact on the long-time wake dynamics on the aerodynamic drag has not been fully understood yet. Furthermore, very little is known on the effects produced on the same dynamics by changes in the curvature of the shear layers bounding the wake and the way they interact between each other.

The present work aims to provide a contribution to this field, by investigating the unsteady behaviour of the wake developing behind a simplified square-back geometry, the Windsor body, its sensitivity to small perturbations (i.e. an increase in free stream turbulence intensity, changes in the model ride height, different trailing edge taper angles, small variations in the model yaw angle as well as pitch angle) and whether the same unsteady features can still be observed when wheels (either stationary or rotating) are added to the main body. The work is experimental, consisting of balance, pressure tapping, particle image velocimetry and single point velocity measurements carried out at a Reynolds number (based on the model height) of $Re_H = 7.7 \times 10^5$.

The manuscript is organised as follows.

- **Chapter 2** provides a detailed description of all the experimental techniques employed in the present investigation as well as the post-processing tools used to extract additional information from the available datasets. A description of the model used in the tests is also provided.

- **Chapter 3** looks at the characterisation of the unsteady features of the wake developing behind a simple square-back model without wheels. The low frequency bi-stable mode is characterised and its sensitivity to changes of the ground clearance C^*, yaw angle Ψ and inlet turbulence intensity is assessed. Low order models are then used to describe the topology of each lateral symmetry breaking state and characterise the switch between the different states. The global modes are also investigated. The results are compared with the literature and a new interpretation of the pumping mode is presented.

- **Chapter 4** focuses on the characterisation of the effects produced by different horizontal trailing edge taper angles on the time averaged wake topology and wake dynamics, with a particular emphasis on the influence of the top and bottom shear layers on the lateral symmetry breaking instability. Aspects such as the impact of different levels of upwash and downwash on the global modes as well as the link between wall velocity and base drag are also investigated.
- In **Chapter 5**, the suppression of the long-time bi-stable mode through the application of side trailing edge tapers is discussed. Changes in the time averaged wake topology are reported and related to the drag reductions recorded in these conditions. The sensitivity of the wake to small changes in the model pitch angle Θ is also investigated.
- **Chapter 6** deals with the effects produced by stationary and rotating wheels on the time averaged and unsteady features of the wake. The effect of the wheels is initially investigated by considering the simple square-back geometry studied in **Chapter 3**. The level of complexity is then further increased by considering the effects of 12° tapers applied either to the horizontal or the vertical trailing edges of the model.
- The most important results are then summarised in the **Conclusions**.

Chapter 2

Experimental methodology

The work described in the present manuscript is experimental, consisting of wind tunnel tests, performed in the Loughborough University Large Wind Tunnel. Balance measurements, pressure tappings, PIV acquisitions and single point velocity measurements were carried out, with the aim of characterising the time averaged and the main unsteady features of the wake developing downstream of a simplified automotive square-back shape. The Windsor body was used throughout the experimental campaign. A description of the model and the wind tunnel, as well as all experimental techniques employed, is provided in this chapter. Some aspects concerning the techniques used for the post-processing of the data are also discussed.

2.1 The Windsor body

The experimental programme employed the Windsor body described in § 1.2.2. Its slanted front-end generates a flow field considered to be more representative of real cars than the widely used Ahmed body (Ahmed et al, 1984). At the scale used here, the model is approximately equivalent to a 1/4 scale small hatchback car. When not specified differently, the ground clearance C was set at $50\,mm$ (resulting in a non dimensional value of $C^* = 0.173$, when normalised considering the model height H as reference length), with a tolerance of 0.2° for the pitch angle Θ. In some cases, however, C was varied between $40\,mm$ and $60\,mm$ (or $0.138 \leq C^* \leq 0.208$). Pitch variations between $\Theta = -2.0°$ and $\Theta = +2.0°$ were also considered.

The model was mounted via four pins (M8 threaded bar) to the six component balance located beneath the working section (see §2.3). In the no-wheel case (Fig. 2.1a), the pins were in locations representative of the front and rear axles and $10\,mm$ inboard of the model sides. The SAE coordinate system (SAE, 2010) is used throughout; the x axis is aligned with the flow in the streamwise direction, the z axis is vertical, positive upwards, and the y axis follows a right handed coordinate system. The origin is on the ground plane at mid wheelbase, mid track. All tests were performed with a free-stream velocity V_∞ of $40\,m/s$, corresponding to a Reynolds number Re_H of 7.7×10^5 based on the model height H. In these conditions, the wake

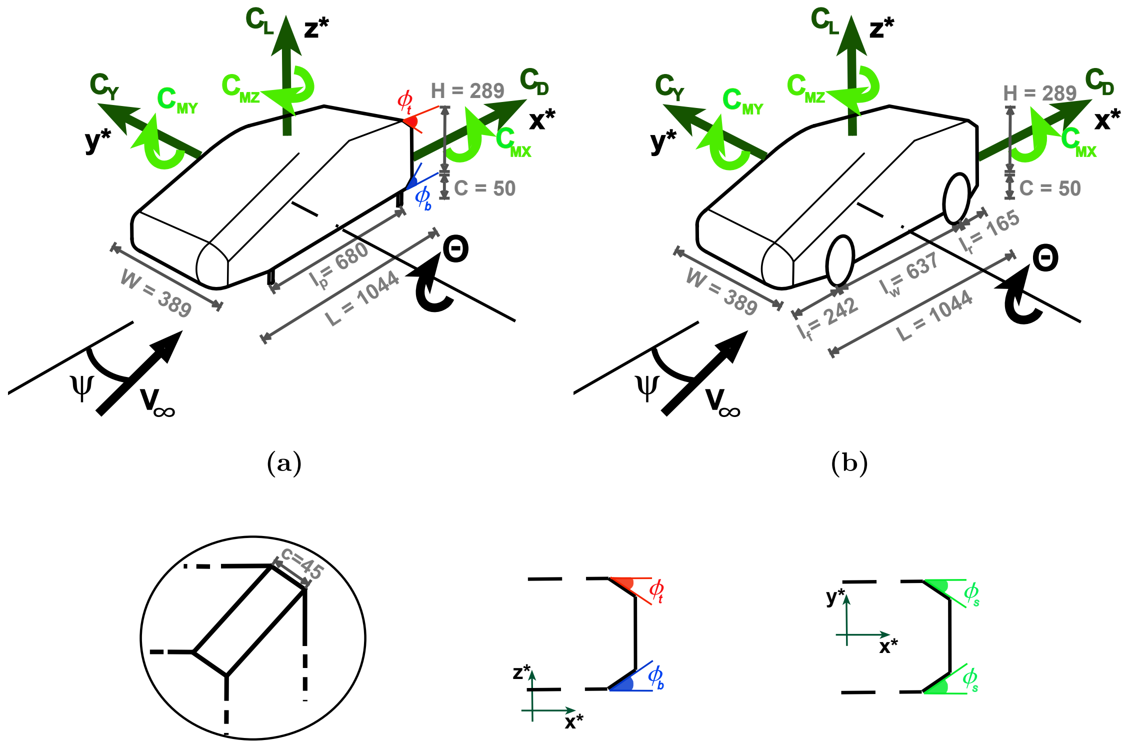

(a)

(b)

(c)

Figure 2.1: Schematic representations of the Windsor body: **a** model without wheels; **b** model with wheels; **c** trailing edge tapers. All dimensions reported are expressed in *mm*. For the reference system see SAE (2010).

developing downstream of the body is fully turbulent and no appreciable variation is seen in the aerodynamic coefficients if the Reynolds number is further increased (Littlewood, 2013).

All quantities presented throughout the thesis have been normalised using the model height H as reference length and the value of the free-stream velocity V_∞. They are denoted with the superscript "$*$". In particular, u^*, v^* and w^* are used to indicate the normalised components of the velocity V^* along x^*, y^* and z^*. For the sake of clarity, all time averaged quantities are denoted with the symbol "$-$" whilst the diacritical mark "$\sim$" is used to denote quantities extracted from conditional averaged fields. The base of the model is located at $x^* = 1.81$ from the origin of the reference system. x^*_B is used to indicate the streamwise location of a generic point from the base.

In order to study the effects of stationary and rotating wheels on the vehicle's wake, a second model with the same external shape was also manufactured. This model allows the addition of four rotating aluminium wheels, machined from solid, to the main body, in order to make the setup more relevant for real cars (see Fig. 2.1b and 2.2). Each wheel has an external diameter D_w of $150\,mm$ and a maximum width of W_w of $55\,mm$. The front axle is

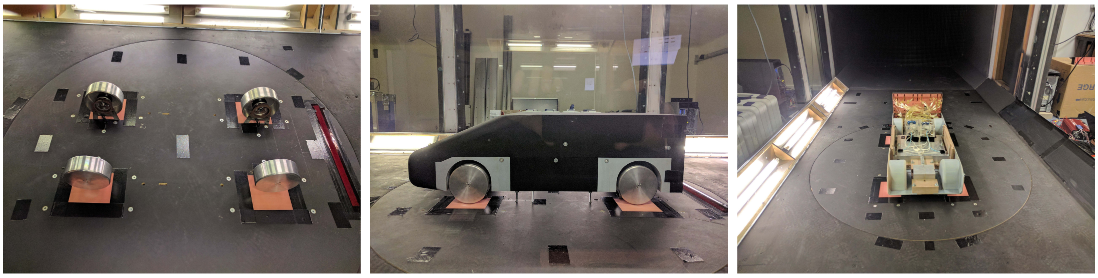

(a) **(b)** **(c)**

Figure 2.2: Pictures of the model as installed in the test section of the Loughborough University Large Wind Tunnel: **a** wheel test rig; **b** square-back model with stationary wheels; **c** model with the upper parts removed.

placed $280\,mm$ upstream of the centre of the model while the rear axle is located $357\,mm$ downstream of the same point, resulting in a wheelbase l_w of $637\,mm$, with the front and the rear overhangs measuring respectively $l_f = 242\,mm$ and $l_r 165\,mm$. In order to leave space for the wheels, the location of the pins connecting the model with the underfloor balance was moved between the two axles (the distance separating front and rear pins was reduced from $l_p = 680\,mm$ to $l_p = 286\,mm$), minimising their aerodynamic interference with the rest of the model. Each wheel was housed inside a 3D printed wheel-arch, with a diameter D_{wa} of $170\,mm$ and a depth of $96\,mm$ at the front and $76\,mm$ at the rear. No connection was present between the wheels and the main body. Having the wheels detached from the rest of the model (Fig. 2.2a), was a requirement dictated by the need to protect the balance from the vibrations created by the wheels themselves when spinning. It also allowed to easily change the ground clearance and the pitch angle of the model while keeping the two axles always in the same locations. The torque needed to spin the wheels was provided by four KDE® *330 Kv* electrical brushless motors, with an external diameter D_m of $60\,mm$ and a maximum width of W_m of $48\,mm$. The motors were mounted inside each wheel and connected in parallel to a $50\,A$ power supply, with a maximum voltage output of $30\,V$. During the tests, the rotational speed was set at $5100 \pm 50\,RPM$ (matching the free-stream velocity of $40\,m/s$) using a servo tester connected to the motor electronic speed control units. Contact with the ground was prevented by a $3\,mm$ deep recess located at the contact patch of each wheel. This model was also used for some additional tests in the no-wheel configuration. When the wheels were not in use, the wheel-arches were replaced with four 3D printed covers mounted flush with the side and underbody surfaces.

Both models, with and without wheels, were equipped with a removable rear section that allowed testing of multiple rear taper configurations, similar to those used in Littlewood (2013) and Perry (2016b) (Fig. 2.1c). Each taper has a chord c of $45\,mm$. Besides the pure square-back configuration, different combinations of either horizontal or vertical tapers were studied. For the sake of clarity, ϕ_t denotes the angle formed by the top taper with the flat section of model's

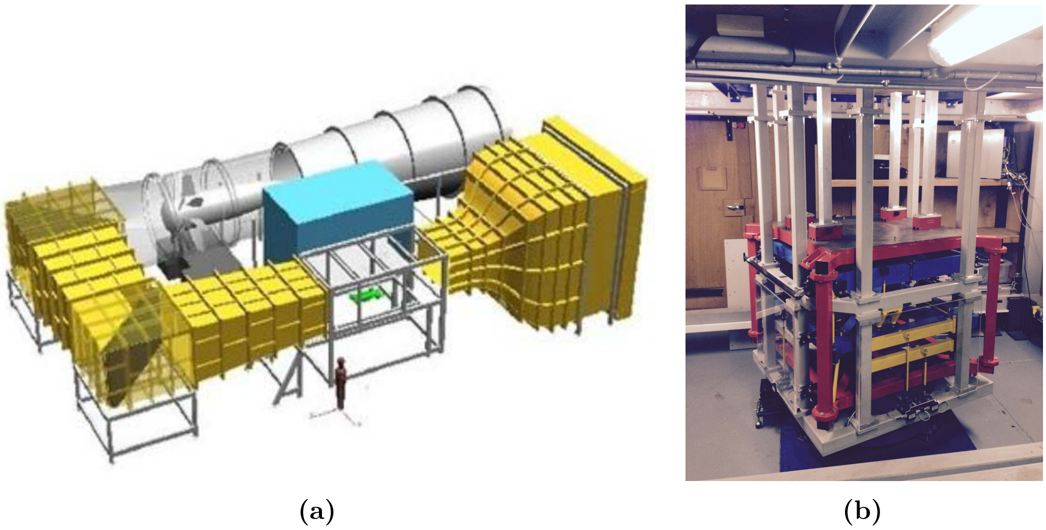

(a) (b)

Figure 2.3: **a** Loughborough University Large Wind Tunnel (sketch from Johl et al (2004)); **b** wind tunnel force balance.

roof, ϕ_b represents the angle between the bottom chamfer and the flat underbody, whereas ϕ_s indicates the angle formed between each vertical taper and the model's sides.

2.2 The wind tunnel

All experiments were carried out in the Loughborough University Large Wind Tunnel. This test facility (Fig. 2.3a), features a closed test section and an open circuit with a horseshoe shaped layout, which allows to test 1/4 scale vehicle models with low blockage ($< 5\%$) in a relatively constrained space (the tunnel fits within an $18\,m \times 10\,m \times 7.5\,m$ envelope). Wind is generated through a $2.65\,m$ diameter, variable-speed, fixed pitch fan, with nine blades featuring a free vortex design. The fan is located downstream of the working section; it is powered by a $140\,kW$ electric motor housed in the nacelle and cooled through eight hollow straightener vanes. It was designed to allow for wind speeds up to $45\,m/s$, at the start of the working section. More information can be found in Johl (2010).

The test section measures $1.92\,m \times 1.32\,m \times 3.6\,m\,(W_T \times H_T \times L_T)$, and is equipped with a fixed floor without any upstream boundary layer treatment. Although it is recognised that this layout may be source of unrealistic interactions between the model lower sections and the ground, it was preferred to that with a moving ground system because of its intrinsic simplicity, especially considering the fact the primary scope of the present investigation is that to gain an understanding of a fundamental aerodynamic problem rather than trying to find an optimum solution for a particular design. A tunnel blockage of $B = 4.4\%$ was obtained for the model considered in the present work. This value increased up to $B = 4.65\%$ when wheels were applied to the model (still below the 5% threshold recomended in Barlow et al (1999) for low speed wind tunnel testing).

Tunnel speed was set through a control PC, with an accuracy of $\pm 0.1\,m/s$. Wind speed readings were made using a Pitot-static tube mounted at the start of the test section, $1.87\,m$ (or 6.47 times the model height H) upstream of the model, $100\,mm$ beneath the tunnel roof. Total and static pressures were recorded through a Furness Control® 332 digital manometer, with a measurement range of $\pm 250\,mm\,H_2O$. A thermocouple attached to the same pitot tube was used to record the air temperature (T_{ref}) inside the working section, whilst the atmospheric pressure (P_{ref}) was monitored using a Druck® DPI 142 barometer, placed in the control room. The values of the pressure readings were manually entered into the wind tunnel's control software at the start of each test. In empty conditions, the free-stream turbulence level inside the test section was found to be approximately 0.2%, with a flow uniformity of ±0.4% of the mean flow value. In this state, the boundary layer thickness at the model origin was measured to be equal to $\delta_{99} = 64\,mm$.

2.3 Balance measurements

The aerodynamic loads were recorded by means of an Aerotech® six-component virtual centre balance, located under the working section of the wind tunnel (Fig. 2.3b). It features analogue to digital conversion at the load cell to minimise signal degradation, and an automated yaw mechanism with a positional accuracy of $\pm 0.1^o$. Further information can be found in Johl (2010).

The aerodynamic loads were sampled at $100\,Hz$ for $t = 630\,s$ (corresponding to $8.720 \cdot 10^4$ convective units t^*, with $t^* = t \cdot V_\infty / H$). The sampling time was reduced to $t = 150\,s$ (or $t^* = 2.226 \cdot 10^4$) in case of yaw sweeps. Before starting to log the data, a $30\,s$ ($t^* = 4.152 \cdot 10^3$) settling time was used for all measurements. The recorded values of the forces were normalised as seen in §1.1.4 and §1.2.1, leading to Eq. 2.1:

$$C_{Fi} = \frac{Force}{0.5 \rho V_\infty^2 S_{Body}} \tag{2.1}$$

where $S_{Body} = 0.1124\,m^2$, and $\rho = P_{ref}/(RT_{ref})$ (with R referring to the specific gas constant, assumed to be $\approx 287\,J/(kgK)$ in the case of air). The coefficients were corrected for blockage effects using the MIRA correction (based on continuity):

$$C_{Fi_{Cor}} = C_{Fi}(1-B)^2 \tag{2.2}$$

where B denotes the blockage value, given by the ratio between the model frontal area S_M and the tunnel working section cross sectional area S_T. When the wheels were added to the model, the portion of the cross-sectional area of the wheels directly exposed to the wind (i.e.

not shielded by the main body) was added to S_M, thus increasing the value of B (see §2.2). The coefficients are accurate within ±2 counts (Johl, 2010).

2.3.1 Wavelet analysis

The effects of the long-time mode described in §1.3.1 on the three components of the aerodynamic force were investigated by means of wavelet analysis, using the Matlab® toolbox developed by Grinsted et al (2004). This technique allows to determine the frequency content of a discrete time series $f(t)$ whilst assessing its variation in time. This goal is achieved by projecting the signal onto a set of continuous functions $\Xi_{s,\tau}(t)$. These functions, called *wavelets*, are derived from the translation and dilatation of a basis function $\Xi_0(t)$, known as *mother wavelet*, according to the relation:

$$\Xi_{s,\tau}(t) = \frac{1}{\sqrt{s}}\Xi_0\left(\frac{t-\tau}{s}\right), \tag{2.3}$$

where s and τ are real parameters, corresponding respectively to a dilatation in frequency and a translation in time of the original mother wavelet $\Xi_0(t)$. If τ and s are varied continuously, the convolution of $f(t)$ with $\Xi_{s,\tau}(t)$ results in the *continuous wavelet transform* (CWT) of the signal:

$$W^f(s,\tau) = \int_{-\infty}^{+\infty} f(t)\Xi'_{s,\tau}(t)dt, \tag{2.4}$$

where $'$ refers to the conjugate of $\Xi s, \tau(t)$. To be considered as a *wavelet*, the analysing function must be admissible, hence have zero mean, and be localised in both frequency and time (Farge, 1992). An example of such a function is the so called *'Morlet wavelet'*:

$$\Xi_0(\kappa) = \pi^{-1/4} e^{i\zeta_0\kappa_\tau} e^{-\frac{1}{2}\kappa_\tau{}^2}, \tag{2.5}$$

where κ_τ is the dimensionless time and ζ_0 is the dimensionless frequency (considered in this case equal to 6 in order to fulfil the admissibility condition). This function provides a good trade-off between localisation in time and frequency, which is subjected to the classical Heisenberg's principle of indetermination (Grinsted et al, 2004). Since $\Xi_0(\kappa)$ is a complex function, its wavelet transform $W^f(s,\tau)$ is also complex. Therefore it can be divided into a real part and an imaginary part. A *wavelet power spectrum* $|W^f(s,\tau)|^2$ can be also defined. This allows to easily represent the level of correlation between the wavelet function $\Xi(t)$ and the original time series $f(t)$ at different times and dilatation scales throughout the entire time-frequency domain of $f(t)$.

When two different signals $f(t)$ and $g(t)$ are considered, a *cross wavelet transform* (XWT) can be defined as:

$$W^{f,g}(s,\tau) = W^f(s,\tau) \cdot W^g(s,\tau)', \tag{2.6}$$

where $W^f(s,\tau)$ and $W^g(s,\tau)$ are the wavelet transforms of the two considered time series. The related power spectrum $|W^{f,g}(s,\tau)|^2$ can be used to identify regions in the time-frequency

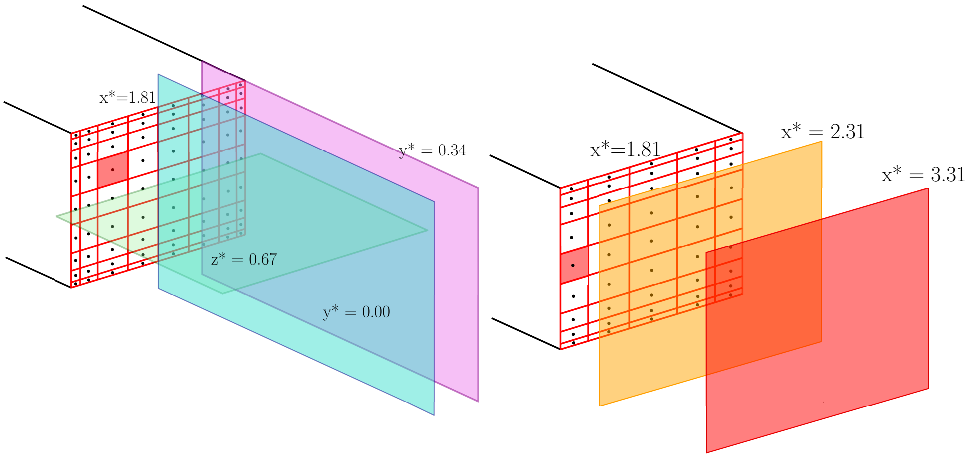

(a)

(b)

Figure 2.4: Representation of the model base with the locations of the pressure taps and PIV planes considered in the present work: **a** two scanner arrangement combined with the locations of the 2D-2C PIV planes; **b** single scanner arrangement combined with the locations of the 2D-3C PIV cross-planes. The base is located at $x^* = 1.81$ from the origin of the reference system defined in Fig 2.1. The red square on the model base denotes the area associated with the i^{th} tap used for the estimation for the area weighted drag.

domain where the two series have a high common power. The existence of a high level of correlation between two time series, however, does not necessarily imply that there is any kind of connection between the two. For this reason it is important to consider the phase relationship:

$$\chi^{f,g}(s,\tau) = \tan^{-1}\left(\frac{Im\left(\langle s^{-1}W^{f,g}(s,\tau)\rangle\right)}{Re\left(\langle s^{-1}W^{f,g}(s,\tau)\rangle\right)}\right), \tag{2.7}$$

where the operator $\langle\rangle$ refers to a suitable smoothing operator (Torrence and Compo, 1998). A strong causal connection in fact can be defined only when the oscillations between the two series are locked in phase.

2.4 Pressure measurements

The pressure acting over the base and the tapers was recorded by populating the rearward facing surfaces with a grid of pressure taps connected via flexible urethane tubes (with a length of $550\,mm$) to a pair of Chell® CANdaq miniature pressure scanners (with a manufacturer quoted accuracy of $\pm 1.47\,Pa$), mounted inside the model (Fig. 2.2c). Each scanner is equipped with 64 piezoresistive pressure sensors, paired to temperature sensors to allow for the correction of inaccuracies introduced by temperature drift. Up to 126 taps were used, depending on the configuration. The taps were placed with a finer distribution close to the model edges and on the tapered surfaces, to get a more accurate representation of the pressure distribution in the regions with the highest gradients (see Fig. 2.4a). In some cases the pressure distribution along the model centreline was also measured (see Fig. 5.12b and 6.1a). Pressure data was recorded at $260\,Hz$ for $630\,s$ ($t^* = 8.720 \cdot 10^4$). The free-stream dynamic and static pressures were acquired using the same Pitot-static tube described in §2.2. The pressure signals were corrected for magnitude and phase distortions caused by the tubing, applying the correction already used in Wood (2015) and based on the method proposed by Sims-Williams and Dominy (1998). Once the pressure coefficients were calculated, Eq. 2.8, the results were corrected for blockage using the MIRA correction (based on continuity), Eq. 2.9:

$$C_{p_i} = \frac{p_i - p_\infty}{0.5 \rho S_{Body} V_\infty^2} \tag{2.8}$$

$$1 - C_{p_{i_{corr}}} = (1 - C_{p_i})(1 - B)^2 \tag{2.9}$$

where p_∞ is the freestream static pressure. The drag of the rearward facing surfaces was then estimated by integrating the measured pressure field:

$$\overline{C}_{D_{Rear}} = -\frac{1}{S} \int\int_S \overline{C}_p \cdot dS \simeq -\frac{1}{S} \sum_{i=1}^{N_{tap}} \overline{C}_{p_i} S_i, \tag{2.10}$$

where $\overline{C}_{p_i}$ is the time averaged value of the pressure coefficient recorded by the i^{th} tap and S_i is the projection of the area associated with the same tap on a plane orthogonal to the direction of the onset flow (for $\Psi \approx 0°$, see Fig. 2.4).

Since the flow field analysed in the present study is highly sensitive to any asymmetry present in the experimental setup, the model was yawed to the onset flow until the most symmetric base pressure distribution was achieved, following a similar procedure to that adopted by Evrard et al (2016). The resulting value of Ψ was assumed to be where the model axis and onset flow axis were aligned.

The regions with the highest level of unsteadiness were localised considering the distribution of the root mean square of the pressure fluctuation ($RMS(\Delta C_p)$) over the model base, calculated as follow:

$$RMS(\Delta C_{p_i}) = \sqrt{\frac{\sum_{n=1}^{N_t} \left(C_{p_i}^n - \overline{C}_{p_i} \right)^2}{N_t}}, \tag{2.11}$$

where $C_{p_i}^n$ denotes the n^{th} value recorded in time by the i^{th} tap and N_t indicates the number of samples in time.

2.4.1 POD

The main features of the unsteady pressure field were extracted by means of *Proper Orthogonal Decomposition* (POD). This technique was introduced into turbulence research by Lumley (1967); it allows to decompose a generic unsteady field into a set of orthogonal modes which are ranked by their energy content. The first few modes therefore are representative of the most dominant coherent unsteady structures and can be used to built a reduced order model describing the main dynamic features of the considered field.

A generic dataset $\mathbf{F}(\mathbf{x},\mathbf{t})$ is decomposed as:

$$\mathbf{F}(\mathbf{x},t) = \mathbf{F}_0(\mathbf{x}) + \mathbf{F}'(\mathbf{x},t) = \mathbf{F}_0(\mathbf{x}) + \sum_{n=1}^{N_t} \mathbf{\Phi}^n(\mathbf{x}) a_n(t), \tag{2.12}$$

where N_t indicates the number of measurement points in time, $\mathbf{F'}_0$ the mean of the considered field and $\mathbf{F}'(\mathbf{x},t)$ its fluctuating components. The basis functions $\mathbf{\Phi}^n(\mathbf{x})$ are the so called *'POD modes'* and are defined as the eigenfunctions of the covariance matrix $\mathbf{R}(\mathbf{x},\mathbf{x})$:

$$\mathbf{R}(\mathbf{x},\mathbf{x}) = \sum_{n=1}^{N_t} \mathbf{F}'(\mathbf{x},t_n) \cdot \mathbf{F}'^T(\mathbf{x},t_n) = \mathbf{X} \cdot \mathbf{X}^T, \tag{2.13}$$

where $\mathbf{X}$ is a matrix with

$$\mathbf{X} = \left[\mathbf{F}'(\mathbf{x},t_1), \mathbf{F}'(\mathbf{x},t_2), ..., \mathbf{F}'(\mathbf{x},t_n)\right] \in \mathbf{R}^{N_s \times N_t} \tag{2.14}$$

and N_s refers to the number of points sampled in space. The basis functions $\mathbf{\Phi}^n(\mathbf{x})$ can therefore be determined by solving the eigenvalue problem:

$$\mathbf{R}\mathbf{\Phi}^n = \lambda^n \mathbf{\Phi}^n, \quad \mathbf{\Phi}^n \in \mathbf{R}^{N_s} \tag{2.15}$$

with $\lambda^1 \geq ... \geq \lambda^n$. The eigenvalues λ^n associated with the POD modes are representative of the energy content of the fluctuations captured by each mode. A low order model can then be written as:

$$\mathbf{F}(\mathbf{x},t) \simeq \mathbf{F}_0(\mathbf{x}) + \sum_{n=1}^{M} \mathbf{\Phi}^n(\mathbf{x}) a_n(t), \tag{2.16}$$

with $M < N_t$ and the temporal coefficients $a_n(t)$ determined projecting each spatial mode $\mathbf{\Phi}^n$ on the original dataset $\mathbf{F}'(\mathbf{x},t)$:

$$a_n(t) = \langle (\mathbf{\Phi}^n(\mathbf{x}))^T, \mathbf{F}'(\mathbf{x},t) \rangle. \tag{2.17}$$

Since the frequency resolution of the pressure measurements was high enough to resolve most of the temporal scales characteristic of the flow field analysed in the present work (Volpe et al, 2015), the power spectral density (PSD) of the POD temporal coefficients was determined using the *Welch periodogram* (Welch, 1967). This method derives from the standard Fourier spectrum approach, but trades frequency resolution for a lower noise level. Given a generic discrete signal S_n (with $n = 1, ..., N_t$), a window function w_n (with $0 \leq w_n \leq 1$) is used to smooth the signal. This, however, leads to a decrease of the signal power, that can be mitigated by normalising the Fourier transform with the averaged power of the window function employed $\overline{w_n^2}$. The PSD at the frequency f is therefore given by:

$$\mathbf{P}(f) = \frac{2}{N_t^2 \cdot \overline{w_n^2}} \left| \sum_{n=1}^{N_t} S_n w_n e^{-i2\pi(f/f_s)n} \right|^2, \tag{2.18}$$

where $0 \leq f \leq f_s/2$ and f_s refers to the sampling frequency. In the present case, the original signal was split into short intervals of $\approx 15.75\,s$ each, with a 50% overlap. The PSD was calculated separately for each interval using a bell-shaped *Hann window* (Harris, 1978). The final spectrum was then obtained by averaging the PSDs from all segments, with an accuracy of $\delta f = \pm 0.067\,Hz$ or $\delta St_H = \pm 4.4 \cdot 10^{-4}$.

For the sake of simplicity, most of the unsteady analysis was performed considering only the data recorded over the model base (i.e. the vertical rear surface excluding the slants). As a consequence, one scanner was used in most cases, rather than the two scanner setup needed for estimating $\overline{C}_{D_{Rear}}$. Spatial resolution was in this case a less stringent requirement as there was no longer the need to accurately resolve the strong pressure gradients developing over the slanted surfaces. Between 45 and 49 taps were employed (depending on the configuration), arranged as shown in Fig. 2.4b. The drag estimated in this case using Eq. 2.10 refers to the base only and it will be indicated as *'base drag'* ($C_{D_{Base}}$); with $C_{D_{Base}} = C_{D_{Rear}}$ in the square-back case only, due to the absence of tapered rearward facing surfaces.

2.4.2 Coherence analysis

A limitation of POD is that it is not able to isolate the frequencies of different unsteady modes, as the spectrum of the POD temporal coefficients usually contains more than one peak (Taira et al, 2017). To overcome this issue, the coherence between signals recorded by taps placed at different locations along the trailing edges of the model was considered, following the approach proposed by Duell and George (1999). The magnitude of the coherence between two generic synchronised signals i and j was calculated according to the equation:

$$\mathbf{\Lambda_{ij}}(f) = \frac{|\mathbf{P_{ij}}(f)|^2}{\mathbf{P_{ii}}(f) \cdot \mathbf{P_{jj}}(f)}, \tag{2.19}$$

where $\mathbf{P_{ij}}(f)$ is the cross-spectrum and $\mathbf{P_{ii}}(f)$ and $\mathbf{P_{jj}}(f)$ are the auto-spectra of the signals. The phase relationship between the two signals was then determined as:

$$\chi_{\mathbf{ij}}(f) = \left| \tan^{-1} \left(\frac{Im\left(\mathbf{P_{ij}}(f)\right)}{Re\left(\mathbf{P_{ij}}(f)\right)} \right) \right|, \tag{2.20}$$

considering for simplicity the absolute value of the phase angle. Conversion in the frequency domain was performed using the same approach presented in Eq. 2.18. In this case, however, intervals of $\approx 1.97\,s$ where considered for each Hann window, with an accuracy of $\delta f = \pm 0.51\,Hz$ or $\delta St_H = \pm 3.5 \cdot 10^{-3}$.

2.5 PIV measurements

Particle Image Velocimetry (PIV) was employed in the present investigation to gather information on the topology of the time averaged near wake and isolate the most coherent unsteady structures. PIV is a non-intrusive optical technique which allows quantitative measurements of the instantaneous velocity field across a planar section of a generic flow field to be performed (Fig. 2.5). The flow is seeded with tiny, neutrally buoyant particles (*'tracers'*) and illuminated using a double pulsed laser beam, expanded into a 2D sheet through an arrangement of cylindrical lenses. The particles immersed in the flow field are illuminated twice, with a small time separation *dt* between flashes. The light scattered from the tracers is then captured, usually in two different frames, by one or more cameras placed perpendicular to the laser sheet (in the case of planar PIV, §2.5.1), or forming an angle $< 90°$ (when a stereoscopic arrangement is considered, §2.5.2). The frames are then stored into a PC, that usually is used also for the processing of the data acquired. During the processing, each recording is divided into small subareas, or *'interrogation windows'*. A local displacement vector is determined for each window, performing cross-correlation between the two frames:

$$\mathbf{C}(x_0, y_0) = \mathbf{I}_1(t, x_0, y_0) \cdot \mathbf{I}_2(t + dt, x_0, y_0), \tag{2.21}$$

where $\mathbf{I}_1$ and $\mathbf{I}_2$ refer to the interrogation windows from the 1^{st} and the 2^{nd} frame, at image position (x_0, y_0). The *'Fast Fourier Transform'* (FFT) algorithm is usually used to perform this operation. The most likely displacement of the particle ensemble contained in the interrogation window is given by the highest correlation peak detected in the correlation plane. Knowing the particle displacement and the time *dt* between the two illuminations, a velocity vector can be calculated. The vectors extracted from all interrogation windows are then combined together to yield the vector field of the whole image. The process can be performed iteratively for increased accuracy. The resolution can be improved by decreasing the size of the interrogation windows during each iteration and offsetting the windows according to the displacement obtained from the previous iteration. A more complete description of PIV and its applications is provided in

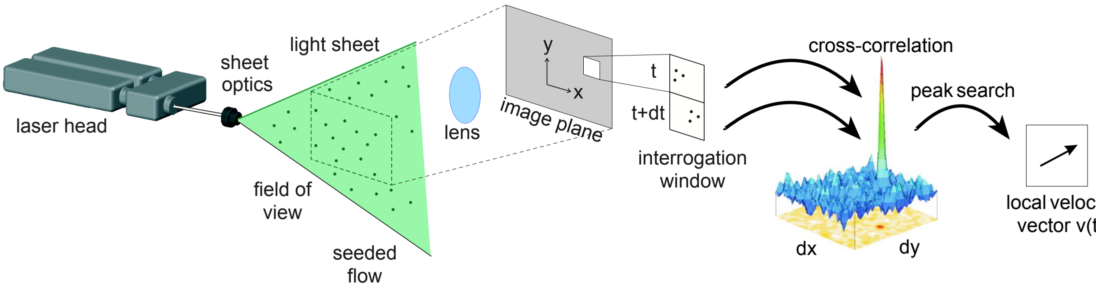

Figure 2.5: PIV working principle. Sketch from LaVision (2015) (edited).

Adrian and Westerweel (2011) and Raffel et al (2018).

The time delay between the two pulses is a function of the flow velocity and the magnification factor of the camera lens. It has to be chosen in such a way that an adequate displacement of the tracer particles can be seen between the two frames. To obtain accurate results it is important that the shift of the seeding particles is about 1/4 of the size of the final interrogation window. At the same time, the tracers should not occupy less than 2 pixels, in order to avoid *peak-locking* effects (Adrian and Westerweel, 2011), in which the curve-fit scheme used to locate the correlation peak with sub-pixel accuracy fails and the peak location is biased towards the nearest pixel (Prasad, 2000a). A minimum of 7 particles for each interrogation window is also recommended for high signal-to-noise ratio (Coupland and Pickering, 1988).

Planar (2D-2C) and stereoscopic (2D-3C) PIV acquisition were performed during the experiments described in the present work. The former was used to investigate the flow field along streamwise planes, aligned in either vertical or horizontal directions (§2.5.1); the latter was employed in the case of cross-flow planes (§2.5.2), where the out-of-plane component of the velocity u could not be neglected when compared with the in-plane components v and w (Prasad, 2000b). In all cases, the flow was seeded using a *PIVTec 45* atomiser, generating $1\mu m$ droplets of *Di-Ethyl-Hexyl-Sebacat* (DEHS) through a system of Laskin nozzles (Kähler et al, 2002). These particles are known to have good tracing characteristics, i.e. fast response time and low velocity lag, when used in air (Adrian and Westerweel, 2011). During the acquisitions, the seeder was run continuosly, since the open-circuit configuration of the wind tunnel did not allow to recirculate the particles. Two seeding rakes were employed. The primary rake was located at the start of the contraction, just downstream of the settling chamber, while a second rake was located flush with the floor at the start of the working section. A Litron® $200\,mJ$ double pulsed Nd:YAG laser was used as light source, with a maximum repetition rate of $15\,Hz$. The laser was mounted on a purpose built frame placed outside the wind tunnel and located either on the tunnel rooftop (for vertical planes and cross-flow planes) or inside a dedicated room situated on the right-hand side of the working section (for horizontal planes). Optical mirrors were used to guide the beam from the laser head to the sheet optic. The emission of the laser beam was synchronised with the cameras using a LaVision® *Programmable Timing*

Unit. Data was stored and processed using a workstation equipped with an Intel ® *Xenon* motherboard featuring 16 physical cores and $128GB$ of RAM.

2.5.1 Planar PIV

Two-dimensional PIV fields were taken on three orthogonal planes. Two vertical and one horizontal streamwise planes were considered (Fig. 2.4a), using a setup similar to that described in Perry (2016b). The first vertical plane ($y^* = 0$) was placed along the model centreline whilst the second plane ($y^* = 0.34$) was located at 1/4 of the model width (on the right-hand side of the model), where y^* is the distance of the plane from model centreline (normalised considering the model height H). In a similar way, the horizontal plane ($z^* = 0.67$) was placed at the middle of the model base, where z^* is the non-dimensional distance of the plane from the ground (see Fig. 2.4a).

Up to two LaVision® *Imager Pro X 4M* dual frame cameras were employed, with a resolution of 2048×2048 pixels and a pixel size of $7.4\mu m^2$. Each camera was equipped with a Nikon® *Nikkor* lens, with a focal length of $50mm$; the aperture was set at $f_{\#} = 5.6$. Two cameras were used for the vertical planes, mounted on a purpose built frame placed outside the wind tunnel. The cameras were placed next to each other, giving an $800mm \times 400mm\,(L_{FOV} \times H_{FOV})$ field of view, with a $50mm$ overlapping region. Optical access was provided by the wind tunnel glass side walls. One single camera was employed for the horizontal plane, giving a $400mm \times 400mm$ field of view. In this case, optical access was provided by a glass panel mounted on the wind tunnel roof.

During each acquisition, 1000 image pairs were captured to ensure reasonable confidence in the mean velocity across all areas of the field of view (Passmore et al, 2010). A capture rate of $7.26Hz$ was used, resulting in an acquisition time of $137.7s$ or $t^* = 1.906 \cdot 10^4$. The data was then processed using *DaVis 8*. A calibration correction based on a pinhole model was applied, resulting in all cases in a RMS of the fit between the regular grid and the de-warped image of less than 0.3 pixels. Background subtraction was applied to all images to minimise the effects of spurious reflections. For the same reason, the outermost regions of the field of view were discarded using a geometric mask. A multi-pass scheme for cross-correlation was applied (Willert and Gharib, 1991), starting with a squared interrogation window with a size of 64×64 pixels and a 50% overlap between cells and ending with circular windows of 24×24 pixels and a 75% overlap, yielding a final spatial resolution of $6.4 \times 10^{-6} m^2$. In order to cut the computational time required, the computer GPU was preferred over the CPU when performing these operations (Schiwietz and Westermann, 2004). Spurious vectors were then removed using a median filter (Westerweel, 1994). The level of uncertainty associated with the measurements was estimated to be $\approx 0.4\%$ of the mean value of the free-stream velocity for the vertical planes and $\approx 1\%$ for the horizontal plane, having considered a 99% confidence level (Benedict and Gould, 1996).

2.5.2 Stereoscopic PIV

Stereoscopic PIV measurements were performed on planes orthogonal to the onset flow, at two streamwise locations, $x^* = 2.31$ and $x^* = 3.31$ (Fig. 2.4b). These locations were chosen since they correspond approximately to 1/3 of the bubble length and the end of the recirculating region. Two LaVision® *CMOS* cameras with a resolution of 2560×2160 pixels and a pixel size of $6.5\,\mu m^2$ were employed. The cameras were mounted on a pair of aluminium rails placed inside the tunnel working section, following the arrangement already used by Wood (2015). The separation angle between the cameras was $\approx 50°$. Each camera was equipped with a Nikon® *Nikkor* lens, with a focal length of $50\,mm$, mounted on a tilt system in order to satisfy the *Scheimplfug criterion* (Prasad, 2000b). The aperture was set at $f_{\#} = 4$. The resultant field of view ($W_{FOV} \times H_{FOV}$) was $520\,mm \times 400\,mm$.

During each acquisition, 2000 statistically independent image pairs were captured at a sampling frequency of $15.00\,Hz$, resulting in a sampling time of $133.3\,s$ or $t^* = 1.845 \cdot 10^4$. The data was then processed using *DaVis 8*. Image pre-processing was performed in order to mitigate the effects of image distortion, background light intensity as well as spurious reflections. A calibration correction based on a pinhole model was applied; the outermost regions of the field of view were discarded using a geometric mask. The size of the field of view was therefore reduced to $430\,mm \times 340\,mm$. A multi-pass scheme for cross-correlation was applied, starting with an interrogation window with a size of 64×64 pixels and a 50% overlap between cells and ending with windows of 32×32 pixels and a 75% overlap. This resulted in a spatial resolution of $2.8 \times 10^{-6}\,m^2$. Spurious vectors were filtered via *Q-factor* rejection, having defined the *Q-factor* as the ratio between the highest and the second highest peak in the correlation map (Adrian and Westerweel, 2011). This operation, however, prevented the use of the GPU for the calculation of the correlation maps (LaVision, 2015), thus increasing the computational time. A median filter was then applied to the remaining vectors (Westerweel, 1994). The level of uncertainty associated with the measurements was estimated to be $\approx 0.5\%$ of the mean value of the free-stream velocity, having considered a 99% confidence level.

2.5.3 Snapshot POD

As for the base pressure, the main unsteady features of the velocity field were captured by applying POD to the resulting vector fields. The *snapshot method* developed by Sirovich (1987) was applied in this case, due to its higher computational efficiency when the temporal domain is much smaller than the spatial domain ($N_t \ll N_s$). This method relies on solving an eigenvalue problem of smaller size:

$$\mathbf{X}^T\mathbf{X}\mathbf{A}_n = \lambda^n \mathbf{A}_n, \quad \mathbf{A}_n \in \mathbf{R}^{N_t}, \tag{2.22}$$

with $\mathbf{X}$ defined as in Eq. 2.14. The POD modes $\mathbf{\Phi}^n$ are then given by:

$$\mathbf{\Phi}^n = \frac{1}{\sqrt{\lambda^n}}\mathbf{X}\mathbf{A}_n \in \mathbf{R}^{N_s}, \quad n = 1,2,...,N_t, \tag{2.23}$$

whilst the temporal coefficients $a_n(t)$ can still be determined using Eq. 2.17.

2.6 Single point velocity measurements

The unsteady features of the top and side shear layers were investigated using a multi-hole *Cobra Probe* from Turbulent Flow Instrumentation®. It features four high speed pressure transducers, one placed in the front face and the other three equispaced around it (each one forming a 45° angle with the central port).This allows flow velocity and direction within a 90° cone to be measured (Fig. 2.6). The manufacturer quoted accuracy is $0.5\,m/s$. The recorded signal was corrected for phase and amplitude distortion caused by the short length of tubing to achieve a frequency resolution in excess of $1\,kHz$.

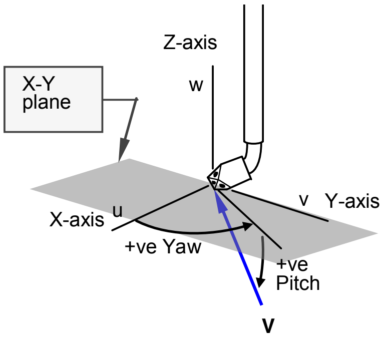

Figure 2.6: Flow axis system respect to the probe head (picture from Instrumentation (2011))

During the tests, pressure measurements were performed at eight different locations, on two planes ($y^* = 0$ and $z^* = 0.67$) at $x^*_B = 1/3$, $x^*_B = 2/3$, $x^*_B = 1$ and $x^*_B = 4/3$, with x^*_B referring to the normalised distance from the model base (see Fig. 2.7a and 2.7b). The probe was mounted on a traverse system equipped with two stepper motors to control its position along the Y and Z axis with an accuracy of $0.1\,mm$. The streamwise position instead was set manually, with a tolerance of about $1\,mm$. The sheer size of the traverse, needed to keep the probe stable at high speed, made the system not suitable for investigating the spectral content of the bottom shear layer, due to the non-negligible interactions between the traverse itself and the model's wake in such conditions.

The probe was connected to an external static port for the reference pressure. Data was acquired for $150\,s$ at $1.25\,kHz$ using an external data acquisition unit connected to a laptop via an USB cable. The spectral content of the signal was retrieved using the same approach based

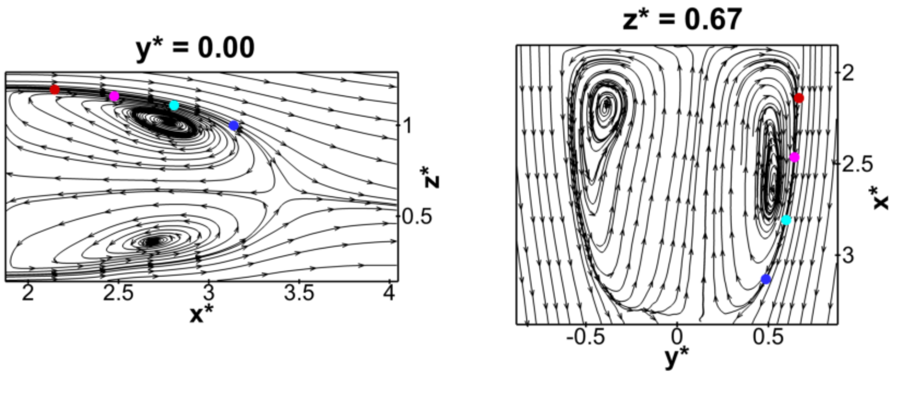

(a) **(b)**

Figure 2.7: **a** and **b** positions of the multi-hole pressure probe along the top and side shear layers (streamlines drawn from PIV data).

on the Welch periodogram described in §2.4.1. In this case the signal was split in intervals of $\approx 4.70\,s$, resulting in an accuracy of $\delta f = \pm 0.213\,Hz$ or $\delta St_H = \pm 1.4 \cdot 10^{-3}$.

Chapter 3

Wake of a square-back geometry

In this chapter, the unsteady behaviour of the wake of a square-back car geometry without wheels is investigated, with a particular emphasis on the characterisation of the long-time bi-stable mode in the case of a model with a less blunt front-end than the Ahmed body commonly employed in the literature (Grandemange et al (2012a), Grandemange et al (2013b), Volpe et al (2015), Evrard et al (2016)). The sensitivity of this mode to small perturbations, such as changes in yaw angle ($-2.0° < \Psi < +2.0°$) and variations of ground clearance ($0.138 \leq C^* \leq 0.208$) is investigated. For the first time, the presence of a clear bi-stable behaviour is also documented for relatively high values of the free-stream turbulence intensity (with $TI^* \approx 1.5\%$). Applying wavelet and cross-wavelet transforms to the balance data, a quasi-steady correlation is demonstrated between the variation of the aerodynamic forces and the bi-stable mode. The nature of these relationships is further investigated by applying proper orthogonal decomposition to the pressure and velocity datasets. A new structure is proposed for each bi-stable state, consisting of a hairpin vortex that originates from one of the two model's vertical trailing edges and bends towards the opposite side, as it merges into one single streamwise vortex downstream. The wake pumping motion is also identified and, for the first time, linked with the motion of the bi-stable vortical structure in the streamwise direction, resulting in out-of-phase pressure variations between the two vertical halves of the model base. A phase averaged low order model is also proposed, with the aim of providing new insights on the mechanisms of the switch between bi-stable states. It is demonstrated that, during the switch, the wake becomes laterally symmetric and, at this point, the level of interaction between the recirculating structures and the base reaches a minimum, yielding a 7% reduction of the base drag compared to the time averaged result.

3.1 Time averaged wake topology

The time averaged results obtained for the square-back configuration are presented in Fig. 3.1. The pressure map shows the existence of a relatively high pressure region slightly below the vertical centre of the base, surrounded by a lower pressure area. This lower pressure region covers most of the base and its shape suggests the existence of the toroidal vortex structures described by Rouméas et al (2009a) for the Ahmed body with a similar rear-end shape. This structure is confirmed by the vertical PIV planes at $y^* = 0.00$ and $y^* = 0.34$, showing the existence of two almost equal recirculations. The free stagnation point is located at $x^*_B = 1.58$ downstream of the model base and is aligned with the rear stagnation point at $z^* = 0.6$, justifying the increase in the static pressure previously described in this region as the result of the impingement of the flow on the model rear-end. As the two vortical structures interact with each other, a local acceleration is seen in the reverse flow region located at the core of the near-wake, with the velocity magnitude increasing up to of 40% of the free stream value, before slowing down in proximity to the base itself.

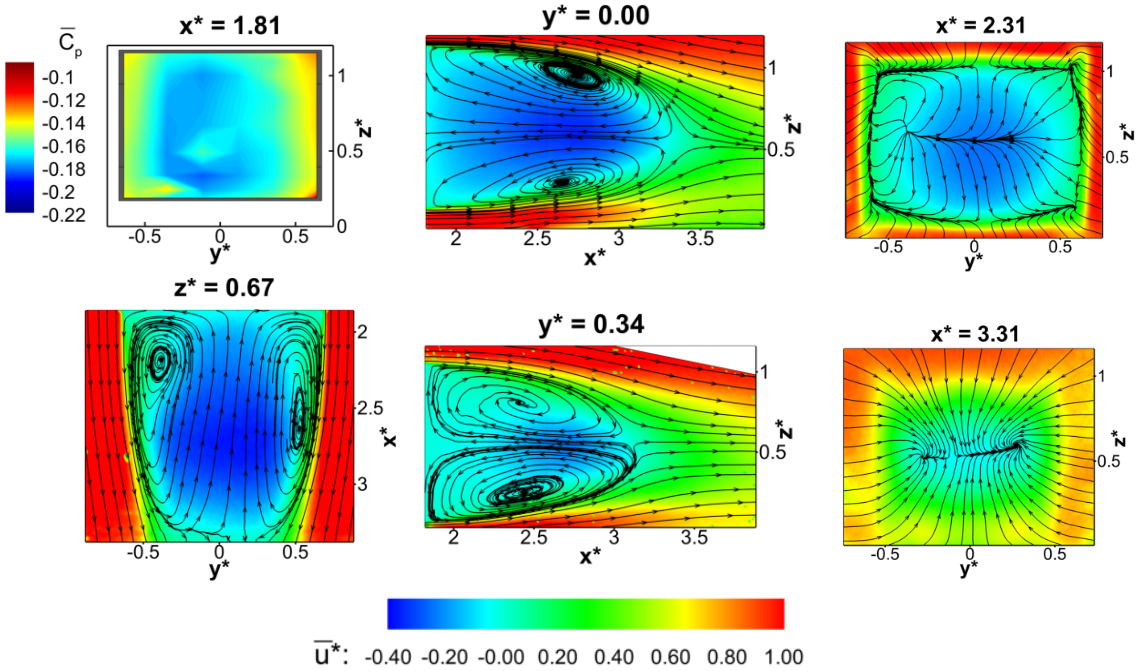

Figure 3.1: Time averaged results for the square-back Windsor body. Clockwise from top left: $\mathbf{x^* = 1.81}$ base pressure distribution; $\mathbf{y^* = 0.00}$ PIV vertical mid-plane; $\mathbf{x^* = 2.31}$ and $\mathbf{x^* = 3.31}$ PIV stereo cross-planes; $\mathbf{y^* = 0.34}$ PIV vertical off-centre plane; $\mathbf{z^* = 0.67}$ PIV horizontal mid-plane. All PIV fields are coloured according to the values of the axial component of the velocity u^*; the streamlines refer to the in plane components.

Similar features are seen in the mid-horizontal plane (Fig. 3.1, $z^* = 0.67$), where the two lobes of the wake torus are still recognisable. However, the cores of the two recirculating regions are now closer to the model base, with the closest being at $x_B^* = 0.39$ from the base ($x_B^* = 0.88$ for the mid-vertical plane), explaining the stronger pressure gradient that characterises the time average pressure map in the horizontal direction. The two horizontal lobes, though, do not show the same shape, with the core of the recirculating region almost circular on the left-hand side and elliptical on the right. Indeed, the reverse flow impinging on the base does not seem to be aligned with the rear stagnation point previously described. The topology of this flow field presents some similarities with one of the two lateral symmetry breaking modes isolated in previous studies such as Grandemange et al (2013b) and Volpe et al (2015). The characteristic time between switches has been reported to be typically greater than $10\,s$ (Volpe et al, 2015) which can lead to bias in the data when the sampling time is not sufficiently long (Grandemange et al, 2013b). This is the case for the PIV data acquired in the present work, as the sampling time was limited to $137.7\,s$ for constant frequency data collection. Such a constraint was not present during the pressure data acquisition, therefore sufficient data was captured to obtain a statistically symmetric average.

A similar level of lateral asymmetry can be seen in the first of the PIV cross-planes taken at $x^* = 2.31$. The asymmetry in this case is highlighted by the presence of a source along the horizontal plane of symmetry, close to the left-hand side of the model. Once the streamlines reach the edges of the base, they converge into four sinks, located at each corner of the model, defining the four shear layers. Downstream ($x^* = 3.31$), as the wake closes, the source is replaced with a pair of sinks, aligned in the horizontal direction, to which the streamlines running from each side of the flow field converge, leading to the formation of a pair of counter-rotating vortices.

3.2 Wake dynamics

3.2.1 Characterisation of the bi-stable mode

Insights into the wake's unsteady behaviour are provided by the root mean square of the pressure fluctuation. In the most symmetric condition ($\Psi \approx 0.0°$), a region with a high level of unsteadiness develops at the centre of each of the two vertical halves of the base (Fig. 3.2a), in correspondence to the gap separating the top and the bottom shear layers (Fig. 3.2b). This unsteadiness is associated with the switching of the rear stagnation point, as confirmed by the bi-modal distribution seen for the *probability density functions* (PDF) associated with the signal of the normalised static pressure recorded by one of the taps placed in the region with the highest values of $RMS(\Delta C_p)$ (Fig. 3.2c), which matches that reported in the literature for bi-stable wakes (see Volpe et al (2015)).

Although several authors have already measured how the bi-stable mode affects the aerodynamic side force (Grandemange et al, 2015), its effect on the other components of the aerodynamic force have only been speculated (Grandemange et al, 2013b) or inferred by per-

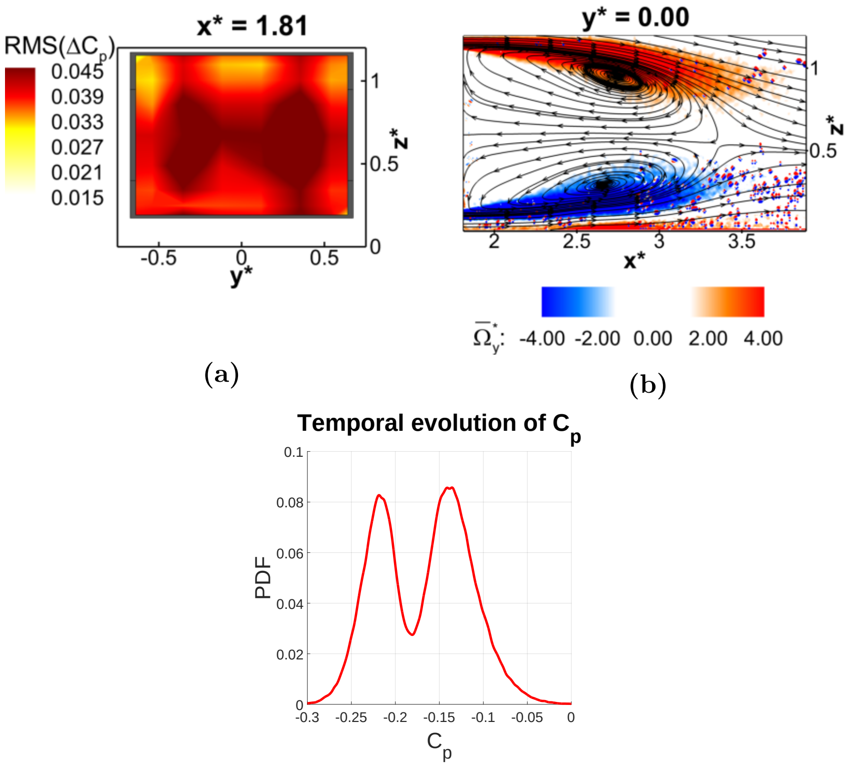

(a) (b)

(c)

Figure 3.2: **a** distribution of the root mean square of the pressure fluctuation over the model base; **b** distribution of time averaged values of the lateral component of the vorticity (at $y^* = 0.00$); **c** probability density function (PDF) of the temporal signal recorded by one of the taps with the highest value of $RMS\Delta(C_p)$.

turbing the wake using external means (Grandemange et al, 2014b). In the present work, these effects have been investigated directly and without any external perturbation by applying wavelet analysis (see §2.3.1) to the unsteady dataset logged from the balance. The results are presented in Fig. 3.3. At very low frequency ($St_H <= 7.1 \cdot 10^{-4}$), there is a strong correlation between the wavelet function $\Xi(t)$ (see 2.3.1) and the time series associated with the values of the side force C_Y recorded at $\Psi = 0.0°$. A much lower level of correlation exists for C_D and C_L at the same frequency, confirming that the bi-stability is mainly affecting the lateral component of the aerodynamic force. Note that in all cases the energy bands centred around $St_H \simeq 4.5 \cdot 10^{-2}$ are the resonant frequencies of the balance (Baden Fuller, 2012). Applying the cross-wavelet transform to the same signals (Fig. 3.4), for simplicity focusing only on the lower portion of the frequency spectrum, the phase angle, represented by the direction of the arrows superimposed on the colour maps, tends to remain constant in the regions characterised by the highest levels of correlation, confirming the existence of a causal relationship between the two correlated signals in that specific portion of the time-frequency domain. In particular, C_Y and C_D appear to be in phase in the high energy region located around $St_H \simeq 1.8 \cdot 10^{-4}$ but C_Y

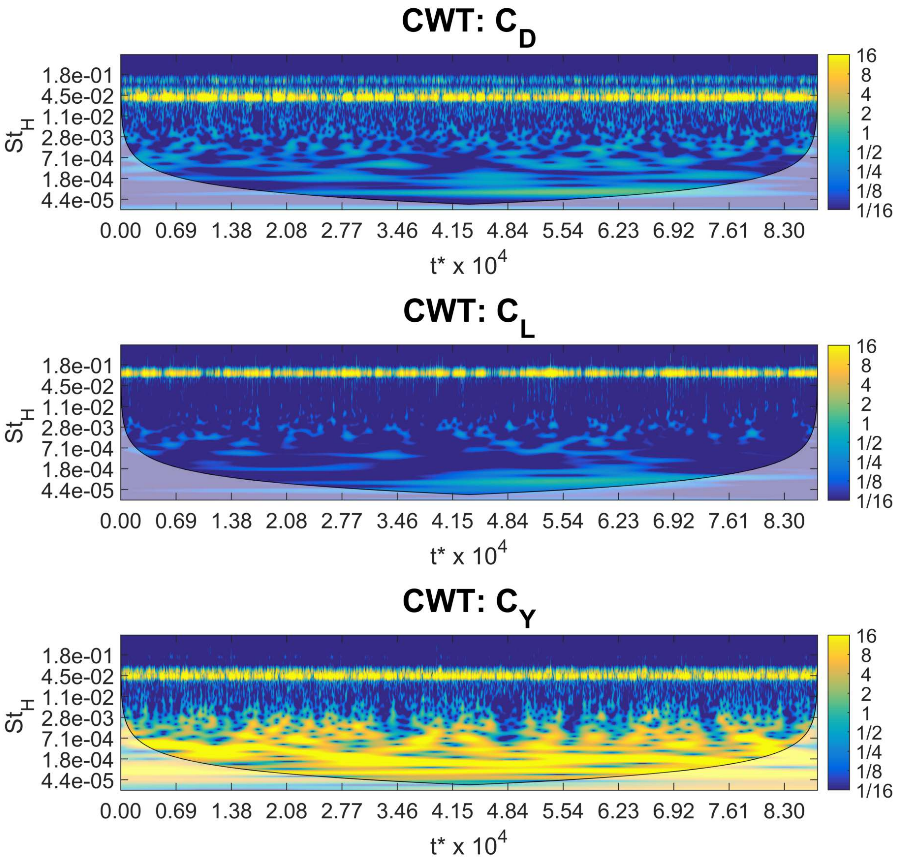

Figure 3.3: Continuous wavelet transform (CWT) of the three components of the aerodynamic force for $\Psi = 0.0°$. The colour scale is proportional to the wavelet power spectrum $|W^f(s,\tau)|^2$ (defined in §2.3.1) and is represented in octaves. The shaded region defines the cone of influence (COI) where the edge effects that might distort the results become predominant. For further information see Grinsted et al (2004).

and C_L are out of phase in the same portion of the time-frequency domain. Since these regions of high cross-correlation are visible at a very low frequency (even lower than that characteristic time of the switch between the bi-stable states) they can be used to infer the existence of a quasi-steady relationship between the different components of the aerodynamic force.

The behaviour noticed in the wavelet spectrum, is confirmed when the signal recorded for C_Y is resampled at $5\,Hz$ (Fig. 3.5). A step trend is seen in this case, with C_Y switching between two equiprobable values (Fig. 3.6a), confirming the existence of a long-time mode, in agreement with that described in Volpe et al (2015). In these conditions ($\Psi \approx 0°$) a bimodal distribution is also seen in the PDFs of the values recorded for the rolling moment C_{MX} and yawing moment C_{MZ} (Fig. 3.6b and 3.6c).

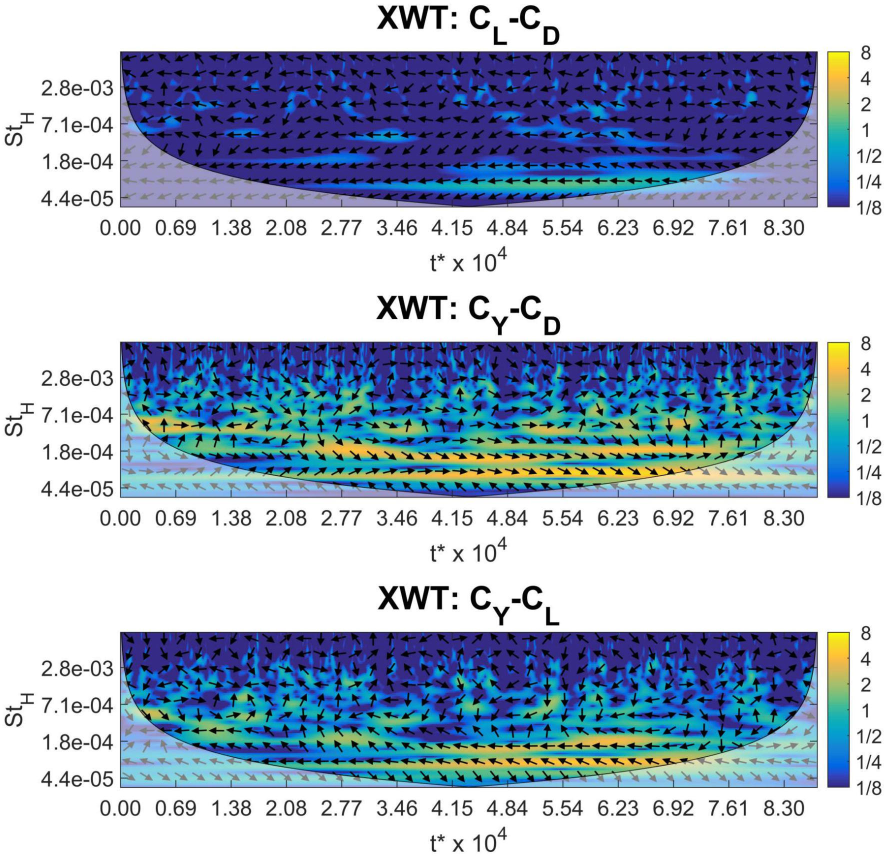

Figure 3.4: Cross wavelet transform (XWT) between C_L and C_D, C_Y and C_D, C_Y and C_L for $\Psi = 0.0°$. For the sake of simplicity only the lower portion of the frequency domain has been reported. The colour scale is proportional to the wavelet power spectrum $|W^f(s,\tau)|^2$ (defined in §2.3.1) and is represented in octaves. The shaded region defines the cone of influence (COI) where the edge effects that might distort the results become predominant. The arrows superimposed on the colour map show the local phase difference between the two signals of each cross-correlation ($\chi^{f,g}(s,\tau)$ in §2.3.1); arrow pointing right: signals in phase; left: signals in phase opposition; down: first signals leading the second signals by 90°. For further information see Grinsted et al (2004).

3.2.1.1 Sensitivity of bi-stability to small perturbations

The extent of the bi-stable domain was investigated by performing a yaw sweep between $-2°$ and $+2°$ with steps of $0.1°$. For each position, the values of the aerodynamic forces were recorded for $150\,s$, with a settling time of $30\,s$. The time averaged results are presented in Fig. 3.6d and 3.6e. The plots clearly show the existence of a linear trend for $C_Y(\Psi)$ (Fig. 3.6d), $C_{MX}(\Psi)$ and $C_{MZ}(\Psi)$ (Fig. 3.6e), apart from $-0.5° < \Psi < +0.3°$, where a non-linear region is seen due to the presence of the wake bi-stability. The edges of this region are identified by the points where the PDFs recorded for the lateral component of the aerodynamic force and the

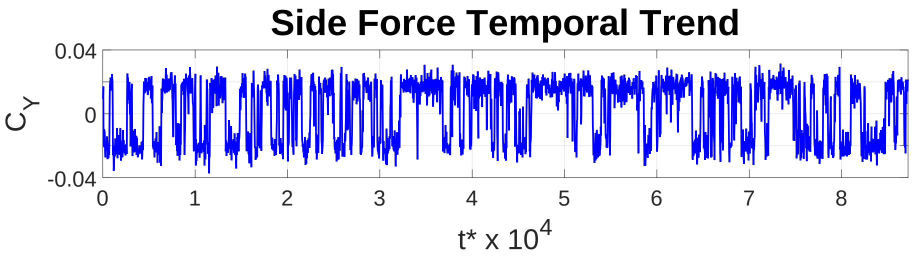

Figure 3.5: Temporal trend of the data recorded for the lateral component of the aerodynamic force (data resampled at $5\,Hz$).

related moments shift from a bimodal distribution towards a normal distribution, as only one single state is selected (Fig. 3.6a, 3.6b and 3.6c). The same trend can be observed in the PDF of the values of the static pressure recorded by one of the tap placed in the region characterised by the highest level of unsteadiness (Fig. 3.7a, top). In these conditions, as $|\psi|$ increases, one single value of C_p is selected. As a consequence, the level of pressure fluctuation over the model base is also reduced (3.7a, bottom). These results are in good agreement with the trends found by Volpe et al (2015) for the base pressure distribution and by Evrard et al (2016) for the

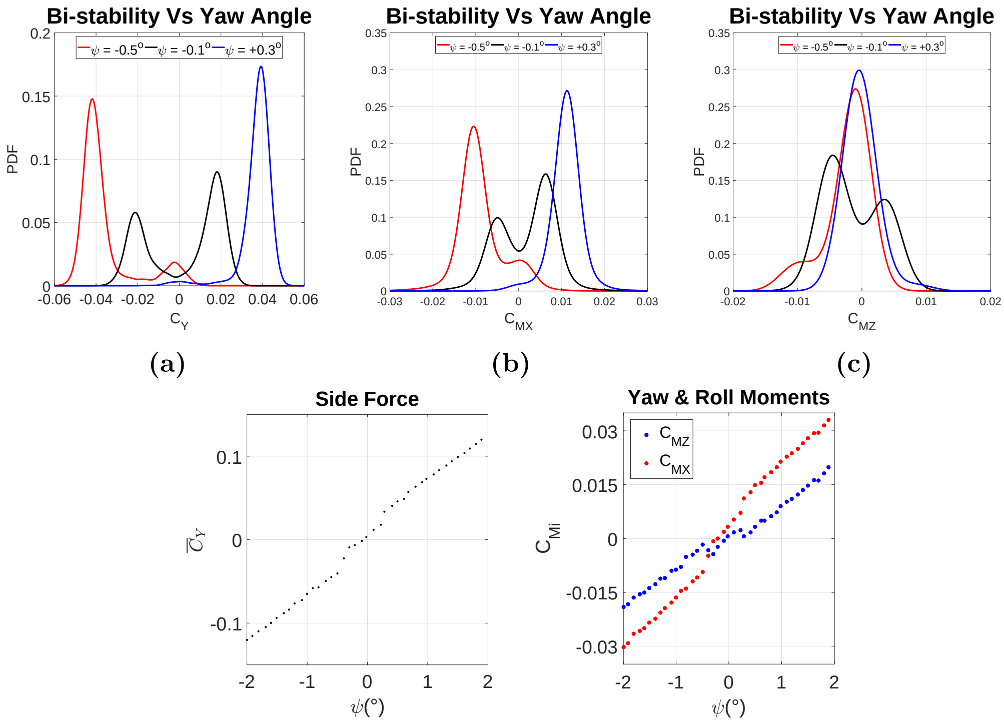

(a) **(b)** **(c)**

(d) **(e)**

Figure 3.6: PDF showing the sensitivity of side force **(a)**, rolling moment **(b)** and yawing moment **(c)** to small variations of the model yaw angle; time averaged values of side force **(d)**, yawing and rolling moments **(e)** recorded for $-2.0^o < \Psi < 2.0^o$.

aerodynamic side force.

The selection of one stable state leads to the disappearing of the very low frequency activity seen in the wavelet spectrum of the side force for $\Psi \approx 0°$. For example, if the model is moved at $\Psi = +0.6°$, just outside the *bi-stable domain* defined in Fig. 3.6, only few energy spikes are still observed in the wavelet spectrum (Fig. 3.7c), suggesting that, although some switches may still occur, the bi-stable mode is much weaker. A look at the time averaged base pressure distribution and velocity fields recorded in these conditions reveals a noticeable change in the wake topology. The two vortices seen from the PIV cross-plane located at $x^* = 3.31$ for $\psi \approx 0°$ are now rotated by 90° and moved towards the windward side of the base (Fig. 3.8). At the same time, two vertically aligned recirculating structures become evident on the opposite side of the base for $x^* = 2.31$. In combination these elements suggest the presence of a single hairpin vortex that starts on the leeward side of the model close to the base and then moves towards the windward side while approaching the wake closure. As a consequence, the base pressure distribution loses its uniformity and a strong gradient appears in the horizontal direction. This contributes to an increase in the side force, which varies from $\overline{C}_Y = 0.002$ at $\Psi = 0.0°$ to $\overline{C}_Y = 0.052$ at $\Psi = +0.6°$. A drag increase is also seen (from $\overline{C}_D = 0.273$ at $\Psi = 0.0°$ to $\overline{C}_D = 0.279$ at $\Psi = +0.6°$) as well as a small variation in the magnitude of the vertical force (from $\overline{C}_L = -0.030$ at $\Psi = 0.0°$ to $\overline{C}_L = -0.033$ at $\Psi = +0.6°$). More noticeable, however, is the change in the lift distribution between the two axles, which goes from $\overline{C}_{L_f} = -0.013/\overline{C}_{L_r} = -0.017$ for $\Psi = 0.0°$ to $\overline{C}_{L_f} = -0.002/\overline{C}_{L_r} = -0.031$ for $\Psi = +0.6°$, arguably due to an alteration of the *A pillar* vortices, as shown in Baden Fuller (2012).

Less noticeable changes in the strength of the bi-stable mode were seen when the ground clearance of the model was changed by $\delta C = \pm 10\,mm$ (or $\delta C^* = 0.035$) from the initial configuration ($C = 50\,mm$ or $C^* = 0.173$). Variations in the model ride height seem to affect mainly the position of the rear stagnation point in the vertical direction. In particular, this point appears to shift upwards as the ground clearance C^* is reduced (Fig. 3.9a, top row), as a consequence of the strengthening of the ground effect, and to move in the opposite direction as C^* is increased (Fig. 3.9b, top row). A similar shift is observed in the bi-lobe distribution seen in the contour map obtained for $RMS(\Delta C_P)$ in the two cases (Fig. 3.9a and 3.9b, bottom row). A further confirmation of the presence of a strong bi-stable mode is provided by the PDFs obtained for the values of C_p recorded by one of the taps placed in the region with the highest level of unsteadiness (Fig. 3.9c), which closely match the distribution recorded for $C^* = 0.173$. The Reynolds number considered in this case is therefore high enough to allow stability bifurcations even at the lowest ride height (Cadot et al, 2015).

The effects produced by an increase in the level of the free stream turbulence intensity on the long-time wake unsteadiness were also investigated. Following the approach proposed by Newnham (2007), a $50\,mm$ square grid using a $2.41\,mm$ gauge wire was placed at the start of the working section, yielding an increase in the free stream turbulence intensity from $TI^* \approx 0.2\%$ to $TI^* \approx 1.5\%$. The results show the development of a stronger suction over the

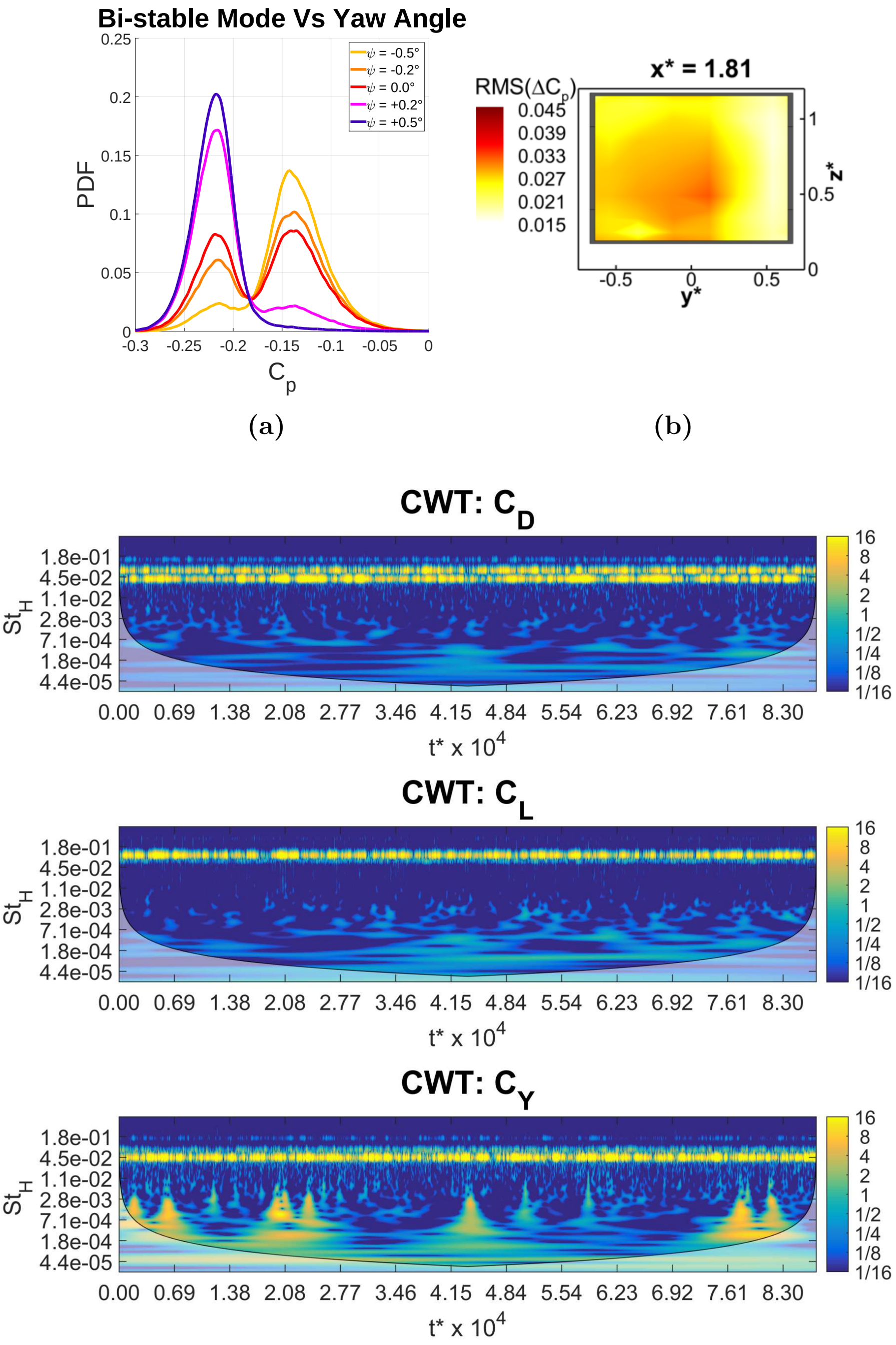

(a) **(b)**

(c)

Figure 3.7: Sensitivity of the bi-stable mode to small variations of the model yaw angle. Top row, pressure tappings results: **a** PDF of the temporal signal recorded by one of the taps with the highest value of $RMS\Delta(C_p)$ for $-0.5° \leq \Psi \leq +0.5°$; **b** distribution of the root mean square of the pressure fluctuation over the model base for $\Psi = +0.6°$. **c** continuous wavelet transform (CWT) of the three components of the aerodynamic force for $\Psi = 0.0°$. The colour scale is proportional to the wavelet power spectrum $|W^f(s,\tau)|^2$ (defined in §2.3.1) and is represented in octaves. The shaded region defines the cone of influence (COI) where the edge effects that might distort the results become predominant.
More information can be found in Grinsted et al (2004).

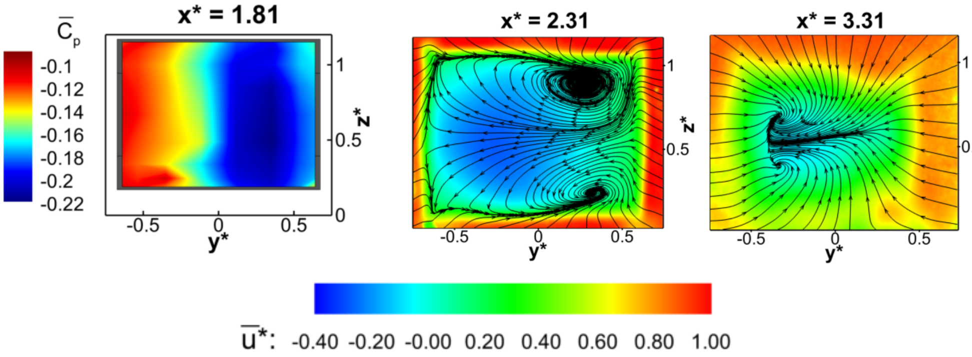

Figure 3.8: Time averaged results for the square-back Windsor body at $\Psi = +0.6^o$. From left to right: $\mathbf{x^* = 1.81}$ base pressure distribution; $\mathbf{x^* = 2.31}$ and $\mathbf{x^* = 3.31}$ PIV stereo cross-planes. All PIV fields are coloured according to the values of the axial component of the velocity u^*; the streamlines refer to the in plane components.

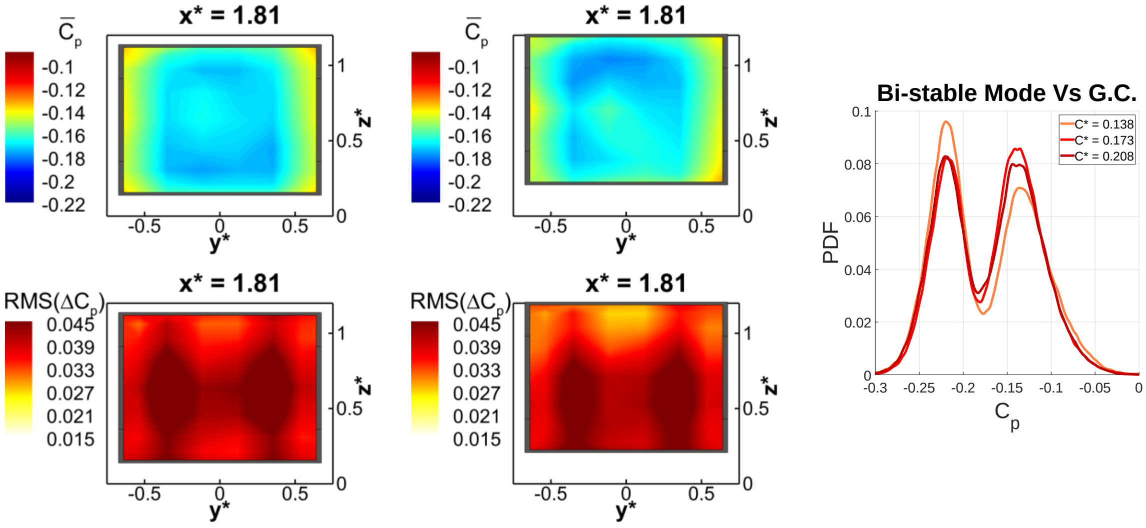

(a) $C^* = 0.138$ **(b)** $C^* = 0.208$ **(c)**

Figure 3.9: Distributions of the time averaged static pressure and the root mean square of the pressure fluctuation over the model base for $C^* = 0.138$ **(a)** and $C^* = 0.208$ **(b)**. **c** PDF of the temporal signal recorded by one of the taps with the highest value of $RMS\Delta(C_p)$ for $C^* = 0.138$, $C^* = 0.173$ and $C^* = 0.208$.

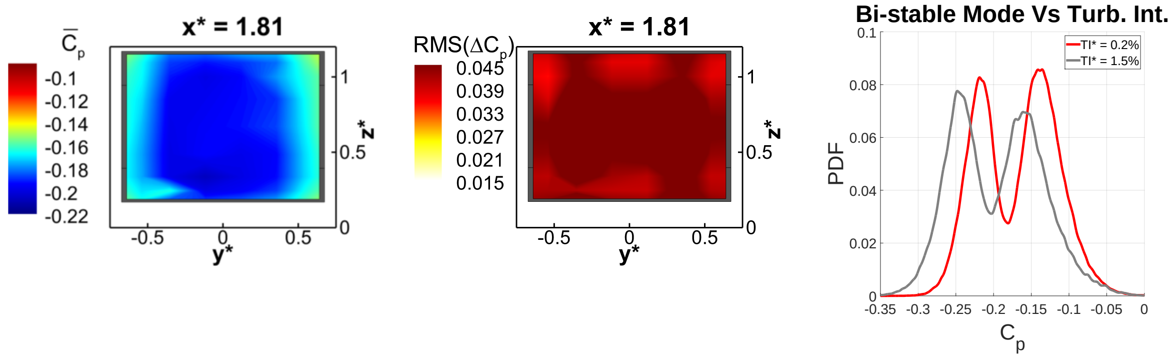

(a) **(b)** **(c)**

Figure 3.10: Effects produced on the bi-stable mode by an increase of the free stream turbulence intensity: **a** and **b** distributions of the time averaged static pressure and the root mean square of the pressure fluctuation over the model base for $TI^* \approx 1.5\%$; **c** PDF of the temporal signal recorded by one of the taps with the highest value of $RMS\Delta(C_p)$, for $TI^* \approx 0.2\%$ and $TI^* \approx 1.5\%$.

model base (Fig. 3.10a), which yields an increase in the base drag over the nominal case (from $\overline{C}_{D_{Rear}} = 0.163$ to $\overline{C}_{D_{Rear}} = 0.185$), confirming the trend found by Newnham (2007). A general growth of the level of unsteadiness is also seen (Fig. 3.10b). Nevertheless, a bi-lobe distribution is still recognisable in the contour map of the base pressure fluctuation. This, combined with the bimodal distribution obtained for the values of C_p recorded by one of the taps located in the region with the highest unsteadiness (Fig. 3.10c), confirms the presence of wake bi-stability also in these conditions.

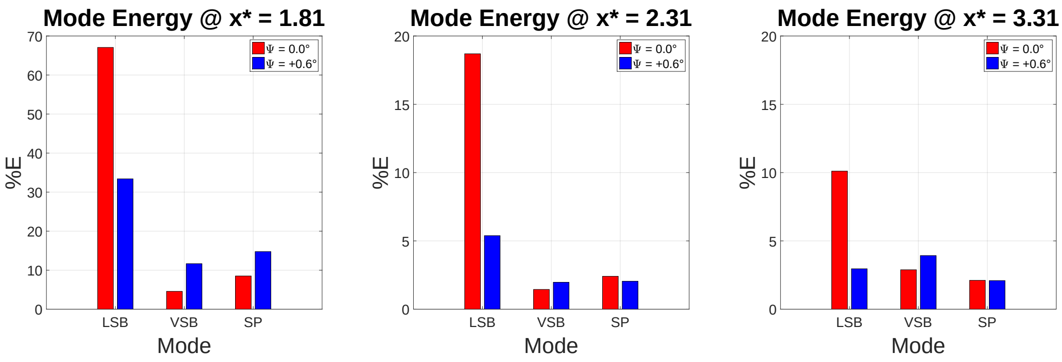

(a) **(b)** **(c)**

Figure 3.11: Energy associated with 3 of the most energetic POD modes: **a** base pressure data; **b** PIV cross-plane at $x^* = 2.31$; **c** PIV cross-plane at $x^* = 3.31$.

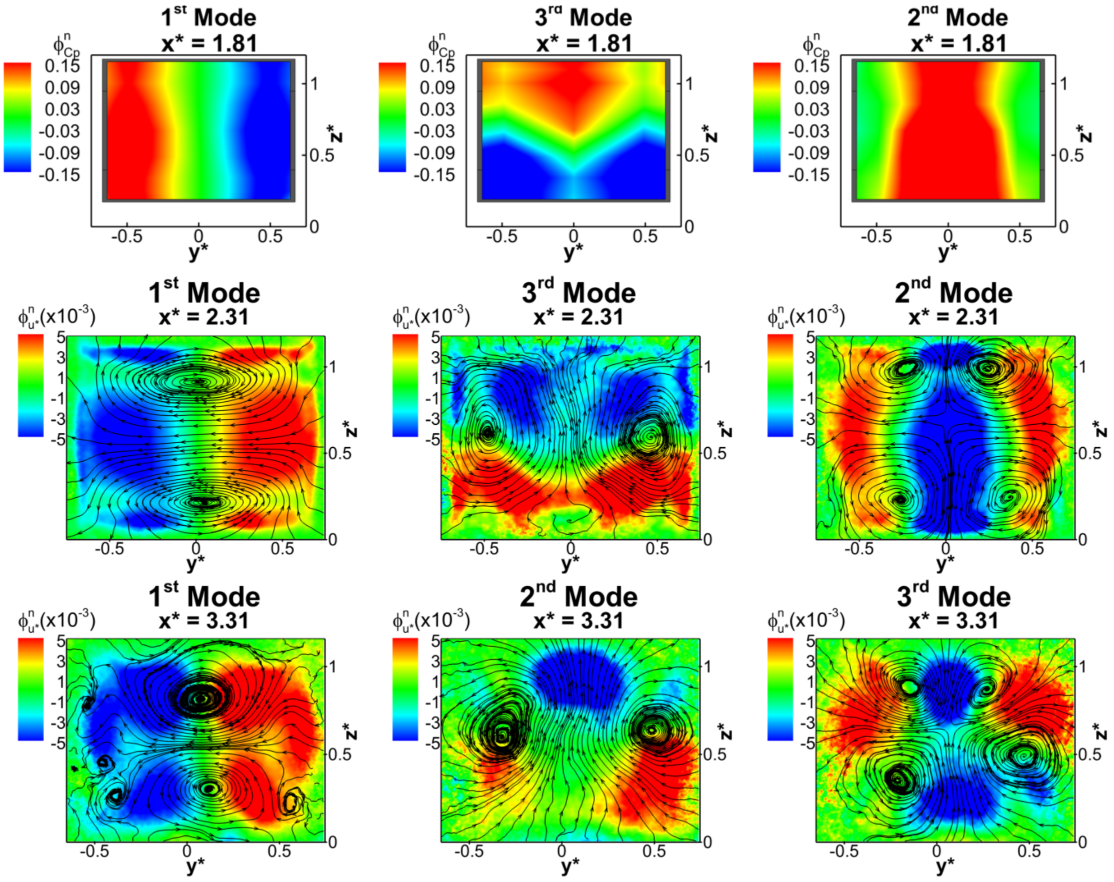

(a) LSB mode (b) VSB mode (c) SP mode

Figure 3.12: Spatial distribution of 3 of the most energetic POD modes extracted from the base pressure distribution (top row), PIV cross-plane at $x^* = 2.31$ (central row), PIV cross-plane plane at $x^* = 3.31$ (bottom row) for $\Psi = 0.0°$. The modes are ordered according to their topology: **a** lateral symmetry breaking mode (LSB), **b** vertical symmetry breaking mode (VSB), **c** symmetry preserving mode (SP). $\phi^n_{C_p}$ refers to the magnitude of the spatial eigen-modes extracted from the field of the pressure fluctuation. The eigenfunctions related to the velocity fluctuation are coloured according to the values of the through plane component $\phi^n_{u^*}$ whereas the streamlines are drawn considering the in-plane components $\phi^n_{v^*}$ and $\phi^n_{w^*}$.

3.2.2 POD modes

The wake dynamics have been further investigated by applying POD to the fluctuating part of both pressure and PIV data recorded for two different yaw angles, $\Psi = 0.0°$ and $\Psi = +0.6°$. Only the first three modes are considered, as they represent respectively about 80% and 60% of the overall energy captured by the pressure fluctuation on the base; with the first mode at $\Psi = 0.0°$ accounting for twice as much energy as the same mode at $\Psi = +0.6°$ due to the weakening of the bi-stable mode (Fig. 3.11a). Similar trends are observed in the energy content associated with POD modes extracted from the two PIV cross-planes considered in the present investigation (Fig. 3.11b and 3.11c), although the energy levels are in these cases much lower

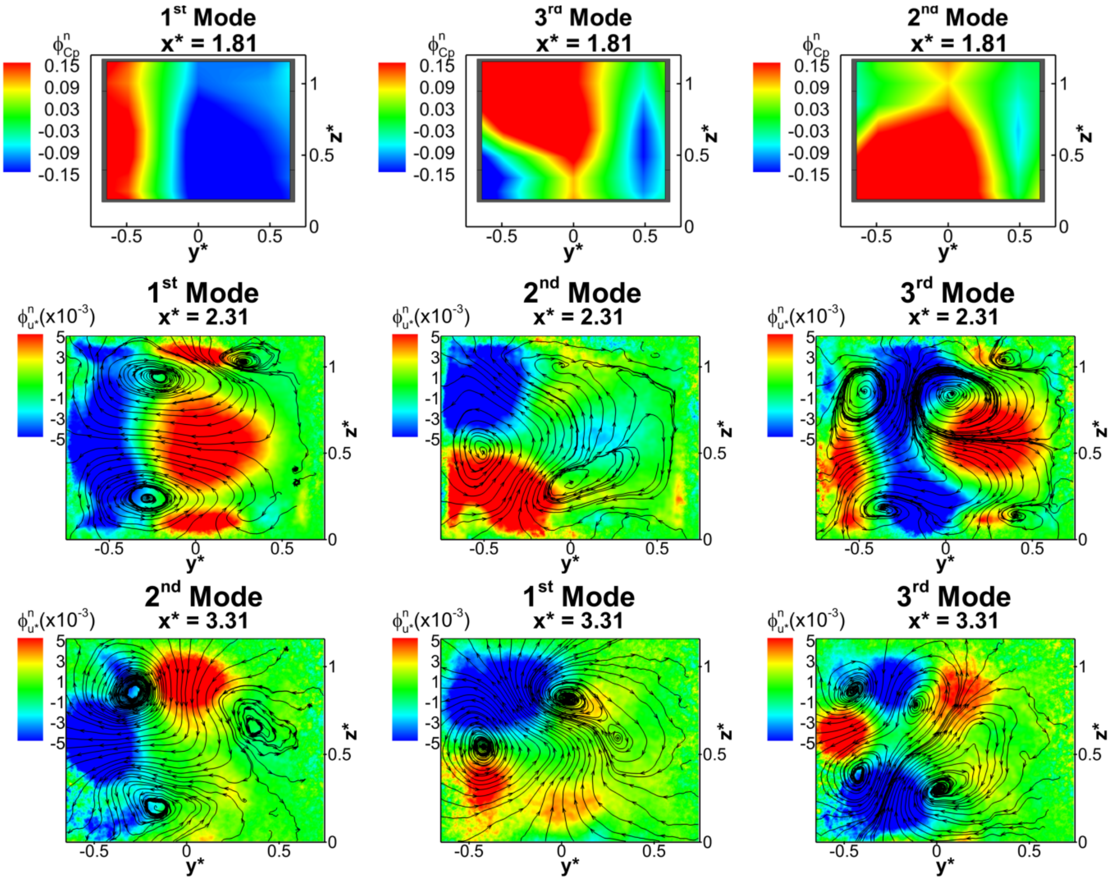

(a) LSB mode **(b)** VSB mode **(c)** SP mode

Figure 3.13: Spatial distribution of 3 of the most energetic POD modes extracted from the base pressure distribution (top row), PIV cross-plane at $x^* = 2.31$ (central row), PIV cross-plane plane at $x^* = 3.31$ (bottom row) for $\Psi = +0.6°$. The modes are ordered according to their topology: **a** lateral symmetry breaking mode (LSB), **b** vertical symmetry breaking mode (VSB), **c** symmetry preserving mode (SP). $\phi^n_{C_p}$ refers to the magnitude of the spatial eigen-modes extracted from the field of the pressure fluctuation. The eigenfunctions related to the velocity fluctuation are coloured according to the values of the through plane component $\phi^n_{u^*}$ whereas the streamlines are drawn considering the in-plane components $\phi^n_{v^*}$ and $\phi^n_{w^*}$.

than those obtained for the pressure data. This is consistent with that seen in the works of Rigas et al (2014) and Gentile et al (2016) and may be a consequence of the shear layer unsteadiness (not captured by the base pressure dataset) that tend to spread the fluctuating energy over a larger number of modes. The eigenfunctions obtained for the first three POD modes are presented in Fig. 3.12 for $\Psi = 0.0°$ and Fig. 3.13 for $\Psi = +0.6°$; the spectrum of the related temporal coefficients is reported in Fig. 3.14.

For $\Psi = 0.0°$, the first POD mode is a *lateral symmetry breaking* (LSB) mode, since it is dominated by a left-to-right asymmetry associated with the action of both the bi-stable mode and the von Karman lateral vortex shedding (Volpe et al, 2015). The asymmetry visible from

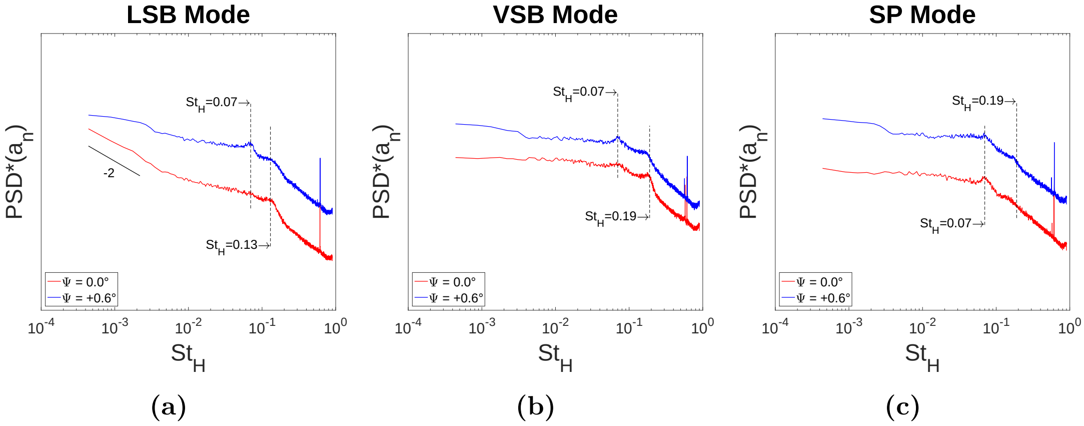

Figure 3.14: Spectra of the POD temporal coefficients associated with: **a** the lateral symmetry breaking mode (LSB), **b** the vertical symmetry breaking mode (VSB), **c** the symmetry preserving mode (SP). The curves have been shifted along the vertical axis. Base pressure data recorded at $\Psi = 0.0°$ and $\Psi = +0.6°$

the pressure field is seen to extend for the entire length of the wake, as highlighted by the two PIV cross-planes (Fig. 3.12a). The 1^{st} eigenfunction extracted from the velocity fields is dominated by two counter rotating vortices aligned along the horizontal direction. These structures are centred with the model base and yield variations in the longitudinal component of the velocity u^* that match the pressure fluctuations recorded over the base. Their size as well as their energy content (Fig. 3.11b and 3.11c) tend to reduce downstream due to the thickening of the side shear layers, in agreement with the findings of Gentile et al (2016). Similar conclusions can be drawn for the 3^{rd} mode extracted from the base pressure distribution and the 3^{rd} and 2^{nd} spatial modes obtained respectively from the first ($x^* = 2.31$) and second ($x^* = 3.31$) PIV cross-plane. These fields are characterised by a strong top-bottom asymmetry (Fig. 3.12b), defining a *vertical symmetry breaking* (VSB) mode (being associated with coherent motions of the wake in the vertical direction). Unlike that seen for the LSB mode, however, the energy content of such a motion tends to increase moving farther from the base (Fig. 3.11b and 3.11c), suggesting that its origin has to be found in the interactions between the near-wake and the surrounding shear layers. The symmetry in the two transverse directions is almost fully restored when the 2^{nd} and 3^{rd} POD modes extracted from the velocity fields located respectively at $x^* = 2.31$ and $x^* = 3.31$ are considered (Fig. 3.12c), justifying the term of *symmetry preserving* (SP) mode. In this case, two pairs of counter rotating vortices appear in the two PIV planes, suggesting the existence of the ovalisation mode of the rear recirculation already described by Gentile et al (2016) for the wake of an axisymmetric body. This quadrupole structure is accompanied with the presence of out-of-phase variations in the streamwise component of the velocity u^* between the central portion and the outermost sections of each plane. A similar distribution is extracted for the 2^{nd} mode of the pressure data.

When the model is yawed by $+0.6°$, the structures previously described are still recognisable, but the left-right and top-bottom asymmetries are now much closer in terms of energy content, due to the weakening of the bi-stable mode and the decrease of its contribution to the fluctuations in the lateral direction. The asymmetric constraint imposed by the model yaw shifts the regions with the highest level of fluctuation towards the windward side accompanied with a stable vortical structure formed along the leeward side, as mentioned in §3.1. By analysing this case, it can be inferred that the fluctuations originating from the short-time motions of the wake in the lateral and vertical direction are the result of the interactions between this vortical structure and the shear layers emanating from the windward side of the base. In a similar way, the fluctuations in the two transverse directions seen at $\Psi = 0.0°$ are the result of the superimposition of the interactions between each one of two lateral symmetry breaking states and the shear layer emanating from the opposite side of the model.

The *power spectral density* (PSD) of the temporal coefficients of the same POD modes (Fig. 3.14) show that in all cases, the turbulent logarithmic decay (§1.1.3) is captured above $St_H > 0.3$. The two spikes appearing at $0.50 \leq St_H \leq 0.60$ are due to the resonant frequencies of the wind tunnel. They are related to the blades of the stator and the fan respectively (Baden Fuller, 2012). The presence of the bi-stable mode is confirmed by the -2 law describing the decrease of the energy captured by the 1^{st} mode at very low frequency for $\Psi = 0.0°$ (Fig. 3.14a), confirming the findings of Grandemange (2013). In the first mode two peaks occur at $St_H = 0.07$ and $St_H = 0.13$, but in the second and third modes (Fig. 3.14b and 3.14c) the latter is replaced with a peak at $St_H = 0.19$. This confirms the existence of three distinct coherent motions of the wake in addition to the bi-stable mode, matching the results of the experiments performed by Volpe et al (2015) for similar values of Re_H.

3.2.3 Topology and duration of the bi-stable states

The two bi-stable states have been isolated from the PIV data by using a similar approach to that proposed by Thacker et al (2010); a low order model was constructed from the time averaged field and the first POD mode according to Eq. 3.1:

$$\mathbf{F}^{LOM_1}(\mathbf{x},t) = \mathbf{F}_0(\mathbf{x}) + \phi^1(\mathbf{x})a_1(t), \tag{3.1}$$

with $a_1(t) \equiv a_{LSB}(t)$.The PDFs related to the first temporal coefficient extracted from the pressure field and all the PIV planes are presented in Fig. 3.15a and 3.15b. In all cases, except the vertical mid-plane ($y^* = 0.00$), the existence of a bimodal distribution is shown, confirming the existence of two different states, as previously shown in the findings of Grandemange et al (2013b) and Volpe et al (2015). The realisations obtained for $\mathbf{F}^{LOM_1}(\mathbf{x},t)$ were filtered from the noise using a moving average filter with a cut-off frequency of $1Hz$ and sorted according to the value of the first temporal coefficient $a_{LSB}(t)$, based on the condition $a_{LSB}(t) \leq \tau$ or $a_{LSB}(t) > \tau$, where $\tau = (max(a_{LSB}(t)) + min(a_{LSB}(t)))/2$. The fields within each group were

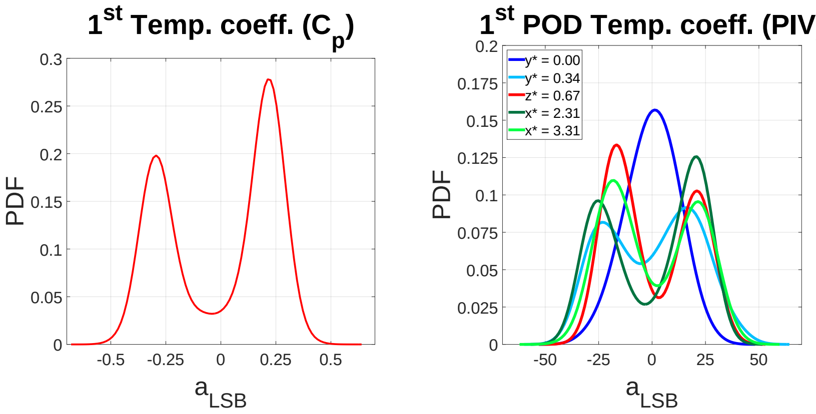

(a) (b)

Figure 3.15: Square-back Windsor body. **a** PDFs for the 1^{st} POD temporal mode extracted from the base pressure data. **b** PDFs for the 1^{st} POD temporal mode extracted from all the PIV planes considered in the present work: $z^* = 0.67$ horizontal mid-plane, $y^* = 0.00$ vertical mid-plane, $y^* = 0.34$ vertical off-center plane, $x^* = 2.31$ vertical cross-plane at $H/2$ downstream of the model base, $x^* = 3.31$ vertical cross-plane at $3/2H$ downstream of the model base. The data refer to the model tested at $\Psi = 0.0°$.

then averaged. The results related to the *R-State* are presented in Fig. 3.16a, coloured according to the values of the streamwise component of the normalised vorticity $\tilde{\Omega}_x^* = \frac{\partial w^*}{\partial y^*} - \frac{\partial v^*}{\partial z^*}$. On each plane, the location of the cores of the vortical structures has been determined by applying the Γ_1 criterion proposed by Graftieaux et al (2001), based on the detection of the local maximum of the function 3.2:

$$\mathbf{\Gamma_1}(\mathbf{P}^*) = \frac{1}{N_p} \int_{\mathbf{M}^* \in S^*_{\Gamma_1}} \frac{(\mathbf{PM}^* \wedge \mathbf{V_M}^*) \cdot \mathbf{n}}{\|\mathbf{PM}^*\| \cdot \|\mathbf{V_M}^*\|} dS^*_{\Gamma_1}, \tag{3.2}$$

where $\mathbf{P}^*$ is a fixed point in the measurement domain, $S^*_{\Gamma_1}$ is a rectangular domain of fixed size surrounding $\mathbf{P}^*$, N_p is the number of points $\mathbf{M}^*$ inside $S^*_{\Gamma_1}$, $\mathbf{n}$ is the unit vector normal to the measurement plane and $\mathbf{V_M}^*$ is the in-plane velocity vector. The circulation around each core was then determined as $\Gamma^* = \int_{S^*_{\Gamma^*}} \Omega_x^* dS^*_{\Gamma^*}$, where $S^*_{\Gamma^*}$ is a squared region with sides of normalised length equal to 0.2 surrounding each vortex core (§1.1.3). For comparison, the time averaged field obtained for $\Psi = +0.6°$ (Fig. 3.16b) was considered too. The results for both cases are reported in Tab. 3.1.

A very similar wake organisation is seen between the two cases for the cross-plane at $x^* = 2.31$, with two counter-rotating vortical structures acting close to the right-hand side of the model base. These structures have similar strengths, as highlighted by the magnitude of the values of the normalised circulation Γ^* reported in Tab. 3.1, with the upper structure (rotating in the clockwise direction) always slightly prevailing over the bottom one (rotating counterclockwise). Bigger differences are noticed when the cross-plane further downstream of the model base (at $x^* = 3.31$) is considered. In this case, two vortical structures can still be

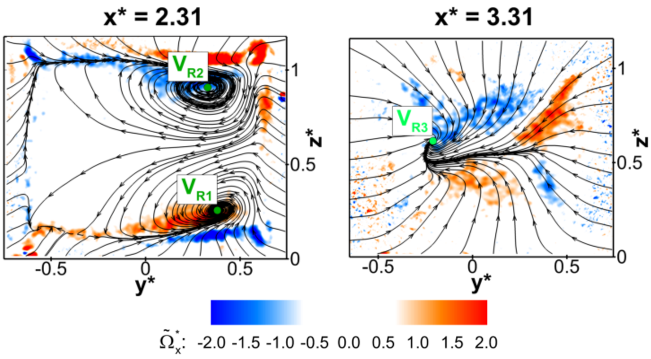

(a) *R-State*

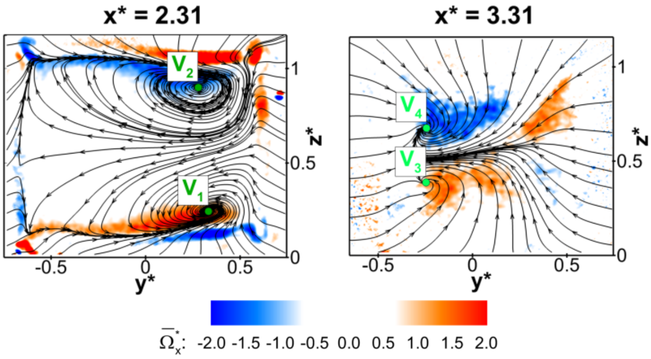

(b) $\Psi = +0.6°$

Figure 3.16: Distribution of the normalised streamwise component of the vorticity Ω_x^* over the PIV planes acquired at $x^* = 2.31$ and $x^* = 3.31$ for **a** one of the two conditionally averaged POD filtered fields (*R-State*) and **b** the time averaged filed at $\Psi = +0.6°$. The streamlines are drawn considering the in-plane components of the velocity field. The green dots denote the locations of the vortex cores, whose coordinates are reported in Tab. 3.1.

recognised for the time averaged field associated with the model tested at $\Psi = +0.6°$, although they are now placed at the opposite side of the base, as already discussed in §3.2.1.1. Compared to the plane at $x^* = 2.31$, the vertical distance between the cores of the vortices is now reduced, as a consequence of the tapering of the wake, and the difference in the value of $\overline{\Gamma}^*$ between the upper and lower structure is accentuated (with the former still prevailing over the latter). Nevertheless, the continuity in the sign of the out-of-plane component of the normalised vorticity $\overline{\Omega}_x^*$ (and therefore the circulation) between the vortices acting on the same horizontal portions of each plane indicates that they are part of the same 'leg' extending downstream of the base. The difference in circulation between the two vortices seen at $x^* = 3.31$ for $\Psi = +0.6°$, reaches a maximum in the case of the conditional averaged state, where only the upper core is detected by the Γ_1 criterion, with a value of $\tilde{\Omega}_x^*$ similar to that of the corresponding vortex seen at $x^* = 2.31$.

***(a)* R-State**

Vortex ID	x^*	y^*	z^*	$\tilde{\Gamma}^*$
V_{R1}	2.31	0.381	0.258	+0.038
V_{R2}	2.31	0.330	0.909	−0.041
V_{R3}	3.31	−0.210	0.612	−0.026

***(b)* $\Psi = +0.6°$**

Vortex ID	x^*	y^*	z^*	$\overline{\Gamma}^*$
V_1	2.31	0.331	0.244	+0.041
V_2	2.31	0.283	0.900	−0.045
V_3	3.31	−0.246	0.389	+0.028
V_4	3.31	−0.244	0.672	−0.043

Table 3.1: Locations of the centres of the vortical structures captured by the PIV planes located at $x^* = 2.31$ and $x^* = 3.31$: *(a)* R-State *for* $\Psi = 0.0°$*;* (b) time averaged field for $\Psi = +0.6°$. The locations of the vortex cores were determined using the Γ_1 criterion proposed by Graftieaux et al (2001). Γ^* refers to the non dimensional value of the circulation with $\Gamma^* = \Gamma/(V_\infty \cdot H)$. For the *Vortex ID* see Fig. 3.16.

The structure of the bi-stable state becomes clearer when the two stereoscopic PIV cross-planes are combined with the PIV fields captured by the 2D-2C streamwise planes (Fig. 3.17). Each state consists of a hairpin vortex that forms parallel to one of the two vertical sides of the base and then splits into two legs that bend horizontally while moving downstream, until they reach the opposite side of the base, with the top leg eventually prevailing over the bottom one. Indeed, the two counter-rotating vortices appear to interact with each other in a way similar to that described by Bristol et al (2004) and Ryan et al (2012), with the weaker bottom vortex wrapping around the top vortex until eventually disappearing. The topology of each lateral symmetry breaking state is responsible for the creation of the horizontal pressure gradient seen over the model base when the two states are isolated (see Fig. 3.17a and 3.17b, top row).

The vortical structures proposed in Fig. 3.17a and 3.17b present some analogies with that speculated by Evrard et al (2016), but in this case all vortices captured by the PIV planes have been included in each structure, thanks to a more complete set of data. A similar organisation has been seen in the wake of a sphere for $Re > 280$ (Chrust et al, 2013). These structures have been shown to originate from the symmetry breaking mode that appears at $Re \approx 210$ (Magarvey and Bishop, 1961) and have been linked to the multi-stable behaviour seen for the

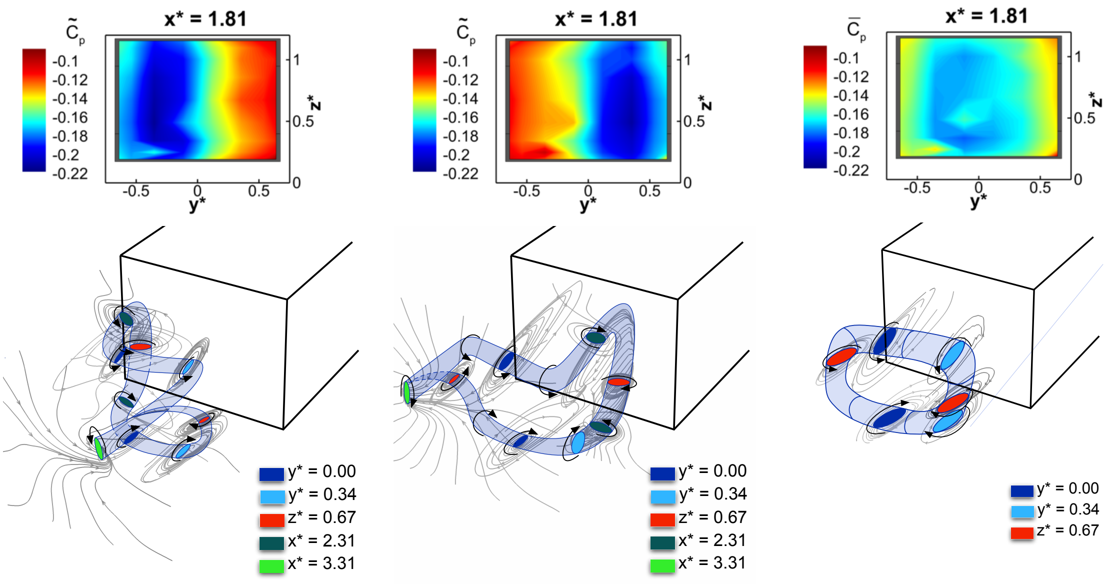

(a) *L-State* **(b)** *R-State* **(c)** *State Average*

Figure 3.17: Schematic representation of the two bi-stable states (**(a)** *L-State* and **(b)** *R-State*) and the *State average* wake topology **(c)**, together with the related base pressure distributions. The representation is based on experimental data; each plane is associated to a different colour, i.e. vortices on the same plane share the same colour.

same geometry at high Reynolds numbers (Grandemange et al, 2014a). Furthermore, their presence seem to explain the formation of the two counter rotating vortices forming downstream of the closure of the time averaged wake, as seen in §3.1.

If the two states generated using the POD conditional average are then combined together, the velocity and pressure fields produced are representative of a statistically balanced wake topology (i.e. the sampling period $t \to \infty$); this is referred here as the *State average* simply because it gives equal weight to the two states. From this, a laterally-symmetric flow field is obtained (Fig. 3.17c) and the wake topology resembles the toroidal structure reported in the literature for the time averaged wake of similar geometries (Krajnovic and Davidson (2003), Rouméas et al (2009a) and Perry et al (2016)), although this is a flow feature that is never present when the results are temporally resolved. Nevertheless, the noticeable differences in terms of topology between this structure and the bi-stable states do not correspond to significative variations in the base drag, as the values of $C_{D_{Rear}}$ calculated for all different states do not differ for more than $1\,count$ from the time averaged result ($\overline{C}_{D_{Base}} = 0.163$).

The filtered values of $a_{LSB}(t)$ have also been used to provide an estimation of the duration of each state (i.e. the time between switches, t_{sw}). The duration of any occurrence of a particular state has been calculated and then averaged over the number of occurrences. A value of $t_{sw} = 9.94\,s$ has been obtained. This is in good agreement with the results of Volpe et al (2015), which reported $t_{sw} = 10.21\,s$ for a square-back Ahmed body tested at the same Reynolds

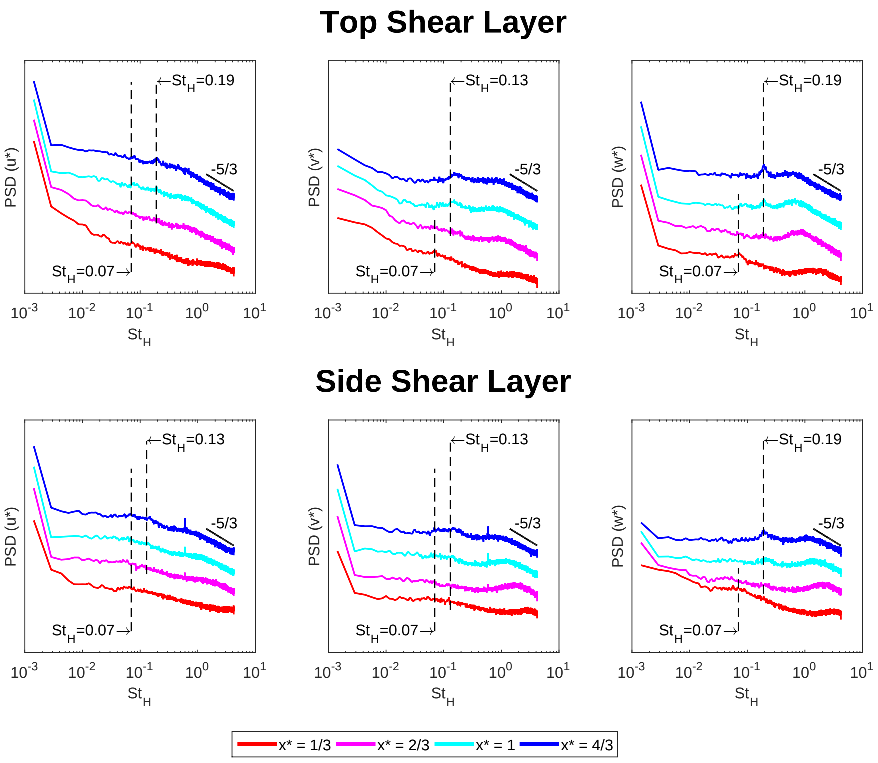

Figure 3.18: Spectra of the three components of the velocity probed at four different streamwise locations along the top shear layer (top row) and side shear layer (bottom row) for $\Psi = 0.0°$. The curves have been shifted along the vertical axis; their colours match those of the dots reported in Fig. 2.7a and 2.7b.

number ($Re_H = 7.7 \cdot 10^5$) as well as the relationship $t_{sw} \approx 10^3 H/U_\infty$ proposed by Grandemange et al (2013b).

3.2.4 Short-time wake dynamics

The short-time wake dynamics have been further investigated by performing single point measurements in four different locations along the top and side shear layers, using the multi-hole pressure probe described in §2.6. The results related to the PSD of the three components of the velocity signal are presented in Fig. 3.18, with the black continuous line referring to the turbulent decay rate predicted by the Kolmogorov theory (see §1.1.3). The only peak visible in the region closest to the base (for $x^*_B <= 2/3$, with x^*_B indicating the distance from the model base) is at $St_H = 0.07$, but as the measurement approaches the wake closure ($x^*_B > 2/3$), peaks corresponding to $St_H = 0.13$ and $St_H = 0.19$ become visible, in agreement with the findings of Volpe et al (2015). These peaks appear to be traces of the oscillating global modes described by Grandemange et al (2013b). In particular, $St_H = 0.13$ is associated with the lateral flapping of the wake, since it is mostly visible in the spectra of u^* and v^* along the side shear layer as well

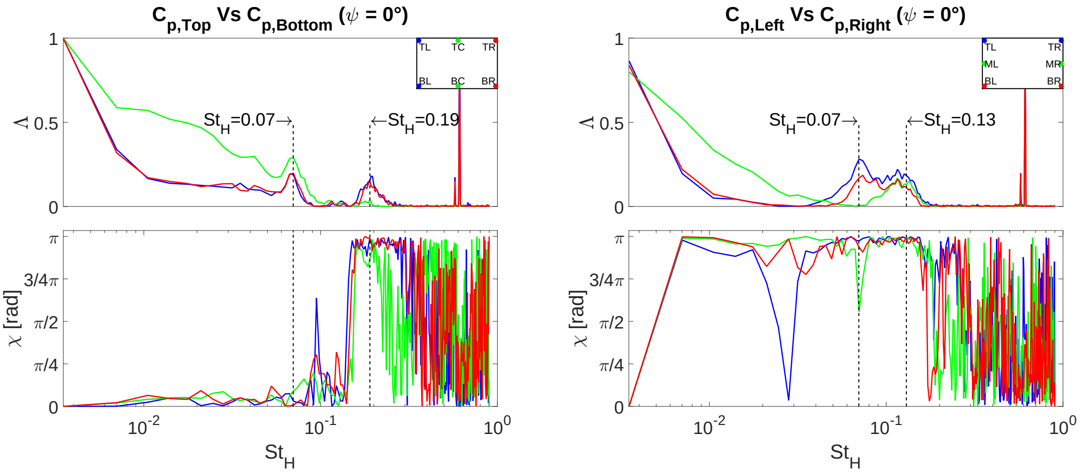

(a) (b)

Figure 3.19: Coherence analysis performed considering the unsteady signal recorded by pressure taps placed at different locations along the trailing edges of the model base for $\Psi = 0.0°$: **a** top-left tap Vs bottom-left tap, top-centre tap Vs bottom-centre tap, top-right tap Vs bottom-right tap; **b** top-left tap Vs top-right tap, mid-left tap Vs mid-right tap, bottom-left tap Vs bottom-right tap.

as the signal recorded for v^* along the top shear layer. $St_H = 0.19$ appears to be linked to the vertical flapping, as it is dominant in the spectra recorded for u^* and w^* along the top shear layer and w^* along the side shear layer. The peak at $St_H = 0.07$ may be associated instead with wake 'pumping' described by Duell and George (1999) for a similarly shaped body. This mode was not observed in Grandemange et al (2013b). An additional broader peak, at $St_H \approx 1$ is also seen. This peak may be linked to the shear layer instability, similar to that found by Duell and George (1999).

To better understand the nature of the motions associated with $St_H = 0.07$, $St_H = 0.13$ and $St_H = 0.19$, the coherence between signals recorded by taps placed in different locations along the model trailing edges has been considered, following the approach described in §2.4.2. The results for $\Psi = 0.0°$ and $\Psi = +0.6°$ are reported in Fig. 3.19 and 3.20. At Strouhal numbers between 0.0 and 0.1, a good level of correlation exists between the tapping at top-centre (TC) and bottom-centre (BC), with a clear peak at $St_H \simeq 0.07$ and a phase angle fixed at $0\,rad$ (Fig. 3.19a). Towards the sides of the model, the correlation between the top and bottom edges of the base decreases, although the peak at $St_H = 0.07$ is still recognisable. In these regions, a second peak appears at $St_H = 0.19$, with a phase angle $\chi(f) \approx \pi\,rad$ that confirms the flapping nature of the coherent motion associated with this frequency. The fact that this last peak is only visible close to the sides of the model supports the thesis that the vertical flapping is the result of the interaction between the two bi-stable states and the top and bottom shear layers emanating from the opposite half of the model base. This is confirmed when the model is yawed

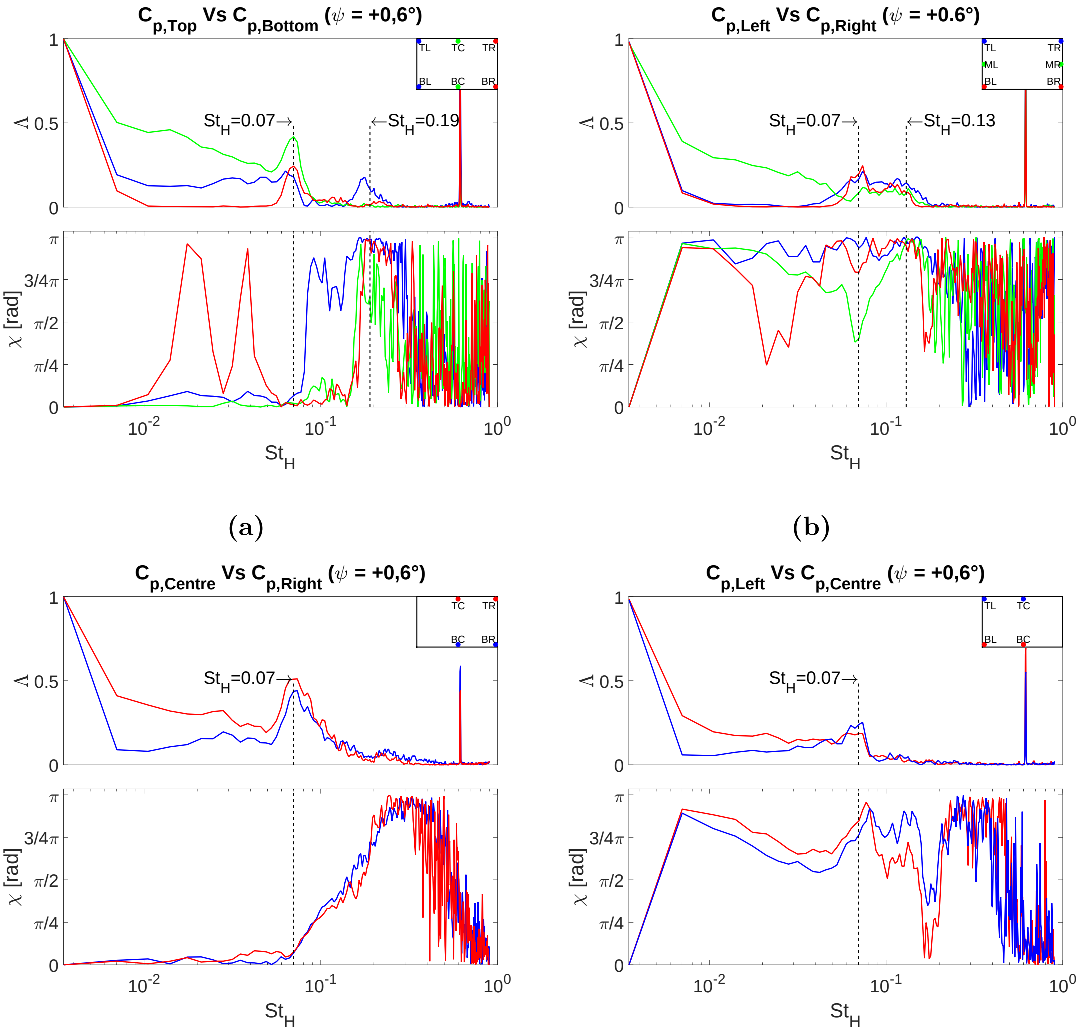

(a)

(b)

(c)

(d)

Figure 3.20: Coherence analysis performed considering the unsteady signal recorded by pressure taps placed at different locations along the trailing edges of the model base for $\Psi = +0.6°$: **a** top-left tap Vs bottom-left tap, top-centre tap Vs bottom-centre tap, top-right tap Vs bottom-right tap; **b** top-left tap Vs top-right tap, mid-left tap Vs mid-right tap, bottom-left tap Vs bottom-right tap; **c** top-centre tap Vs top-right tap, bottom-centre tap Vs bottom-right tap; **d** top-centre tap Vs top-left tap, bottom-centre tap Vs bottom-left tap.

to $\Psi = +0.6°$, as this peak remains visible only in the correlation between the taps placed on the windward side of the base (Fig. 3.20a). The $St_H = 0.07$ peak is still present when the cross-correlation is performed between the top-left (TL) and top-right (TR) taps as well as the bottom-left (BL) and bottom-right (BR) taps, with the model at either $\Psi = 0.0°$ (Fig. 3.19b) or $\Psi = +0.6°$ (Fig. 3.20b) . In this case however the signals recorded on opposite sides of the base are out of phase. Instead of the peak at $St_H = 0.19$, a new peak appears at $St_H = 0.13$. This last peak is the only one that is visible when the cross-correlation is performed between the mid-left (ML) tap and the mid-right (MR) tap and its phase angle of $\chi(f) \approx \pi\, rad$ confirms that it is associated with the lateral flapping of the wake closure. The nature of the motion associated with $St_H = 0.07$ becomes clearer when focusing on the case with the model yawed at $\Psi = +0.6°$, considering the coherence between TC-TR and BC-BR reported in Fig. 3.20c and between TC-TL and BC-BL presented in Fig. 3.20d. For this value of the normalised frequency, it is shown that a strong correlation exists between the taps of the first two pairs, with a $0\, rad$ phase angle; the level of correlation however decreases noticeably when the other two pairs of taps are considered, whilst the phase reaches $\pi\, rad$.

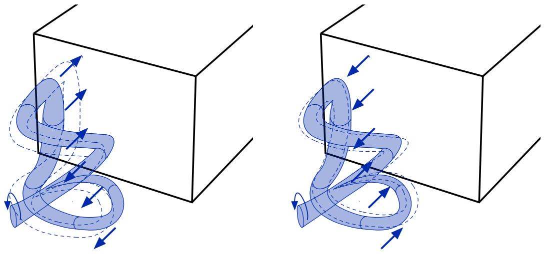

(a) Vortex ‘stretched’ **(b)** Vortex ‘squezeed’

Figure 3.21: Schematic representation of the proposed interpretation for the ‘wake pumping’.

All this information allows for the formulation of a more accurate description of the wake pumping than that provided in previous works (Duell and George (1999) and Volpe et al (2015)). This coherent motion is actually the result of the reciprocal interaction of the inner portions of the hairpin vortex that forms each bi-stable state. As a consequence, the vortex itself is ‘stretched’ and ‘squeezed’ in the streamwise direction, yielding pressure variations over the model base that have opposite signs between the left-hand and the right-hand portion of the base but share the same sign within each side. For example, when the vortex associated with the L-state is ‘stretched’ (Fig. 3.21a), its core is pushed against the left-hand portion of the base, yielding a drop in the value of C_p in that area; simultaneously it is moved further away from the base on the opposite side, allowing an increase in the static pressure in that region. The direction of the motion is reversed when the same vortex is ‘squeezed’ (Fig. 3.21b).

3.2.5 Characterisation of the symmetric state

The scatter plots of the temporal coefficients related to the first three POD modes (Fig. 3.22) provide information concerning the dynamics of the switch between the two bi-stable states. The relationship between the symmetry preserving mode $a_{SP}(t)$ and the lateral symmetry breaking mode $a_{LSB}(t)$ (Fig. 3.22a) shows that $a_{SP}(t)$ reaches its highest positive values only when the first mode is deactivated ($a_{LSB}(t) \to 0$). This, combined with the fact that the 2^{nd} POD mode describes the longitudinal motion of the wake, suggests that a reduction of the interaction between the core of the vortical structure and the base is achieved any time the lateral asymmetry is suppressed. A similar relationship is not found between the vertical symmetry breaking mode $a_{VSB}(t)$ and the symmetry preserving mode $a_{SP}(t)$ (Fig. 3.22c). Furthermore, the restoration of the lateral symmetry does not imply the deactivation of the vertical symmetry breaking mode, as evident when looking at distribution of the scatter plot between $a_{VSB}(t)$ and $a_{LSB}(t)$ reported in Fig. 3.22b.

Applying the same approach to the PIV data at $x^* = 2.31$ (Fig. 3.23a), produces a distribution similar to that obtained by Gentile et al (2016) for the first two modes extracted from stereoscopic PIV cross-planes at a similar distance from the base of an axisymmetric body. In the axisymmetric body case the symmetry breaking mode takes all azimuthal positions so that the values of the temporal coefficients related to the two symmetry breaking modes are arranged around a uniform circular pattern, whereas here the data tends to cluster around two distinct attractors, as the base aspect ratio allows the selection of only two stable symmetry breaking states (Grandemange et al, 2013a). However, since there is still a dispersion of points around the centre of the plot and the related spatial modes are in quadrature, it was decided to fit $A_{VSB}(t)$ and $A_{LSB}(t)$ with a pair of trigonometric functions such that the temporal coefficients could be reordered in phase (see Fig. 3.23b) following an approach similar to that

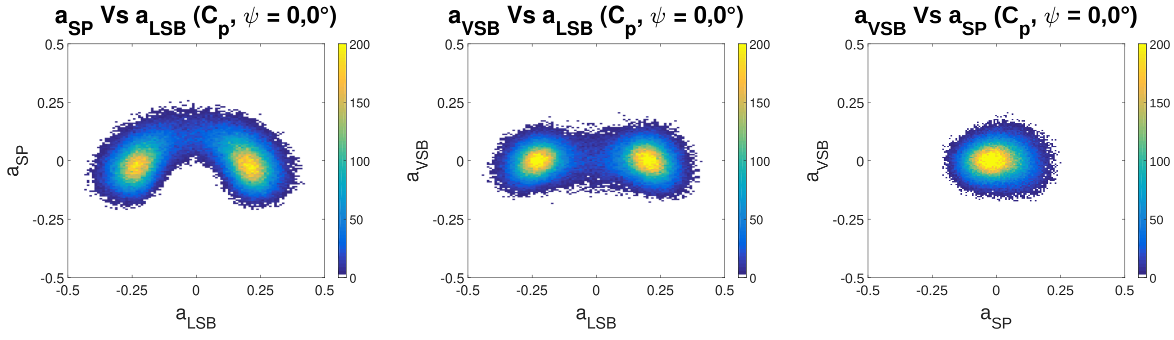

(a) **(b)** **(c)**

Figure 3.22: Scatter plots of the temporal coefficients associated with the first three POD modes extracted from the base pressure data recorded for $\Psi = 0.0°$: **a** $a_{SP}(t)$ Vs $a_{LSB}(t)$; **b** $a_{VSB}(t)$ Vs $a_{LSB}(t)$; **c** $a_{VSB}(t)$ Vs $a_{SP}(t)$. The colour map shows the probability density function of the values of the considered coefficients.

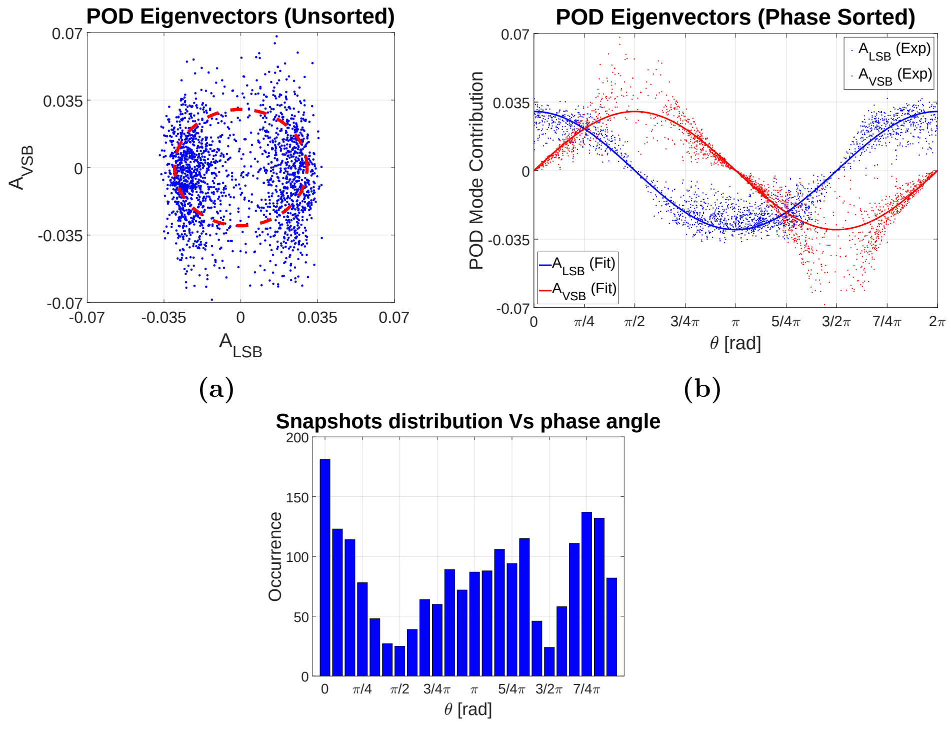

(a) **(b)**

(c)

Figure 3.23: **a** scatter plot of the POD eigenvectors associated with the vertical symmetry breaking mode $A_{VSB}(t)$ and the lateral symmetry breaking mode $A_{LSB}(t)$, extracted from the PIV data using Eq. 2.22; **b** values of $A_{LSB}(t)$ and $A_{VSB}(t)$ sorted along the phase angle θ; **c** number of snapshots contained in each bin ($\Delta\theta = 15°$).

proposed by Van Oudheusden et al (2005) and Legrand et al (2011).

The fitting was done according to the equations:

$$\left(A_{LSB} - r\cos\left(\frac{2\pi\Upsilon}{N_s}\right)\right)^2 + \left(A_{VSB} - r\sin\left(\frac{2\pi\Upsilon}{N_s}\right)\right)^2 = min, \tag{3.3}$$

$$\theta = \frac{2\pi\Upsilon}{N_s}\frac{180}{\pi}, \tag{3.4}$$

where $r = \sqrt{2/N_s}$ and A_{LSB}, A_{VSB} are the eigenvectors obtained from Eq. 2.22 for the lateral and vertical symmetry breaking modes. A low order model, consisting of the time averaged field and the first three POD modes, was then created after having averaged the fluctuating terms in bins of 15°. This is similar to the approach using a conditional average performed by Grandemange (2013) for the wake of a spherical body. The results obtained for eight $\pi/4\,rad$ increments of the phase angle θ are presented in Fig. 3.24 and 3.25 for $x^* = 2.31$ and $x^* = 3.31$, summarising all the configurations of the wake during its unsteady evolution. They are not a reconstruction of a particular periodic behaviour, as the succession of the bi-stable states seems to be a weak chaotic process (Varon et al, 2017a). Nevertheless, they still provide insights into

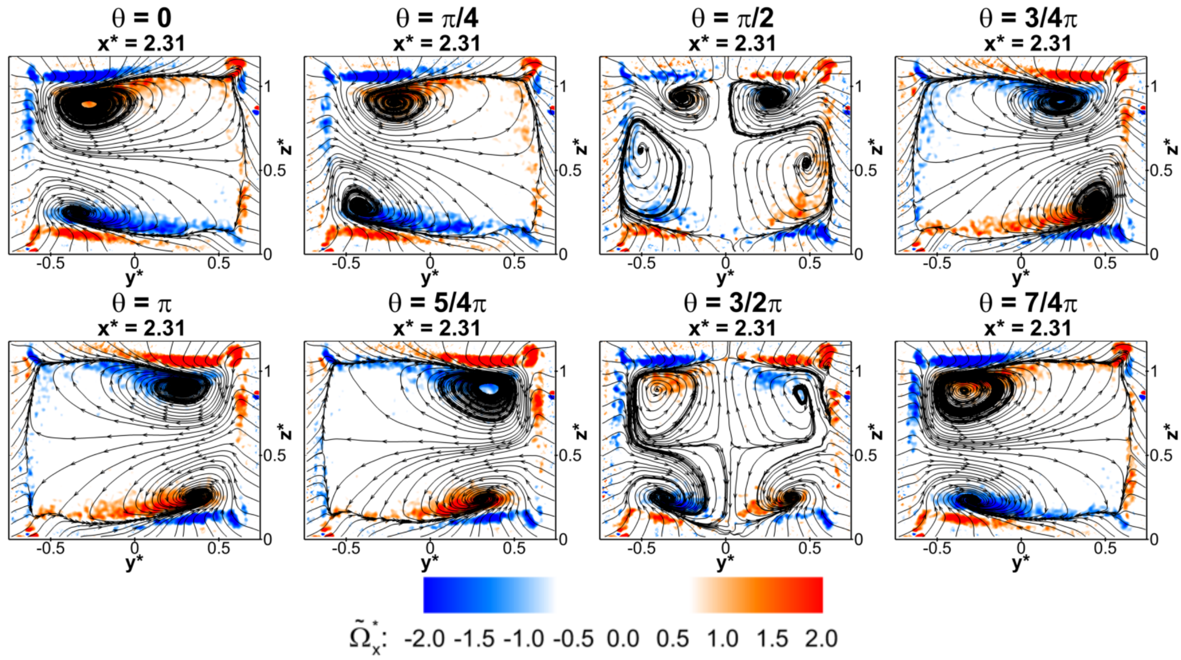

Figure 3.24: Low order phase averaged velocity field at $x^* = 2.31$. The plots are coloured according to the values of the normalised streamwise component of the vorticity $\tilde{\Omega}_x^*$; the streamlines are drawn considering the in-plane components of the velocity field.

how the wake evolves between states. From the results, in fact, four main states can be isolated: the two lateral symmetry breaking bi-stable states (at $\theta = 0\,rad$ and $\theta = \pi\,rad$) and two lateral symmetry preserving states (at $\theta = \pi/2\,rad$ and $\theta = 3/2\pi\,rad$), whose presence is a necessary but not sufficient condition for the switch between the first two states. The distribution of the number of snapshots contained in each bin (Fig. 3.23c) shows for the plane at $x^* = 2.31$ a clear prevalence of the bi-stable states, with the one centred around $\theta = 0\,rad$ occurring more often than that at $\theta = \pi$, justifying the slight lateral asymmetry already discussed in §3.1 for the time averaged results. Small differences are seen in the number of occurrences associated with the two lateral symmetry preserving states, arguably due to the presence of weak interactions between the ground plane and the wake.

Each bi-stable state evolves in time, changing continuously due to the action of the oscillating global modes described in §3.2.4. As a results, the balance between the two recirculations that form the streamwise legs of the hairpin vortices is alternately lost and recovered, until one of the two structures eventually prevails, yielding the definitive loss of symmetry in the vertical direction. As the wake loses symmetry in the vertical plane, the symmetry in the lateral direction is recovered leading to the establishment of one of the two lateral symmetry preserving states ($\theta = \pi/2\,rad$ and $\theta = 3/2\pi\,rad$ in Fig. 3.24 and Fig. 3.25). At this point, the system is in a condition of unstable equilibrium and can either return to the previous lateral symmetry breaking state or switch to the opposite state, depending on any random

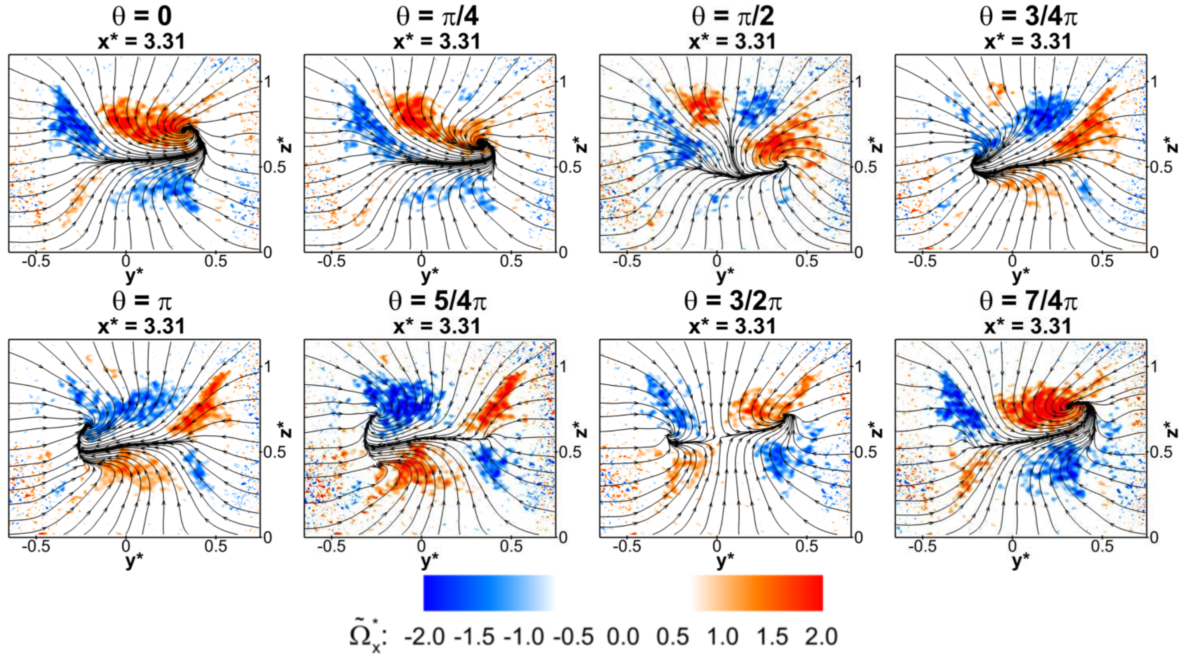

Figure 3.25: Low order phase averaged velocity field at $x^* = 3.31$. The plots are coloured according to the values of the normalised streamwise component of the vorticity $\tilde{\Omega}_x^*$; the streamlines are drawn considering the in-plane components of the velocity field.

perturbation (Brackston et al, 2016). From a topological point of view, the transition from a lateral symmetry preserving state to a bi-stable state resembles the evolution from the steady symmetric state to the steady asymmetric state reported by Grandemange (2013) for the laminar wake developing downstream of an Ahmed body (Fig. 1.17), confirming the laminar origin of this particular instability. In any case, the wake never recovers its full symmetry, since the topology of the lateral symmetry preserving states is always dominated by either the upper or lower recirculation depending on the random perturbation that triggers the transition from the bi-stable state to the lateral symmetry preserving state: a perturbation originating in the lower portion of the bi-stable state will result in a lateral symmetry preserving state dominated by the bottom recirculation whilst a perturbation originating from the upper part of the bi-stable state will lead to a lateral symmetry preserving state dominated by the upper lobe.

The fact that a strong asymmetry is present between the upper and lower portions of the wake any time the lateral symmetry is restored supports the thesis that the bi-stable mode is indeed the result of the interaction between the two horizontal shear layers, as identified by Cadot et al (2015) for a similar model. This asymmetry extends over the entire wake, yielding either a slightly downwash or upwash dominated wake every time the lateral asymmetry is suppressed (Fig. 3.25). This also accords with the cross-wavelet analysis where the out-of-phase relationship between C_Y and C_L (reported in Fig. 3.4) suggests an increase in the magnitude

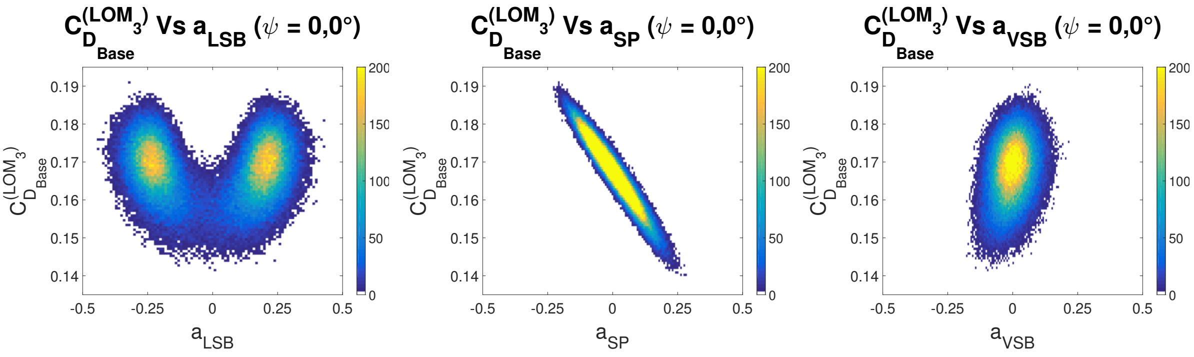

(a) **(b)** **(c)**

Figure 3.26: Scatter plots between the unsteady values of the pressure drag obtained from the low order model $C_{D_{Base}}^{(LOM_3)}(t)$ and the temporal coefficients associated with the first three POD pressure modes for $\Psi = 0.0°$: **a** $C_{D_{Base}}^{(LOM_3)}(t)$ Vs $a_{LSB}(t)$; **b** $C_{D_{Base}}^{(LOM_3)}(t)$ Vs $a_{SP}(t)$; **c** $C_{D_{Base}}^{(LOM_3)}(t)$ Vs $a_{VSB}(t)$. The colour map shows the PDF of the values of the considered coefficients.

of the vertical force as the lateral force tends to zero, consistent with the switching between the bi-stable lateral symmetry breaking states and lateral symmetry preserving states identified in the phase averaged PIV fields.

3.2.5.1 Impact of the symmetric state on the base drag

The in-phase relationship identified between C_Y and C_D in §3.2.1 was further investigated by looking at the contribution of the three POD modes (described in §3.2.2) to the base drag $C_{D_{Base}}$. Using a low order model for the pressure data $C_{pi}^{(LOM_3)}(t)$ (consisting of the time averaged base pressure distribution and the first three POD modes) the corresponding rear drag $C_{D_{Base}}^{(LOM_3)}(t)$ (estimated using Eq. 2.10 replacing $\overline{C}_{p_i}$ with $C_{pi}^{(LOM_3)}(t)$) was correlated with the temporal coefficients of the same POD modes, leading to the scatter plots reported in Fig. 3.26. For the sake of simplicity, data recorded using only one scanner was considered in this case. Compared to the test run with two scanners (§3.1 and §3.2.3), the slight differences in terms of time averaged base pressure distribution (Fig. 3.28a) and pressure drag values (Table 3.2) obtained in this case can be ascribed partly to the different spatial resolution between the two setups, but also to the high sensitivity of the configuration tested to small variations of the pitch angle (which in all tests was set with an accuracy of ±0.2°, as stated in §2.1). The effects of the latter can be inferred from the different location of the rear stagnation point between the two tests (Fig. 3.1 and 3.28a), and will be further discussed, although for a slightly different configuration, in §5.3.

The correlation between $C_{D_{Base}}^{(LOM_3)}(t)$ and $a_{LSB}(t)$ (Fig. 3.26a) shows that a drag reduction can be achieved any time the lateral symmetry of the wake is restored; namely, $a_{LSB}(t) \to 0$. A similar conclusion was drawn by Evrard et al (2016) and Li et al (2016). A deeper understanding

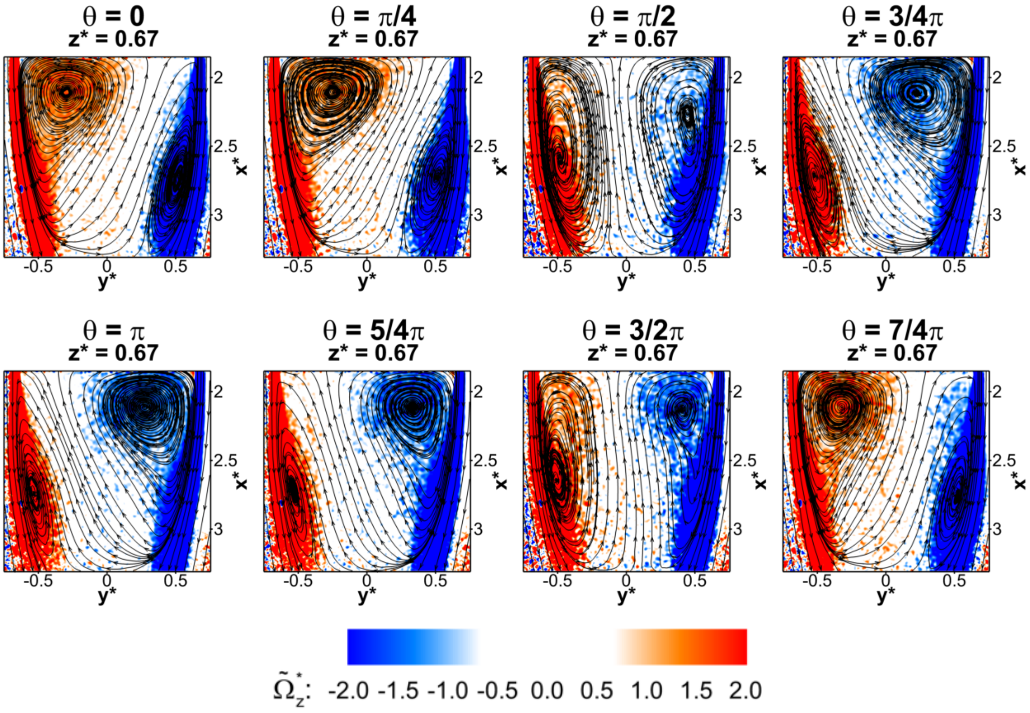

Figure 3.27: Low order phase averaged velocity field at $z^* = 0.67$. The plots are coloured according to the values of the normalised vertical component of the vorticity $\tilde{\Omega}_z^*$; the streamlines are drawn considering the streamwise and spanwise components of the velocity field.

of the origin of this drag reduction can be achieved by looking at the scatter plot between $C_{D_{Base}}^{(LOM_3)}(t)$ and $a_{SP}(t)$ (Fig. 3.26b). An almost linear relationship is seen between the values of the base drag and the values of the temporal coefficients associated with the symmetry preserving POD mode, with the lowest value of $C_{D_{Base}}^{(LOM_3)}(t)$ obtained when $a_{SP}(t) > 0$. This, combined with the fact that $a_{SP}(t)$ assumes its highest positive values when the switch between the two bi-stable modes is most likely to occur (as seen in §3.2.5), confirms that the drag reduction associated with the restoration of the wake lateral symmetry comes from the weakening of the interaction between the core of the recirculating structures and the base of the model, rather than just from the suppression of the lateral asymmetry. No particular correlation exists

$\overline{C}_{D_{Base}}$	$\overline{C}_{D_{Base}}^{(LOM_3)}$	$\tilde{C}_{D_{Base(LSP)}}^{(LOM_3)}$	$\tilde{C}_{D_{Base(L)}}^{(LOM_3)}$	$\tilde{C}_{D_{Base(R)}}^{(LOM_3)}$
0.168	0.168	0.157	0.168	0.168

Table 3.2: Average values of the base drag. The superscript (LOM_3) refers to the POD filtered field while the subscripts *(LSP)*, *(L)* and *(R)* indicate respectively the *lateral symmetry preserving* state and the two bi-stable states (*L-State* and *R-State*).

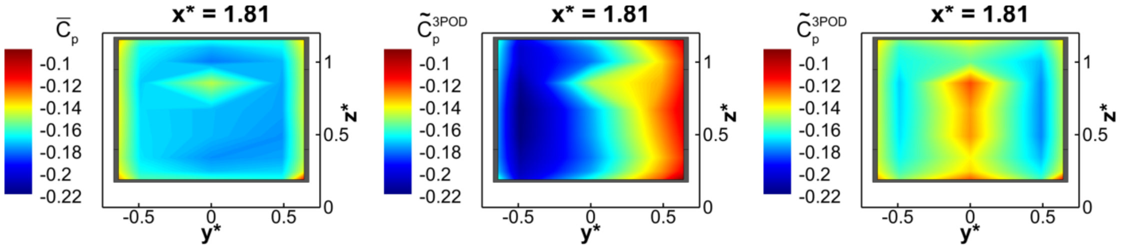

(a) *Averaged Field* **(b)** *L State* **(c)** *LSP state*

Figure 3.28: **a** Time averaged base pressure distribution (from single scanner acquisition); **b** base pressure distribution corresponding to one of the two bi-stable states (L State). **c** base pressure distribution corresponding to the suppression of the bi-stable mode.

between $C_{D_{Base}}^{(LOM_3)}(t)$ and $a_{VSB}(t)$ (Fig. 3.26c), in agreement with that already stated in §3.2.5.

The weakening of the interactions between the vortical structures and the base, occurring any time the wake recovers its lateral symmetry, is also observed in the low order phase averaged velocity field constructed by applying the same technique described in §3.2.5 to the 2D-2C PIV data recorded along a horizontal plane centred with the wake (Fig. 3.27). In this case, the low order model was built using the first four POD modes; their temporal coefficients were ordered in phase according to Eq. 3.3 using the 1^{st} mode and 4^{th} mode as sorting modes, because in this case the vertical symmetry breaking mode has a much lower energy content as there is no through-plane velocity component. The results show that as the lateral asymmetry is suppressed, the large recirculation close to the base in each bi-stable state is stretched downstream and becomes narrower, whilst a change in the opposite direction is observed for the recirculation farther from the base, in good agreement with the description provided in §3.2.4 for the pumping mode. These changes lead eventually to the restoration of the symmetry between the two sides of the wake. At this point, the reverse flow impinging on the base is at its maximum, allowing a better pressure recovery and lower aerodynamic drag, confirming the in-phase relationship between C_Y and C_D seen in §3.2.1: as the lateral symmetry is restored, $C_Y \to 0$, C_D reaches its minimum value.

The drag reduction associated with the suppression of the lateral asymmetry was quantified by averaging the base pressure distributions obtained from the low order model for the condition $0.1 \cdot min(a_{LSB}(t)) \leq a_{LSB}(t) \leq 0.1 \cdot MAX(a_{LSB}(t))$. The resulting base pressure distribution (Fig. 3.28c) is characterised by an increase in both size and magnitude of the 'high' pressure region corresponding to the rear stagnation, compared to the pressure distribution resulting from the time average of the entire dataset (Fig. 3.28a). Two low pressure regions, however, are still visible close to the vertical sides of the base, matching the locations of the recirculating structures seen from the phase averaged velocity fields when the bi-stable state is suppressed ($\theta = \pi/2\,rad$ and $\theta = 3/2\pi\,rad$ in Fig. 3.24, 3.25, 3.27). This base pressure distribution yields a $\approx 7\%$ reduction over the time averaged base drag ($\tilde{C}_{D_{Base(LSP)}}^{(LOM_3)}$, Table 3.2). This is in line with the 8% decrease estimated by Li et al (2016) and the 6% reduction obtained by Grandemange et al (2014b) stabilising the wake using a vertical control cylinder. A slightly higher improvement of $\overline{C}_{D_{Base}}$ was obtained by Evrard et al (2016) applying a cavity at the base of a similar geometry, arguably as a consequence of the further weakening of the interactions between the model base and the vortical structure due to the depth of the cavity. The validity of these results is also confirmed by the fact that the values obtained for $\overline{C}_{D_{Base}}$, $\tilde{C}^{(LOM_3)}_{D_{Base}(L)}$ and $\tilde{C}^{(LOM_3)}_{D_{Base}(R)}$ are within $\pm 1\,count$ confirming the trend already observed in §3.2.3 for the test performed using two scammers. In this case $\tilde{C}^{(LOM_3)}_{D_{Base}(L)}$ and $\tilde{C}^{(LOM_3)}_{D_{Base}(R)}$ have been calculated by averaging the fields extracted from the filtered dataset under the conditions $a_{LSB}(t) < 0.1 \cdot min(a_{LSB}(t))$ and $a_{LSB}(t) > 0.1 \cdot MAX(a_{LSB}(t))$. This further confirms that the only source of drag reduction is found in the transition between the bi-stable states.

3.3 Summary and conclusions

In this chapter, the wake of the Windsor body in the simple square-back configuration has been investigated, with a particular focus on the characterisation of both short-time and long-time dynamics.

The bi-stable lateral symmetry breaking mode, already described in the works of Grandemange et al (2012a), Grandemange et al (2013b), Volpe et al (2015) and Evrard et al (2016) has been isolated for the fist time in the case of a model with a more slanted front-end and characterised in more depth. This mode has been found to exist within a limited range of yaw angles $-0.5^\circ \leq \Psi \leq +0.5^\circ$ and to be less sensitive to small variations of either ground clearance (from $C^* = 0.138$ to $C^* = 0.208$) or free stream turbulence intensity (from $TI^* \approx 0.2\%$ to $TI^* \approx 1.5\%$).

The application of proper orthogonal decomposition to the fluctuating part of the base pressure and PIV data has highlighted the existence of more complex dynamics, consisting of coherent motions of the wake in three different directions: a lateral symmetry breaking mode, a vertical symmetry breaking mode and a symmetry preserving mode. Subsequent analysis confirms that these POD modes are the result of the combination of the long-time bi-stable mode, the global oscillating modes identified in Grandemange et al (2013b) and the pumping mode described in Duell and George (1999).

The global oscillating modes consist of lateral and vertical motions of the wake closure with normalised frequencies of $St_H = 0.13$ and $St_H = 0.19$ and originate from the interactions between the hairpin vortex that forms each one of the two bi-stable states and either the vertical or horizontal shear layers originating from the opposite side of the model base. The pumping mode, with a characteristic frequency of $St_H = 0.07$, is shown for the first time to be the result of the interactions between the inner regions of each hairpin vortex. Due to the action of this mode, the hairpin vortices are alternately ‘stretched’ and ‘squeezed’ in the streamwise direction, yielding out-of-phase variations in the static pressure between the left-hand side and right-hand side portion of the base.

A phase averaged low order model, constructed from the time averaged field and the first three POD modes has been used to provide new insights on the configurations assumed by the wake during its evolution. Indeed, it is shown that the bi-stable mode can be described as the result of the combination of lateral and vertical symmetry breaking modes.

When the wake recovers its lateral symmetry, two different lateral symmetry preserving states appear, depending on the random perturbation that triggers the transition from the bi-stable state to the laterally symmetric state: a perturbation originating in the lower portion of the bi-stable state will result in a lateral symmetry preserving states dominated by the bottom recirculation whilst a perturbation originating from the upper part of the bi-stable state will lead to a lateral symmetry preserving states dominated by the upper lobe. As a result, a quasi-steady out-of-phase relationship is seen between side force and lift when cross-wavelet transform is applied to the signals referring to these two components of the aerodynamic force.

When the wavelet cross-spectrum of side force and drag is considered, a quasi-steady in-phase relationship is found. The origin of this relationship can be ascribed to the reduction of the interactions between the recirculating structures and the base occurring any time the wake switches from a bi-stable state to a lateral symmetry preserving state, resulting in a $\approx 7\%$ decrease of the base drag compared to the time averaged value. This potential gain motivates the application of flow control strategies aiming to stabilising the lateral symmetry preserving states, as proposed for example by Grandemange et al (2014b), Evrard et al (2016), Li et al (2016) and Brackston et al (2016) and suggests the existence of an additional margin for improvement in those cases where the actuated flow is still asymmetric, as in Littlewood and Passmore (2012) and Barros et al (2016).

Chapter 4

Horizontal trailing edge tapering

In this chapter, the effects produced by small horizontal tapers on both the wake's time averaged topology and unsteady behaviour are investigated. Short tapered sections, with a chord of $\approx 4\%$ of the model length, are applied to the horizontal trailing edges of the Windsor body without wheels (as detailed in §2.1). These elements are reported to trigger noticeable changes in the time averaged wake topology and base pressure distribution, that ultimately lead to variations in the steady aerodynamic forces acting over the entire model. In particular, a drag increase is seen to occur every time the wake becomes asymmetric in the vertical direction, as the balance between upwash and downwash is lost. The toroidal shape, seen in Chap. 3 for the time averaged wake forming downstream of the square-back configuration, is replaced by a more complex structure, consisting of a pair of horseshoe vortices that eventually marge with the longitudinal vortical structures forming at the tips of each slanted surface. The predominance of either upwash or downwash leads to the deformation of the horseshoe vortex forming in the region of the shear layer with the highest curvature. In these conditions, the vortical structure loses its coplanarity, assuming a characteristic *'U'* shape. Further insights on the nature of this vortex are provided by the unsteady analysis. The application of POD to the fluctuating part of the base pressure and velocity fields reveals that this structure is more stable than that seen in the square-back case. Indeed, a weakening of the bi-stable lateral symmetry breaking mode as well as the pumping mode is seen as the curvature of the shear layers is increased. On the other hand, a strengthening of the vertical flapping is reported, as a consequence of the increased level of interactions between the top and bottom shear layers. The weakening of the bi-stable mode, however, does not necessarily yield a drag reduction. A decrease in C_D over the square-back case, in fact, is obtained only when the weakening of the bi-stable mode is accompanied with the restoration of the symmetry in the vertical direction.

4.1 Time averaged results

The variation of drag and lift coefficients for different combinations of taper angle is presented in Fig. 4.1. When the top taper angle is zero and the bottom taper angle is increased ($\phi_t = 0°$ in Fig. 4.1), the drag increases for all cases compared to the baseline square-back. Among all configurations tested, the highest value of C_D is seen for $\phi_b = 20°$. As the bottom taper angle is increased the lift decreases to a minimum at 16° before increasing for higher angles as the flow acting over the tapered surface becomes fully separated (see §4.2.1). If the upper taper is varied, while the lower slant is fixed at 0° ($\phi_b = 0°$ in Fig. 4.1), there is a small drag reduction compared to the baseline case as the taper angle is increased up to 12° (as also reported in the work of Littlewood and Passmore (2010)); then the drag increases again, following a parabolic trend, becoming higher than in the square-back case for $\phi_t \geq 16°$. The lift is the mirror image of the bottom taper data, with the maximum value of the lift recorded at $\phi_t = 16°$. The slope of the linear section of the curve, though, is now lower, since in this case the action of the slanted surface is no longer enhanced by the ground effect. With the lower taper angle fixed at its middle position ($\phi_b = 12°$ in Fig. 4.1), the parabolic shape in the C_D plot is preserved although with a steeper trend. In these conditions, a drag minimum is found when a 12° taper is applied to the top trailing edge (*low drag configuration*). The lift curve, on the other hand, is characterised by the same trend already discussed for the $\phi_b = 0°$ case, although with a different value of C_L for $\phi_t = 0$. These trends are in good agreement with those reported in Perry et al (2015), with small discrepancies caused arguably by minor differences in the setups used in the two experiments.

Information on the genesis of the aforementioned variations in the aerodynamic force can be gathered by looking at the distribution of the time averaged values of C_p over the model

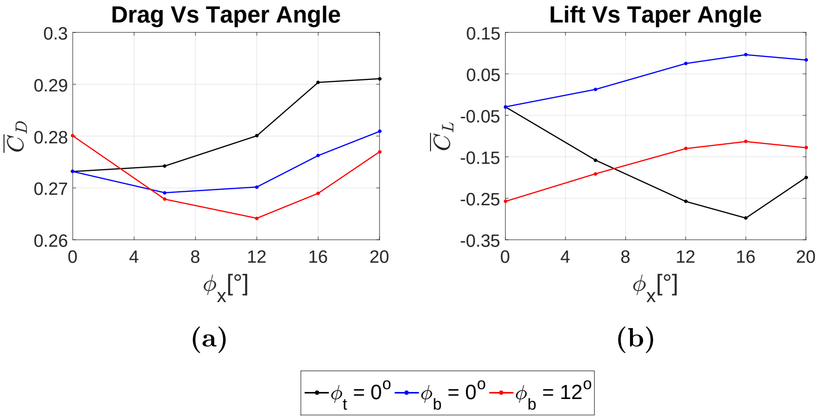

(a) (b)

Figure 4.1: Time averaged drag **(a)** and lift **(b)** recorded for all the configurations tested: $\boldsymbol{\phi_t = 0°}$, top taper fixed at 0° while changing the bottom taper angle; $\boldsymbol{\phi_b = 0°}$, bottom taper fixed at 0° while changing the top taper angle; $\boldsymbol{\phi_b = 12°}$, bottom taper fixed at 12° while changing the top taper angle.

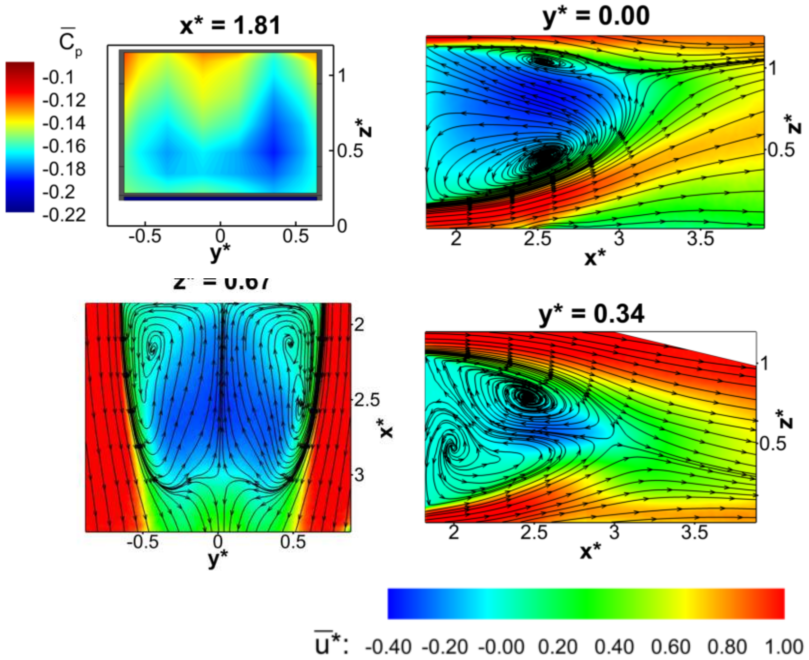

(a) $\phi_t = 0°$, $\phi_b = 12°$

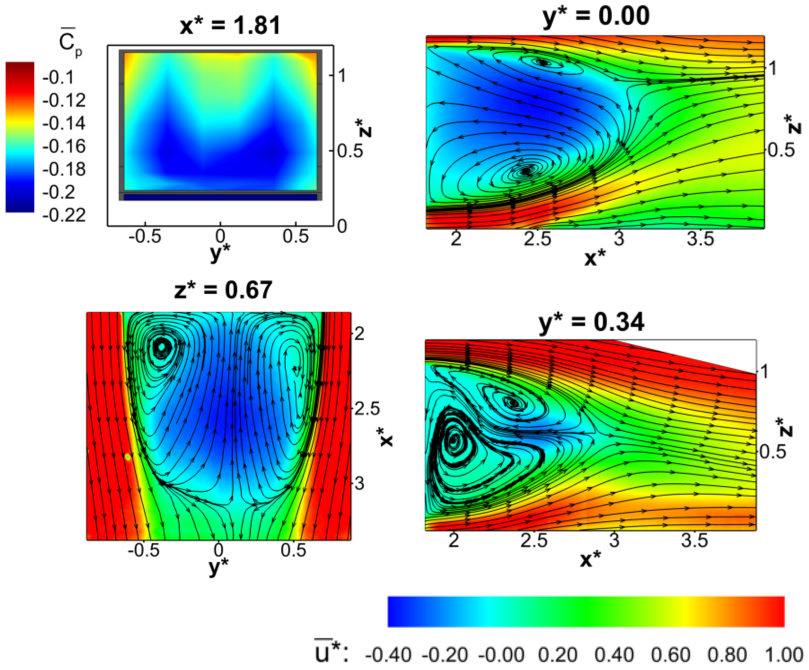

(b) $\phi_t = 0°$, $\phi_b = 20°$

Figure 4.2: Time averaged fields for two different bottom taper angles: **a** $\phi_t = 0°$, $\phi_b = 12°$; **b** $\phi_t = 0°$, $\phi_b = 20°$. Clockwise from top left: $\mathbf{x^* = 1.81}$ base pressure distribution; $\mathbf{y^* = 0.00}$, PIV vertical mid-plane; $\mathbf{x^* = 2.31}$ and $\mathbf{x^* = 3.31}$, PIV stereo cross-planes; $\mathbf{y^* = 0.34}$, PIV vertical off-centre plane; $\mathbf{z^* = 0.67}$, PIV horizontal mid-plane. All PIV fields are coloured according to the values of the axial component of the velocity u^*; the streamlines refer to the in-plane components.

rearward facing surfaces as well as the time averaged velocity field in the near-wake of the model (Fig. 4.2 and 4.3). The application of a chamfer to the horizontal edges of the model base creates a region of suction at the leading edge of the tapered surface. As the angle is increased the low pressure region tends to expand downstream until the flow starts to separate (usually at $\phi_{t,b} = 20°$), leading to a sudden reduction of the size of the low pressure region. As the suction over the slanted surface increases, a pair of trailing vortices forms at the tip of the slant, as can be seen from the PIV cross-plane at $x^* = 2.31$ (Fig. 4.2a and 4.3a). These vortices are similar to those identified by Grandemange et al (2013c) when applying flaps to the top and bottom trailing edges of an Ahmed body. They follow the curvature of the shear layer while moving downstream, until they become the only vortical structures downstream of the wake closure, as shown in the PIV cross-plane located at $x^* = 3.31$. The strength of these vortices is reduced when the flow over the slanted surface becomes fully separated, as in the case of the configuration with $\phi_t = 0°, \phi_b = 20°$ (Fig. 4.2b and 4.6d).

When a taper is applied to the bottom trailing edge (while keeping the top edge squared, as in Fig. 4.2), the high momentum flow passing underneath the model is deflected upwards by the slant and feeds the lower recirculating zone, increasing its size compared to the upper vortex. This leads to the formation of an upawsh dominated wake, as shown in the PIV vertical mid-plane (at $y^* = 0.00$). The symmetry between the top and bottom recirculations previously seen for the square-back case (Chap. 3) is therefore lost. The direction of the flow reversal is tilted upwards forming an angle of up to $\approx 108°$ to the ground plane for $\phi_b = 12°$ and $\phi_b = 16°$. Consequently, the base impingement point moves towards the top trailing edge as does the saddle point that marks the wake closure. The streamlines leaving the saddle point are also angled at a similar trajectory, forming a maximum angle of almost 10° for the configuration generating the lowest lift (downforce). As a result, the length of the recirculation zone is reduced, being about 20% shorter than in the square-back case. The annular low pressure region seen in the square-back case is replaced by a more *'U'* shaped zone, extending throughout the lower portion and the sides of the base. A similar pattern is seen in the 2D streamlines drawn in the plane at $x^* = 2.31$, especially for the configuration with $\phi_t = 0°, \phi_b = 20°$. The effects of the upwash generated by the upswept slant are also visible on the PIV data acquired at $z^* = 0.67$. When the flow is attached to the bottom slant (e.g. Fig. 4.2a for the $\phi_b = 12°$ case) a better lateral symmetry can be seen in the time averaged field when compared to the same plane recorded for the square-back case. The two recirculating regions are pressed against the base and the streamlines close to the saddle point assume a characteristic convex shape. The increase in bottom chamfer angle can also promote separation of the flow from the tunnel floor, as can be seen for example on the plane at $y^* = 0.00$ for $x^* > 2.5$. This region of separation, however, is quite limited and is sufficiently far from the model base that no significant effects are produced on either the base pressure distribution or the aerodynamic drag experienced by the model. The size of this separation zone tends to reduce in the spanwise direction, and is hardly visible in the plane at $y^* = 0.34$. The time averaged velocity field recorded at this

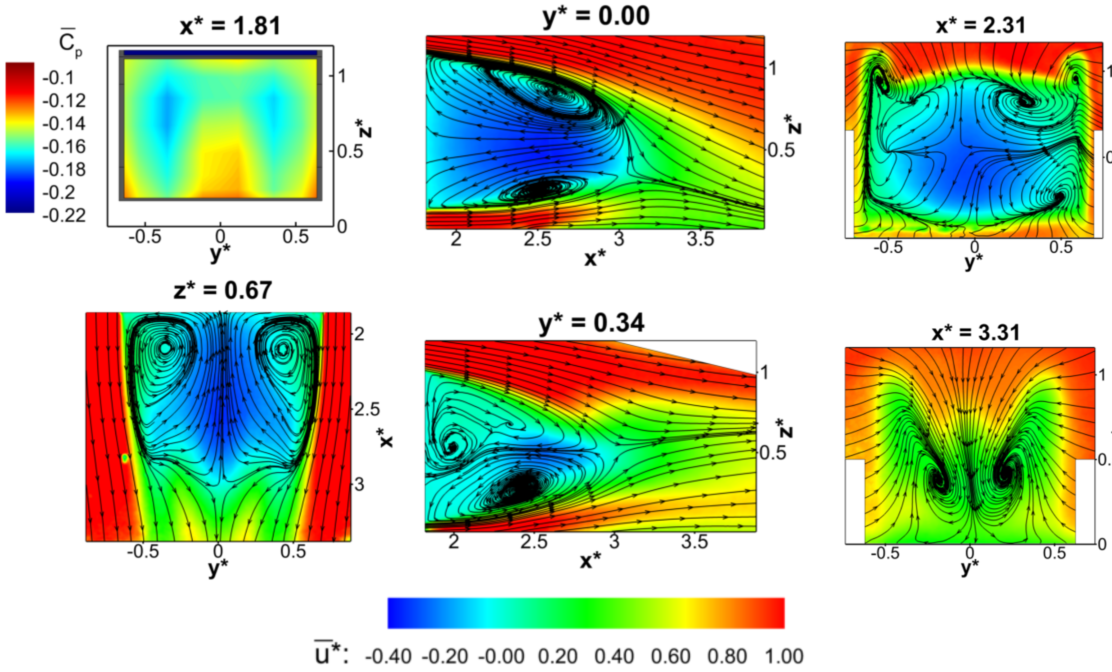

(a) $\phi_t = 16°$, $\phi_b = 0°$

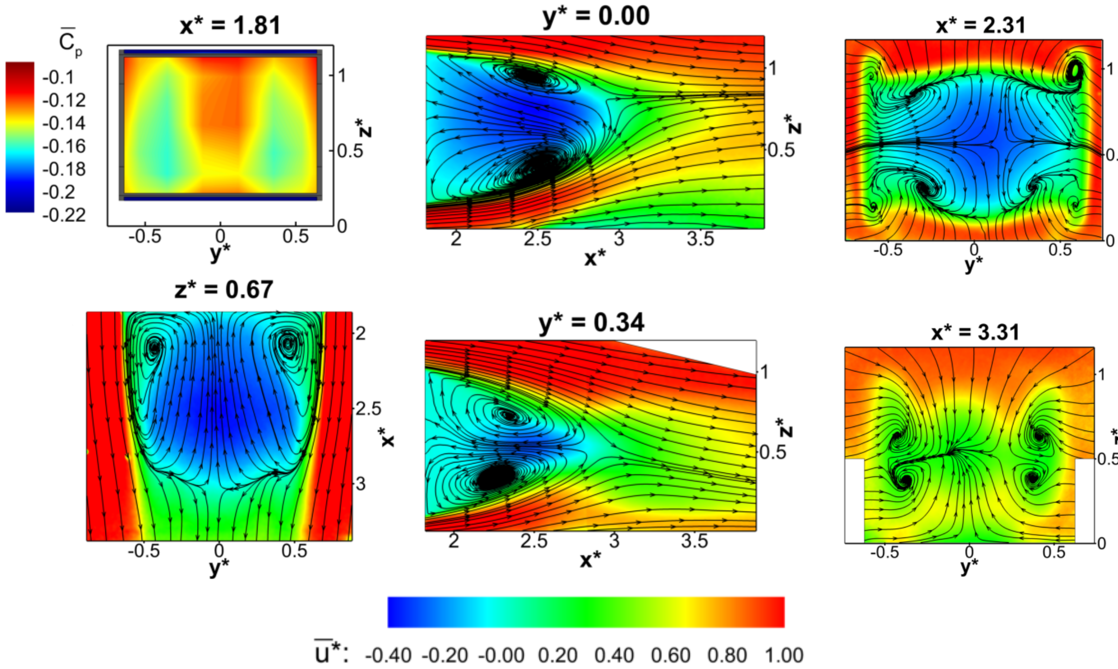

(b) $\phi_t = 12°$, $\phi_b = 12°$

Figure 4.3: Time averaged fields for two different tapered configurations: **a** $\phi_t = 16°$, $\phi_b = 0°$; **b** $\phi_t = 12°$, $\phi_b = 12°$ (low drag configuration). Clockwise from top left: $\mathbf{x^* = 1.81}$ base pressure distribution; $\mathbf{y^* = 0.00}$, PIV vertical mid-plane; $\mathbf{x^* = 2.31}$ and $\mathbf{x^* = 3.31}$, PIV stereo cross-planes; $\mathbf{y^* = 0.34}$, PIV vertical off-centre plane; $\mathbf{z^* = 0.67}$, PIV horizontal mid-plane. All PIV fields are coloured according to the values of the axial component of the velocity u^*; the streamlines refer to the in-plane components.

location shows that the wake is squeezed towards the model base more than that described for the longitudinal symmetry plane ($y^* = 0.00$), arguably by the action of the trailing vortices developing at the tips of the slant. The upward momentum of the flow leaving the model underbody in this region is reduced due to its interaction with the flow passing along the side surfaces. As a consequence, the amount of upwash generated by the bottom slant is lower and the free stagnation point is shifted downwards. The streamlines leaving this point are now noticeably deflected towards the ground, forming an angle of almost $-19°$ for $\phi_b = 16°$. All these elements suggest the existence of a pair of horseshoe vortices, similar to those described in Ahmed et al (1984) and Venning et al (2017). The first vortex runs parallel to the squared top trailing edge; in proximity to the vertical edges of the base its 'tails' align themselves with the direction of the onset flow. The second vortex is found close to the bottom slant; from there it extends over the vertical sides of the base until almost reaching the top trailing edge, where its 'tails' interact with those of the upper, weaker vortex, arguably in a way similar to that described by Bristol et al (2004) and Ryan et al (2012). The same 'tails' then merge with the vortical structures developing at the tips of the bottom slant (Bristol et al, 2004), resulting in the pair of longitudinal counter-rotating vortices that dominate the flow field visible in the PIV cross-plane located at $x^* = 3.31$ (Fig. 4.4a). This allows the formation of the characteristic '*U*' shaped low pressure zone previously described. Once the flow over the slant becomes fully separated (Fig. 4.2b), the upwash is reduced, the length of the rear recirculation increases and the near-wake closure becomes flatter. In these conditions, a certain degree of asymmetry is seen in the time averaged flow field, especially along the horizontal plane (at $z^* = 0.67$).

Similar structures in the wake topology and base pressure distribution can be found when a taper is applied to the top trailing edge leaving the opposite edge squared, as shown in Fig. 4.3a for the $\phi_t = 16°, \phi_b = 0°$. In this case, however, the downwash tends to prevail over the upwash; the streamlines close to the saddle point visible in the PIV plane at $z^* = 0.67$ become concave and the vortical structures previously described are turned upside down. In this case, the only vortices still visible downstream of the wake closure (at $x^* = 3.31$) are those originating at the tips of the top slant.

The symmetry seen in the vertical direction for the square-back case is almost fully recovered when the low drag configuration is considered (Fig. 4.3b). In this case, the two horizontal shear layers are deflected towards the centre of the wake almost with the same strength. Therefore, although the free stagnation point visible at $y^* = 0.00$ is still located above mid-base height, the reverse flow features a shallower angle to the horizontal plane, as clearly shown in the plane at $y^* = 0.34$. This, combined with the reduction of the size of the near-wake recirculation, ultimately results in a better pressure recovery over the model base, in agreement with the findings of Grandemange et al (2013c). A more uniform sizing between the recirculations is seen on the planes at $y^* = 0.00$, $y^* = 0.34$ and $z^* = 0.67$. Nevertheless, the vortex cores visible from the plane at $z^* = 0.67$ appear to be closer to the base than those seen on the two streamwise planes. They are responsible for the formation of the low pressure area that appears at the

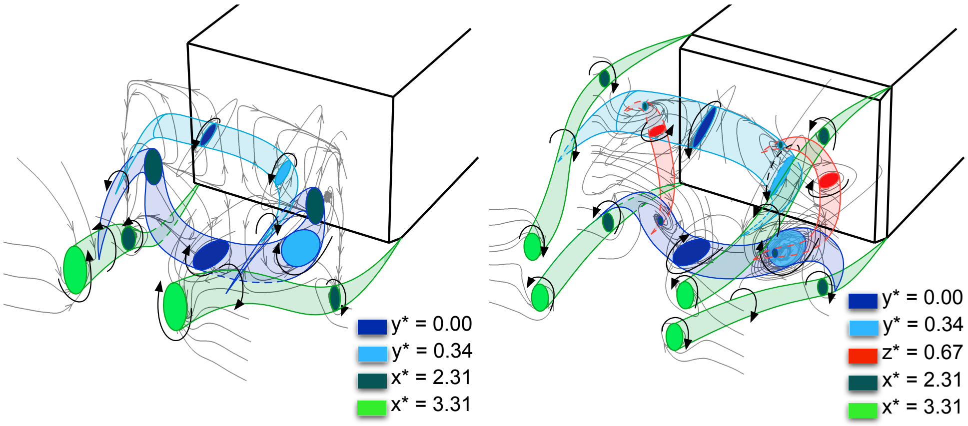

(a) $\phi_t = 0° \ \phi_b = 12°$ **(b)** $\phi_t = 12° \ \phi_b = 12°$

Figure 4.4: Schematic representation of the wake structure, based on PIV results. Proposed 3D wake topology for $\phi_t = 0°, \phi_b = 12°$ **(a)** and $\phi_t = 12°, \phi_b = 12°$ **(b)**.

centre of each half of the model base and extends vertically from the bottom trailing edge to the top trailing edge. All these elements contribute to define a wake topology different to that described in the case of an upwash or downwash dominated wake (Fig. 4.4b). Each of the two horseshoe vortices previously described extends now parallel to the ground plane (i.e. without bending in the vertical direction) and merges with the pair of trailing vortices forming at the tips of the corresponding slant. An additional pair of transverse vortices, extending in the vertical direction, develops close to the side trailing edges of the model. These vortical structures tend to stay closer to the base, originating the suction zones previously described.

4.1.0.1 Contribution of the rear wall velocity to the drag

The effects of the wake on the aerodynamic drag experienced by the entire model were studied by correlating the values of the time averaged drag $\overline{C}_D$, measured using the balance, with the values of the time averaged rear drag $\overline{C}_{D_{Rear}}$ estimated by integrating the pressure recorded over the rearward facing surfaces using Eq. 2.10. In this case the rear drag was calculated including the contribution of the slants. The results, presented in Fig. 4.5a, show the existence of a strong correlation between $\overline{C}_D$ and $\overline{C}_{D_{Rear}}$ for all the configurations considered in the present study. This is line with the results obtained by Parezanović and Cadot (2012) when investigating a D-shaped 2D bluff body. It is shown indeed that the drag generated by the rearward facing surfaces is the dominant contribution to $\overline{C}_D$ (Littlewood and Passmore, 2010) and drives the variations recorded for different combinations of the horizontal slants (Perry et al, 2015), having kept constant the contribution of the fore-body (§1.1.4).

The link between changes in wake topology and different base pressure distributions, qualitatively described in §4.1, has then been further investigated by considering the normalised value of the magnitude of the tangential wall velocity w^*_{Wall}. This is defined as the spatial

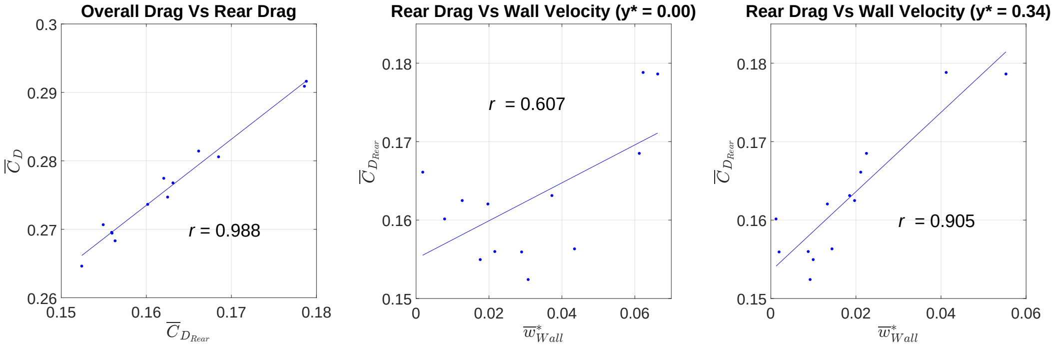

(a) **(b)** **(c)**

Figure 4.5: **a** correlation between the aerodynamic drag and the pressure drag associated with the rearward facing surfaces; correlation between the pressure drag and the tangential wall velocity for $y^* = 0.00$ **(b)** and $y^* = 0.34$ **(c)**.

average of the time averaged value of the vertical component of the velocity $\overline{w^*}$, estimated using the vertical PIV planes taken at $y^* = 0.0$ and $y^* = 0.34$, having considered a domain S^*_{wake} delimited by the top and the bottom shear layers and extending in the streamwise direction for $\delta x^* = 0.1$ from the model base, according to the Eq. 4.1:

$$\overline{w^*_{Wall}} = \left| \frac{1}{S^*_{wake}} \int\int_{S^*_{wake}} \overline{w^*} \cdot dS^* \right| . \tag{4.1}$$

Since the bi-stable lateral symmetry breaking mode described in Chap. 3 is still clearly visible in many of the configurations tested here (as detailed in §4.2.1), and its effects are particularly visible on the off-centre plane at $y^* = 0.34$, the state average fields (defined as the average of the states isolated from Eq. 3.1) rather than the time averaged fields have been used for this plane. This has contributed to minimise any distortion in the results, as the state average contains equal weighting for the two states. The results for the vertical mid-plane ($y^* = 0.00$, Fig. 4.5b) show the existence of a weak correlation between w^*_{Wall} and $\overline{C}_{D_{Rear}}$ ($r = 0.607$), suggesting that a single centreline 2D PIV plane is not sufficient to fully characterise the topology of the highly three-dimensional wake generated by such a bluff body (Grandemange et al (2013c) and Perry et al (2016)). However, when a plane located closer to the low pressure region described in §4.1 is considered (as for $y^* = 0.34$), a strong correlation between w^*_{Wall} and $\overline{C}_{D_{Rear}}$ is found ($r = 0.905$, Fig. 4.5c). This result suggests the existence of a direct relation between the low pressure acting on the model base and the vortical structures shed in the near-wake region. As a consequence of the predominance of either upwash or downwash, the vortex closer to the lower or the upper portion of the model base respectively expands, at the expenses of the recirculation acting on the opposite side (as clearly shown in Fig. 4.2a and Fig. 4.3a). This yields an increase in the magnitude of the velocity tangent to the base, that ultimately results in a reduction of the static pressure acting in the same region. When the vortical structures are squeezed towards the base, as in the case of the plane located at $y^* = 0.34$, this relation becomes even stronger, in agreement with the results of the numerical simulations performed by Bruneau et al (2010). This mechanism may also explain the drag reduction obtained in Littlewood et al (2011), where the application of small horizontal slats to the lower half of the base of the same model considered here resulted in an increase of C_p.

4.2 Unsteady results

4.2.1 Sensitivity of the long-time wake dynamics to taper angle

An analysis of the unsteady characteristics of the wake was conducted to investigate the impact of different levels of upwash\downwash induced by the tapers on the bi-stable mode. The results related to the RMS of the pressure fluctuation are presented in Fig. 4.6. Compared to the square-back case (Fig. 3.2), the bi-stable region, identified by the area with the highest level of fluctuation, is modified in both extension and position by the upwash or downwash generated by the small slants, as shown by the deflection of the shear layers visible in the normalised vorticity fields included in Fig. 4.6, with $\tilde{\Omega}_y^* = \frac{\partial w^*}{\partial x^*} - \frac{\partial u^*}{\partial z^*}$ representing the lateral component of the vorticity. When a chamfer is applied to the bottom trailing edge, the region of highest $RMS(\Delta C_p)$ is shifted upwards (Fig. 4.6a); it moves in the opposite direction when the same chamfer is applied to the top trailing edeg (Fig. 4.6b). As the wake is deformed from its original torus and the distance between the top and bottom shear layers is shortened, the size of the high fluctuation region is also reduced and a low fluctuation zone develops on the opposite side of the base. This is a direct consequence of the growth of the 'U' shaped horseshoe vortex developing close to the shear layer with the highest curvature. The role of the shear layers in determining the size and the position of the region with the highest values of $RMS(\Delta C_p)$ becomes even clearer when the low drag configuration is considered ($\phi_t = 12°$, $\phi_b = 12°$, Fig. 4.6c). In this case, the area with the highest level of fluctuation is shifted back to the middle of the base as in the square-back case, following the restoration of a symmetric condition between the two vortical recirculating structures. The reduced gap between the top and bottom shear layers, however, yields a reduction of the extension of this region as well as a decrease in the magnitude of the fluctuation, allowing the formation of a more 'stable' wake. Conversely, when the flow over the slanted surface is fully separated (as in the case of the $\phi_t = 0°$, $\phi_b = 20°$ configuration reported in Fig. 4.6d, for which high pressure fluctuations can be seen over the entire slant), the distance between the two horizontal shear layers is increased as a consequence of the reduced upwash, leading to a more 'open' and therefore bi-stable wake, as highlighted by the larger region of high $RMS(\Delta C_p)$ developing over the model base.

The tendency of the wake to switch between the two different states has been further investigated by looking at the 1^{st} POD mode extracted from the base pressure recordings as well as the two cross-flow PIV planes. Results for selected configurations are illustrated in Fig.

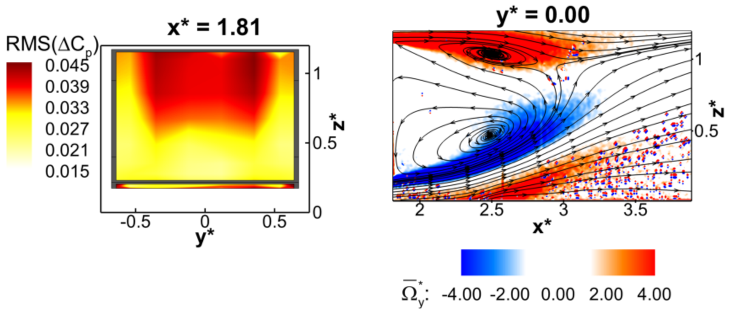

(a) $\phi_t = 0°$, $\phi_b = 16°$

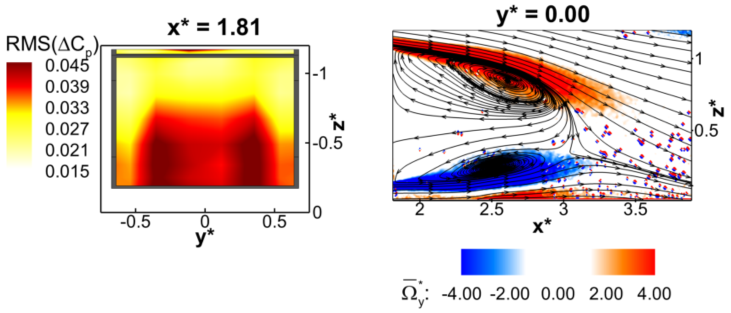

(b) $\phi_t = 16°$, $\phi_b = 0°$

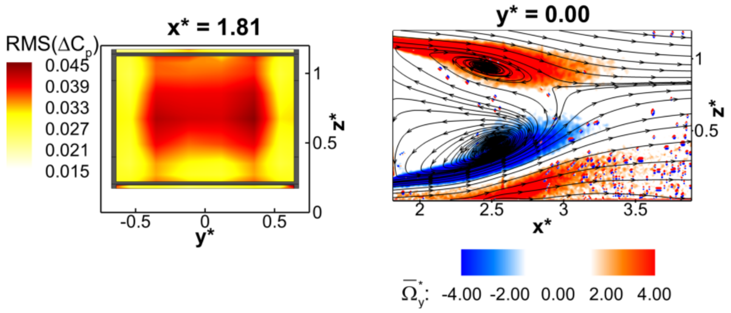

(c) $\phi_t = 12°$, $\phi_b = 12°$

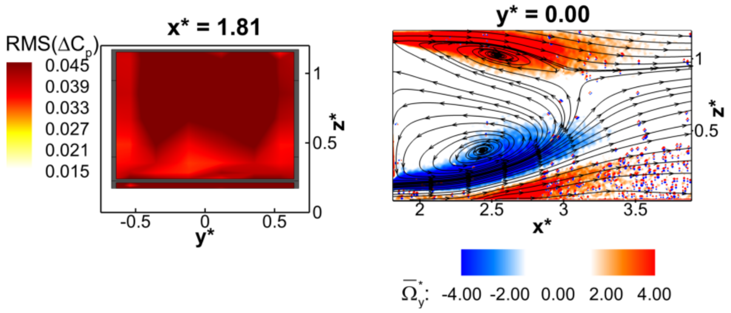

(d) $\phi_t = 0°$, $\phi_b = 20°$

Figure 4.6: Base pressure fluctuation and time averaged values of the lateral component of the vorticity $\tilde{\Omega}_y^*$ at $y^* = 0.00$ for: **a** low lift ($\phi_t = 0°$, $\phi_b = 16°$), **b** high lift, ($\phi_t = 16°$, $\phi_b = 0°$), **c** low drag ($\phi_t = 12°$, $\phi_b = 12°$) and **d** high drag ($\phi_t = 0°$, $\phi_b = 20°$) configuration.

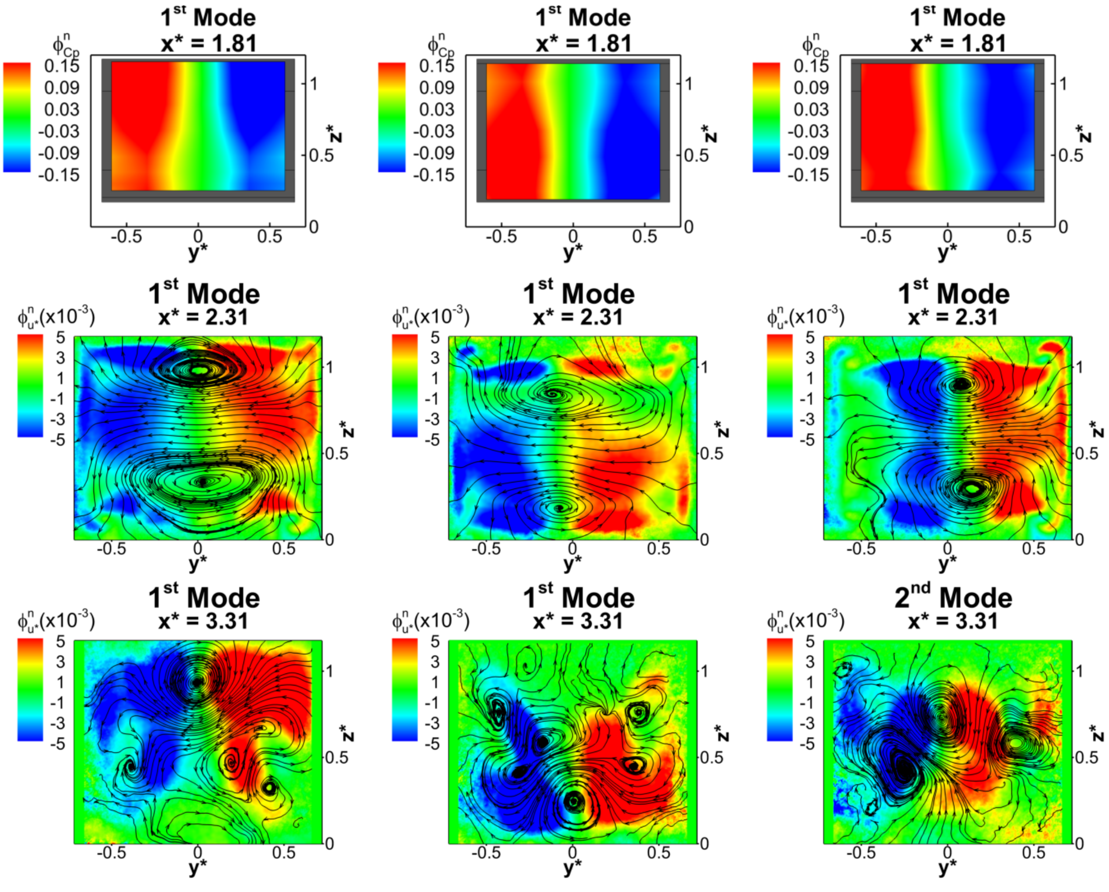

(a) $\phi_t = 0°$, $\phi_b = 12°$ **(b)** $\phi_t = 12°$, $\phi_b = 0°$ **(c)** $\phi_t = 12°$, $\phi_b = 12°$

Figure 4.7: Sensitivity of bi-stability to different taper angles (1): first POD spatial mode extracted from base pressure distribution (top row) and two different PIV planes, at $x^* = 2.31$ (central row) and $x^* = 3.31$ (bottom row), for **a** $\phi_t = 0°$, $\phi_b = 12°$; **b** $\phi_t = 12°$, $\phi_b = 0°$; **c** $\phi_t = 12°$, $\phi_b = 12°$. $\phi^n_{C_p}$ refers to the magnitude of the spatial eigen-modes extracted from the field of the pressure fluctuation. The eigen-functions related to the velocity fluctuation are coloured according to the values of the through plane component ϕ^n_{u*} whereas the streamlines are drawn considering the in-plane components ϕ^n_{v*} and ϕ^n_{w*}.

4.7 and 4.8. A strong similarity with that observed in Fig. 3.12a for the square-back case is seen. In all cases, the spatial functions obtained for the base pressure distribution as well as the velocity fields suggest the existence of a lateral symmetry breaking mode. Changes in the topology of this mode however can be seen as the balance between upwash and downwash is modified. The application of the small slants to the horizontal trailing edges tends to stabilise the shear layers by increasing the curvature of the streamlines bounding the rear recirculation (Liou, 1994). As such, the amount of reverse flow in the wake affected by the lateral instability is reduced. This is particularly visible when considering the 1^{st} POD mode from the pressure data (top row in Fig. 4.7) as well as the same mode extracted from the PIV plane at $x^* = 3.31$ (bottom row in Fig. 4.7). As in the square-back case, the spatial distributions obtained from the

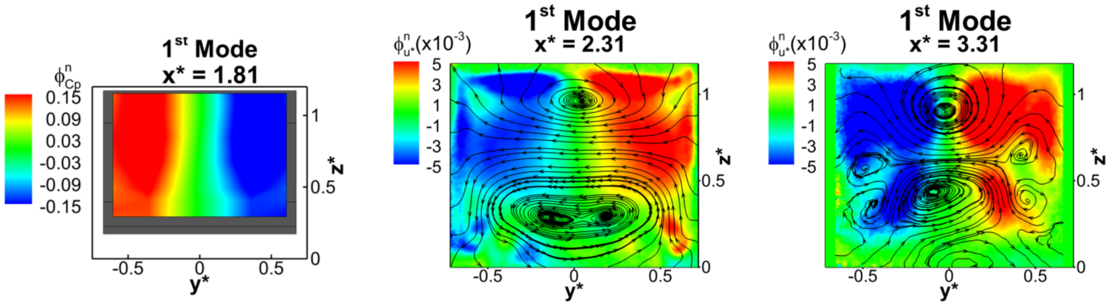

Figure 4.8: First POD spatial mode extracted from base pressure distribution (left column) and two different PIV planes, at $x^* = 2.31$ (central column) and $x^* = 3.31$ (right column), for $\phi_t = 0°$, $\phi_b = 20°$. $\phi^n_{C_p}$ refers to the magnitude of the spatial eigen-modes extracted from the field of the pressure fluctuation. The eigen-functions related to the velocity fluctuation are coloured according to the values of the through plane component $\phi^n_{u^*}$ whereas the streamlines are drawn considering the in-plane components $\phi^n_{v^*}$ and $\phi^n_{w^*}$.

pressure datasets closely match those previously seen for $RMS(\Delta C_p)$. This further confirms the fact that the lateral instability is the main source of the high level of unsteadiness on the model base. The 1^{st} mode alone, indeed, is able to capture between $\approx 58\%$ and $\approx 45\%$ of the overall fluctuating energy measured in all cases (Fig. 4.9a and 4.9d). Nevertheless, these values are seen to decrease as the wake tends towards one single laterally symmetric state. This can be seen by examining the plots presented in Fig. 4.9a, referring to the pressure fields obtained from a sweep of the bottom slant with a squared top trailing edge. It is shown that, as the level of upwash is increased, the energy content of the first mode drops, suggesting the formation of a more stable wake. However, when separation occurs at the bottom slant, the energy level grows again. The stabilising effect of the upwash can also be inferred from the change in shape of the PDFs referring to the values of the temporal coefficients related to the same mode (Fig. 4.9b). As the bottom chamfer angle is increased, the PDFs gradually change, moving from a bi-modal distribution towards a single near zero value, as one of the two states becomes more probable.

The results presented in Fig. 4.9 were obtained performing POD analysis on datasets recorded using two scanners (§2.4). The same trends, however, is observed when the same analysis is performed considering a coarser grid of tappings (thus requiring one scanner). This is the case of the results presented in Fig. 4.10a. Some differences are seen in the absolute values recorded with the two setups, as for example in the case of the energy content of the 1^{st} POD mode. These discrepancies are to be ascribed to the differences in spatial resolution. A coarser grid is less sensitive to localised fluctuations (that would be captured only by higher order modes) than a finer grid. As a consequence, only the most coherent motions are captured (i.e. low order modes) and their contribution to the overall fluctuating energy appears to be higher. This is not a limitation in the present study, being its focus on the global (and therefore most coherent) modes.

An additional way to quantify the degree of bi-stability was found in the estimation of the

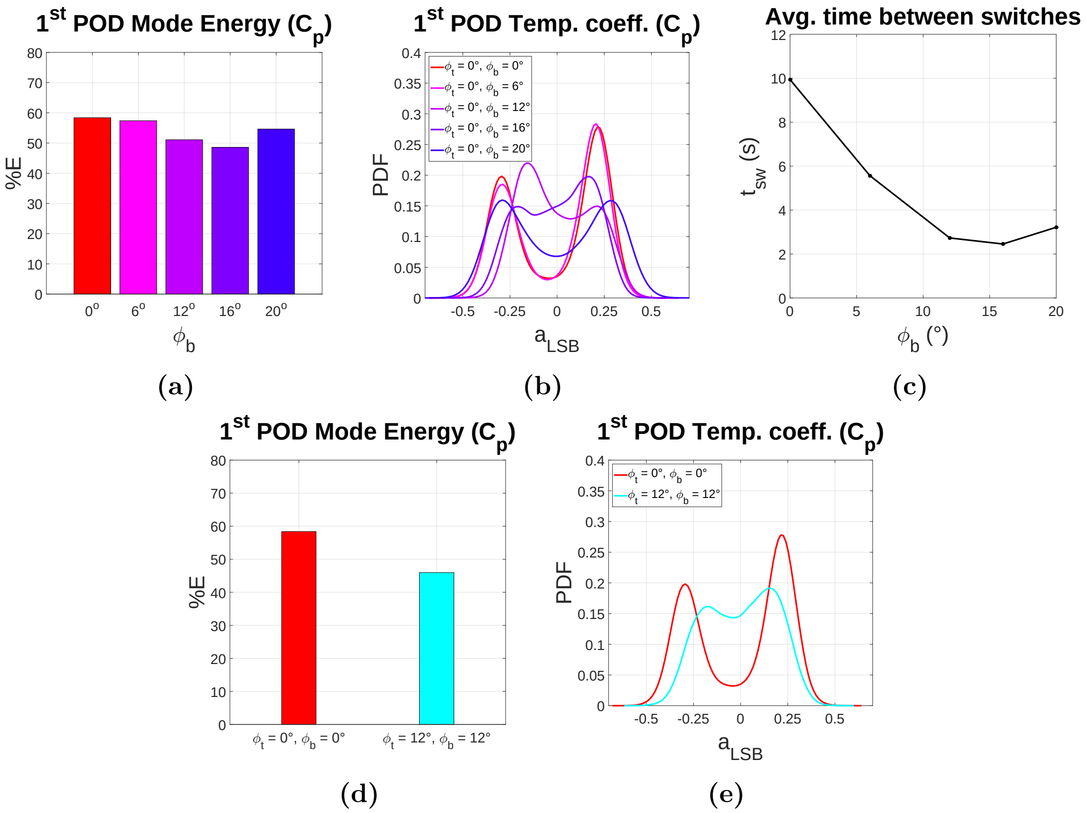

(a) (b) (c)

(d) (e)

Figure 4.9: Sensitivity of bi-stability to different taper angles (2): **a** fluctuating energy captured by the 1st POD mode; **b** PDFs for the temporal coefficient related to the same mode; **c** averaged time between switches. **d** fluctuating energy captured by the same POD mode obtained for the square-back and the low drag configurations; **e** PDFs of the values of the 1st POD temporal mode for the same two cases. Base pressure data recorded using two scanners (see §2.4).

average time between switches (t_{sw}), calculated following the same procedure used in §3.2.3 for the square-back case. As shown in Fig. 4.9c, a reduction of t_{sw} is observed indeed when a bottom taper is applied to the model (suggesting a weakening of the bi-stable mode). A minimum of $t_{sw} = 2.46\,s$ is obtained for the low lift configuration ($\phi_t = 0°$, $\phi_b = 16°$). The value of t_{sw} then grows again once the flow over the bottom slant becomes fully separated.

Besides the lateral symmetry breaking mode, the asymmetry seen in the vertical direction in the case of an upwash or downwash dominated wake yields also changes in the topology of the symmetry preserving mode (Fig. 4.11b). In this case, in fact, only the vertical plane of symmetry is preserved. This is particularly visible when looking at the pressure distribution over the model base as well as the velocity field at $x^* = 3.31$. The energy content of the mode is also reduced, when compared to its counterpart extracted from the square-back case (Fig. 4.10a). A change is also seen in the way the symmetry preserving mode interacts with the lateral symmetry breaking mode. Considering, for example, the case with $\phi_t = 0°$ and $\phi_b = 12°$,

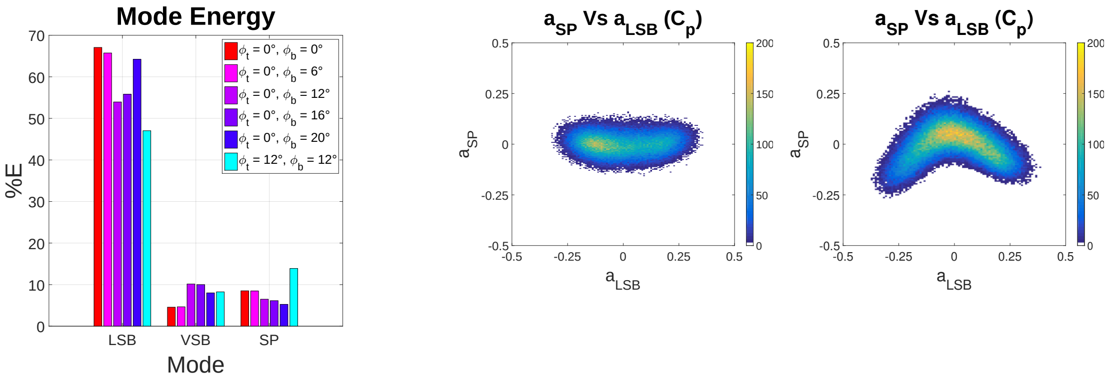

(a) **(b)** **(c)**

Figure 4.10: **a** energy levels associated with the *LSB*, *VSB* and *SP* modes extracted from the base pressure data of some of the tested configurations; **b** and **c** scatter plots of the temporal coefficients associated with the *SP* and *LSB* POD modes extracted from the base pressure data recorded for $\phi_t = 0°$, $\phi_b = 12°$ **(b)** and $\phi_t = 12°$, $\phi_b = 12°$ **(c)**.

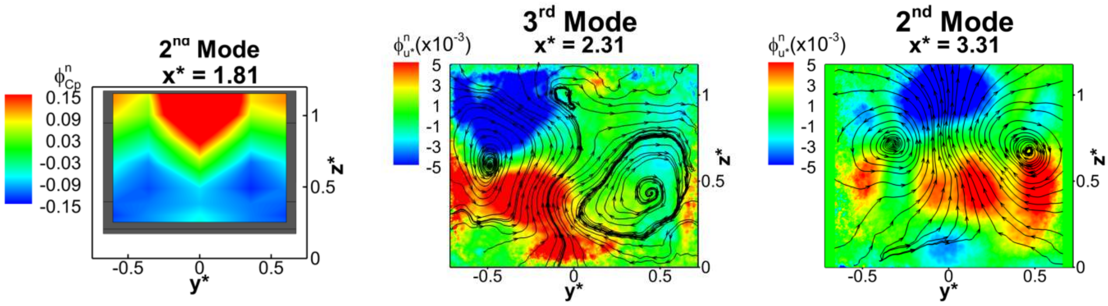

(a) VSB Mode

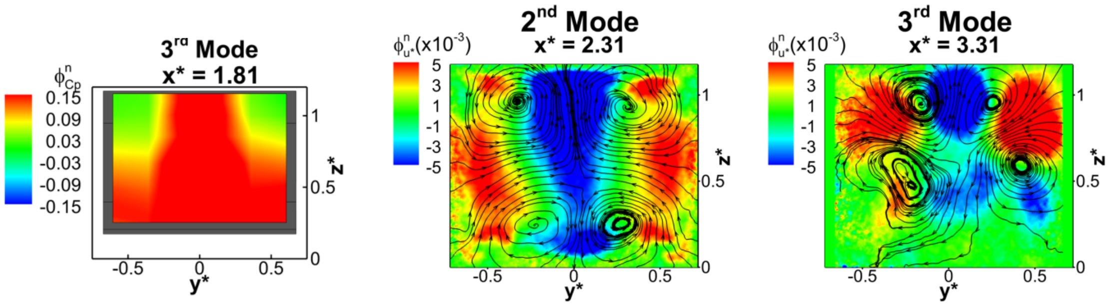

(b) SP Mode

Figure 4.11: Vertical symmetry breaking mode (*VSB*, **a**) and symmetry preserving mode (*SP*, **b**) for $\phi_t = 0°$, $\phi_b = 12°$. From left to right: base pressure distribution, PIV cross-plane at $x^* = 2.31$, PIV cross-plane plane at $x^* = 3.31$. $\phi^n_{C_p}$ refers to the magnitude of the spatial eigen-modes extracted from the field of the pressure fluctuation. The eigen-functions related to the velocity fluctuation are coloured according to the values of the through plane component ϕ^n_{u*} whereas the streamlines are drawn considering the in-plane components ϕ^n_{v*} and ϕ^n_{w*}.

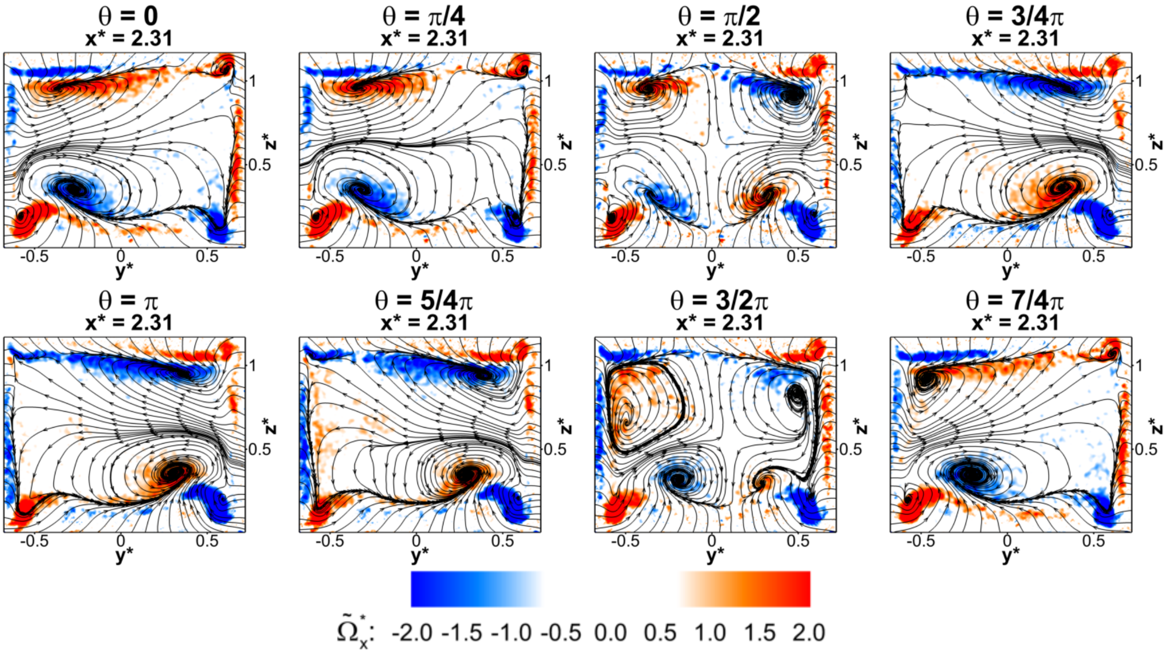

Figure 4.12: Low order phase averaged velocity field at $x^* = 2.31$, for $\phi_t = 0°$, $\phi_b = 12°$. The plots are coloured according to the values of the normalised axial component of the vorticity $\tilde{\Omega}_x^*$; the streamlines are drawn considering the in-plane components of the velocity field.

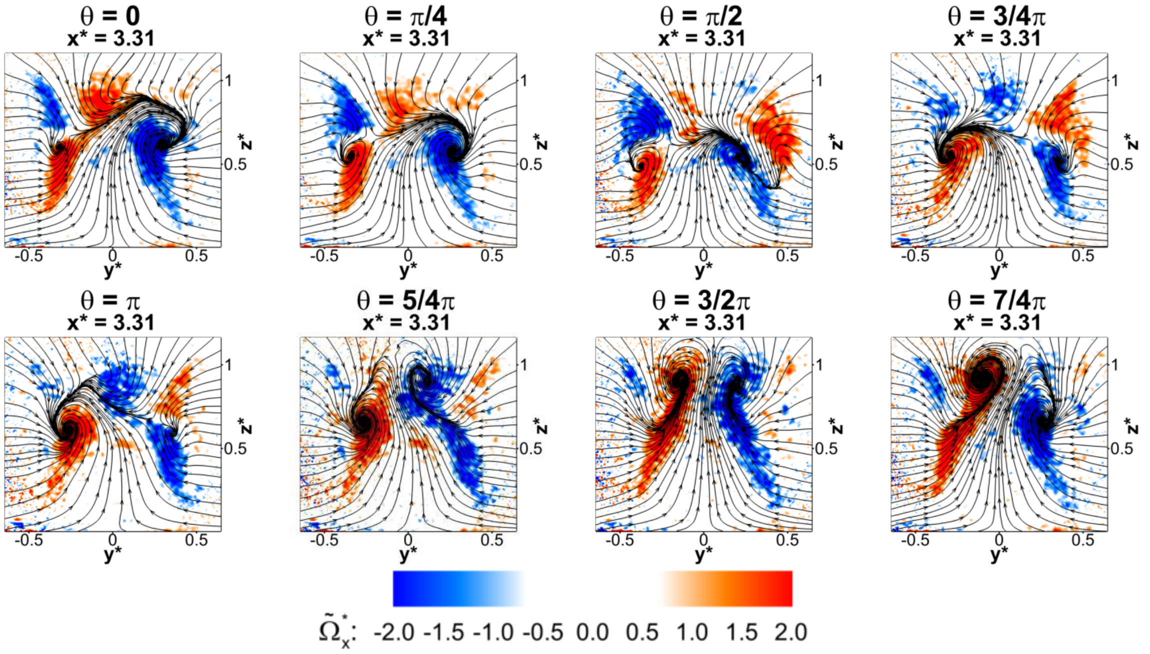

Figure 4.13: Low order phase averaged velocity field at $x^* = 3.31$, for $\phi_t = 0°$, $\phi_b = 12°$. The plots are coloured according to the values of the normalised axial component of the vorticity $\tilde{\Omega}_x^*$; the streamlines are drawn considering the in-plane components of the velocity field.

the scatter plot between the values of a_{SP} and a_{LSB} (Fig. 4.10b) is in this case much ‘flatter’ than that discussed in §3.2.5 for the square-back configuration. As such, identifying a particular arrangement of the vortical structures between the spanwise and streamwise directions, every time a switch between bi-stable states occurs, becomes more difficult.

An opposite trend is observed instead in the energy content of the vertical symmetry breaking mode. The shape of this mode (Fig. 4.11a) does not undergo significant changes compared to that seen in Chap. 3, apart from a slight lateral asymmetry visible in the PIV field at $x = 2.31^*$, arguably due to a not perfect alignment between the model and the direction of the onset flow when the test was performed (Evrard et al, 2016). Nevertheless, the contribution of this mode to the overall fluctuating energy is seen to increase with ϕ, until the flow over the slant becomes fully separated or the symmetry of the wake in the vertical direction is restored (Fig. 4.10a).

A phase averaged low order model was then built considering the time averaged field and the three POD modes described above, following the same approach discussed in §3.2.5. The result obtained for the model with $\phi_t = 0°$ and $\phi_b = 12°$ are presented in Fig. 4.12 and Fig. 4.13 for the PIV cross-planes respectively at $x^* = 2.31$ and $x^* = 3.31$. As for the square-back case, four main states can be isolated: the two lateral symmetry breaking bi-stable states (at $\theta = 0 rad$ and $\theta = \pi rad$) and two lateral symmetry preserving states (at $\theta = \pi/2 rad$ and $\theta = 3/2\pi rad$). Unlike the square-back case, however, a predominance of the bottom recirculation is always seen in both lateral symmetry breaking states and no downwash dominated lateral symmetry preserving state can be observed. Furthermore, a clear difference is seen in the strength of the two counter-rotating vortices developing downstream of the wake closure, every time one of the two bi-stable states is selected. An explanation for this disparity can be found in the topology proposed in §3.2.3 for each lateral symmetry breaking state. When one of the two states is selected, the size of streamwise vortex seen at $x^* = 3.31$, on the side opposite to that of the base where the asymmetry develops, increases. This is due to the fact that this vortex is now the result of the merger between two distinct vortical structures; the tail of the hairpin vortex described in §3.2.3 and the vortex developing at the tip of the slant placed on the same side where the stronger vortex is seen (as sketched in Fig. 4.20c).

A further attenuation of the bi-stable behaviour is noted when the low drag configuration is considered. In this case, the tendency toward the selection of one single symmetric state is highlighted by a further drop in the energy captured by the 1^{st} POD pressure mode (Fig. 4.9d) as well the flatter shape that characterises the PDF obtained for the values of $a_{LSB}(t)$ (Fig. 4.9e). Nevertheless, as for the bottom taper sweep, the left-to-right asymmetry can still be observed (Fig. 4.7c). No particular changes are seen in the topology of the vertical symmetry breaking mode either (Fig. 4.14a). The restoration of the symmetry in the vertical direction in the time averaged pressure and velocity fields (Fig. 4.3b) is highlighted by the fact that, as in the square-back case, two orthogonal planes of symmetry can now be observed in the contour plots of the spatial functions referring to the symmetry preserving POD mode (Fig. 4.14b).

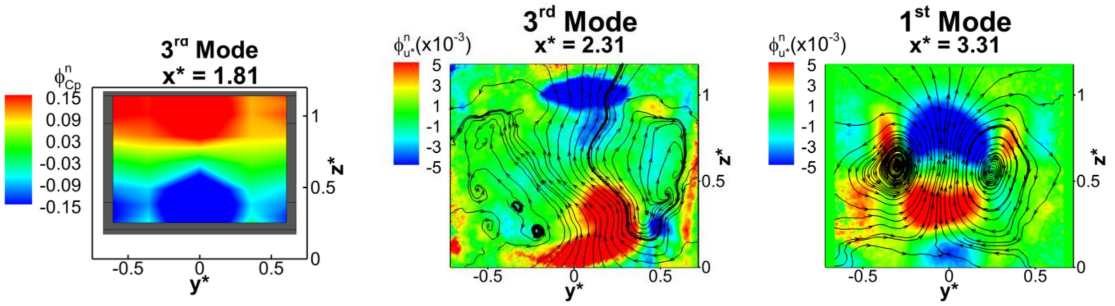

(a) VSB Mode

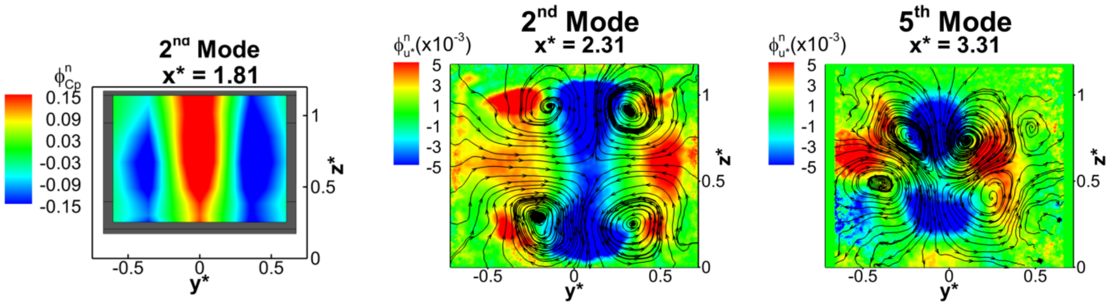

(b) SP Mode

Figure 4.14: Vertical symmetry breaking mode (VSB, **a**) and symmetry preserving mode (SP, **b**) for $\phi_t = 12°$, $\phi_b = 12°$. From left to right: base pressure distribution, PIV cross-plane at $x^* = 2.31$, PIV cross-plane plane at $x^* = 3.31$. $\phi^n_{C_p}$ refers to the magnitude of the spatial eigen-modes extracted from the field of the pressure fluctuation. The eigen-functions related to the velocity fluctuation are coloured according to the values of the through plane component $\phi^n_{u^*}$ whereas the streamlines are drawn considering the in-plane components $\phi^n_{v^*}$ and $\phi^n_{w^*}$.

This coincides with an increase in the energy content of the same mode (Fig. 4.10a). Unlike that seen for square-back case, however, the points of the scatter plot between a_{SP} and a_{LSB} appear to be clustered around one single attractor at $a_{SP} \approx a_{LSB} \approx 0$ (Fig. 4.10c). This is a direct consequence of the disappearing of the bi-modal distribution in the PDF of the values of a_{LSB} (Fig. 4.9e). As a result, the wake tends to deviate less from the lateral symmetry preserving state, as can be noticed by looking at the evolution of the phase averaged low order model obtained for the PIV data acquired at $x^* = 2.31$ (Fig. 4.15). Indeed, the deviation from the laterally symmetric state over different values of the phase angle θ is much less evident that that seen in either Fig. 3.24 or Fig 4.12. This state appears to be more symmetric with respect to the horizontal plane too. The fact that in this case there is a clear disparity between the two lateral symmetry breaking states (i.e. the number of vortical structures seen in dead water region drops from four to two only in the case of the *L State*) is to be ascribed to the presence of small residual asymmetries in the experimental setup that was not possible to remove within the tolerances of the instrumentation available.

From that written so far, it is clear that horizontal trailing edge tapering tends to stabilise the lateral symmetry preserving state while shortening the length of the rear recirculation.

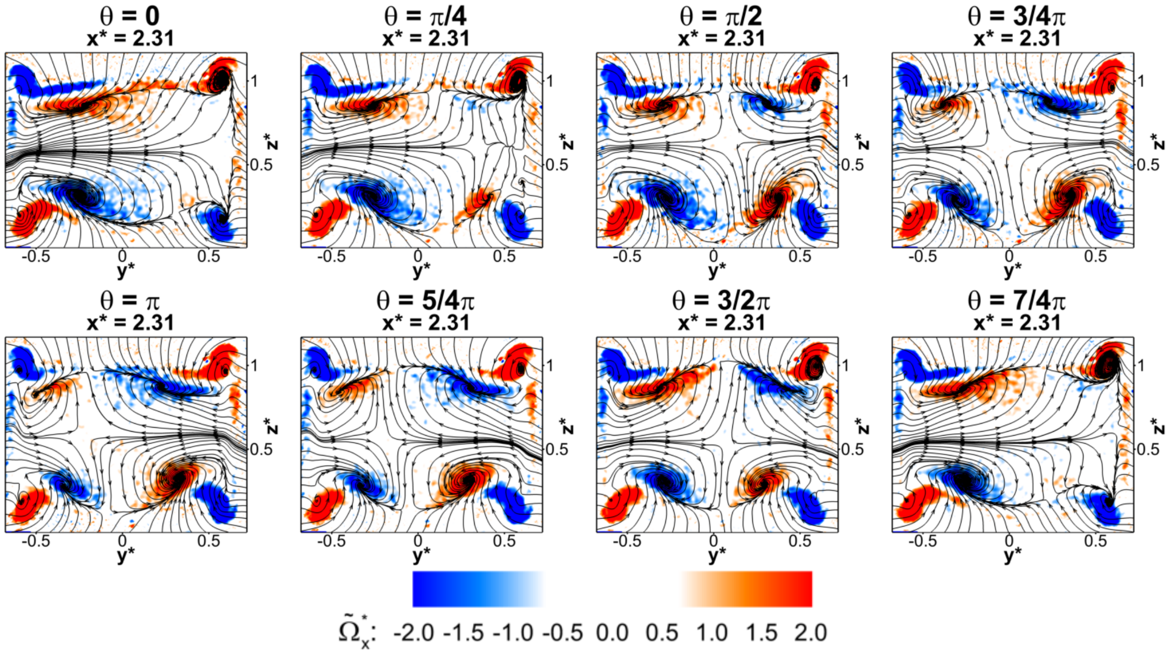

Figure 4.15: Low order phase averaged velocity field at $x^* = 2.31$, for $\phi_t = 12°$, $\phi_b = 12°$. The plots are coloured according to the values of the normalised axial component of the vorticity $\tilde{\Omega}^*_x$; the streamlines are drawn considering the in-plane components of the velocity field.

Although it should be clear at this point that a connection between these two elements exists (i.e. a 'more open', and therefore longer, wake is more affected by bi-stability and vice versa) this is not a sufficient condition for achieving a drag reduction. $\overline{C}_D$ is seen to decrease in fact only when this action is paired with the restoration of the symmetry in the vertical direction, as in the case of the configuration with $\phi_t = \phi_b = 12°$. In the plot presented in Fig. 4.5c, the values of $\overline{w^*_{Wall}}$ associated with this configuration and the square-back configuration are both in the region corresponding to the lowest wall velocity ($\overline{w^*_{Wall}} < 0.02$), indicating a comparable level of symmetry in the vertical direction between the two cases. However, the former configuration yields a $\approx 3.3\%$ reduction in $\overline{C}_D$ over the latter and it is characterised by a shorter as well as 'more stable' wake. As known from the literature, however, a shortening of the wake length does not necessarily yields a base drag reduction. In fact, for bluff bodies with blunt trailing edges, it has be shown that a decrease in the recirculation length is always accompanied with an increase in the suction acting over the base. This applies to 2D geometries (Bearman (1965), Parezanović and Cadot (2012)) as well as 3D shapes (Mariotti et al (2015) and Barros et al (2016)), but not necessarily to the case of geometries with symmetric boat tailing (Khalighi et al (2012), Mariotti et al (2017)). On the other hand, the results presented in Chap. 3 seem to suggest that limiting the bi-stable behaviour while keeping the symmetry in the vertical direction might have a positive effect on the rear drag. Further evidence to support this thesis has been obtained by applying to this case the same approach, based on a low order model,

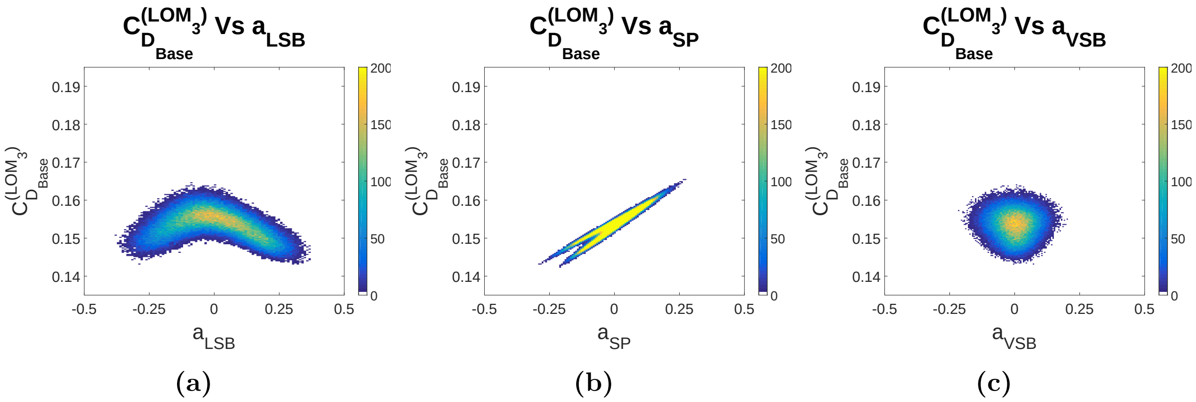

Figure 4.16: Scatter plots between the unsteady values of the base drag obtained from the low order model $C_{D_{Base}}^{(LOM_3)}(t)$ and the temporal coefficients associated with the first three POD pressure modes for the configuration with $\phi_t = \phi_b = 12°$: **a** $C_{D_{Base}}^{(LOM_3)}(t)$ Vs $a_{LSB}(t)$; **b** $C_{D_{Base}}^{(LOM_3)}(t)$ Vs $a_{SP}(t)$; **c** $C_{D_{Base}}^{(LOM_3)}(t)$ Vs $a_{VSB}(t)$. The colour map shows the PDF of the values of the considered coefficients.

already employed in §3.2.5.1 for assessing the links between the evolution of the base drag $C_{D_{Base}}^{(LOM_3)}(t)$ and the three most energetic POD modes extracted from the base pressure dataset. The results, in the form of scatter plots between $C_{D_{Base}}^{(LOM_3)}(t)$ and $a_{LSB}(t)$, $a_{SP}(t)$ and $a_{VSB}(t)$ respectively, are presented in Fig. 4.16. Unlike that seen for the square-back case, a weaker relationship is observed between $C_{D_{Base}}^{(LOM_3)}(t)$ and the lateral symmetry breaking mode $a_{LSB}(t)$ (Fig. 4.16a). The range of variation of the values of the base drag estimated using the low order model is indeed much narrower than that reported for the square-back case (Fig. 3.26a), as a consequence of the fact that the wake is more stable. The same conclusions can be extended to the scatter plot between $C_{D_{Base}}^{(LOM_3)}(t)$ and the symmetry preserving mode $a_{SP}(t)$ (Fig. 4.16b), whilst no particular trend can be observed in the scatter plot between $C_{D_{Base}}^{(LOM_3)}(t)$ and the vertical symmetry breaking mode $a_{VSB}(t)$. In all three scatter plots reported in Fig. 4.16 the points tend to cluster around $C_{D_{Base}}^{(POD)} \approx 0.155$, which is in line with the base drag value estimated in §3.2.5.1 for the lateral symmetry preserving state. This value represents a $\approx 8\%$ improvement over the square-back case. The fact that the gain in terms of overall drag reduction (ΔC_D) is a more modest -3.3% is to be ascribed to the detrimental contribution of the pair of longitudinal vortices developing at the tip of each slant, that leads to an increase of the vortex drag term in Eq. 1.27. This agrees with that already noticed in Grandemange et al (2013c) and Grandemange et al (2015). In the same plots, however, it also appears that an even lower value of base drag ($C_{D_{Base}}^{(POD)} < 0.150$) may be achieved by slighly destabilising the wake. This is a consequence of the fact that, as already explained in §4.1, the time averaged base pressure distribution is dominated in this case by the suction zones created by the transverse vortices developing close to the model vertical trailing edges. The contribution of these structures is well captured by the symmetry preserving mode, whose shape in terms of pressure variation strongly resembles the time averaged pressure map shown in Fig. 4.3b. The contribution of these zones is mitigated when negative values of $a_{SP}(t)$ are considered. This, however, leads to the selection of one of the two lateral symmetry breaking states, being in such conditions $a_{LSB}(t) \neq 0$ (Fig. 4.10c). This is not in contradiction with that stated in §3.2.5. A drag reduction indeed is obtained when the wake recovers its lateral symmetry because of two different contributions: the vortical structures are moved further downstream from the base and the amount of flow impinging on the base is maximised. In the case considered here, is the exploitation of only the latter contribution that yields a drag reduction. Therefore, a further improvement may be obtained by increasing the distance between the vortical structures seen in the plane at $z^* = 0.67$ (Fig. 4.3b) and the model base.

4.2.2 Short-time wake dynamics

The three most energetic POD modes have been also used to gather information on the effects of horizontal trailing edge tapering on the short-time wake dynamics. A valuable contribution is given by the spectral content of the temporal coefficients extracted from the pressure dataset, as can be seen in the PSD plots presented in Fig. 4.17 for some of the tested configurations. Considering the first coefficient (a_{LSB}, Fig. 4.17a), an increase in the angle of the bottom chamfer, besides weakening the bi-stable mode (as discussed in §4.2.1), leads also to a reduction of the lateral flapping. Indeed, the peak associated with this mode (at $St_H = 0.13$) tends to become shallower as ϕ_b is increased. At the same time, the characteristic frequency of this mode is seen to increase, ranging from $St_H = 0.13$ for the square-back configuration up to $St_H = 0.17$ for the model with $\phi_t = 0°$ and $\phi_b = 16°$. A drop in frequency is observed only when the flow over the slant becomes fully separated ($\phi_b = 20°$). In these conditions, the height of the peak associated with this motion is also increased. A second, much broader, hump is seen at low frequency in the case of the low drag configuration. This hump appears to be centred around $St_H = 0.03$ and may be linked with the short average time between switches characteristic of this case, suggesting that a ‘less bi-stable’ wake (that tends to deviate less from the symmetric state) is also a ‘faster’ wake (with a shorter time between switches), in line with that already pointed out by Evrard et al (2016).

Unlike the lateral flapping case, the application of a taper to at least one of the two horizontal trailing edges appears to reinforce the vertical flapping motion of the wake. This is evident in the plot presented in Fig. 4.17b, related to the PSD of the temporal coefficients associated with the vertical symmetry breaking mode. When a taper is applied to the bottom trailing edge, while keeping the top edge squared, the peak seen for the square-back case at $St_H = 0.19$ becomes more and more pronounced as ϕ_b is increased, until full separation occurs over the slanted surface. A shift in frequency is also seen in these conditions, as the peak moves from $St_H = 0.19$ for $\phi_t = 0°$, $\phi_b = 0°$ to $St_H = 0.22$ for $\phi_t = 0°$, $\phi_b = 16°$, and then it goes back to $St_H = 0.20$ for $\phi_t = 0°$, $\phi_b = 20°$. The highest frequency (at $St_H = 0.24$) has been recorded for

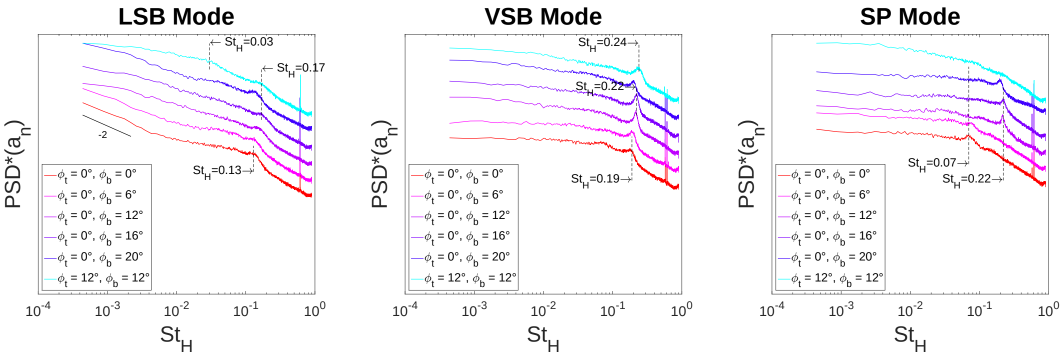

(a) **(b)** **(c)**

Figure 4.17: Spectra of the POD temporal coefficients associated with the lateral symmetry breaking mode (LSB, **a**), the vertical symmetry breaking mode (VSB, **b**), the symmetry preserving mode (SP, **c**). The curves have been shifted along the vertical axis.

the $\phi_t = 12°$, $\phi_b = 12°$ configuration, arguably due to the fact that in this case the top and bottom shear layers are both 'actively' contributing to the vertical flapping. A similar trend was reported by Kowata et al (2008) and Tunay et al (2014), investigating respectively the effects of different underbody slant angles and roof slants angles on the wake of an Ahmed body without wheels. As pointed out by Luo et al (1994), the shift in the values of St_H is to be ascribed to the increase in the level of interaction between the top and bottom shear layers as the distance between them is reduced by the upwash\downwash generated by the slanted surfaces. This also explains the shortening of the recirculation length seen in §4.1, in agreement with trend seen by Roshko (1954) studying 2D geometries.

In some cases the vertical flapping becomes so strong that its presence can also be noted in the PSD of the temporal coefficients related to the symmetry preserving mode (Fig. 4.17c). This coincides with the loss of the horizontal plane of symmetry in the spatial functions related to the same mode, as already discussed in §4.2.1. In the same conditions, the peak at $St_H = 0.07$ associated with the wake pumping (§3.2.4) is seen to disappear too. An exception to this trend may be represented by the low drag configuration, for which hardly any peaks are visible.

The trends observed in the PSD plots related to the three most energetic POD modes are confirmed when coherence analysis, between signals recorded by taps placed in different locations along the model trailing edges, is performed, following the approach already described in §2.4.2. For the sake of simplicity, only the results referring to two different configurations (namely those with $\phi_t = 0°$, $\phi_b = 12°$ and $\phi_t = 12°$, $\phi_b = 12°$) will be discussed. The results are presented in Fig. 4.18 and Fig. 4.19 respectively.

A strong peak at $St_H = 0.22$ is seen in the first case. This peak appears to be linked with the vertical flapping motion of the wake, as suggested by the out-of-phase variations of pressure recorded by taps located close to the top and bottom trailing edges of the model (Fig. 4.18a) and the in-phase variations seen when taps placed on either side of the model base are

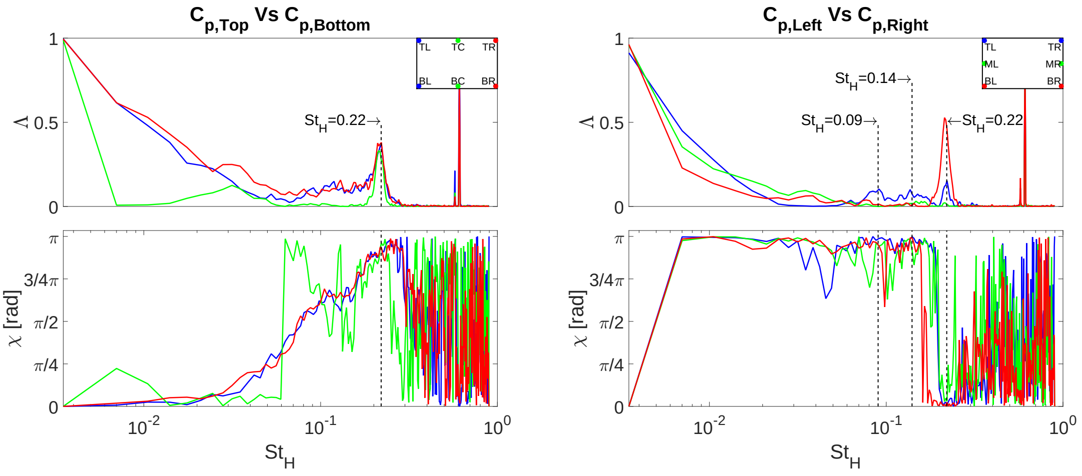

(a) **(b)**

Figure 4.18: Coherence analysis performed considering the configuration with $\phi_t = 0°$, $\phi_b = 12°$. The unsteady signal was recorded by pressure taps placed at different locations along the trailing edges of the model base: **a** top-left tap Vs bottom-left tap, top-centre tap Vs bottom-centre tap, top-right tap Vs bottom-right tap; **b** top-left tap Vs top-right tap, mid-left tap Vs mid-right tap, bottom-left tap Vs bottom-right tap.

considered (Fig. 4.18b). Similar trends were reported by Vino et al (2005), although at higher frequency due to the larger slant considered in that case. Another two peaks can be seen in the plot presented in Fig. 4.18b, respectively at $St_H = 0.09$ and $St_H = 0.14$. Both peaks are associated with out-of-phase pressure variations and are visible only in the spectrum referring to the correlation between the uppermost pair of taps, top-left tap (TL) Vs top-right tap (TR) in Fig. 4.18b. The first peak can be related to the wake pumping whilst the second peak is likely to be caused by the lateral flapping. The fact that these motions are now limited to the upper portion of the wake is in good agreement with that found by McArthur et al (2016) in the case of upwash dominated wakes and further confirms the stabilising effect of horizontal trailing edge tapering (at least as far as the lateral and longitudinal motions of the wake are concerned).

Similar considerations can be extended to the results obtained from the coherence analysis performed considering the low drag configuration (Fig. 4.19). In this case, the peak corresponding to the pumping motion is no longer visible, confirming that reported from the analysis of the POD modes. A (small) peak related to the lateral flapping can still be seen in the correlation between the mid-left (ML) and mid-right (MR) taps. An additional correlation peak is observed at $St_H = 0.025$ for all pairs of taps considered but the TC-BC (top-centre, bottom-centre) pair. The correlation peaks at this frequency are associated with out-of-phase pressure variations between the two vertical sides of the model and in-phase pressure variations between the top and bottom trailing edges, further confirming the fact that this frequency is indeed related to

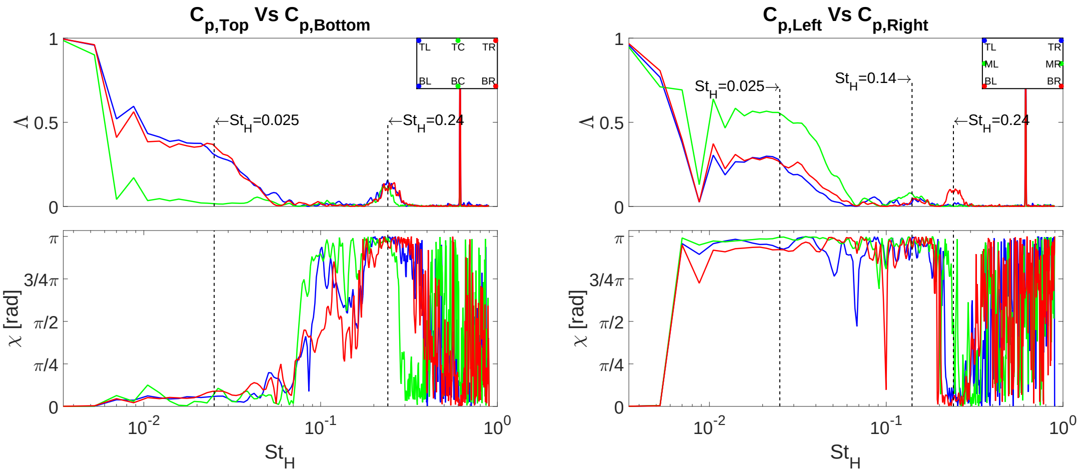

(a) **(b)**

Figure 4.19: Coherence analysis performed considering the configuration with $\phi_t = 12°$, $\phi_b = 12°$. The unsteady signal was recorded by pressure taps placed at different locations along the trailing edges of the model base: **a** top-left tap Vs bottom-left tap, top-centre tap Vs bottom-centre tap, top-right tap Vs bottom-right tap; **b** top-left tap Vs top-right tap, mid-left tap Vs mid-right tap, bottom-left tap Vs bottom-right tap.

the characteristic time of the lateral symmetry breaking mode for this configuration.

Additional information on the spatial location of the coherent motions described above has been gathered by performing single point velocity measurements. The multi-hole pressure probe described in §2.6 was used for these tests. The probe was located close to the top shear layer at two different locations, $x_B^* = 1/3$ and $x_B^* = 4/3$ with x_B^* indicating the non dimensional distance from the model base. The results related to the PSD of the vertical component of the velocity signal are presented in Fig. 4.20, with the black continuous line referring to the turbulent decay rate predicted by the Kolmogorov theory (see §1.1.3). At $x_B^* = 1/3$ (Fig. 4.20a), the wake is dominated by the characteristic frequency of the pumping motion (at $St_H = 0.07$) and the Kelvin-Helmholtz instability (at $St_H \approx 1$). The pumping motion, however, is not always visible. The peak at $St_H = 0.07$ is not seen when a strong upwash is present, as for $\phi_t = 0°$, $\phi_b = 16°$ and it is barely visible in the $\phi_t = 12°$, $\phi_b = 12°$ case. This is a consequence of the increased curvature of the shear layers that, besides weakening the bi-stable mode as already stated in §4.2.1, tends also to suppress the fluctuation in the longitudinal direction. Similar results were also reported by Khalighi et al (2012) applying symmetric boat tailing to all four edges of a similarly shaped body. In that case, however, a weakening of the flapping motion was also reported. Moving further downstream of the base, at $x_B^* = 4/3$ (Fig. 4.20b), the only peak the stands out in the PSD plot is that one corresponding to the frequency characteristic of the vertical flapping. The trend previously seen in the POD modes is indeed confirmed. An increase in upwash leads to a shift in the location of the peak from $St_H = 0.19$ for the square-back case

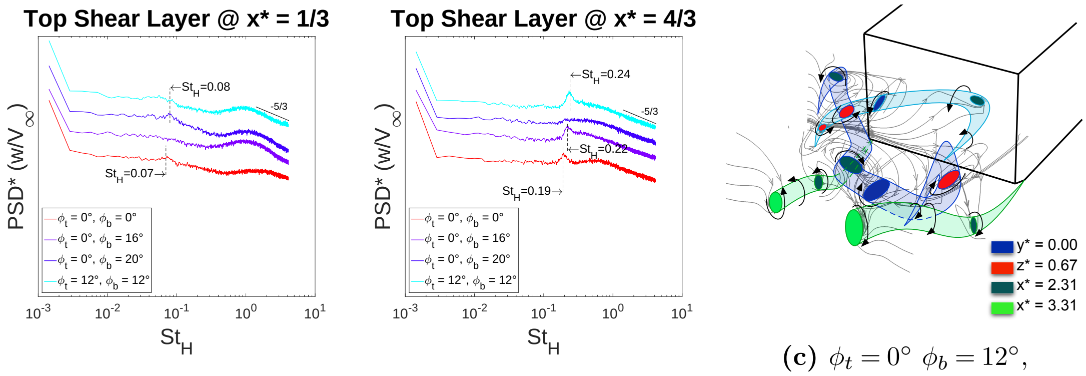

(a) **(b)** **(c)** $\phi_t = 0°$ $\phi_b = 12°$, L State

Figure 4.20: Spectra of the vertical component of the velocity probed at two different streamwise locations downstream of the model base: **a** $x^*_B = 1/3$; **b** $x^*_B = 4/3$. **c** proposed structure for one of the two bi-stable states in the presence of a strong upwash. In **a** and **b** the curves have been shifted along the vertical axis.

up to $St_H = 0.22$ for the low lift configuration ($\phi_t = 0°$, $\phi_b = 16°$), until reaching a maximum at $St_H = 0.24$ for $\phi_t = \phi_b = 12°$. A noticeable drop in both the magnitude of the peak and its frequency is seen when the flow over the bottom slant becomes fully separated ($\phi_t = 0°$, $\phi_b = 20°$).

The link between the bi-stable reflectional symmetry breaking mode and the vertical flapping motion has been further investigated considering the magnitude of the coherence between signals recorded by a tap placed in correspondence to either the left-hand side or the centre of the top trailing edge and all the remaining taps located on the base, at the vertical flapping frequencies previously isolated. The results are shown in Fig. 4.21. For the square-back case, the vertical flapping appears to be one-sided, since a good level of correlation is observed at $St_H = 0.19$ only when taps placed on the same side of the base are considered (Fig. 4.21a). This confirms that already seen in the two-point correlation discussed in §3.2.4 and fits with the structure proposed in §3.2.3 for each bi-stable state. This instability, in fact, seems to correspond with the portion of the hairpin vortex that extends further downstream from the base. Nevertheless, when the long-time instability is weakened and the wake is forced into a more laterally symmetric state, as in the case of the model with $\phi_t = 0°$ and $\phi_b = 12°$, the vertical flapping is seen to involve the entire span of the model. In these conditions, a good level of coherence is observed at $St_H = 0.22$ across the upper and the lower portions of the base (Fig. 4.21b), having considered the signal recorded by either the top-left tap or top-centre tap in Eq. 2.19. A schematic representation of this process is presented in Fig. 4.20c, having isolated one of the two lateral symmetry breaking states. The results obtained for the configuration with $\phi_t = \phi_b = 12°$, appears to be a hybrid between these two cases (Fig. 4.21c). The vertical flapping appears to be a one-sided motion when the correlation is performed considering the top-left tap. On the other hand, it seems to develop in the spanwise direction when the top-centre tap is considered. This apparent

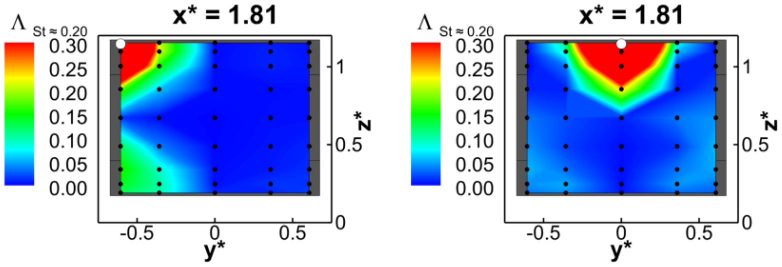

(a) $\phi_t = 0°$, $\phi_b = 0°$

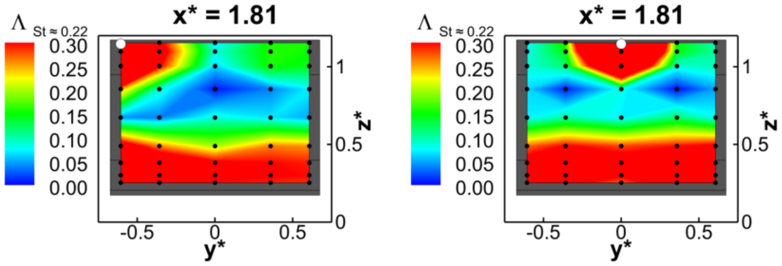

(b) $\phi_t = 0°$, $\phi_b = 12°$

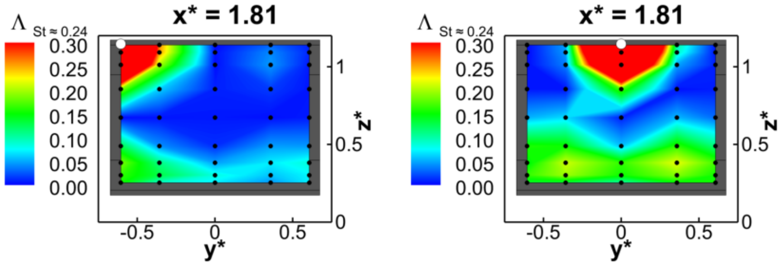

(c) $\phi_t = 12°$, $\phi_b = 12°$

Figure 4.21: Contour maps showing the coherence magnitude between the signal recorded by either the top-left tap (top row) or the top-centre tap (bottom row) and all the remaining taps on the base at the vertical flapping frequency: **a** $\phi_t = 0°$, $\phi_b = 0°$; **b** $\phi_t = 0°$, $\phi_b = 12°$; **c** $\phi_t = 12°$, $\phi_b = 12°$.

contradiction becomes clearer when looking at the wake topology proposed in Fig. 4.4b. The one-sided motion may be caused by the transverse vortices forming at either side of the model whereas the spanwise motion may be the result of the interactions between the top and bottom vortical structures. All these elements seem to suggest the existence of a stronger dependence of this unsteady global mode on the degree of lateral asymmetry in the wake than that suggested, for example, in Grandemange et al (2013b).

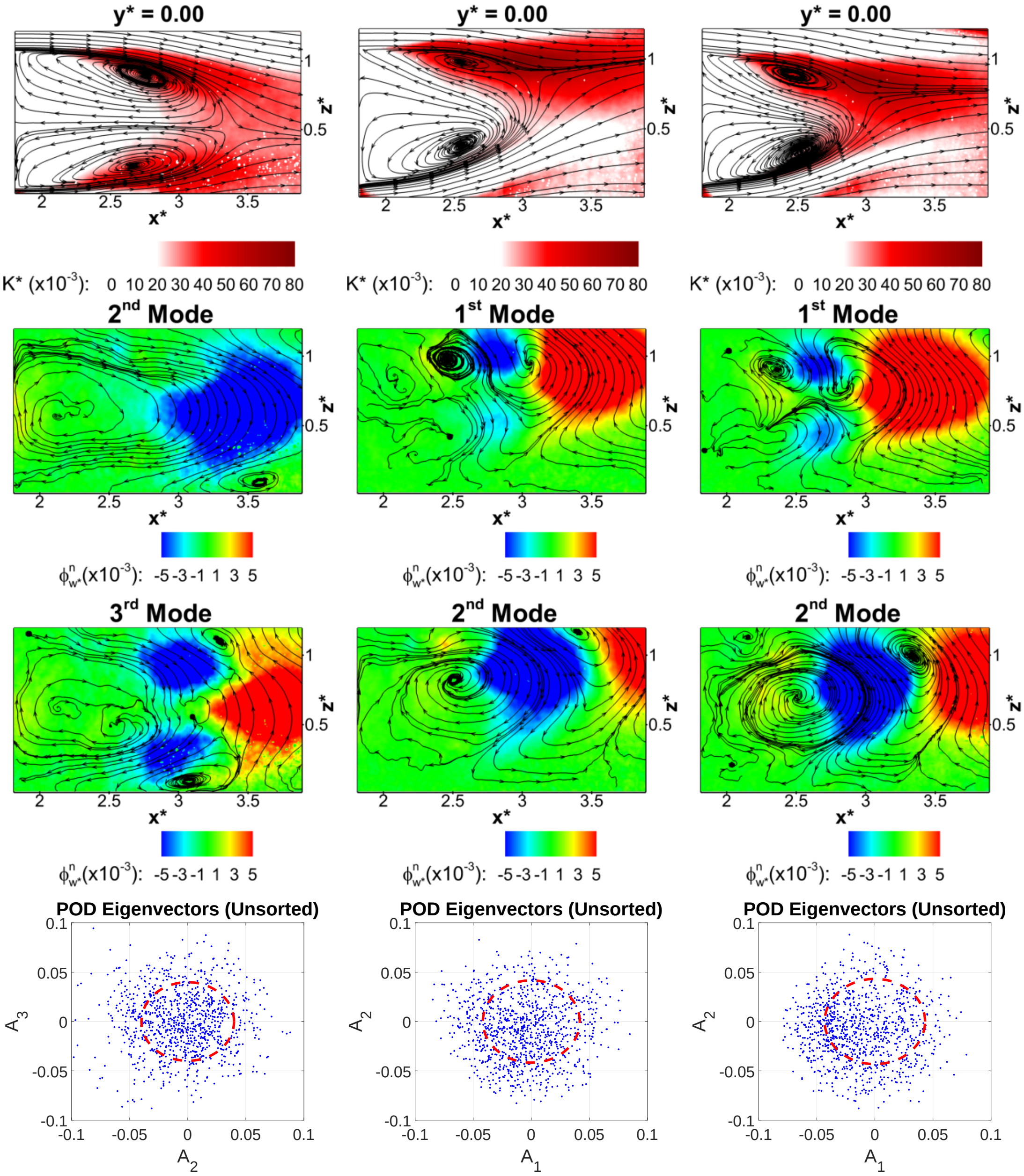

(a) $\phi_t = 0°$, $\phi_b = 0°$ (b) $\phi_t = 0°$, $\phi_b = 12°$ (c) $\phi_t = 12°$, $\phi_b = 12°$

Figure 4.22: From top to bottom: non dimensional turbulent kinetic energy K^* at $y^* = 0.00$; first pair of convective POD modes at $y^* = 0.00$; scatter plot of the temporal coefficients associated with the same POD modes. Plots for **a** $\phi_t = 0°$, $\phi_b = 0°$; **b** $\phi_t = 0°$, $\phi_b = 12°$; **c** $\phi_t = 12°$, $\phi_b = 12°$. In the first column, the values of K^* are plotted together with the streamlines of the in-plane components of the velocity. In the second and third columns, the eigen-functions related to the velocity fluctuation are coloured according to the values of the axial component ϕ^n_{u*} whereas the streamlines are drawn considering the in-plane components ϕ^n_{u*} and ϕ^n_{w*}.

4.2.2.1 Origin of the asymmetry in the vertical direction

As pointed out in §4.1.0.1, a strong relationship seems to exist between the drag experienced by the model and the degree of asymmetry in the vertical direction seen in the time averaged wake (i.e. a more symmetric wake is usually associated with a lower value of C_D). The origin of the asymmetry in the vertical direction described in §4.1 has been further investigated by looking at the unsteady features of the velocity field recorded in the near-wake region. For the sake of simplicity, only the data captured at $y^* = 0.00$ was considered. The obtained results are presented in Fig. 4.22. For the square-back case (first plot in Fig. 4.22a), a high level of unsteadiness, in the form of high values of turbulent kinetic energy $K^* = 1/2(\overline{u'^{*2}} + \overline{w'^{*2}})$, is seen in both top and bottom shear layers for $x^* > 2$, following the onset of the Kelvin-Helmholtz instability (as observed in §4.2.2). The unsteady region tends to spread while moving downstream until covering the entire wake closure, with no noticeable differences seen between the two horizontal shear layers. This is consistent with the distribution of the Reynolds stresses reported by Grandemange et al (2013b) for the wake developing downstream of a square-back Ahmed body tested at a similar distance from the ground. A change in the distribution of K^* is seen when the symmetry in the vertical direction is broken, for example by applying a 12° slant to the bottom trailing edge (first plot in Fig. 4.22b). A drop in the values of K^* is observed in the region of the bottom shear layer, as consequence of the deflection of high-momentum flow into the wake. As proposed by McArthur et al (2016), an additional contribution to the stabilisation of the bottom shear layer may also come from the inhibition of the Kelvin-Helmholtz instability in the same region, as a result of the increased curvature of the shear layer (Liou, 1994). A certain level of unsteadiness, however, is still visible near the ground, where flow separation occurs.

Following the stabilisation of the bottom shear layer, the unsteady region moves towards the upper portion of the wake, closer to the top shear layer (Fig. 4.22b, top row). A similar trend was found by Khalighi et al (2012). As in the square-back case, the saddle point seen at the wake closure is still inside the region with the highest level of unsteadiness. Indeed, the saddle point seems to follow the shift of this region as the balance between upwash and downwash is altered. This becomes particularly evident when the configuration with $\phi_t = 12°$ and $\phi_b = 12°$ is considered (Fig. 4.22c, top row). In this case, as the saddle point moves towards the centre of the base, following the recovery of the symmetry in the vertical direction, so does the region with highest level of velocity fluctuation.

Further details on the nature of these fluctuations can be found looking at the topology of the first pair of convective POD modes extracted from the same datasets. For the square-back configuration, the 1^{st} mode has not been considered as it is still related to the lateral symmetry breaking bi-stable mode (Chap. 3). The results are reported in the second and third row of Fig. 4.22. In the square-back case (Fig. 4.22a), the most coherent motions of the wake are seen in the region of the wake closure. The 2D streamlines drawn considering the in-plane components ϕ^n_{u*} and ϕ^n_{w*} suggest a vertical oscillation (or flapping, as discussed in §4.2.2) of the saddle point. Vortical structures developing in proximity to the two shear layers are also observed. The flapping motion of the saddle point appears to be limited to the upper portion of the base in the case of an upwash dominated wake (Fig. 4.22b). In this case, vortices are shed from the top shear layer only and no coherent structures are seen in the region of the bottom recirculation. The flapping motion is shifted back towards the centre of the model base when 12° tapers are applied to both horizontal trailing edges (Fig. 4.22c). Unlike the square-back case, however, the vertical displacement of the saddle point appears to be more limited, explaining the narrowing of the region with the highest level of velocity fluctuation.

If the data is rearranged using the same approach already employed in §3.2.5, additional insights on the wake evolution can be gained. A phase averaged low order model has been therefore built considering the time averaged field and the first pair of convective POD modes. The temporal coefficients obtained from the same modes have been used for sorting the snapshots in phase, according to Eq. 3.3. Compared to that seen in Van Oudheusden et al (2005), in this case a higher level of scattering is seen around a theoretical circle in the scatter plots (A_i, A_j) reported at the bottom of Fig. 4.22. This is due to the higher level of 'noise' that affects the present experiment, as a consequence of the higher Reynolds number (Yang et al, 2017) as well as the presence of three dimensional effects, as highlighted by the fact that the vertical flapping can occasionally be a one-sided motion (§4.2.2). The reconstructed fields are presented in 4.23. In the square-back case (Fig. 4.23a), an alternated expansion and shrinkage of the two recirculations is observed, similar to that described in Zhang et al (2015). When coherent structures are shed from one of the two recirculations ($\theta = \pi/2\,rad$ and $\theta = 3/2\pi\,rad$ in Fig. 4.23a), the size of the recirculation decreases leaving space for the growth of the vortical structure acting on the opposite side of the base. The process goes on until the expanding recirculation 'bursts' under it own pressure. At this point, small vortices are shed downstream and the recirculation starts to shrink leaving space for the opposite structure to grow again. The process repeats over time resulting in vertical oscillations of the wake saddle point and, ultimately, in the vertical flapping previously described. The loss of symmetry in the vertical direction in the time averaged wake topology coincides with the stabilisation of the recirculation downstream of the taper generating the highest amount of inflow. This is particularly visible in the case of the model tested with a 12° bottom slant, as shown in Fig. 4.23b. During each cycle, vortical structures develop and are shed from the top shear layer whilst no significant variations are seen in the bottom recirculation. The vertical flapping is therefore limited to the upper portion of the model base. Similar conclusions were drawn by McArthur et al (2016), while investigating the unsteady behaviour of similar wakes. Small vortices are arguably still shed by the bottom recirculation, as shown for example in Zhang et al (2015), but they are too small and not coherent enough to be captured by the low order model presented here. The disparity in the unsteady behaviour of the two recirculating regions is at the origin of the non-zero wall velocity seen in §4.1.0.1, that ultimately leads to a higher suction over the

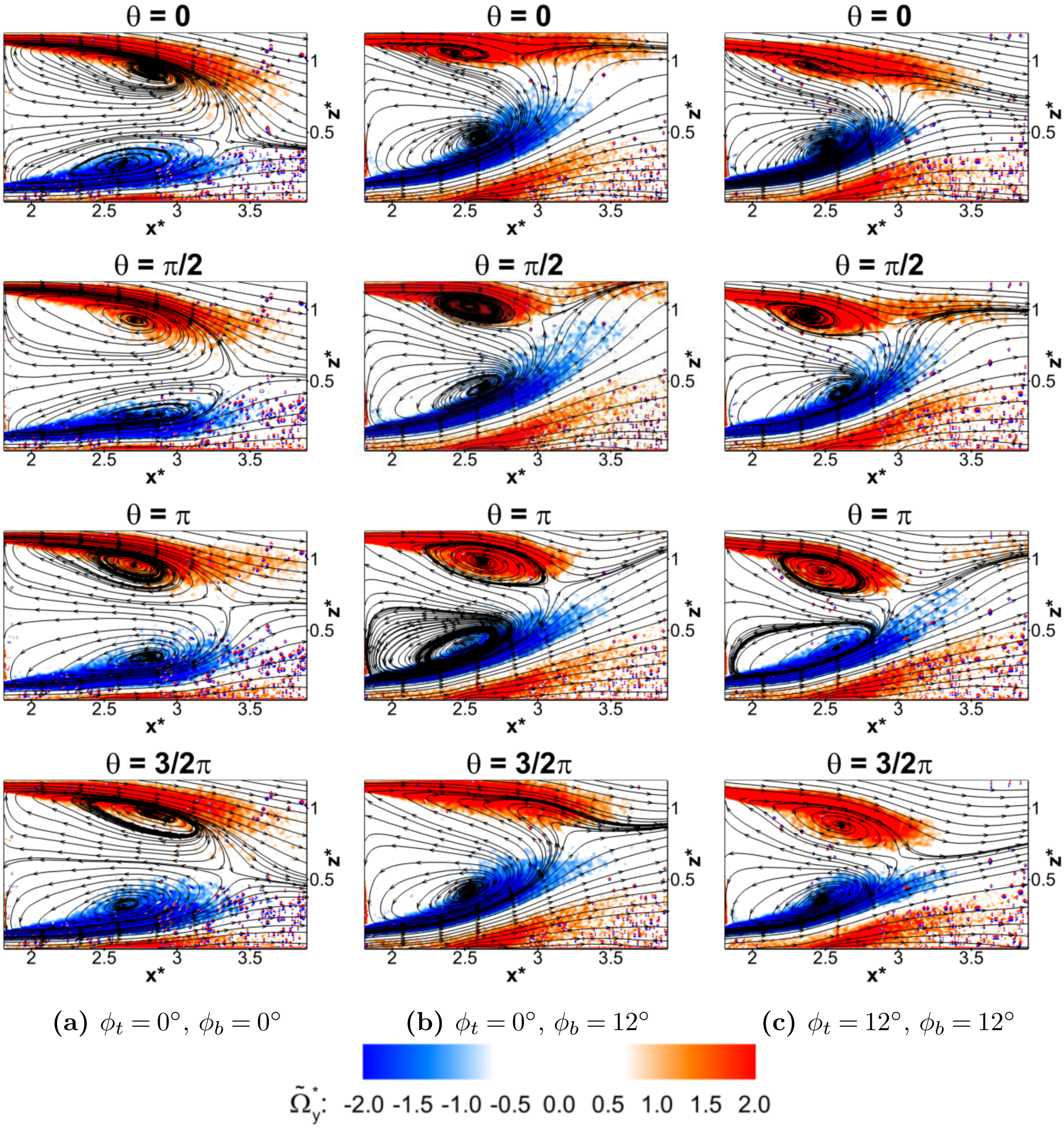

(a) $\phi_t = 0°$, $\phi_b = 0°$ **(b)** $\phi_t = 0°$, $\phi_b = 12°$ **(c)** $\phi_t = 12°$, $\phi_b = 12°$

Figure 4.23: Low order phase averaged velocity field at $y^* = 0.00$ for: **a** $\phi_t = 0°$, $\phi_b = 0°$; **b** $\phi_t = 0°$, $\phi_b = 12°$; **c** $\phi_t = 12°$, $\phi_b = 12°$. The plots are coloured according to the values of the normalised lateral component of the vorticity $\tilde{\Omega}^*_y$; the streamlines are drawn considering the in-plane components of the velocity field.

base. These differences tend to be reduced when the symmetry in the vertical direction is restored. A step forward in this direction is made with the $\phi_t = 12°$, $\phi_b = 12°$ configuration (Fig. 4.23c). In this case, the upper recirculation is seen to expand at the expenses of the bottom recirculation, until the two structures are almost matched in size ($\theta = 3/2\pi\, rad$ in Fig. 4.23c). Nevertheless the top recirculation is never seen to prevail over the bottom one, suggesting that, at least on the plane at $y^* = 0.00$, there is still room for further improvement in terms of wake symmetrisation and (potentially) drag reduction.

4.3 Summary and conclusions

In this chapter, the aerodynamic effects produced by high aspect ratio tapers applied to the top and bottom trailing edges of the Windsor body have been investigated. Compared to that seen for the simple square-back case described in Chap. 3, noticeable changes have been reported in the time averaged wake topology and base pressure distribution, resulting ultimately in variations of the steady aerodynamic forces acting over the entire model. In particular, an increase in C_D has been documented every time the wake loses symmetry in the vertical direction, as the balance between upwash and downwash is lost. The time averaged wake topology has been seen to switch from the toroidal shape seen in Chap. 3 for the square-back case towards a more complex structure, consisting of a pair of horseshoe vortices that eventually merge with the longitudinal vortical structures forming at the tips of each taper. This topology present similarities with that usually described in the literature (Ahmed et al (1984) and Venning et al (2017)) in the case of larger slants. An additional pair of transverse vortices develops close to the vertical trailing edges of the model. The predominance of either upwash or downwash has been reported to change the shape of the horseshoe vortex forming in the region of the shear layer with the highest curvature. In these conditions, this vortical structure loses its coplanarity, as it merges with the transverse vortices acting along to the vertical trailing edges, assuming a characteristic *'U'* shape. Further insights on the nature of this structure have been gained performing unsteady analysis.

The application of POD to the fluctuating part of base pressure and velocity datasets, together with the coherence analysis performed considering the signal recorded by some of the pressure taps, has highlighted the existence of a more laterally stable wake than that seen for the simple square-back configuration. Indeed, an increase in the curvature of the shear layers has been shown to yield a weakening of both the lateral flapping and the pumping motion of the wake. On the other hand, a strengthening of the vertical flapping has been reported, as a consequence of the increased level of interactions between the top and bottom shear layers (Luo et al, 1994). This has also been linked with a reduction in the length of the wake recirculation (Roshko, 1954). As done in Chap 3, the spatial locations of these motions have been determined by means of single point velocity measurements carried out in correspondence to the top shear layer. The results have pointed out that the pumping motion, when present, can be seen in the region of flow reversal close to the model base whereas the vertical flapping is stronger in proximity to the wake closure.

The reduced distance between the top and bottom shear layers as well as their increased curvature has been found to weaken also the bi-stable lateral symmetry breaking mode. An increase in the level of upwash\downwash in the near-wake has been shown to reduce the energy content of this mode, while also decreasing the deviation of each bi-stable state from the most laterally symmetric configuration. In the same conditions, a shortening of the average time between switches has also been reported, in agreement with that found by Evrard et al (2016) when trying to stabilise the wake using base cavities of different depths. The weakening of the bi-stable mode, however, has been reported to yield a decrease in C_D over the square-back case only when accompanied with the restoration of the symmetry in the vertical direction. In this case, the symmetry preserving state has been observed to become the most stable configuration, resulting in a base drag reduction of $\approx 8\%$, in line with the value predicted by the model presented in 3.2.5.1. This, however, has been achieved by maximising the amount of reverse flow impinging on the base, without increasing the distance between the recirculating structures and the base itself, suggesting that there may still be space for further reductions of the aerodynamic drag.

Chapter 5

Vertical trailing edge tapering

The present chapter focuses on the investigation of the effects of side trailing edge tapers on the time averaged topology and unsteady behaviour of the wake of a simplified square-back vehicle. Short tapered sections, similar to those described in Chap. 4, are applied to the vertical trailing edges of the Windsor body without wheels (as detailed in §2.1), leaving the model's horizontal trailing edges squared. The tapered surfaces are observed to trigger a switch from a laterally asymmetric bi-stable wake to a stable wake, asymmetric in the vertical direction. The wake structure described in Chap in 3 for a lateral symmetry breaking state is seen to rotate by 90° as the angle of lateral tapered surfaces ϕ_s is increased. As a result, the horizontal pressure gradient seen in the case of lateral symmetry breaking states is replaced by a vertical pressure gradient. A downwash dominated wake is observed in these conditions. A $\approx 6\%$ drag reduction over the square-back case is recorded for chamfer angles between 6° and 12°. This gain is found to be the result of the 'stretching' of the circular vortex responsible for the suction zone visible in any symmetry breaking state. The sensitivity of such a wake to small variations of the model pitch angle is also assessed. In particular, as the pitch angle Θ is reduced from 0° to $-2°$ (having fixed the side edge taper angle at 12°) the time averaged wake is seen to switch from a downwash dominated topology to un upwash dominated topology. An increase in the wake unsteadiness is observed when the symmetry in the vertical direction is recovered, for $\Theta = -1°$. This is found to be linked with a strengthening of the bi-stable lateral symmetry breaking mode and is accompanied with a 4.9% reduction in the base drag over the same model tested at zero degree pitch, suggesting that a lower drag wake is not necessarily a more stable wake.

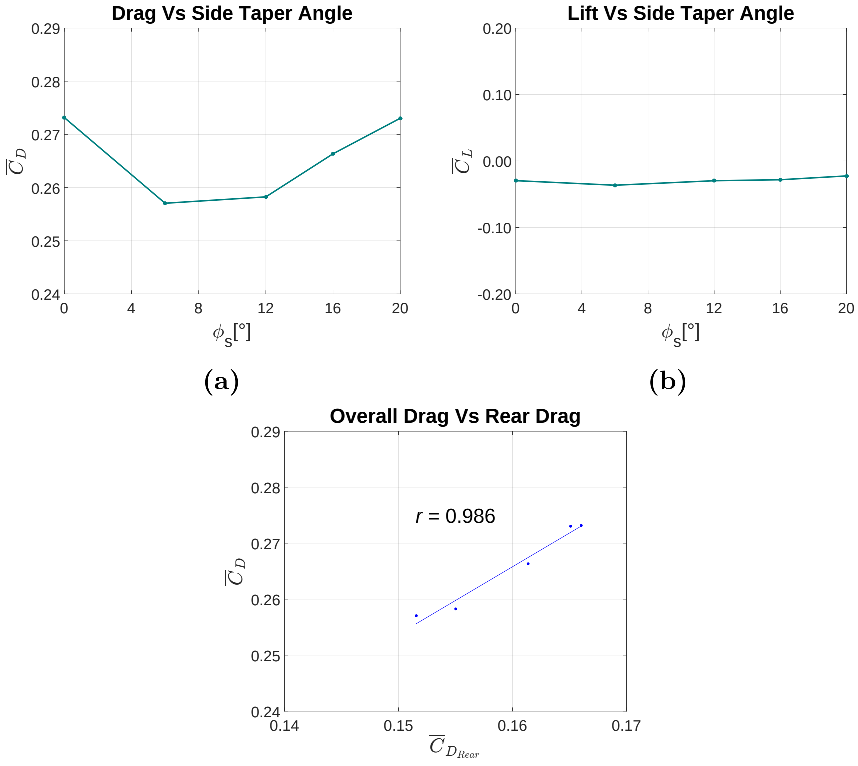

(a) **(b)**

(c)

Figure 5.1: Time averaged drag **(a)** and lift **(b)** recorded for all the configurations tested. **c** correlation between aerodynamic drag and pressure drag.

5.1 Time averaged results

The application of tapers to the model's vertical trailing edges yields a drag reduction of up $\approx 6\%$ over the square-back case, for chamfer angles $\phi_s \leq 12°$ (Fig. 5.1a). This represents a $\approx 2.5\%$ improvement over the low drag configuration studied in Chap. 4. $\overline{C}_D$ is then seen to increase for larger taper angles, until reaching a value similar to that obtained for the square-back configuration at $\phi_s = 20°$, in agreement with the findings reported by Perry et al (2015) for a similar case. No particular changes, on the other hand, are observed in the time averaged values obtained for the lift force in the same conditions (Fig. 5.1b). As seen in the case of horizontal tapering (§4.1.0.1), a good correlation is found between the drag acting over the entire model $\overline{C}_D$ and the pressure drag generated by the model rearward facing surfaces $\overline{C}_{D_{Rear}}$, calculated according Eq. 2.10 (Fig. 5.1c). This confirms the fact that the variations seen in $\overline{C}_D$ when increasing ϕ_s are the result of changes in the pressure distribution over the model rear-end, which in turn are triggered by alterations of the time averaged wake topology, as evident when looking at the pressure maps and velocity fields presented in Fig. 5.2, 5.3, 5.4.

In particular, when 6° tapers are applied to the model vertical trailing edges, the time averaged wake changes its orientation, aligning parallel to one of the two diagonals of the base

(Fig. 5.2). This is particularly visible when considering the base pressure distribution, showing a negative pressure gradient developing from the bottom-right corner to the top-left corner. A similar orientation, although with a pressure gradient of opposite sign, was reported by Cabitza (2014) for the lowest drag configuration (with $\Delta\overline{C}_D = -13.1\%$ over the baseline configuration), obtained in that case by controlling the wake of a square-back body with $W/H = 0.86$ using synthetic jets applied to all four trailing edges of the model, with a non dimensional actuating frequency of $St_H = 13.9$ and a blowing coefficient $C_\mu = 0.168$ (Fig. 1.38b). The genesis of this pressure distribution becomes clearer when looking at the PIV cross-plane taken at $x^* = 2.31$. Two counter rotating vortices, similar to those seen in Chap. 3 for a lateral symmetry breaking state, are visible in this plane. Unlike that seen in Fig. 3.8, however, the 2D streamlines separating the two vortices are no longer aligned with the model horizontal edges but form an angle of $\approx 31°$ with the horizontal plane. Therefore, the symmetry in the vertical direction is lost. This is visible on both streamwise PIV planes considered in the present work (at $y^* = 0.00$ and $y^* = 0.34$), showing an expansion of the upper recirculation and a simultaneous shrinking of the lower vortical structure. At the same time, the distance between the centre of the vortical structures and the base of the model is also changed. The upper vortex is brought closer to the base whilst the bottom recirculation is moved further downstream. This agrees with the fact that the suction region is shifted towards the upper portion of the base.

The re-orientation of the time averaged wake topology becomes even more evident when the configuration with $\phi_s = 12°$ is considered (Fig.5.3). In this case, the asymmetry in the vertical direction already reported for the $\phi_s = 6°$ case is further accentuated. The lateral symmetry, on the other hand, is fully restored, as shown by the mid-horizontal PIV plane taken by Perry (2016a). At this location, the data shows a decrease in the width of the rear recirculation as a consequence of the boat tailing effect of the tapered surfaces. With the loss of symmetry in the vertical direction, a negative pressure gradient develops over the base. The suction region is confined to the upper portion of the rearward facing surface, while the rear stagnation is moved towards the bottom trailing edge. The changes in pressure distribution correlate well with the variations seen in the velocity fields captured in the two PIV cross-planes considered in the present work. The two counter rotating structures seen in the PIV plane at $x^* = 2.31$ are now aligned with the top trailing edge of the model. Two additional vortical structures are also observed close to the ground in correspondence to the second cross-plane (at $x^* = 3.31$). Overall, a downwash dominated wake is present.

This may appear to contradict the trend previously described for the vertical component of the aerodynamic force (Fig. 5.1b), but becomes clearer when the velocity field recorded at $y^* = 0.00$ is considered. In this location, a circular vortex is seen forming close to the upper portion of the base whilst a smaller, elliptically shaped vortical structure is observed in the lower portion of the wake, further downstream from the model base. This topology is consistent with the time averaged base distribution previously described. The streamlines leaving the top and bottom shear layers tend to quickly realign with the ground, resulting in a rather 'squared'

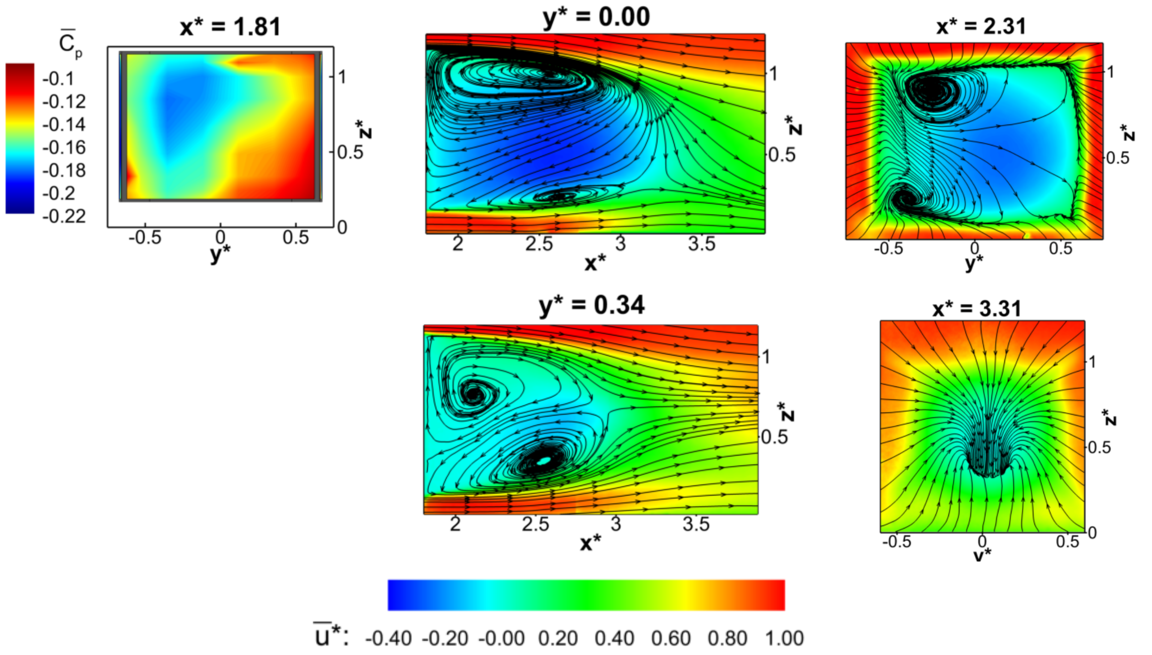

Figure 5.2: Time averaged fields for $\phi_s = 6^o$. Clockwise from top left: $\mathbf{x^* = 1.81}$, base pressure distribution; $\mathbf{y^* = 0.00}$, PIV vertical mid-plane; $\mathbf{x^* = 2.31}$ and $\mathbf{x^* = 3.31}$, PIV stereo cross-planes; $\mathbf{y^* = 0.34}$, PIV vertical off-centre plane. All PIV fields are coloured according to the values of the axial component of the velocity u^*; the streamlines refer to the in-plane components.

wake closure. This differs from the more 'rounded' wake closure seen in the case of horizontal tapered surfaces (Chap. 4) and may explain the limited variations in terms of $\overline{C}_L$ observed in this last case over the square-back configuration.

The topology described for the plane at $y^* = 0.00$ strongly resembles that reported in Chap. 3 and described also by Volpe et al (2015) and Evrard et al (2016), when characterising the lateral symmetry breaking state on a horizontal plane centred with the model base. Unlike that seen in the case of a simple square-back configuration, however, this vortical structure appears to have been 'stretched' in the streamwise direction and, in the case of the configuration with $\phi_s = 6°$, the distance between the core of the vortex and the model base is also increased. A similar trend is observed for the vortical structures seen in the mid-horizontal plane ($z^* = 0.67$ in Fig. 5.3). These changes in the time averaged wake topology may explain the $\approx 15\%$ reduction in base drag obtained for $6° \leq \phi_s \leq 12°$ over the square-back case, that ultimately leads to the $\approx 6\%$ improvement in the values recorded for both $\overline{C}_{D_{Rear}}$ and $\overline{C}_D$. A similar topology was reported by Perry (2016b), in the case of a stable asymmetric wake, developing downstream of a simplified square-back body, with $W/H \approx 1$ and a leading edge with a radius of $r/W \approx 0.10$ (tested at $C^* \approx 0.2$). The change in shape of the larger recirculation seen in the plane at $y^* = 0.00$, also seems to explain the increase in drag reported in Fig. 5.1a when chamfers

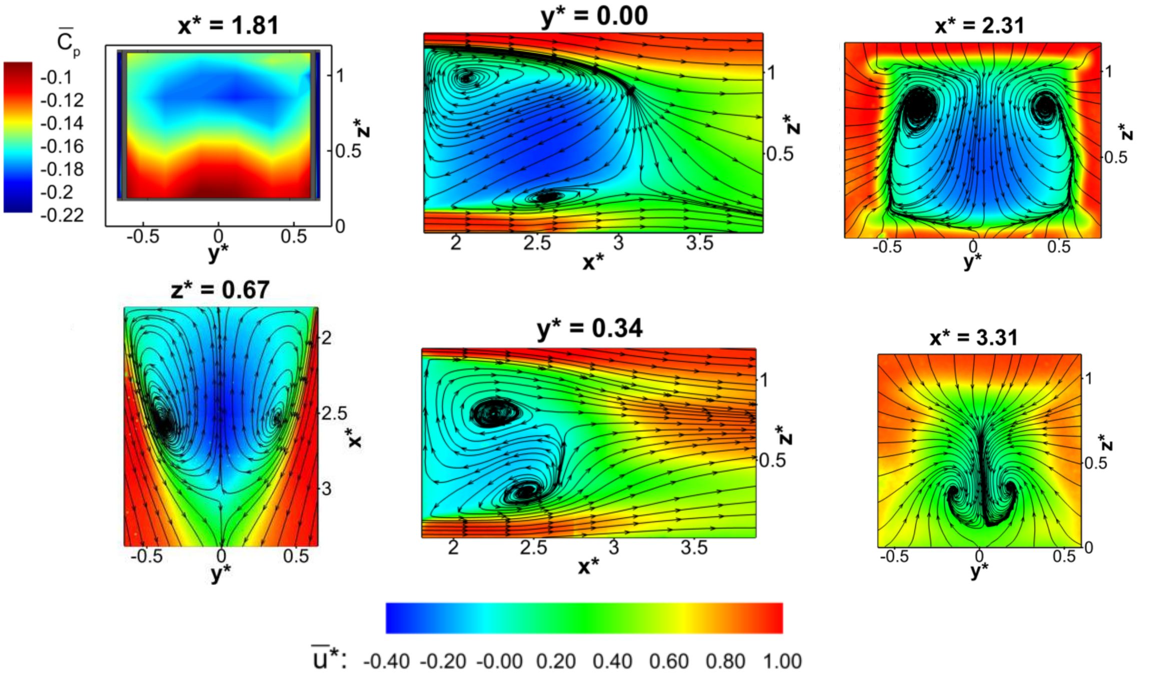

Figure 5.3: Time averaged fields for $\phi_s = 12^o$. Clockwise from top left: $\mathbf{x^* = 1.81}$, base pressure distribution; $\mathbf{y^* = 0.00}$, PIV vertical mid-plane; $\mathbf{x^* = 2.31}$ and $\mathbf{x^* = 3.31}$, PIV stereo cross-planes; $\mathbf{y^* = 0.34}$, PIV vertical off-centre plane; $\mathbf{z^* = 0.67}$, PIV horizontal mid-plane. All PIV fields are coloured according to the values of the axial component of the velocity u^*; the streamlines refer to the in-plane components. The additional plane at $\mathbf{z^* = 0.67}$ is from Perry (2016a).

angles ≥ 16° are applied to the model's side trailing edges. Indeed, as large chamfer angles are considered, the inflow generated by the tapered surfaces increases, yielding a shortening of the rear recirculation in the streamwise direction but also a strengthening of the vortices developing at the tips of each slant, as a consequence of the growth of the suction acting on the tapers themselves. At the same time, the larger of the two vortical structures seen in the plane at $y^* = 0.00$, is 'pushed' against the model base, assuming a rather characteristic triangular shape, thus further decreasing the pressure over the base. This is clear in Fig. 5.4, when the velocity field recorded at $y^* = 0.00$ and $y^* = 0.34$ as well as the pressure distribution acquired at $x^* = 1.81$ are considered. In these conditions, a progressive loss of lateral symmetry is also noted. This is seen in the base pressure map as well as the velocity field recorded at $x^* = 2.31$, but becomes even more evident when the cross-plane located in proximity to the wake closure (at $x^* = 3.31$) is considered, suggesting that its origin is in the shear layer instability triggered by flow separation over the slants (see §5.2) rather than in long-time motions of the flow reversal.

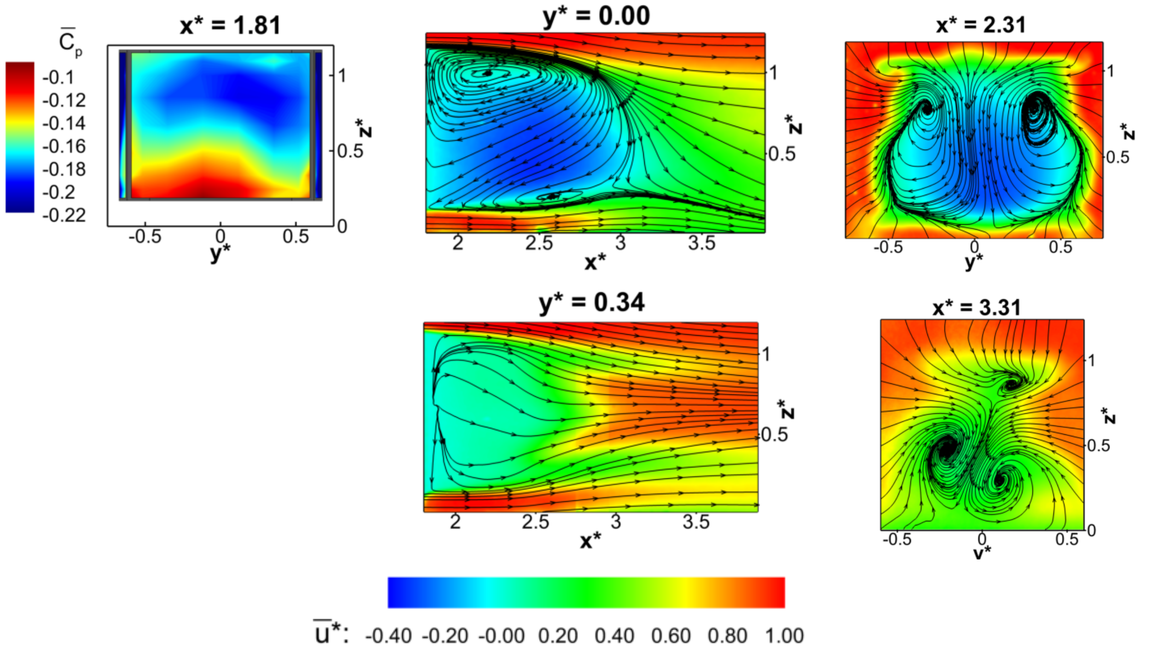

Figure 5.4: Time averaged fields for $\phi_s = 20^o$. Clockwise from top left: $\mathbf{x^* = 1.81}$, base pressure distribution; $\mathbf{y^* = 0.00}$, PIV vertical mid-plane; $\mathbf{x^* = 2.31}$ and $\mathbf{x^* = 3.31}$, PIV stereo cross-planes; $\mathbf{y^* = 0.34}$, PIV vertical off-centre plane. All PIV fields are coloured according to the values of the axial component of the velocity u^*; the streamlines refer to the in-plane components.

5.2 Unsteady results

Besides the changes in the time averaged wake topology described in §5.1, the application of small chamfers to the vertical trailing edges yields also non-negligible variations in the unsteady flow field behind the model. As ϕ_s is increased, the extension of the region associated with the highest values of pressure fluctuation is gradually reduced (Fig. 5.5a). The bi-lobe distribution observed in Chap. 3, for the contour plot of $RMS(\Delta C_p)$ obtained for the square-back case, is seen to disappear, replaced (for $\phi_s \geq 12°$) by a single region of high pressure fluctuation located in proximity to the rear stagnation point (Fig. 5.5b). A further reduction in the level of unsteadiness over the model base is noticed for $\phi_s = 20°$ (Fig. 5.5c). In this last case, however, a greater level of fluctuation is seen close to the tapered surfaces, as the flow fails to reattach over the slants, in analogy with that reported in Chap. 4, when studying the effects of horizontal trailing edge tapers with similar values of ϕ. This localised increase of $RMS(\Delta C_p)$ may be the element causing the loss of lateral symmetry observed in §5.1 in the time averaged results (Fig. 5.4).

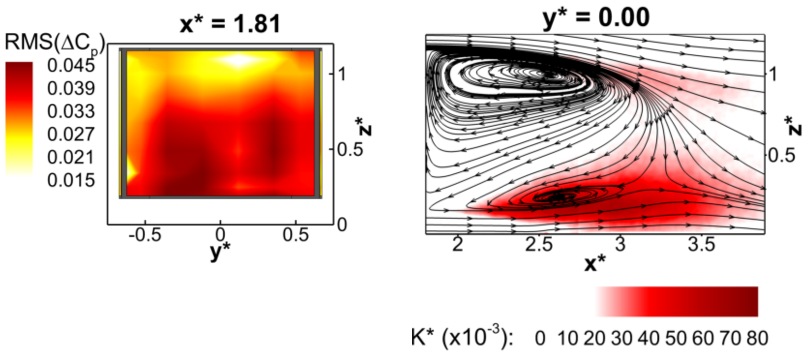

(a) $\phi_s = 6^o$

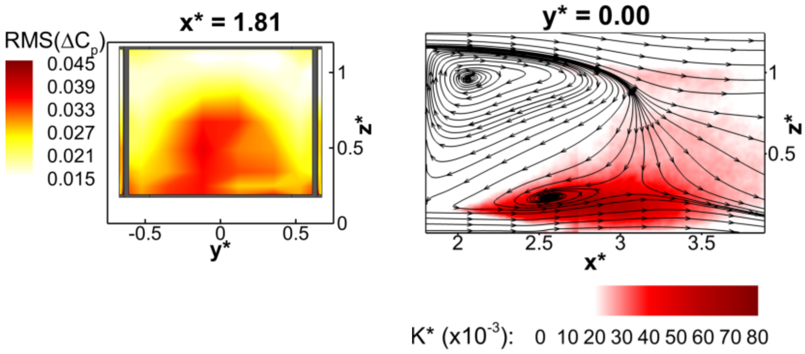

(b) $\phi_s = 12^o$

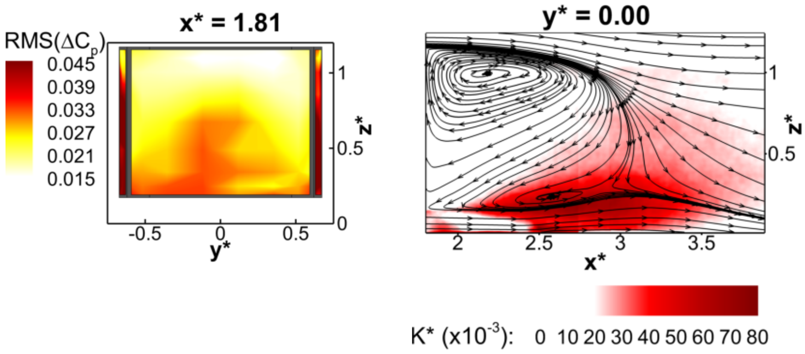

(c) $\phi_s = 20^o$

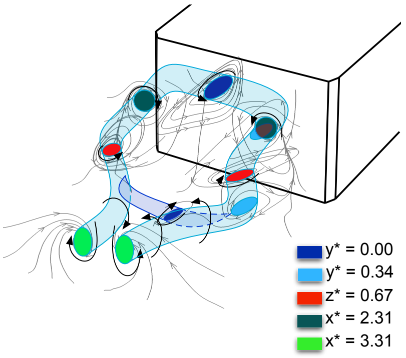

(d) Proposed wake topology ($\phi_s = 12^o$)

Figure 5.5: Base pressure fluctuation and non dimensional turbulent kinetic energy (at $y^* = 0.00$) for $\phi_s = 6^o$ **(a)**, $\phi_s = 12^o$ **(b)** and $\phi_s = 20^o$ **(c)**. **d** Schematic representation of the proposed wake topology for the configuration with $\phi_s = 12^o$.

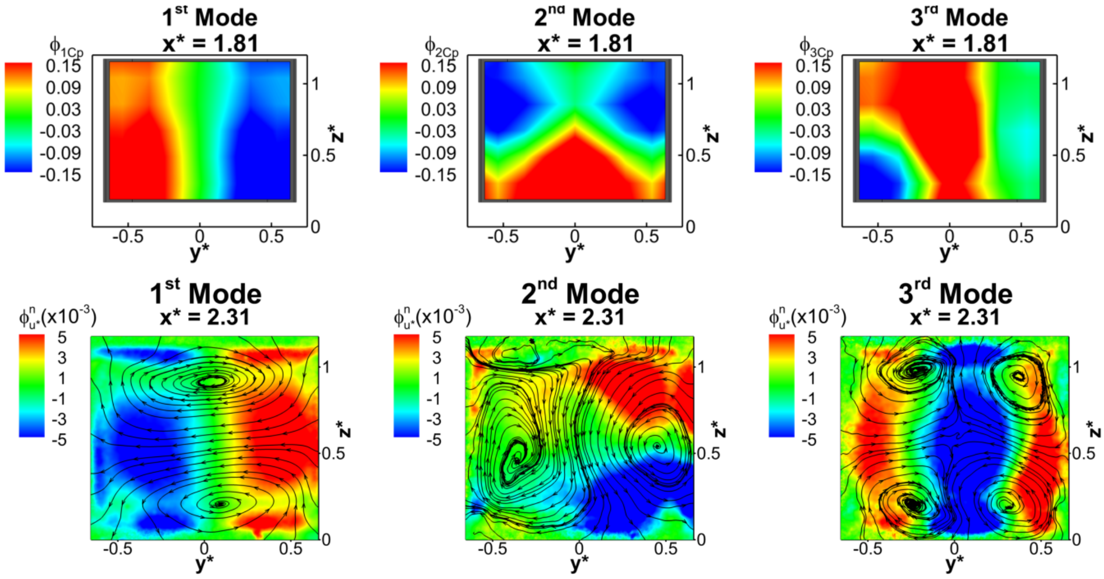

(a) LSB mode **(b)** VSB mode **(c)** SP mode

Figure 5.6: Spatial distribution of 3 of the most energetic POD modes extracted from the base pressure distribution (top row) and PIV cross-plane at $x^* = 2.31$ (bottom row) for $\phi_s = 6°$. The modes are ordered according to their topology: **a** lateral symmetry breaking mode (LSB), **b** vertical symmetry breaking mode (VSB), **c** symmetry preserving mode (SP). $\phi^n_{C_p}$ refers to the magnitude of the spatial eigen-modes extracted from the field of the pressure fluctuation. The eigen-functions related to the velocity fluctuation are coloured according to the values of the through plane component $\phi^n_{u^*}$ whereas the streamlines are drawn considering the in-plane components $\phi^n_{v^*}$ and $\phi^n_{w^*}$.

Changes are also observed in the distribution of the velocity fluctuations in the near-wake region. The loss of symmetry in the vertical direction seen in the time averaged flow field is accompanied with the development of a strong disparity in the distribution of turbulent kinetic energy $K^* = 1/2(\overline{u'^{*2}} + \overline{w'^{*2}})$ between the two horizontal shear layers, as it is evident in the vertical mid-planes ($y^* = 0.00$) reported in Fig. 5.5 for three different configurations ($\phi_s = 6°$, $\phi_s = 12°$ and $\phi_s = 20°$). The trend already pointed out in §4.2.2 in the case of asymmetries induced by different horizontal taper angles is now further accentuated. One of the main unsteady features of the wake is represented by the interactions between the larger, stable recirculation forming downstream of the upper portion of the base and the bottom shear layer. Because of these interactions, smaller transverse vortices roll up close to the ground and are periodically shed downstream. These structures appear to be separate from the main horseshoe vortex depicted in Fig. 5.5d, whose existence can be inferred from the experimental evidence discussed so far. This structure is similar to the 'hairpin' vortex isolated in Chap. 3 for each lateral symmetry breaking state, but with two main differences: the different orientation of the vortex, as it appears now to be rotated by 90°, and the presence of two streamwise vortices downstream of the wake closure. Strong similarities are seen with the horseshoe-like

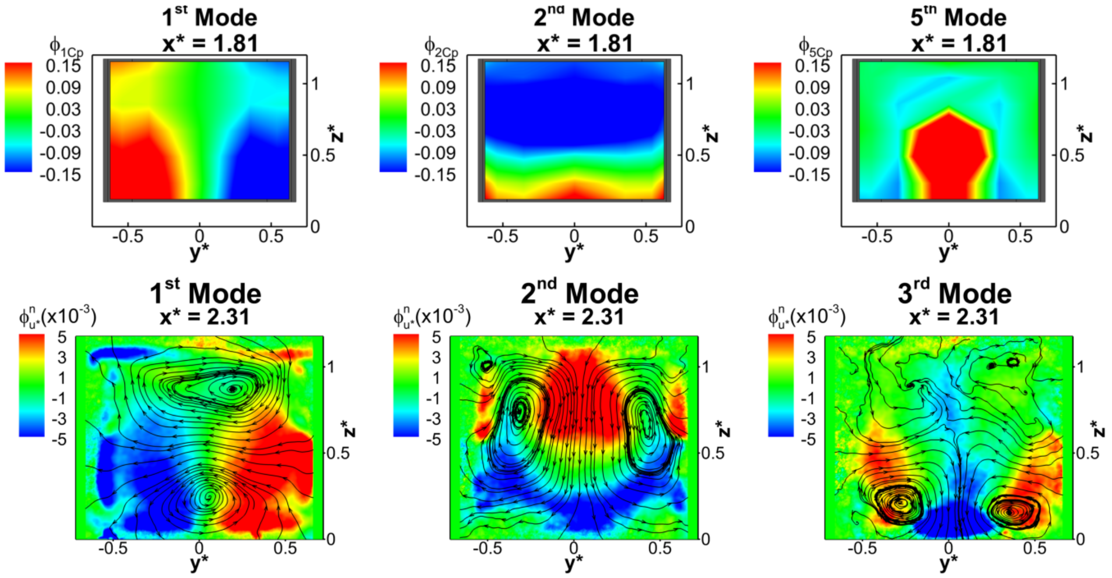

(a) LSB mode **(b)** VSB mode **(c)** SP mode

Figure 5.7: Spatial distribution of 3 of the most energetic POD modes extracted from the base pressure distribution (top row) and PIV cross-plane at $x^* = 2.31$ (bottom row) for $\phi_s = 12°$. The modes are ordered according to their topology: **a** lateral symmetry breaking mode (LSB), **b** vertical symmetry breaking mode (VSB), **c** symmetry preserving mode (SP). $\phi^n_{C_p}$ refers to the magnitude of the spatial eigen-modes extracted from the field of the pressure fluctuation. The eigen-functions related to the velocity fluctuation are coloured according to the values of the through plane component $\phi^n_{u^*}$ whereas the streamlines are drawn considering the in-plane components $\phi^n_{v^*}$ and $\phi^n_{w^*}$.

vortex reported by Grandemange et al (2012b) when describing the topology of the near-wake developing downstream of an axisymmetric blunt body, subjected to a perturbation with an azimuthal number of $m = 2$ (see §1.1.7).

Besides altering the spatial distribution of the pressure fluctuation on the model rearward facing surfaces, the sidewash induced by the lateral tapers also yields changes in the nature of the fluctuations themselves. As ϕ_s is increased, the PDF of C_p recorded by one of the taps in the region of highest unsteadiness switches from a bi-modal symmetrical shape for $\phi_s = 0°$ to a bi-modal non-symmetrical shape for $\phi_s = 6°$, with one of the two states clearly prevailing over the other. A normal distribution is eventually observed for $\phi_s \geq 12°$ (Fig. 5.8a). In the same conditions, the energy content of the 1^{st} POD mode (LSB), still referring to motions of the wake in the lateral direction (Fig. 5.6a and 5.7a), drops by more than 20 percentage points. This drop is only marginally counterbalanced by the slight increase (about 6 percentage points) observed in the energy associated with the second symmetry breaking POD mode (VSB, Fig. 5.8b), related to motions of the wake in the vertical direction (Fig. 5.6b and 5.7b). The 'stabilising' action of the tapers is also reported to trigger changes in the spatial functions associated with the same modes. Although the POD modes extracted for the configuration

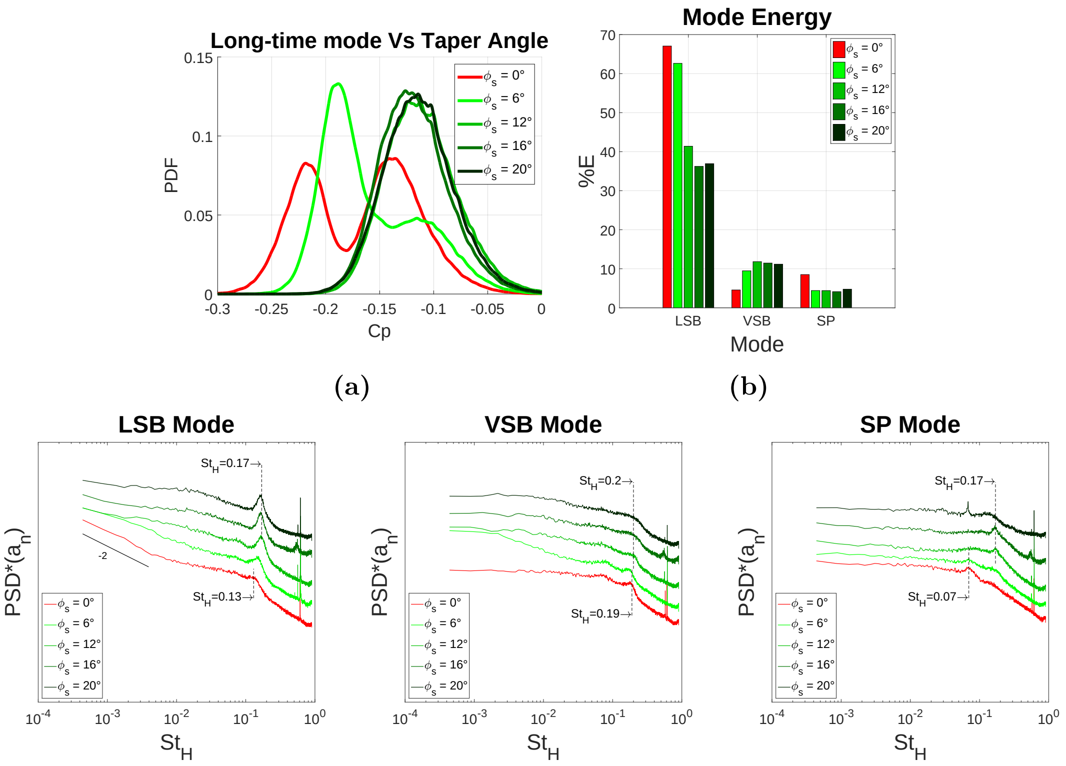

(a) **(b)**

(c) **(d)** **(e)**

Figure 5.8: Top row: **a** PDF of the values of C_p recorded by one of the pressure taps placed in the region of highest pressure fluctuation; **b** energy associated with 3 of the most energetic POD modes (base pressure data). Bottom row: spectra of the POD temporal coefficients associated with **c** the lateral symmetry breaking mode (LSB); **d** the vertical symmetry breaking mode (VSB); **e** the symmetry preserving mode (SP). The curves have been shifted along the vertical axis.

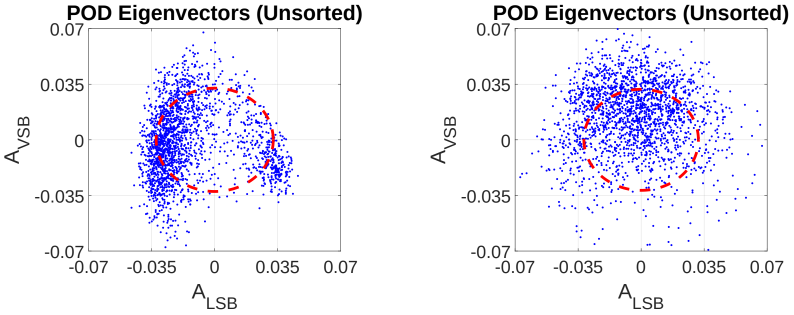

(a) **(b)**

Figure 5.9: Scatter plot of the POD temporal coefficients associated with the VSB mode ($a_2(t)$) and the LSB mode ($a_1(t)$) for $\phi_s = 6°$ **(a)** and $\phi_s = 12°$ **(b)**, referring to the PIV data recorded at $x^* = 2.31$.

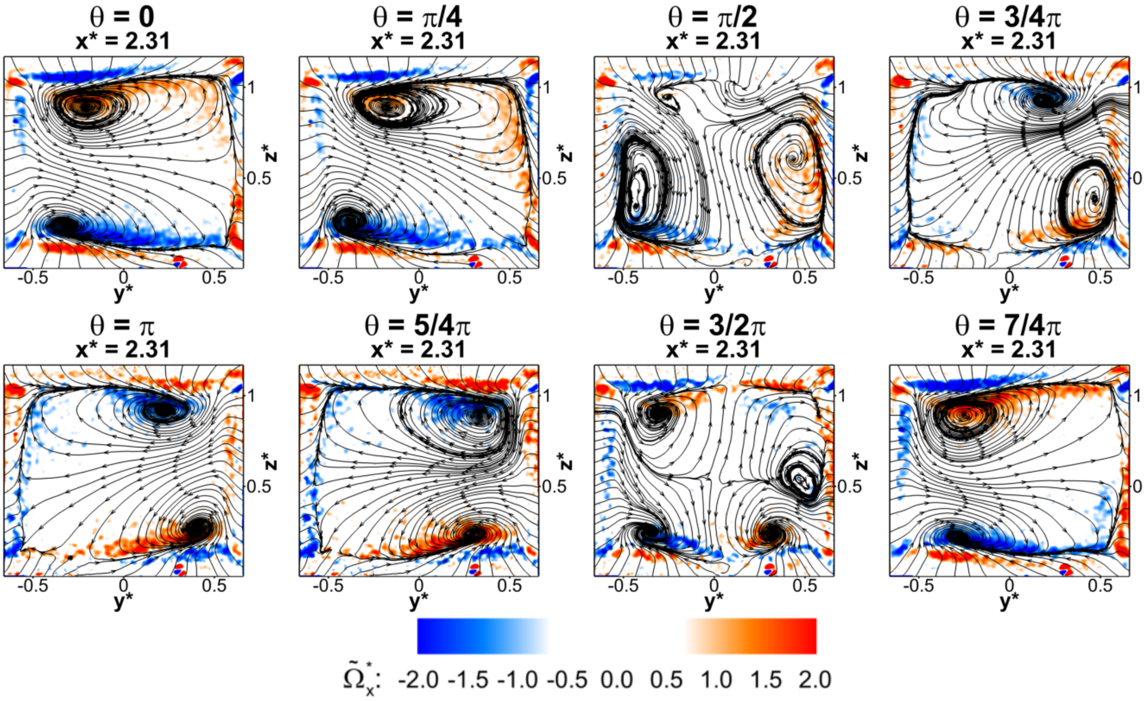

Figure 5.10: Low order phase averaged velocity field at $x^* = 2.31$ for $\phi_s = 6°$. The plots are coloured according to the values of the normalised streamwise component of the vorticity $\tilde{\Omega}^*_x$; the streamlines are drawn considering the in-plane components of the velocity field.

with $\phi_s = 6°$ from either the pressure dataset and the velocity field acquired at $x^* = 2.31$ (Fig. 5.6) strongly resemble those described in §3.2.2 for the square-back case, the stabilisation of the upper portion of the wake seen for taper angles $\geq 12°$ is accompanied with the suppression of all coherent motions previously reported in the same region of the flow field. Indeed, only the lower half of the wake is seen to 'move' in this case (Fig. 5.7), further confirming the observation in Fig. 5.5. Even bigger differences over the square-back configuration are reported when the symmetry preserving mode (SP) is considered. The spatial functions presented in Fig. 5.7c show that the horizontal plane of symmetry disappears following the loss of symmetry in the vertical direction discussed in §5.1 for the time averaged flow field, so that only the lateral symmetry is preserved. This is accompanied with a $\approx 50\%$ reduction in energy compared to the same mode extracted from pressure dataset related to the square-back configuration (Fig. 5.8b).

Additional information is extracted from the scatter plots between the eigenvectors A_{VSB} and A_{LSB} (determined from the dataset recorded at $x^* = 2.31$ according to Eq. 2.22), presented in Fig.5.9. Compared to that seen in §3.2.5 for the square-back case, a gradual change in the distribution of points is observed as the chamfer angle is increased. For $\phi_s = 6°$ the points on the A_{VSB}, A_{LSB} plane start to shift towards a new attractor, located in the upper portion of the same plane (at $A_{VSB} > 0$, Fig. 5.9a). This highlights the establishment of a multi-stable

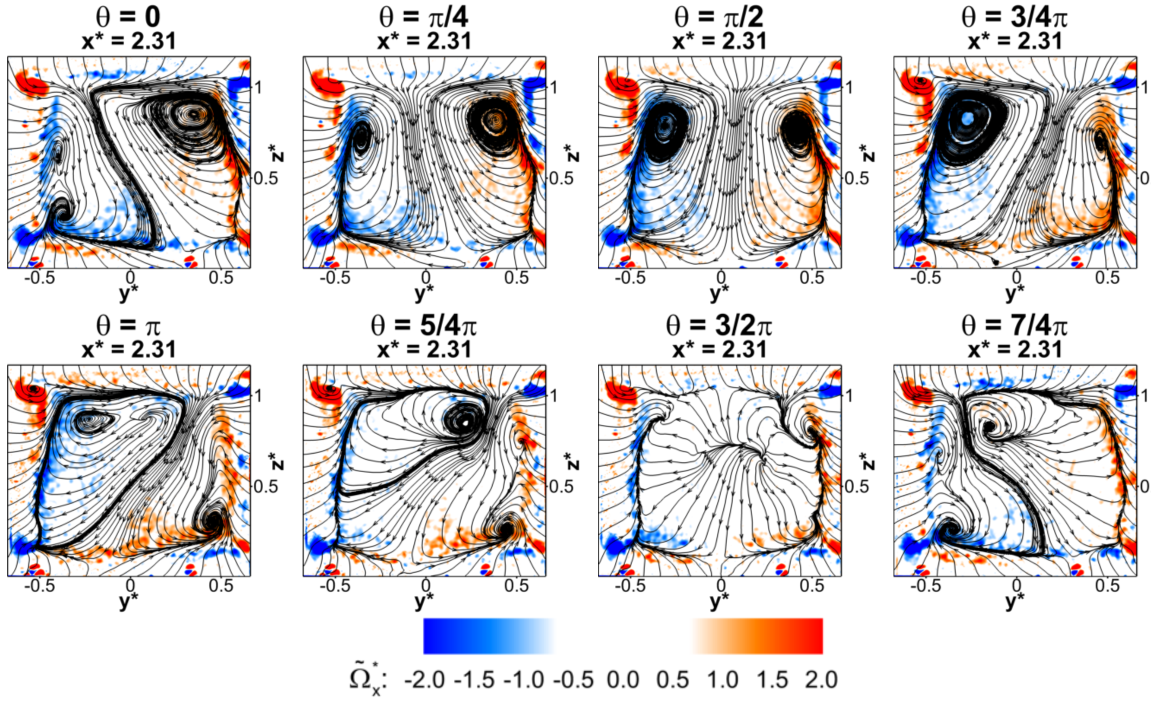

Figure 5.11: Low order phase averaged velocity field at $x^* = 2.31$ for $\phi_s = 12°$. The plots are coloured according to the values of the normalised streamwise component of the vorticity $\tilde{\Omega}_x^*$; the streamlines are drawn considering the in-plane components of the velocity field.

condition, that presents some similarities with that reported by Rigas et al (2014) and Gentile et al (2016) in the case of axisymmetric bodies. The new attractor eventually becomes the only state for $\phi_s = 12°$ (Fig. 5.9b). In this case, the points tend to concentrate in the portion of the scatter plot with $A_{VSB} > 0$ and, although there is a higher level of dispersion compared to that seen in previous cases, the two attractors reported for the square-back configuration are no longer visible. All these changes result in noticeable variations in the long-time evolution of the wake, as seen once the phase averaged low order model, built considering the dataset acquired at $x^* = 2.31$ (following the procedure described in §3.2.5), is considered. Two lateral symmetry breaking states are still clearly visible for $\phi_s = 6°$ (Fig. 5.10). Nevertheless, the reflectional symmetry preserving states seen at $\theta = \pi/2\,rad$ and $\theta = 3/2\pi\,rad$ are no longer mirror images of each other. The differences in topology observed between these two states are even more pronounced than those reported in the case of the upwash dominated wake described in §4.2.1 for $\phi_t = 0°$ and $\phi_b = 12°$. In particular, a downwash dominated state is visible for $\theta = \pi/2\,rad$. This state eventually becomes the only stable configuration for $\phi_s \geq 12°$ (Fig. 5.11). Indeed, the wake developing downstream of the model with 12° side edge tapers appears to be locked in a symmetry breaking configuration, with the asymmetry developing in the vertical direction ($\theta = \pi/2\,rad$ in Fig. 5.11). A swinging motion around this state is seen throughout the different phase angles. However, coherence is lost (i.e. the vortical structures burst into smaller eddies) whenever the wake tries to switch to a lateral symmetry breaking state. The transition between a laterally asymmetric bi-stable wake and a stable wake, asymmetric in the vertical direction, is consistent with that found by Barros et al (2017) when perturbing the underbody flow of an Ahmed body with a similar aspect ratio.

Less evident changes are seen in the dynamics of the global oscillating modes. The application of tapers to the model vertical trailing edges does not seem to affect the vertical flapping, unlike that seen in Chap. 4, in the case of tapers applied to the horizontal edges of the same model. An inflection point around $St_H = 0.20$ is seen in the PSD plot obtained for the temporal coefficients associated with the vertical symmetry breaking mode, for all chamfer angles considered in the present investigation (Fig. 5.8d). No variations in either location or amplitude of this point are observed as ϕ_s is increased. More significant changes are reported for the lateral flapping. As the side shear layers are deflected inwards by the inflow generated by the tapered surfaces and their separation is reduced, stronger aerodynamic interactions are observed between the two sides of the model. This ultimately results in a strengthening of the wake's oscillations in the lateral direction, as highlighted by the growth in amplitude of the peak seen at $St_H \approx 0.17$ in the PSD plot obtained for the temporal coefficient referring to the lateral symmetry breaking POD mode (Fig. 5.8c). In analogy with that seen in §4.2.2 for the horizontal case, the frequency at which the peak is located is seen to change with the taper angle, shifting from $St_H = 0.13$ for the square-back configuration to $St_H = 0.17$ for $\phi_s \geq 12°$. The same frequency was also reported by McArthur et al (2016) when studying the dynamics of the wake developing downstream of a square-back body with $H > W$. For chamfer angles grater than 12°, this mode becomes so strong that the frequency peak at $St_H = 0.17$ becomes the only one visible in the spectrum of the temporal coefficient related to the symmetry preserving mode (Fig. 5.8e), whereas a small hump is seen for $\phi_s \leq 12°$ around at $St_H = 0.07$, corresponding to the wake pumping described in §3.2.4. The peak seen at $St_H = 0.068$ for $\phi_s = 20°$ appears to be different. The narrower bandwidth associated with this peak suggests that its origin is to be found in the wind tunnel itself. This frequency corresponds to the fan rotational speed needed to achieve a free-stream velocity of $40\,m/s$ inside the wind tunnel test section and is a sub-harmonic of the blade passing frequency isolated in §3.2.2.

5.3 Sensitivity of the wake dynamics to small variations of the model pitch angle

As already discussed in §5.1, the trend observed in the present investigation between the drag of the entire model $\overline{C}_D$ and the side taper angle ϕ_s appears to be in good agreement with that described in the work of Perry et al (2015) for a similar case. Nevertheless, noticeable differences are observed in the pressure distribution on the model rearward facing surfaces. The pressure maps reported in Perry et al (2015) for different values of ϕ_s are all characterised by a

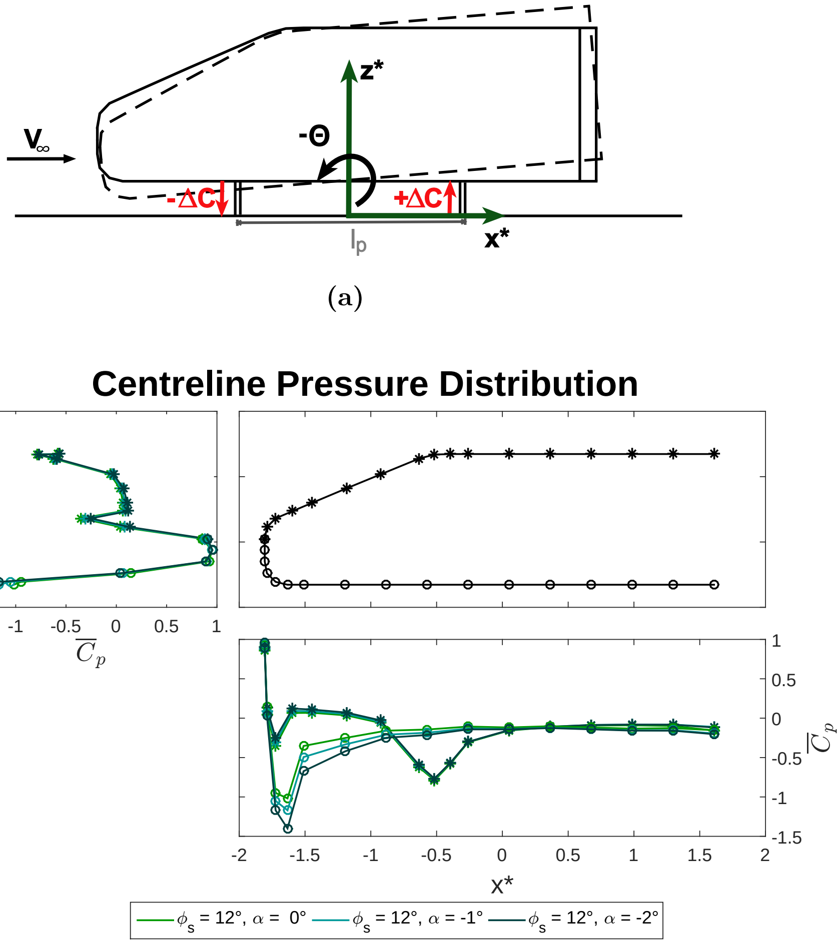

(a)

(b)

Figure 5.12: **a** schematic representation of the pitch angle variation; **b** centreline pressure for the configuration with $\phi_s = 12^o$, tested at $\Theta = 0.0^o$, $\Theta = -1.0^o$ and $\Theta = -2.0^o$. In **b** the symbol '$*$' denotes the taps located on the upper surfaces whilst '$\circ$' refers to the taps placed on the lower half of the model.

positive pressure gradient in the vertical direction, with the region of lower pressure located close to the bottom trailing edge. This appears to be in contrast with the results obtained here, showing a wake asymmetric in the vertical direction, but with $\frac{\partial C_p}{\partial z} < 0$ (Fig. 5.3 and 5.4). In order to shed some light on the origin of these discrepancies, bearing in mind the high level of sensitivity shown by axisymmetric bodies' wakes to small pitch angle variations (as pointed out by Grandemange et al (2012b), Wolf and Stumpf (2014) and Gentile et al (2017)), an investigation into the effects of limited changes of the model pitch angle Θ on the main time averaged and unsteady features of the wake developing downstream of the Windsor body with side trailing edge tapers was carried out. For the sake of simplicity the chamfer angle was fixed at 12°. The model was pitched 'nose down' ($\Theta < 0$) in order to force the wake to switch from the downwash dominated configuration described in §5.1 to an upwash dominated state. The pitch angle was changed by varying the distance between the model and the ground using the pins connecting the model with the underfloor balance. The fore-body was lowered by ΔC (with $\Delta C = (l_p/2)\tan(\Theta)$, where l_p denotes the distance separating front and rear pins), whilst the aft-body was raised by the same amount, as depicted in Fig. 5.12a. Two different values of Θ were considered, respectively equal to $-1°$ and $-2°$.

	$\Theta = 0.0°$	$\Theta = -1.0°$	$\Theta = -2.0°$
$\partial C_p/\partial z^*$	-0.177	0.114	0.206

Table 5.1: Vertical pressure gradient for different values of the model pitch angle Θ. $\partial C_p/\partial z^*$ was determined considering two taps located on the centreline of the base at $z^* = 0.490$ and $z^* = 0.856$.

During the experiment, the pressure acting on the model base was recorded using a single scanner, as discussed in §2.4. A second scanner was employed to determine the pressure distribution on the model centreline. 33 pressure taps were used in this case, with a finer distribution in the locations where the strongest pressure gradients were expected. The time averaged values of C_p are presented in Fig. 5.12b. The decrease of Θ is shown to yield a reduction in the static pressure recorded on the model underbody. This is particularly visible at the bottom leading edge of the model's nose, where the suction already seen for $\Theta = 0.0°$ is further accentuated. The pressure then gradually increases while moving downstream, although the values of C_p measured close to the model trailing edges for the pitched configurations are still $\approx 30\%$ lower than those recorded at $\Theta = 0.0°$. A pressure increase of similar magnitude is observed on the upper surfaces, further confirming the upwards shift of the location of the front stagnation point. As a result, the pressure difference between the upper and lower surfaces in the region of the model trailing edges is seen to increase.

For $\Theta = -1°$, a positive pressure gradient is observed on the base, in the vertical direction (Tab. 5.1). Nevertheless, the magnitude of $\partial C_p/\partial z^*$ is $\approx 36\%$ lower than that measured at $\Theta = 0.0°$, suggesting a more uniform pressure distribution. In these conditions, a 4.7% drop is observed in the base pressure drag ($\overline{C}_{D_{Base}}$). A region of lower pressure starts to form close to the bottom trailing edge (Fig, 5.13a, first column), matching that shown in the contour plots presented in Perry et al (2015). The region of suction increases in size and strength when the pitch angle is further decreased (Fig, 5.13b, first column), resulting in a vertical pressure gradient even stronger in magnitude that that recorded at $\Theta = 0°$ (Tab. 5.1). At the same time, $\overline{C}_{D_{Base}}$ is reported to increase by 8.1% over the same case.

As previously discussed in §5.1, the changes in pressure distribution observed over the model base are the result of modifications in the time averaged wake topology. In particular, the

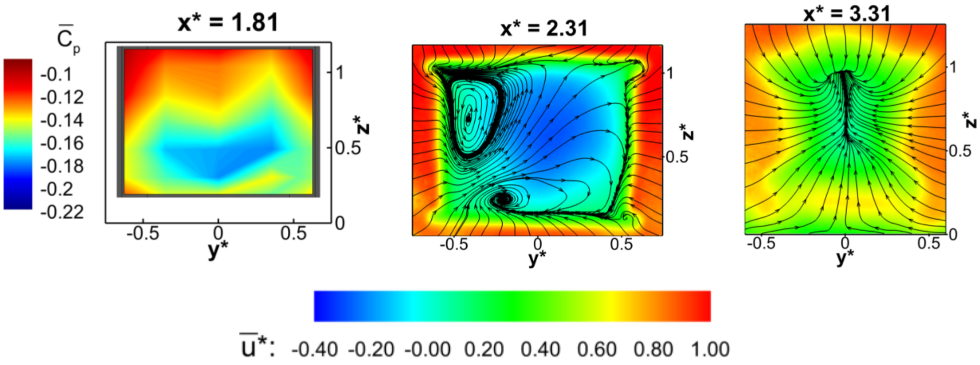

(a) $\phi_s = 12^o$, $\Theta = -1.0^o$

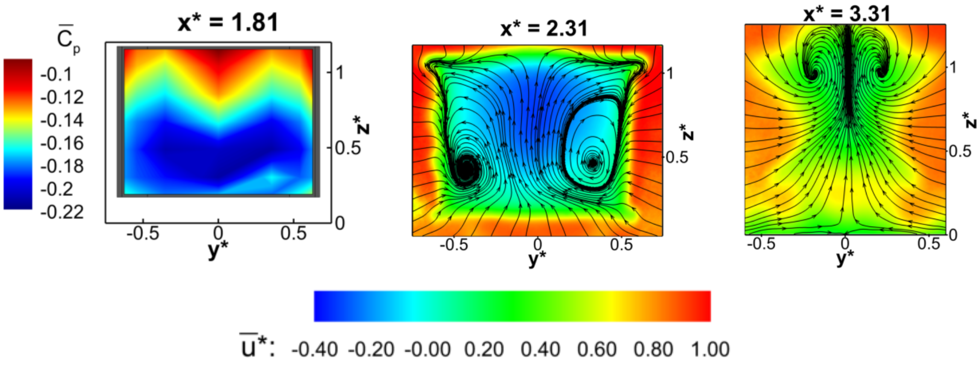

(b) $\phi_s = 12^o$, $\Theta = -2.0^o$

Figure 5.13: Time averaged results for the configuration with $\phi_s = 12^o$, tested at $\Theta = -1.0^o$ **(a)** and $\Theta = -2.0^o$ **(b)**. From left to right: $\mathbf{x^* = 1.81}$, base pressure distribution; $\mathbf{x^* = 2.31}$ and $\mathbf{x^* = 3.31}$, PIV stereo cross-planes. All PIV fields are coloured according to the values of the axial component of the velocity u^*; the streamlines refer to the in-plane components of the velocity.

wake is seen to rotate around the centre of the model base as Θ is decreased. The symmetry in the vertical direction is almost fully restored for $\Theta = -1.0°$. This is particularly evident when looking at the PIV vertical mid-plane reported in Fig. 5.14a and the cross-plane located downstream of the wake closure ($x^* = 3.31$ in Fig. 5.13a). Something different, however, is seen when the cross-plane located at $x^* = 2.31$ is considered (Fig. 5.13a). In this location the wake is aligned along a diagonal running from the bottom-left corner to the top-right corner of the model base. This is similar to that seen in §5.1 for the configuration with the 6° side edge tapers, although the alignment in that case is with the opposite diagonal. Unlike that observed in §5.1, however, bigger discrepancies are seen when the wake topology captured on this plane is related to the base pressure distribution. From the location of the two vortical structures seen at $x^* = 2.31$, one would expect a larger suction on the left-hand side of the base and a better pressure recovery on the opposite side. Instead, a good level of lateral symmetry

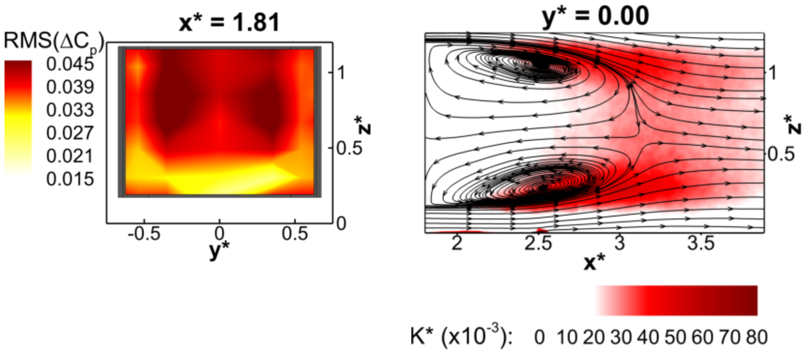

(a) $\phi_s = 12^o$, $\Theta = -1.0^o$

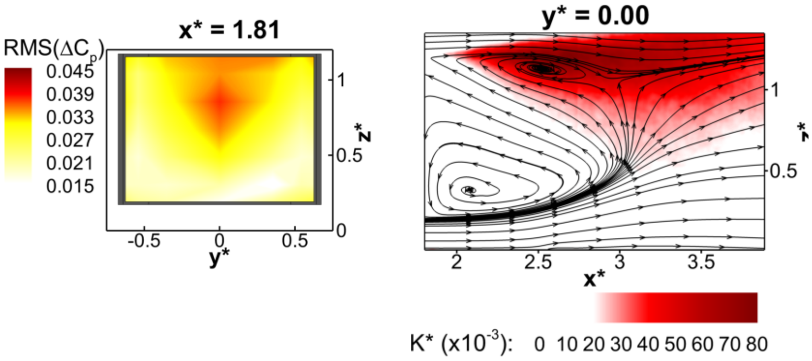

(b) $\phi_s = 12^o$, $\Theta = -2.0^o$

Figure 5.14: Base pressure fluctuation and non dimensional turbulent kinetic energy (at $y^* = 0.00$) for the configuration with $\phi_s = 12^o$, tested at $\Theta = -1.0^o$ **(a)**, $\Theta = -2.0^o$ **(b)**.

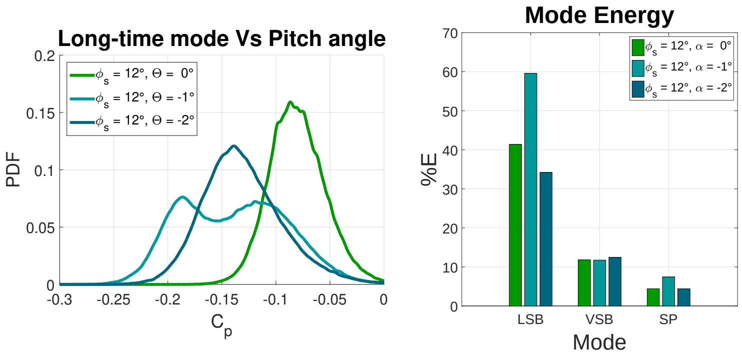

(a) (b)

Figure 5.15: **a** PDF of the values of C_p recorded by one of the pressure taps placed in the region of highest pressure fluctuation; **b** energy associated with 3 of the most energetic POD modes (base pressure data).

is observed in the pressure map reported in Fig. 5.13a. The reason of these differences is to be found in the shorter duration of the PIV recordings ($T_{samp} \approx 137\,s$) compared to the duration

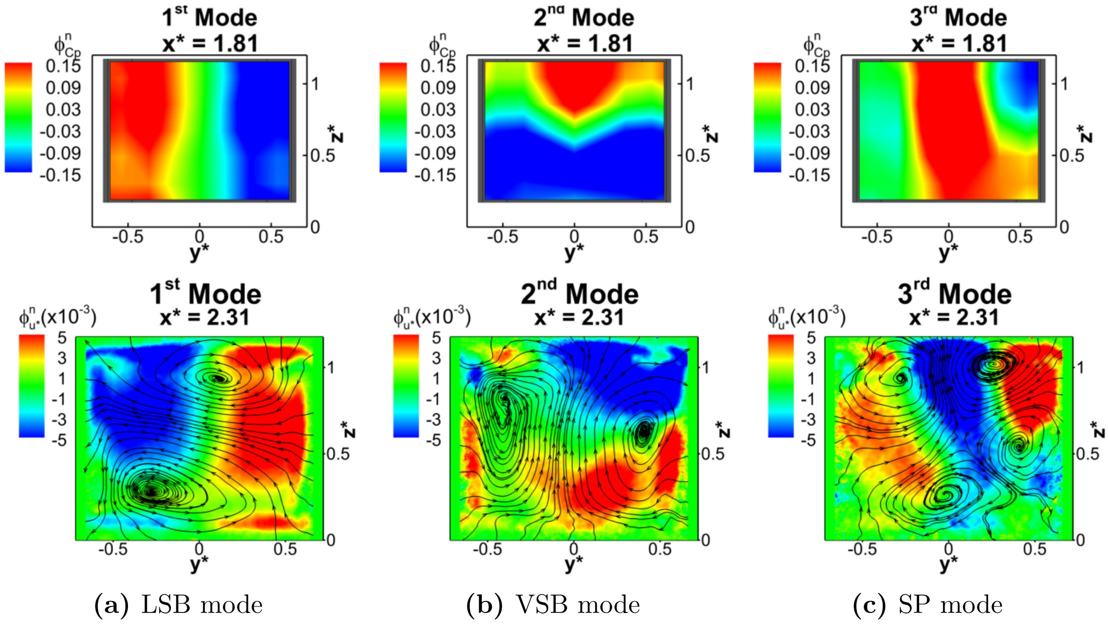

(a) LSB mode **(b)** VSB mode **(c)** SP mode

Figure 5.16: Spatial distribution of 3 of the most energetic POD modes extracted from the base pressure distribution (top row) and PIV cross-plane at $x^* = 2.31$ (bottom row) for the configuration with $\phi_s = 12°$, tested at $\Theta = -1.0^o$. The modes are ordered according to their topology: **a** lateral symmetry breaking mode (LSB), **b** vertical symmetry breaking mode (VSB), **c** symmetry preserving mode (SP). $\phi^n_{C_p}$ refers to the magnitude of the spatial eigen-modes extracted from the field of the pressure fluctuation. The eigen-functions related to the velocity fluctuation are coloured according to the values of the through plane component $\phi^n_{u^*}$ whereas the streamlines are drawn considering the in-plane components $\phi^n_{v^*}$ and $\phi^n_{w^*}$.

of the pressure tapping acquisition ($T_{samp} = 630\,s$). In the case of bi-stable or multi-stable wakes, indeed, a short sampling time may lead to a bias of the time averaged results towards one state, as it is difficult to guarantee that all states are explored for the same amount of time (especially in presence of average time between switches grater than $5\,s$). In addition, from that written in Chap 3, it is also clear that, as a bi-stable or multi-stable condition is approached, the effect of small misalignments in the experimental setup can be amplified, increasing the occurrence of a particular state. This has already been observed in the case of variations of the yaw angle (as discussed in §3.2.1.1), and, in analogy with that seen in the case of axisymmetric bodies by Gentile et al (2017), it also seems to apply to changes in the pitch angle.

The long-time instability, that almost completely disappears when 12° side tapers are applied to the model at 0° pitch (see §5.2), is seen to gain strength when the model pitch angle is changed to $\Theta = -1.0°$ and the symmetry in the vertical direction in the time averaged wake topology is recovered. This becomes clear when looking at the unsteady results presented in Fig. 5.14a. As the symmetry in the vertical direction is restored, a more even distribution of turbulent kinetic energy is observed between the two horizontal shear layers. Indeed, having a similar amount of turbulent activity between two opposite shear layers seems to be a necessary

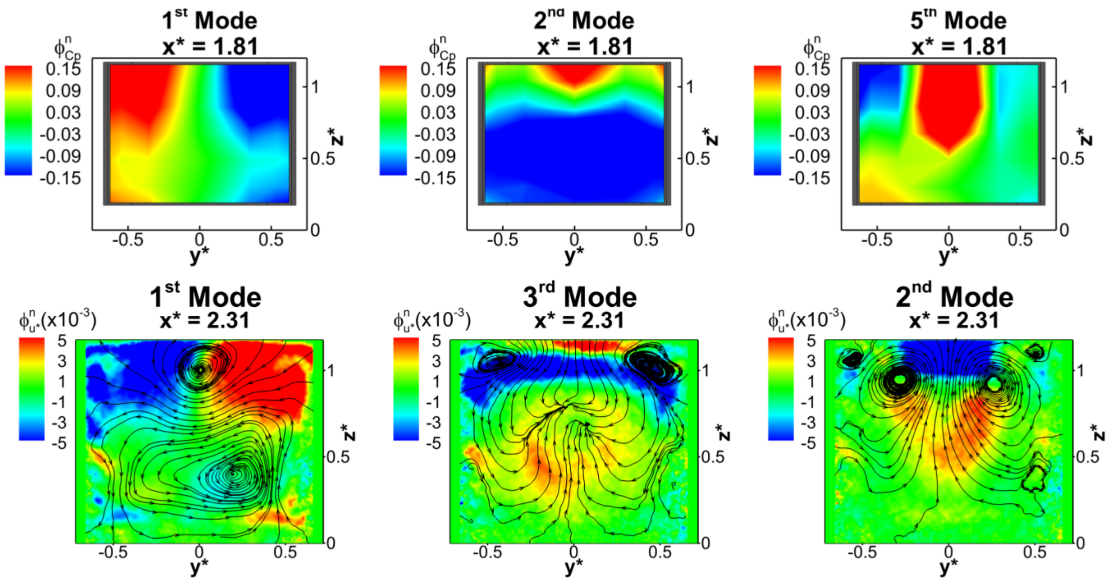

(a) LSB mode **(b)** VSB mode **(c)** SP mode

Figure 5.17: Spatial distribution of 3 of the most energetic POD modes extracted from the base pressure distribution (top row) and PIV cross-plane at $x^* = 2.31$ (bottom row) for the configuration with $\phi_s = 12°$, tested at $\Theta = -2.0^o$. The modes are ordered according to their topology: **a** lateral symmetry breaking mode (LSB), **b** vertical symmetry breaking mode (VSB), **c** symmetry preserving mode (SP). $\phi^n_{C_p}$ refers to the magnitude of the spatial eigen-modes extracted from the field of the pressure fluctuation. The eigen-functions related to the velocity fluctuation are coloured according to the values of the through plane component $\phi^n_{u^*}$ whereas the streamlines are drawn considering the in-plane components $\phi^n_{v^*}$ and $\phi^n_{w^*}$.

condition for the wake symmetry, confirming the trends already observed in §4.2.2. An increase in the level of unsteadiness is also noted on the base. The region of high pressure fluctuation is reported to increase in size and the highest values of $RMS(\Delta C_p)$ tend to cluster around two lobes, similar to that seen in the case of bi-stable wakes. A larger scatter is observed in the values of C_p recorded in this region. Indeed, as shown in Fig. 5.15a, the PDF of the signal recorded by one of the taps located in this area tends towards a bi-modal distribution, similar to that reported in §3.2.1 for the square-back case. But the similarities with the square-back configuration go further than that. Strong analogies between the two cases are seen in the distribution of the fluctuating energy between the first three modes (Fig. 5.15), with the lateral symmetry breaking mode alone accounting for at least 60% of E (resulting in a $\approx 50\%$ increase over the energy captured by the same mode for the configuration with $\phi_s = 12°$, tested at $\Theta = 0.0°$), and in the shape of the spatial functions associated with the modes themselves. As shown in Fig. 5.16a and 5.16b, the first two orthogonal symmetry breaking modes extend for the entirety of the base as well as the wake cross-section measured at $x^* = 2.31$, like that seen in §3.2.2 for the square-back case. Similar considerations apply to the symmetry preserving mode, whose energy content is more than 60% higher than that reported at $\Theta = 0.0°$ (Fig.

5.15b). Furthermore, two planes of symmetry are seen in the spatial function related to this mode when the PIV cross-plane located at $x^* = 2.31$ is considered (second row in Fig. 5.16c). Unlike that seen in the square-back configuration, however, the two planes are not aligned with the two symmetry planes of the base but form an angle of $\approx 45°$. This may be related to the fact that in this case the time averaged wake appears to be oriented diagonally.

The re-activation of the long-time instability is accompanied with the appearance of multiple states. This is clear when looking at the scatter plot between the temporal eigenvectors related to the two symmetry breaking modes, reported in Fig. 5.18a. Unlike that seen for the model tested at $\Theta = 0.0°$ (Fig. 5.9b), the points on the A_{VSB}, A_{LSB} plane tend to cluster around multiple attractors, resulting in a 'U' shaped cloud similar to that seen for the configuration equipped with 6° side edge tapers (Fig. 5.9a), apart from the fact that the third attractor is now located in the lower half of the plot ($A_{VSB} < 0$) rather than being in the upper portion ($A_{VSB} > 0$). The wake indeed is seen to switch between two lateral symmetry breaking states and a vertical symmetry breaking state, as shown in the phase averaged low order model reported in Fig. 5.19, built using the dataset recorded at $x^* = 2.31$ (following the procedure described in §3.2.5). Another difference with the multi-stable case discussed in §5.2 is the fact that the vertical symmetry breaking state (now observed at $\theta = 3/2\pi$) appears to be upwash dominated rather than downwash dominated. This is linked to the different distributions seen in the scatter plot on the A_{VSB}, A_{LSB} plane between the these two cases. From the plots presented in Fig. 5.19, it is also evident that only one symmetry preserving state is retained ($\theta = \pi/2$ in Fig. 5.19). As pointed out in previous cases, this state is still characterised by the presence of four recirculating structures. These structures, however, are now diagonally aligned, spanning from the bottom-left corner to the top-right corner of the base, following the same orientation seen for the symmetry preserving mode.

From that seen so far, it can be inferred that the reduction in base drag observed at $\Theta = -1.0°$ is to be ascribed mainly to the symmetrisation of the time averaged wake rather

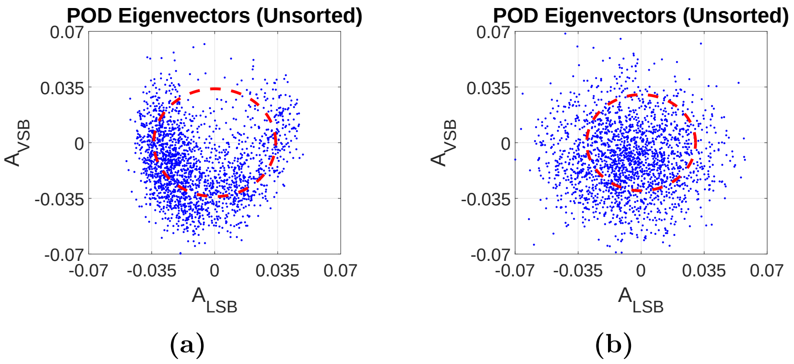

Figure 5.18: Scatter plots of the POD temporal coefficients associated with the VSB mode and the LSB mode for the configuration with $\phi_s = 12°$, tested at $\Theta = -1.0^o$ **(a)** and $\Theta = -2.0^o$ **(b)**. Data referring to the PIV cross-plane recorded at $x^* = 2.31$.

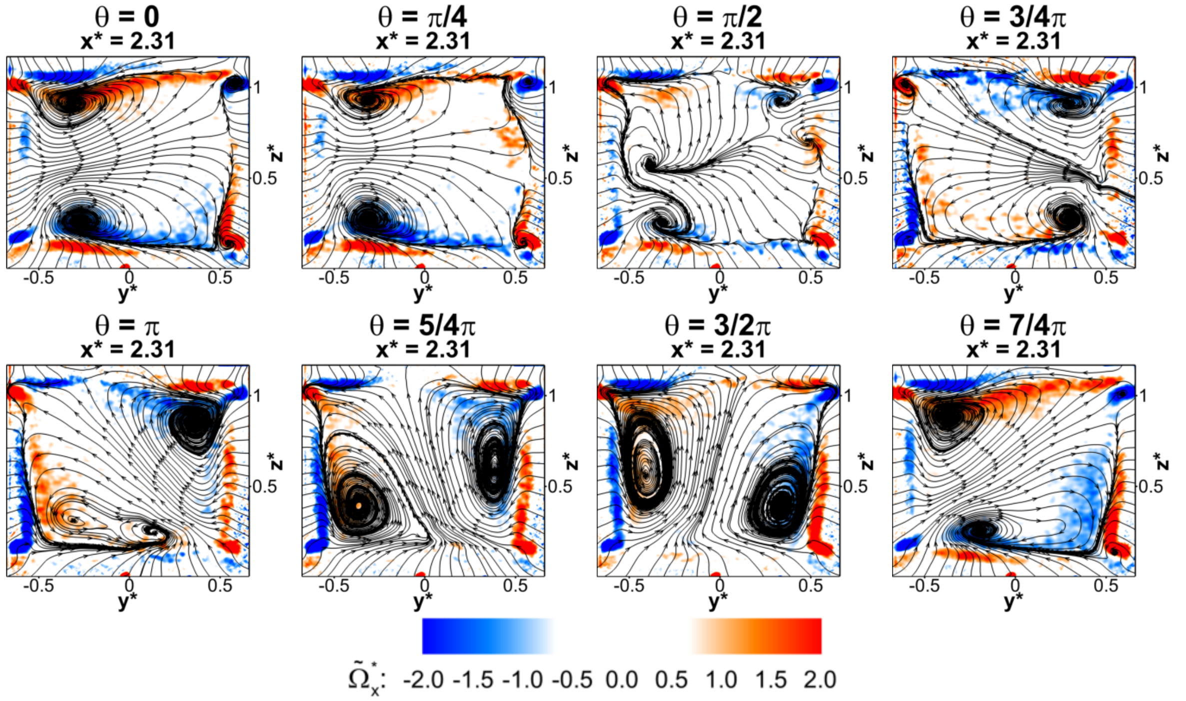

Figure 5.19: Low order phase averaged velocity field at $x^* = 2.31$ for the configuration with $\phi_s = 12°$, tested at $\Theta = -1.0^o$. The plots are coloured according to the values of the normalised streamwise component of the vorticity $\tilde{\Omega}_x^*$; the streamlines are drawn considering the in-plane components of the velocity field.

than being a consequence of the suppression of the long-time instability, which in fact appears to be much stronger than that seen at $\Theta = 0.0°$. This further reinforces the conclusions drawn at the end of Chap. 4.

The upwash dominated vertical symmetry breaking state becomes eventually the only state when the pitch angle of the model is decreased to $\Theta = -2.0°$ (Fig. 5.20). In these conditions, the wake locks into a stable state, which appears to be the mirror image of that proposed in Fig. 5.5d for the same configuration tested at $\Theta = 0.0°$. The level of unsteadiness seen in the pressure field on the model base, as well as the velocity field measured at $y^* = 0.00$, is greatly reduced compared to that seen for $\Theta = -1.0°$. Fluctuations are now limited to the region around the top shear layer (Fig. 5.14b). This is the only portion of the flow field where coherent motions in the lateral (LSB), vertical (VSB) and longitudinal (SP) directions are still visible (Fig. 5.17). A similar trend was reported by Gentile et al (2017) when changing the pitch angle of an axisymmetric body with a blunt trailing edge. The disappearance of the long-time instability is accompanied with a noticeable reduction of the amount of fluctuating energy captured by the LSB mode. Indeed, as shown in Fig. 5.15b, the energy associated with this mode drops to a level even lower than that obtained for the downwash dominated stable wake observed for $\Theta = 0.0°$. Further confirmations of the absence of a multi-stable condition are given by

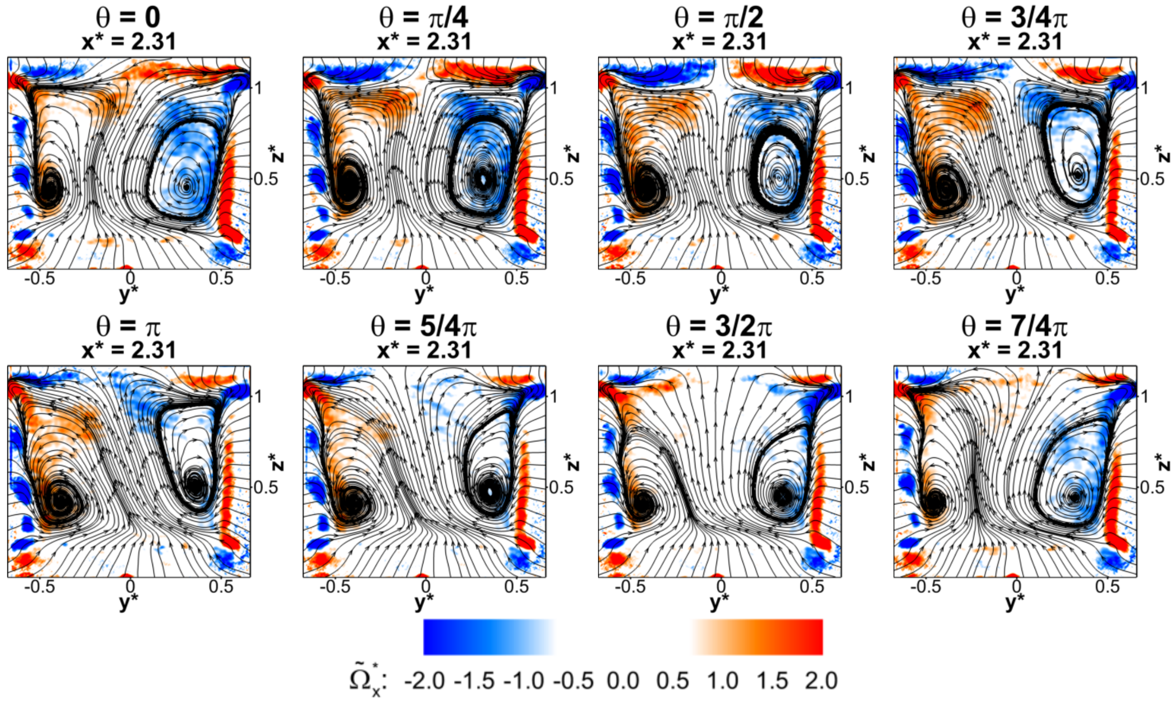

Figure 5.20: Low order phase averaged velocity field at $x^* = 2.31$ for the configuration with $\phi_s = 12°$, tested at $\Theta = -2.0^o$. The plots are coloured according to the values of the normalised streamwise component of the vorticity $\tilde{\Omega}_x^*$; the streamlines are drawn considering the in-plane components of the velocity field.

the shape of the PDF of C_p, in the region of the base characterised by the highest level of fluctuation (Fig. 5.15a), and the increased level of scattering observed among the points in the A_{VSB}, A_{LSB} plane (Fig. 5.18b). Nevertheless, an attractor located at $A_{VSB} < 0$, corresponding to the upwash dominated state observed in the phase averaged low order model reported in Fig. 5.20, is still present. The motion of the wake in this case is reduced to limited variations in the orientation of the flow reversal, as it oscillates from the top-left corner to the top-right corner of the base. These oscillations may be linked with the hump at $St_H \approx 0.015$ seen in the plots referring to the magnitude of the two-point coherence analysis performed between the top-left (TL) and top-right (TR) taps as well as the bottom-left (BL) and bottom-right (BR) taps, following the procedure described in §2.4.2 (Fig. 5.21c). The $\pi\, rad$ phase angle observed for this hump seems to further support this thesis.

An inflection point at a similar frequency is also seen for the case with $\Theta = 0.0°$ (Fig. 5.21a), but it disappears for $\Theta = -1.0°$ when the long-time instability, characterised by random switches between states, takes place (Fig. 5.21b). As far as the global oscillating modes are concerned, the unsteady behaviour of the wake is dominated by the lateral flapping at $St_H = 0.17$. This is evident when considering the plots referring to the two-point coherent analysis presented in Fig. 5.21 as well as the PSD of the POD temporal coefficients presented in Fig. 5.23. The

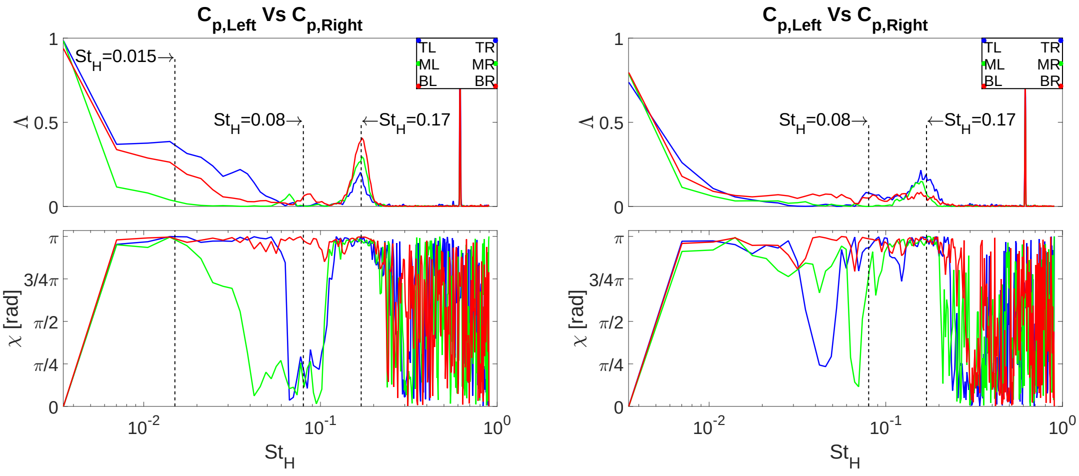

(a) $\Theta = 0.0^o$ **(b)** $\Theta = -1.0^o$

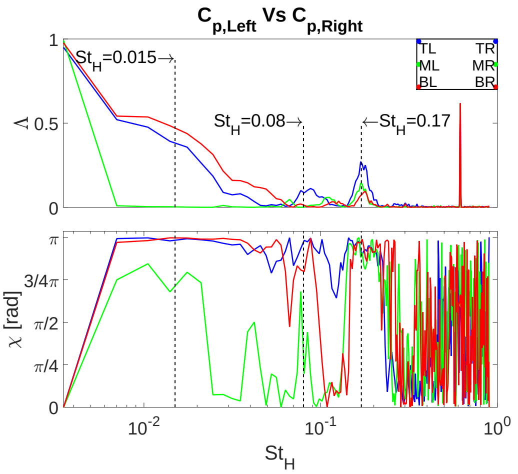

(c) $\Theta = -2.0^o$

Figure 5.21: **a**, **b**, **c** two-point coherence analysis performed considering the unsteady signal recorded by pressure taps placed at different locations along the vertical trailing edges of the model base, for the configuration with $\phi_s = 12°$ tested at different pitch angles: $\Theta = 0.0^o$ **(a)**; $\Theta = -1.0^o$ **(b)**; $\Theta = -2.0^o$ **(c)**.

'strength' of this motion, however, appears to change along the vertical direction depending on the orientation of the wake, matching the changes seen in the spatial function related to the *LSB* mode reported in Fig. 5.7a and 5.17a. Indeed the highest peak, in terms of coherence magnitude recorded at $St_H = 0.17$, is seen between the lower pairs of taps in the case of a downwash dominated wake ($\Theta = 0.0°$, Fig. 5.21a), but then moves to the upper pair of taps for an upwash dominated wake ($\Theta = -2.0°$, Fig. 5.21c), following the stabilisation of the upper and lower recirculations respectively. A similar trend is also observed for the peak located at $St_H = 0.08$ and associated with the 'wake pumping' (Duell and George, 1999). Unlike that

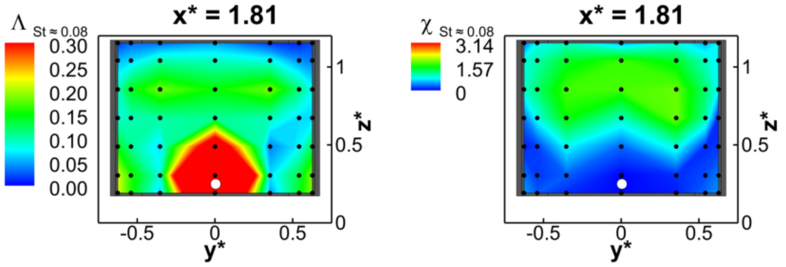

(a) $\Theta = 0.0^o$

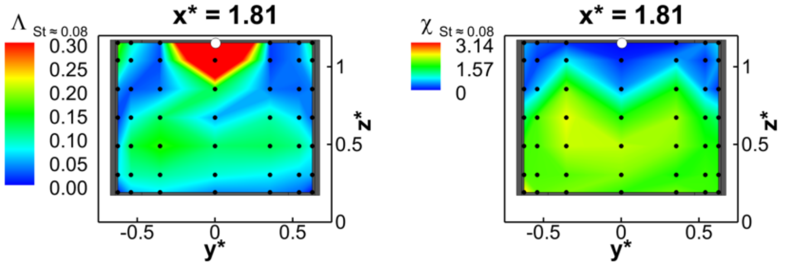

(b) $\Theta = -2.0^o$

Figure 5.22: Contour maps showing the coherence magnitude and phase between the signal recorded by the tap closest to the rear stagnation point and all the remaining taps on the base at $St_H \approx 0.07$ for $\Theta = 0.0^o$ **(a)** and $\Theta = -2.0^o$ **(b)**.

seen in §3.2.4 in the case of laterally bi-stable wakes, however, the mode associated with this frequency appears to be linked with a swinging motion of the horseshoe vortex depicted in Fig. 5.5d around the rear stagnation point, rather than being the result of an alternated 'stretching' and 'squeezing' in the streamwise direction alone. The coherence analysis performed at $St_H \approx 0.08$ between one of the taps closest to the rear stagnation point and all the remaining pressure sensors placed on the base shows indeed the presence of a large region with relatively good coherence ($\Lambda > 0.1$) and a phase angle $\chi(f) \approx \pi/2 rad$, which seems to be compatible with the existence of such a motion. This is observed at $\Theta = 0.0°$ (Fig. 5.22a) as well as $\Theta = -2.0°$ (Fig. 5.22b).

A trend similar to that described in §4.2.2 is observed for the non-dimensional frequency associated with the vertical flapping. The PSD plot obtained for the temporal coefficient related to the vertical symmetry breaking POD mode (Fig. 5.23b) shows that the frequency characteristic of this motion drops from $St_H = 0.20$ to $St_H = 0.17$ when the symmetry in the vertical direction is recovered in the wake and the gap separating the top and bottom shear layers is widened (at $\Theta = -1.0°$), for then increasing to $St_H = 0.21$ when the pitch angle of the model is changed to $\Theta = -2.0°$ and an upwash dominated wake is formed.

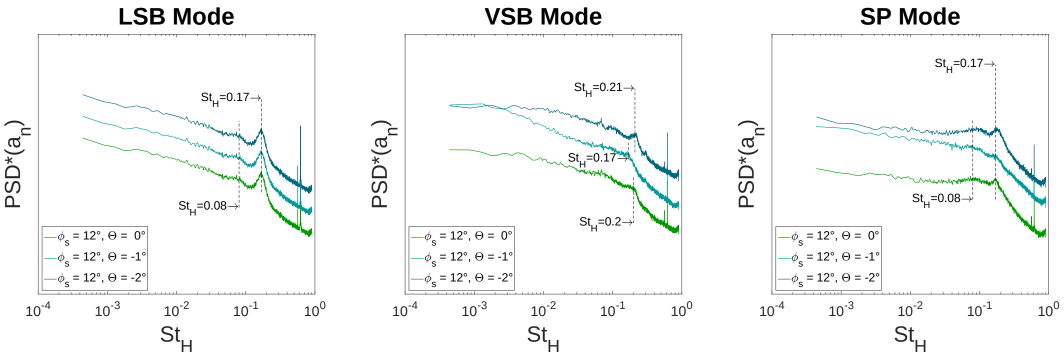

(a) (b) (c)

Figure 5.23: Spectra of the POD temporal coefficients associated with the lateral symmetry breaking mode (LSB, **a**), the vertical symmetry breaking mode (VSB, **b**), the symmetry preserving mode (SP, **c**). The curves have been shifted along the vertical axis.

5.4 Summary and conclusions

In this chapter, the aerodynamic effects produced by high aspect ratio tapers applied to the side trailing edges of the Windsor body have been investigated. The tapered surfaces have been shown to trigger a switch from a laterally asymmetric bi-stable wake to a stable wake, asymmetric in the vertical direction. The wake has been observed to retain a topology similar to that described for the lateral symmetry breaking states downstream of the simple square-back case (see Chap. 3), although rotated by 90°. As the chamfer angle ϕ_s is increased, the horizontal pressure gradient seen in the case of lateral symmetry breaking states is replaced by a negative vertical pressure gradient, being the result of the formation of a downwash dominated wake.

A $\approx 6\%$ drag reduction compared to the square-back case is reported for taper angles between 6° and 12°. This gain is to be ascribed to the circular vortex, responsible for the suction zone visible in any symmetry breaking state, that tends to ‘stretch’ in the streamwise direction, resulting in a $\approx 15\%$ reduction of the base pressure drag. No particular changes are observed in the short-time wake dynamics, except from a noticeable strengthening of the lateral flapping motion, as a consequence of the higher level of interactions between the two lateral shear layers, and a weakening of the pumping motion as ϕ_s is increased.

A better understanding of the transition from a laterally asymmetric bi-stable wake to a stable wake, asymmetric in the vertical direction, has been achieved by applying the phase averaged low order model already discussed in Chap. 3. For $\phi_s = 6°$, the wake has been observed to switch between two lateral symmetry breaking states and a vertical symmetry breaking state, resulting in a multi-stable condition that presents some similarities with that reported by Rigas et al (2014) and Gentile et al (2016) in the case of axisymmetric bodies. The latter state eventually becomes the only stable configuration of the wake for $\phi_s \geq 12°$. In these conditions the wake loses coherence every time the vortical structures come closer to the side shear layer.

The long-time instability is replaced by a swinging motion around the rear stagnation point, with a characteristic frequency of $St_H \approx 0.015$. A similar change is seen in the mode associated with frequency peak located at $St_H = 0.08$.

The transition between these two scenarios is consistent with that found by Barros et al (2017) when perturbing the underbody flow of a similarly shaped body. The fact that a similar behaviour is obtained regardless of the shear layer to which the perturbation is applied, suggests that the long-time instability is indeed the result of the establishment of a condition of equilibrium among all four shear layers bounding the wake. This may also explain the link between the direction of the long-time symmetry breaking mode and the model aspect ratio found by Grandemange et al (2013a). The fact that the wake is seen to switch laterally for $W > H$ and vertically for $W < H$ may be ascribed to the existence of stronger interactions between the horizontal shear layers in the first case and the vertical shear layers in the second case. This trend is consistent with that seen for the global oscillating modes, with a vertical flapping stronger than the lateral flapping when the gap between the horizontal shear layers is less than that one separating the vertical shear layers (see Chap. 3) and vice-versa.

A further confirmation of the fact that the long-time instability is the result of a condition of global equilibrium, and not just a function of the state of perturbation of a single shear layer, has been obtained by studying the sensitivity of the wake to small variations of the model pitch angle. A strengthening of the long-time instability is evident every time the symmetry in the vertical direction in the time averaged wake is recovered. In the same conditions, a further reduction of the base drag over the same model tested at zero degree pitch has also been observed (with $\Delta\overline{C}_{D_{Base}} = -4.9\%$). This is in good agreement with the findings of Grandemange et al (2015) and seems to suggest that a lower drag wake is not necessarily a more stable wake. Furthermore, a pitch angle variation of $\approx -1^\circ$ has been found to be sufficient to force the time averaged wake to switch from a downwash dominated topology to an upwash dominated topology. This high level of sensitivity may explain the differences when comparing the time averaged results obtained in the present investigation with those reported in the literature (Perry et al, 2015). The perturbation applied to the model in this case, in fact, is much weaker than that used for example in Castelain et al (2018) to trigger a similar switch, further confirming the existence of a delicate equilibrium among all shear layers that may also be at the origin of the high level of variability seen in the wake topologies reported by Makihara et al (2016) when considering more realistic vehicle shapes.

Chapter 6

Towards a more realistic geometry

In this chapter, wheels (either stationary or rotating) are applied to the simplified automotive geometry described in §2.1. Their impact on both the time averaged and unsteady features of the near-wake developing downstream of the main body is investigated. For the pure square-back configuration, the results show a general increase in base drag accompanied with the loss of vertical symmetry, particularly evident in the regions located behind each rear wheel. Here, the bottom recirculation is observed to increase in size at the expenses of the top one and move closer to the base, resulting in a decrease of the static pressure acting over the model rearward facing surfaces. In the same conditions, the stabilisation of the wake is also observed. The lateral symmetry breaking bi-stable mode is seen to weaken, replaced by a swinging motion of the reverse flow impinging on the upper portion of the base, with a non-dimensional frequency of $St_H \approx 0.02$. The pumping motion is also seen to disappear. The sensitivity of the wake to variations of the model's trailing edge geometry is then assessed. The slanted surfaces already used in Chap. 4 and 5 are applied to either the horizontal or the vertical trailing edges of the model, with the chamfer angle fixed at 12°. Different wake topologies are seen depending on the number and position of the tapers. A 'fully stable' wake is observed when a bottom diffuser is added to the model, resulting in an upwash dominated wake. In these conditions, the long-time instability is replaced by a lateral flapping motion, with a non-dimensional frequency of $St_H = 0.035$. In common with that seen in previous cases, a decrease in drag is seen every time the symmetry in the vertical direction is recovered. This, however, is not necessarily accompanied with the disappearing of the long-time instability. Indeed, the lowest base drag value is recorded for the model equipped with 12° side edge tapers, tested at +2° pitch in order to counteract the upwash seen for the same configuration at 0° pitch angle. In these conditions, the restoration of the continuity in the bottom shear layer is seen to coincide with the appearance of a multi-stable mode involving the entire near-wake recirculation.

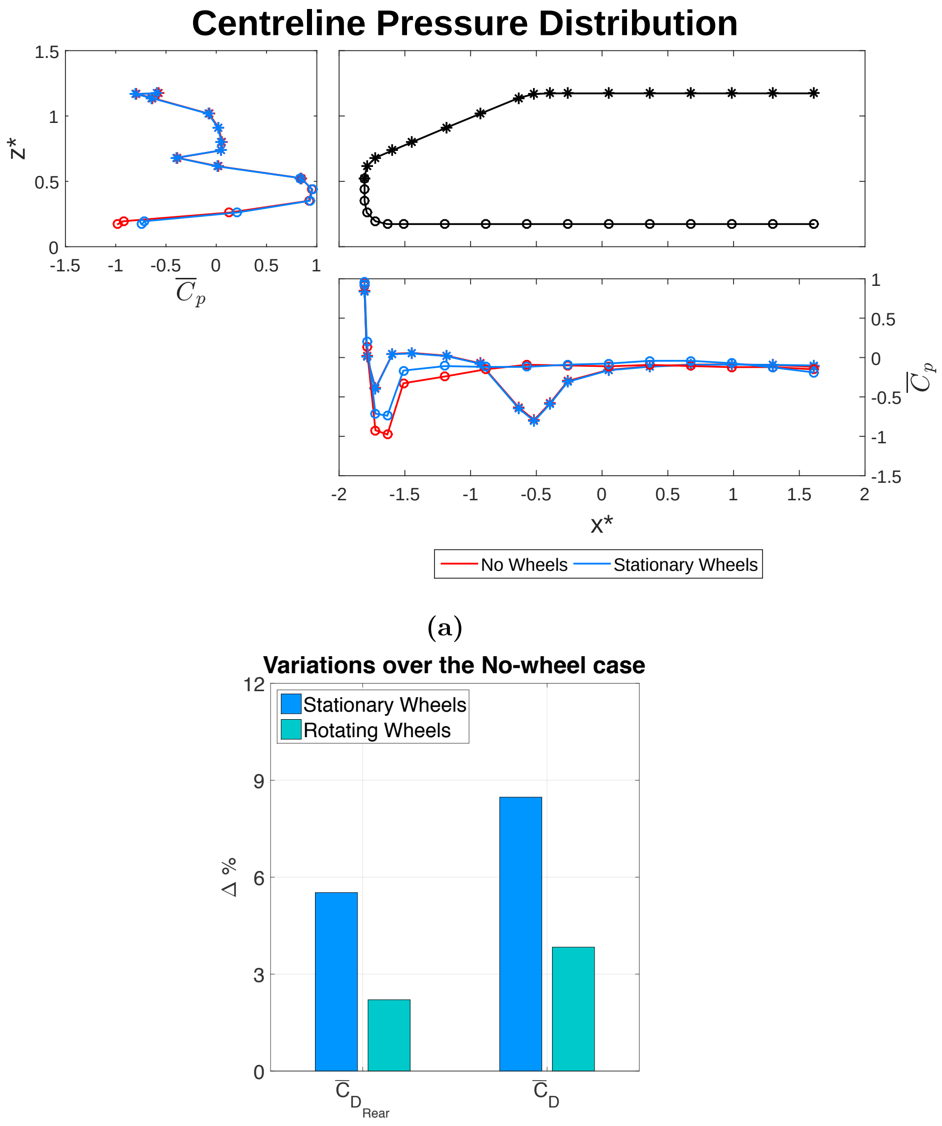

(a)

(b)

Figure 6.1: **a** centreline pressure for the square-back configuration with and without wheels; **b** effects of the wheel rotation on the time averaged aerodynamic drag acting on the main body (see §2.1).

6.1 Square-back configuration with wheels

When wheels are added to the square-back model, noticeable changes are observed in the pressure field under the model itself, as can be inferred from the variations in the centreline pressure distribution presented in Fig. 6.1a. The increased underbody blockage leads to a reduction of the suction seen at the bottom leading edge of the model's nose. The pressure

Config.	$\overline{C}_{D_{Rear}}$	$\overline{C}_D$	$\overline{C}_L$
No wheels	0.166	0.282	−0.025
Stationary wheels	0.175	0.306	0.173
Rotating wheels	0.170	0.293	0.182

Table 6.1: Time averaged values of the aerodynamic forces recorded for different wheel configurations. The results reported for the no-wheel configuration differ from those reported in Chap 3, as they were measured considering the second of the two models described in §2.1. Although the two models are characterised by the same shape, they present some differences in terms of pin location as well as panel gaps that may have affected the measurements. These small differences, however, are not believed to have had significant impact on the wakes developing downstream of the two bodies.

then gradually increases while moving downstream. Indeed, with wheels in place, higher values of static pressure are measured at the model centreline for most of the length of the underbody surface, with the only exception being the region downstream of the rear axle, where a decrease in C_p over the no-wheel case is observed. No significant changes are reported in the pressure distribution recorded on the upper surfaces between the two cases. The increase in C_p observed along the model underbody, combined with the pressure build up inside each wheel-well (Fabijanic, 1996), contributes to a $\approx 200\,count$ rise in the time averaged value of the lift coefficient measured on the main body (Tab. 6.1). A more limited increment is seen in the drag acting on the same body, with a 8.5% increase observed in the stationary-wheel case over the no-wheel case (Fig. 6.1b and Tab. 6.1). A similar trend is also observed in the values of the pressure drag acting over the model rearward facing surfaces ($\overline{C}_{D_{Rear}} = +5.4\%$), suggesting that a significant contribution to the drag increase experienced by the main body comes from changes in the pressure distribution over the rear-end. This becomes clear when looking at the time averaged base pressure map reported in the first column of Fig. 6.2. The uniform distribution seen in Chap. 3 for the square-back configuration without wheels (with $\partial C_p/\partial z^* \approx 0$ and $\partial C_p/\partial y^* \approx 0$) is replaced by a distribution asymmetric in the vertical direction, featuring a *'U'* shaped low pressure region developing close to the bottom trailing edge, similar to that seen in Chap. 4 when high aspect ratio tapers are added to the model's bottom trailing edge, leaving the top trailing edge squared.

However, no indication of the *'U'* shaped lower vortical structure, described in §4.1 in the case of upwash dominated wakes, is found when considering the velocity fields. Stronger similarities are instead seen with the $\phi_t = 12°, \phi_b = 12°$ case, as can be inferred from the results obtained for the cross-plane at $x^* = 2.31$. Four vortical structures are observed in this case, although with different sizes. A pair of bigger vortices is seen over the upper portion of the base, whereas two smaller vortices form close to the bottom trailing edge, in proximity to the gap separating the rear wheels. This is similar to that seen in the low drag case investigated in

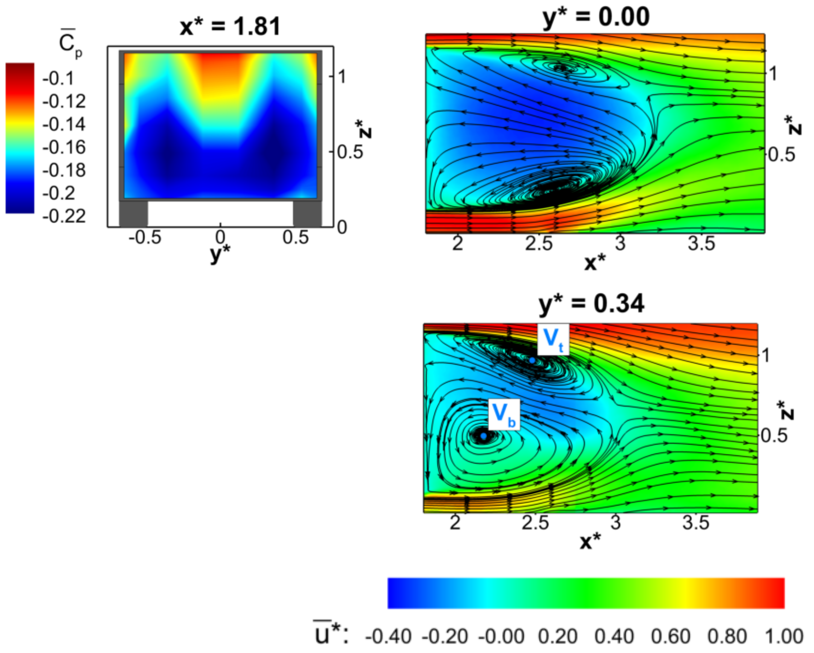

Figure 6.2: Time averaged fields for the square-back configuration with stationary wheels. Clockwise from top left: $\mathbf{x}^* = \mathbf{1.81}$ base pressure distribution; $\mathbf{y}^* = \mathbf{0.00}$ PIV vertical mid-plane; $\mathbf{x}^* = \mathbf{2.31}$ and $\mathbf{x}^* = \mathbf{3.31}$ PIV stereo cross-planes; $\mathbf{y}^* = \mathbf{0.34}$ PIV vertical off-centre plane. All PIV fields are coloured according to the values of the axial component of the velocity u^*; the streamlines refer to the in-plane components of the velocity. The blue dots denote the locations of the vortex cores on the plane at $y^* = 0.34$ (see Tab. 6.2).

***(a)* Stationary wheels**

Vortex ID	x^*	y^*	z^*
V_t	2.483	0.34	0.968
V_b	2.174	0.34	0.503

***(a)* Roating wheels**

Vortex ID	x^*	y^*	z^*
V_t	2.577	0.34	0.965
V_b	2.222	0.34	0.486

Table 6.2: Locations of the centres of the vortical structures captured by the PIV planes located at $y^* = 0.34$ (see Fig. 6.2 and 6.3): *(a) stationary wheels;* (b) rotating wheels. The locations of the vortex cores were determined using the Γ_1 criterion proposed by Graftieaux et al (2001).

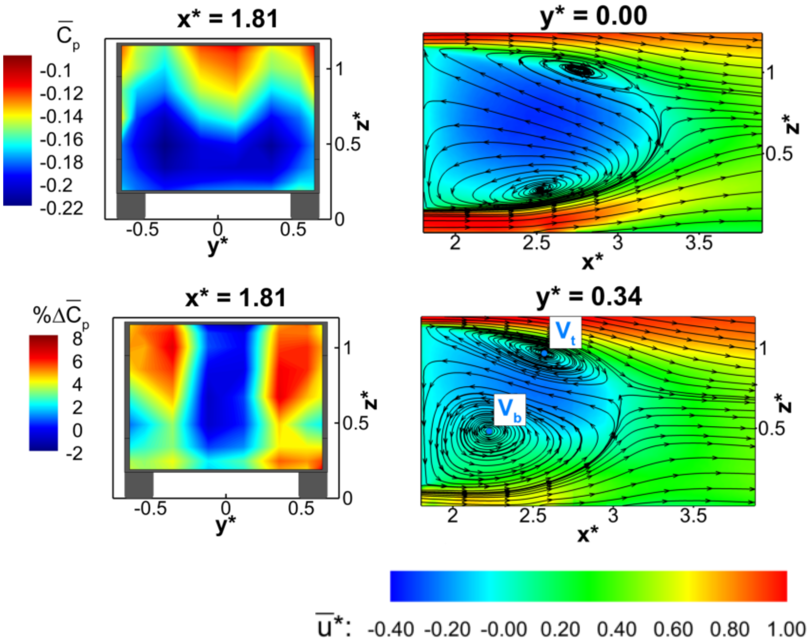

Figure 6.3: Time averaged fields for the square-back configuration with rotating wheels. Clockwise from top left: $\mathbf{x}^* = \mathbf{1.81}$, base pressure distribution; $\mathbf{y}^* = \mathbf{0.00}$, PIV vertical mid-plane; $\mathbf{y}^* = \mathbf{0.34}$, PIV vertical off-centre plane; pressure variation over the stationary wheel case, calculated considering the state average pressure fields (see §4.1.0.1). All PIV fields are coloured according to the values of the axial component of the velocity u^*; the streamlines refer to the in-plane components of the velocity. The blue dots denote the locations of the vortex cores on the plane at $y^* = 0.34$ (see Tab. 6.2).

Chap. 4, although without the same level of symmetry in the vertical direction, as the upper pair of vortices is seen to grow in size at the expense of the bottom pair. The disruption of the wake symmetry in the vertical direction is driven by the velocity deficit originating from the regions of separation developing behind the rear wheels as well as around the wheel-arches (see Regert and Lajos (2007), Krajnovic et al (2011) and Aljure Osorio (2017)). As this flow is entrained into the main body's wake, it feeds each side of the bottom recirculation, which in turn starts to expand (as seen in the plane at $y^* = 0.34$), leading to the formation of an upwash dominated wake, as shown by the PIV cross-plane captured at $x^* = 3.31$. The perturbing effect of the wheels is less evident when the vertical mid-plane is considered (at $y^* = 0.00$). A more balanced topology is seen in fact in this plane.

A more limited drag increase is observed in the case of rotating wheels, with $\Delta\overline{C}_D$ dropping by 4.2 percentage points over the stationary case (Fig. 6.1b and Tab. 6.1). This can be ascribed to the narrowing of the wheels' wake, as pointed out by Elofsson and Bannister (2002) and Wäschle (2007), which leads to a reduction of the pressure losses inside the wheel-wells together with an improvement of the pressure recovery over of the model base. This is confirmed by the time averaged pressure maps reported in Fig. 6.3. Although the overall topology of the

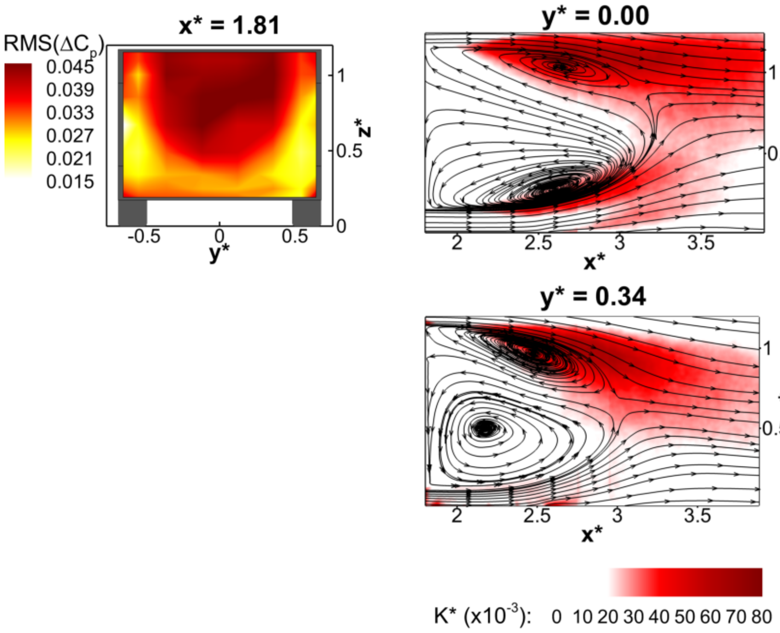

(a) Square-back, stationary wheels

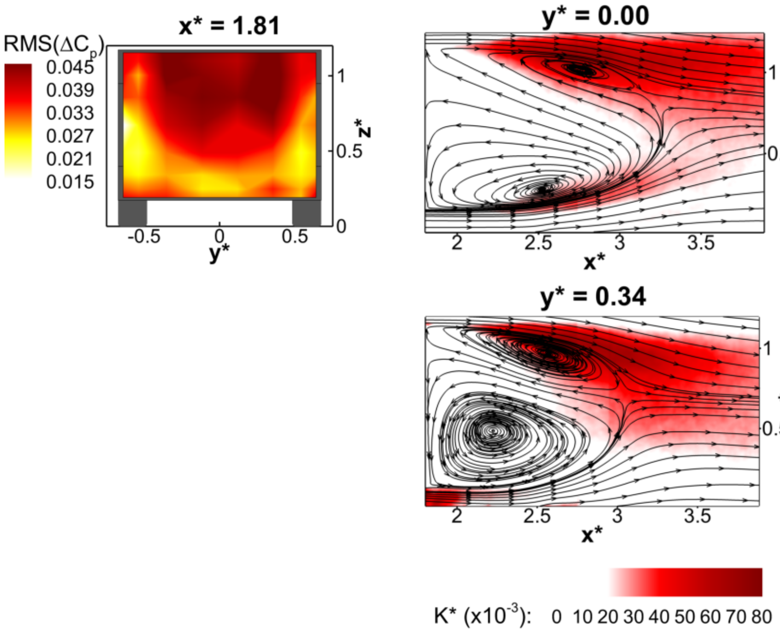

(b) Square-back, rotating wheels

Figure 6.4: Base pressure fluctuation and non dimensional turbulent kinetic energy (at $y^* = 0.00$ and $y^* = 0.34$) for the square-back configuration with stationary wheels **(a)** and rotating wheels **(b)**. The streamlines refer to the time averaged in-plane components of the velocity.

time averaged pressure distribution is preserved when compared to the stationary wheel case (top left plot in Fig. 6.3), an increase in static pressure is observed at each side of the base (at $|y^*|> 0.2$) in the rotating wheel case (bottom left plot in Fig. 6.3). Interestingly, most of the pressure recovery is seen on the upper portion of the base. This is in agreement with the findings of Wang et al (2018) and highlights the presence of changes in the recirculating structures on a 'global' scale, as becomes clear when considering the changes in location of the vortical structures seen on the plane at $y^* = 0.34$, calculated using the Γ_1 criterion proposed by Graftieaux et al (2001) and already discussed in §3.2.3 (Tab. 6.2). Indeed, the streamwise location of the core of the bottom recirculation seen at at $y^* = 0.34$ is reported to shift from $x^* = 2.174$, for the stationary case, to $x^* = 2.222$, for the rotating case, whilst the core of the upper vortex is reported to move from $x^* = 2.483$ to $x^* = 2.577$ in the same conditions (see dots in Fig. 6.2 and 6.3). No further changes, however, are noted in the topology of the time averaged wake. Strong similarities between the two cases are also seen when looking at the distribution of the turbulent kinetic energy K^* on the same planes (second and third column in Fig. 6.4). In the rotating case, an increase in the values of K^* is observed on the plane at $y^* = 0.34$, in the region located close to the ground just downstream of the rear wheels. This may be a consequence of the growth in the level of unsteadiness associated with the vortical structures developing around the wheel-arches when rotation is applied to the wheels, as suggested by the findings of Koitrand et al (2014). On the other hand, the level of unsteadiness is seen to decrease in proximity to the floor separation visible on the plane at $y^* = 0.00$, arguably as a result of an improvement in the boundary layer mixing in the latter case.

As already observed in Chap. 4 and 5, the loss of symmetry in the vertical direction is strictly linked to changes in the unsteady behaviour of the wake itself. In the case of a square-back configuration equipped with wheels, as the bottom recirculation grows in size, it also tends to become more stable. Indeed, compared to that seen in Chap. 3 and 4 for the no-wheel case, the region with the highest level of turbulent kinetic energy is shifted upwards, towards the top shear layer, whilst a zone of low pressure fluctuation is seen to develop between the side trailing edges and the lower portion of the base, as shown in the contours plot reported in the first column of Fig. 6.4. Nevertheless, high values of $RMS(\Delta C_p)$ are still seen over the upper portion of the base. The PDF of the C_p values recorded by one of the taps located in this region reveals the existence of a large scattering (Fig. 6.5a), although without featuring the bi-modal distribution observed in §3.2.1 for the same configuration without wheels. A similar trend is reported for the PDF of the values of the temporal coefficient associated with the lateral symmetry breaking POD mode (Fig. 6.5b). The weakening of the long-time instability is confirmed by the ≈ 30 percentage point drop observed in the energy associated with the same mode (Fig. 6.5c). Changes are also noticed in the shape of the spatial function related to this mode (Fig. 6.6a). Coherent motions of the wake in the lateral direction are seen only in the upper half of the base, as a consequence of the 'stabilisation' of the lower portion of the wake. In fact, more complex motions are seen to develop in the latter region, as can be inferred

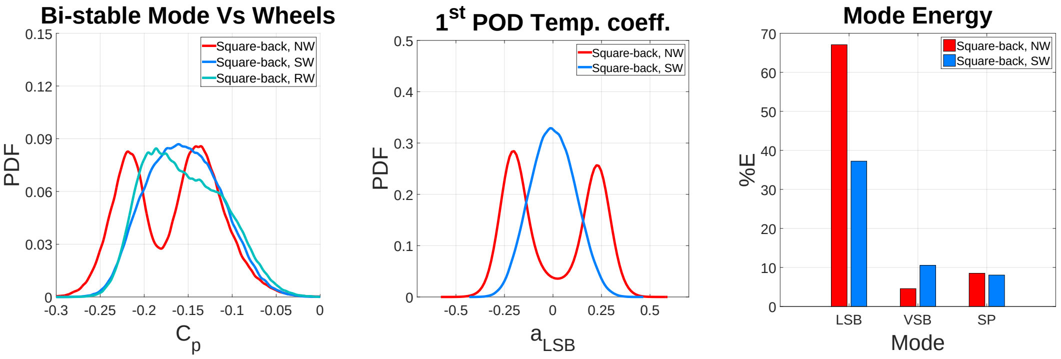

(a) (b) (c)

Figure 6.5: a PDF of the values of C_p recorded by one of the taps located in the region of high pressure fluctuation; **b** PDF of the values of first POD temporal coefficient; **c** energy associated with 3 of the most energetic POD modes. (NW) model with no wheels; (SW) model with stationary wheels; (RW) model with rotating wheels.

by looking at the shape of 1^{st} POD spatial mode extracted from the velocity field recorded recorded at $x^* = 2.31$. The two-vortex structure seen in §3.2.2 for the square-back configuration without wheels is now replaced by a more 'intricate' topology, with the lower vortex replaced by two pairs of smaller recirculations. This suggest the presence of more complex dynamic motions, arguably linked to the shedding of vortical structures from the wheels, as documented by Croner et al (2013).

The loss of symmetry in the vertical direction is also reported to trigger changes to the POD mode associated with motions of the wake in the same direction (VSB mode in Fig. 6.6b). Although the energy content of this mode tends to increase compared to the no-wheel case (from $\approx 5\%$ to $\approx 10\%$, as shown in Fig. 6.5c), the amplitude of the vertical oscillation is reduced, being now limited to the region surrounding the top shear layer. This is consistent with the concentration of turbulent kinetic energy seen in the 2D-PIV planes presented in Fig. 6.4 and matches that seen in Chap 5 for stable asymmetric wakes. Further similarities between these two cases can be noted when looking at the spatial function associated with the symmetry preserving POD mode (SP mode in Fig. 6.6c). In both cases, indeed, the loss of symmetry in the vertical direction in the time averaged wake topology coincides with the disappearance of the horizontal plane of symmetry in the spatial function associated with the SP mode.

Further insights on the effects produced by the addition of wheels on the long-time lateral wake dynamics are provided by the low order phase averaged model described in §3.2.5. As shown in Fig. 6.7 for $x^* = 2.31$, the wake appears to be 'locked' into a lateral symmetry preserving, upwash dominated state. Only a swinging motion of the flow reversal in the upper portion of the wake is observed, similar to that seen in §5.3 for the model equipped with 12° side edge tapers, tested at −2° pitch. This swinging motion appears to be quite different from the lateral oscillating mode described in §4.2.1 for the no-wheel configuration featuring

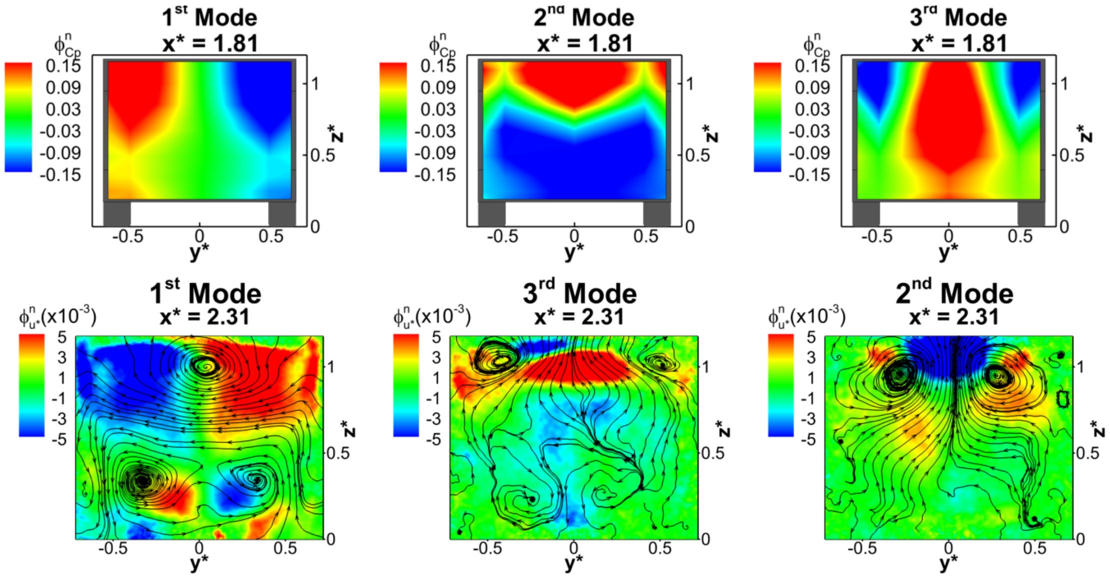

(a) LSB mode **(b)** VSB mode **(c)** SP mode

Figure 6.6: Spatial distribution of 3 of the most energetic POD modes extracted from the base pressure distribution (top row) and PIV cross-plane at $x^* = 2.31$ (bottom row) for the square-back configuration with stationary wheels. The modes are ordered according to their topology: **a** lateral symmetry breaking mode (LSB), **b** vertical symmetry breaking mode (VSB), **c** symmetry preserving mode (SP). $\phi^n_{C_p}$ refers to the magnitude of the spatial eigen-modes extracted from the field of the pressure fluctuation. The eigen-functions related to the velocity fluctuation are coloured according to the values of the through plane component $\phi^n_{u^*}$ whereas the streamlines are drawn considering the in-plane components $\phi^n_{v^*}$ and $\phi^n_{w^*}$.

12° tapers on both horizontal trailing edges, despite the similarities observed in the time averaged results between the two cases. The origin of these differences may be found in the different process driving the suppression of the bi-stable mode. For the configuration with $\phi_t = 12°, \phi_b = 12°$ and no wheels, the weakening of the lateral instability is a consequence of the increase in the curvature of both horizontal shear layers, as well as the reduction of the gap separating them, over the entire width of the base. In the case of the square-back model equipped with wheels, on the other hand, the stabilisation of the wake seems to be a consequence of the formation of a stable circular shaped vortical structure, which appears to be located downstream of each rear wheel (Fig. 6.4) rather than being centred with the model centreline. The symmetry in the vertical direction, indeed, is mainly lost in these regions, whereas a good balance between the upper and lower recirculations is still seen in the wake for $y^* = 0.00$ (Fig. 6.2 and 6.3). Nevertheless, the two motions feature similar time scales. This becomes evident when considering the PSD of the temporal coefficient referring to the lateral symmetry breaking POD mode, presented in Fig. 6.8a. As seen in the $\phi_t = 12°, \phi_b = 12°$ case discussed in §4.2.1, the -2 law decay, observed for the square-back configuration without wheels at very low frequency and linked by Grandemange (2013) to the presence of the bi-stable

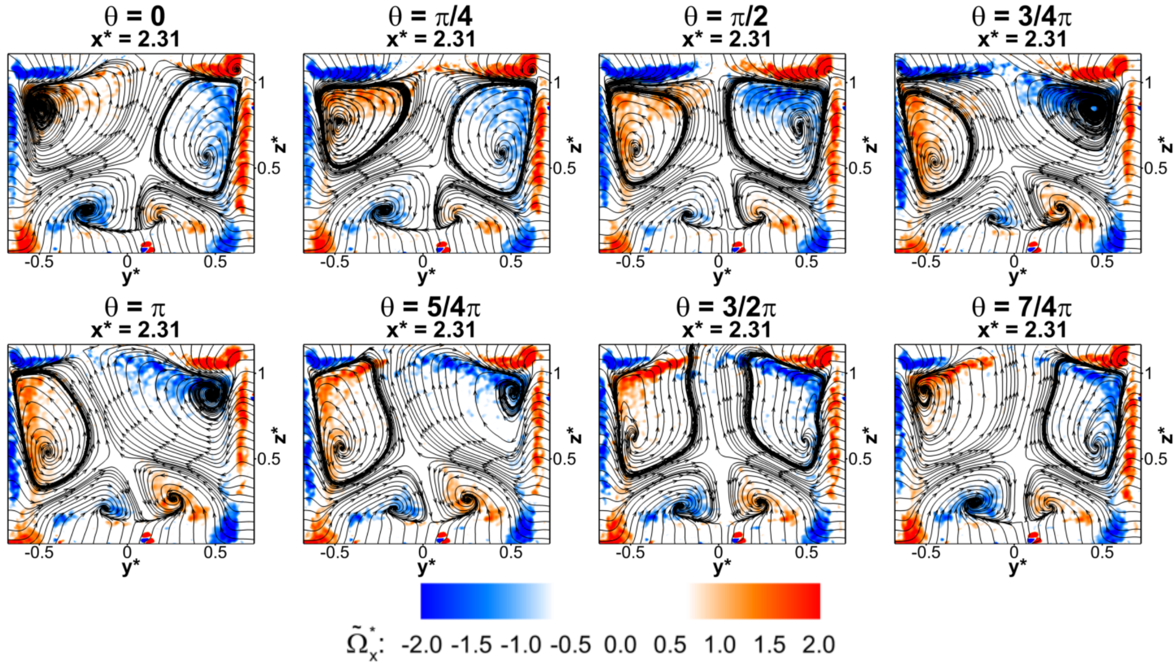

Figure 6.7: Low order phase averaged velocity field at $x^* = 2.31$ for the square-back configuration with stationary wheels. The plots are coloured according to the values of the normalised streamwise component of the vorticity $\tilde{\Omega}_x^*$; the streamlines are drawn considering the in-plane components of the velocity field.

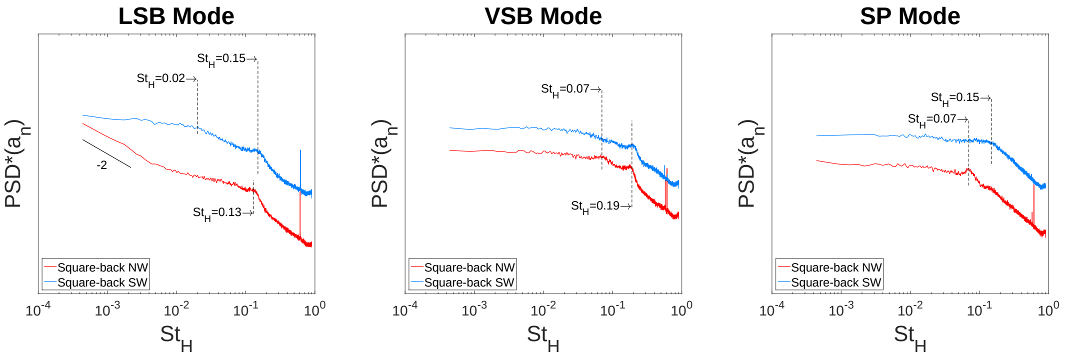

(a) **(b)** **(c)**

Figure 6.8: Spectra of the POD temporal coefficients associated with: **a** the lateral symmetry breaking mode (LSB), **b** the vertical symmetry breaking mode (VSB), **c** the symmetry preserving mode (SP). The curves have been shifted along the vertical axis. Base pressure data recorded for the square-back configuration with wheels (SW) and without wheels (NW).

mode, is replaced by an inflection point at $St_H \approx 0.02$, suggesting the switch from a random long-time dynamics to a 'faster' oscillating mode. This is confirmed by the two point coherence analysis performed considering some of the taps located in proximity to the edges of the base (Fig. 6.9). A hump at $St_H \approx 0.02$ is observed in the magnitude Λ when the coherence analysis

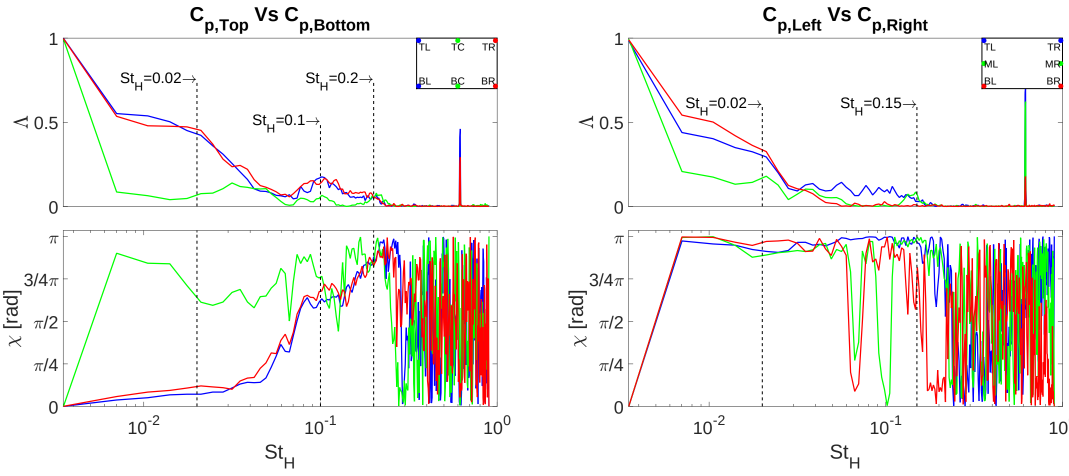

(a) **(b)**

Figure 6.9: Coherence analysis performed considering the configuration with $\phi_t = 0°$, $\phi_b = 0°$ and stationary wheels. The unsteady signal was recorded by pressure taps placed at different locations along the trailing edges of the model base: **a** top-left tap Vs bottom-left tap, top-centre tap Vs bottom-centre tap, top-right tap Vs bottom-right tap; **b** top-left tap Vs top-right tap, mid-left tap Vs mid-right tap, bottom-left tap Vs bottom-right tap.

is performed considering either the top-bottom or the left-right pairs of taps. The value of the phase angle, however, is seen to switch from $\chi \approx 0\,rad$ in the first case to $\chi \approx \pi\,rad$ in the second case, which is consistent with the existence of a lateral motion.

Changes are also observed in the short-time wake dynamics. The peak at $St_H = 0.07$, seen for the square-back configuration without wheels in the PSD plot of $a_{SP}(t)$ (Fig. 6.8c) and associated with the ‘wake pumping’ (§3.2.4), is reported to disappear when wheels are added to the same model. A similar behaviour is reported in the case of the ‘low drag’ configuration investigated in Chap. 4, suggesting that the disappearance of the pumping motion may be a consequence of the stabilisation of the four-vortex structure seen in the cross-plane at $x^* = 2.31$. This is not the case for the other two global oscillating modes. A peak is seen at $St_H = 0.15$ in the frequency spectrum obtained for $a_{LSB}(t)$ (Fig. 6.8a), suggesting the existence of a lateral flapping. A second peak, at $St_H \approx 0.2$, is observed in the PSD plot of $a_{VSB}(t)$ (Fig. 6.8b), and linked with periodic oscillations of the wake in the vertical direction. The coherence analysis performed considering pairs of taps located respectively at the top-bottom and left-right trailing edges, however, suggests that these modes are weaker than those seen in Fig. 3.19, for the square-back configuration without wheels. In Fig. 6.9a, a third peak at $St_H = 0.1$ is also seen, when considering the coherence analysis performed between the top-left tap (TL) and the bottom-left tap (BL) as well as the top-right tap (TR) and the bottom-right tap (BR). The phase angle associated with this peak ($\chi \approx 3/4\pi$) seems to suggests that it is related to localised flapping motions mainly oriented in the vertical direction.

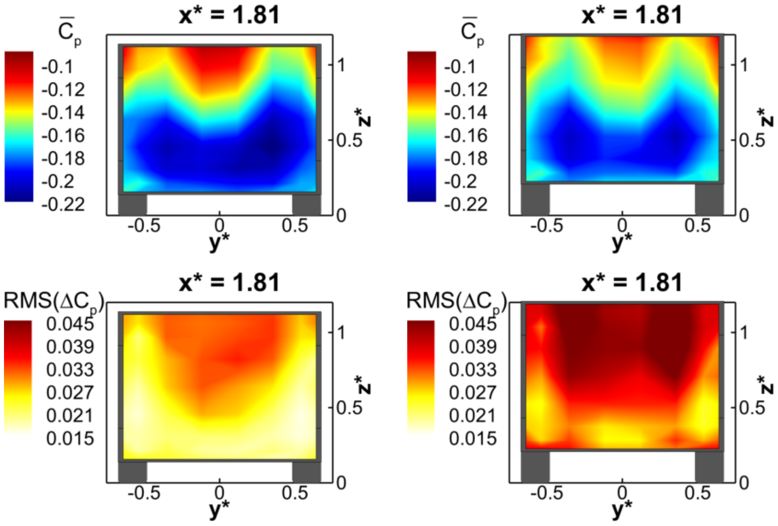

(a) $C^* = 0.138$ **(b)** $C^* = 0.208$

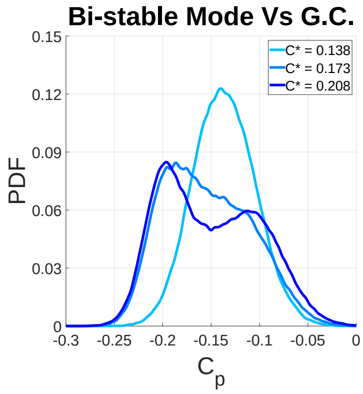

(c)

Figure 6.10: Distribution of the time averaged static pressure and the root mean square of the pressure fluctuation over the model base for $C^* = 0.138$ **(a)** and $C^* = 0.208$ **(b)**. **c** PDF of the temporal signal recorded by one of the taps with the highest value of $RMS\Delta(C_p)$ for $C^* = 0.138$, $C^* = 0.173$ and $C^* = 0.208$. The data refer to the configuration with rotating wheels.

A further 'stabilisation' of the wake is reported when the model's ground clearance is reduced. The PDF of the values of C_p recorded by one of the taps located in the region with the highest level of fluctuation is observed to become narrower when the ride height is reduced from $C^* = 0.173$ to $C^* = 0.138$ (Fig. 6.10c). This is accompanied with a further reduction in the level of pressure fluctuation seen over the entire base (Fig. 6.10a). Indeed, a higher level of sensitivity to changes in the distance between the model and the ground is observed, compared with that seen in §3.2.1.1 for the same square-back geometry without wheels. In that case, the bi-stable mode is still clearly visible at $C^* = 0.138$, confirming the results of Grandemange et al (2013a), who reported a suppression of the long-time instability only for

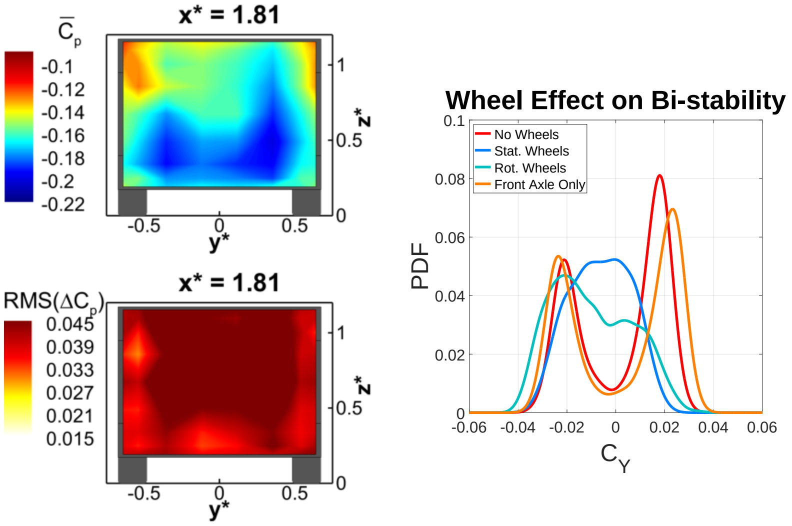

(a) **(b)**

Figure 6.11: I
mpact of the wheel-base separation on the time averaged and unsteady flow field. **a** distributions of the time averaged static pressure and the root mean square of the pressure fluctuation over the base for the square-back model with the front axle only (rotating wheels). **b** PDF of the temporal signal recorded for the side force (data resampled at $5\,Hz$).

$C^* < 0.08$. This threshold appears to be shifted upwards when wheels are added to the model. Indeed, the increased underbody blockage yielded by the addition of the wheels is found to have a stabilising effect on the wake, in agreement with the findings of Castelain et al (2018). An opposite trend is observed when the distance between the model and the ground is brought to $C^* = 0.208$. In this case, the region of high pressure fluctuation seen on the upper portion of the base starts to increase in size again, at the expenses of the low-fluctuation zone observed closer to the bottom trailing edge (Fig. 6.10b). In addition, the highest values of $\Delta RMS(C_p)$ start to cluster around two attractors, resulting in a bi-lobe distribution similar to that described in Chap. 3. Two distinct peaks become visible in the PDF of C_p recorded by the taps located in these two regions (Fig. 6.10c). This suggest a strengthening of the bi-stable mode, similar to the trend seen in 4.2.1. In the same conditions, the low pressure region located at the lower portion of the base is seen to reduce in size, as the size of the bottom recirculation is also reduced. This becomes even more evident when the rear wheels are removed, while keeping the ground clearance at $C^* = 0.173$ (Fig. 6.11a). A further pressure increase is observed in these conditions close to the bottom trailing edge, regardless of the condition of the front axle (with either stationary or rotating wheels). As C_p rises, the region of low pressure fluctuation tends to disappear, until the lateral instability is fully restored. The effects of the strengthening of the bi-stable mode can also be seen when looking at the side force acting over the main body. Unlike the case when all four wheels are considered, a clear bi-modal shape can be recognised in the PDF obtained for the values recorded for C_Y (resampled at $5Hz$, as explained in §3.2.1) and presented in Fig. 6.11b. This is very close to the that seen for the same configuration without wheels.

6.2 Horizontal trailing edge tapering (model with wheels)

The sensitivity of the wake to small changes in the shape of the body's trailing edges has been investigated by applying small tapered surfaces to the horizontal edges of the base, as done in Chap. 4 for the same model without wheels. For the sake of simplicity the chamfer angle has been fixed at 12°. A first series of tests was performed by applying the taper to just the top or the bottom trailing edge, leaving the opposite edge squared. A third test was performed considering the same chamfer angle for both horizontal trailing edges. The results are presented in Tab. 6.3 as well as in Fig. 6.12 (in terms of percentage variations of $\overline{C}_D$, $\overline{C}_{D_{Rear}}$ and $\overline{C}_L$ over the square-back case discussed in §6.1).

The drag acting on the main body is seen to increase (up to 4%) when the taper is applied to the bottom trailing edge only, leaving the top edge squared. An opposite trend is observed when the same taper is applied to either the top trailing edge only or both horizontal edges, resulting in a reduction of $\overline{C}_D$ up to $\approx 3\%$. A similar tendency is noticed when focusing on the pressure drag contribution of the rearward facing surfaces (Fig. 6.12b), with $\Delta\overline{C}_{D_{Rear}}$ going

(a) **Stationary wheels**

Config.	$\overline{C}_{D_{Rear}}$	$\overline{C}_D$	$\overline{C}_L$
$\phi_t = 0°$, $\phi_b = 0°$	0.175	0.306	0.173
$\phi_t = 0°$, $\phi_b = 12°$	0.190	0.318	0.118
$\phi_t = 12°$, $\phi_b = 0°$	0.167	0.297	0.308
$\phi_t = 12°$, $\phi_b = 12°$	0.169	0.298	0.242

(b) **Rotating wheels**

Config.	$\overline{C}_{D_{Rear}}$	$\overline{C}_D$	$\overline{C}_L$
$\phi_t = 0°$, $\phi_b = 0°$	0.170	0.293	0.182
$\phi_t = 0°$, $\phi_b = 12°$	0.184	0.304	0.121
$\phi_t = 12°$, $\phi_b = 0°$	0.163	0.284	0.311
$\phi_t = 12°$, $\phi_b = 12°$	0.164	0.283	0.243

Table 6.3: Time averaged values of the aerodynamic forces recorded for different horizontal trailing edge taper configurations with either *(a)* stationary wheels or *(b)* rotating wheels.

up by 8.6% in the first case and dropping by 4.6% and 3.4% respectively in the other two cases. The agreement observed in the trends obtained for $\overline{C}_D$ and $\overline{C}_{D_{Rear}}$, confirms once again that the variations seen in the aerodynamic force acting over the vehicle are mainly driven by changes in the pressure distribution over the rearward facing surfaces. This is shown in the time averaged results reported in Fig. 6.13, 6.14, 6.15. For the sake of simplicity only the stationary wheel case will be considered, since, as shown in §6.1, the differences produced by the wheels' rotation on the wake's time averaged topology and unsteady behaviour are marginal. This can be inferred also by looking at the results reported in Tab. 6.3 and Fig. 6.12. When compared to the stationary case, wheel rotation seems to slightly mitigate the variations in base pressure distribution observed between the different configurations tested in the present investigation (Fig. 6.12b), whilst always contributing to a reduction of the overall drag acting on the main body (Fig. 6.12a). Nevertheless, in all cases the differences between stationary and rotating setups are less than 1 percentage point. Bigger variations are seen in the vertical component of the aerodynamic force (Fig. 6.12c), with the rotating case always yielding a lift reduction over the stationary case. These results are in good agreement with the trends reported by Wäschle (2007) when measuring the forces on the entire vehicle ($main\,body + wheels$).

From the results presented in Fig. 6.13, 6.14, 6.15 it can be noted that the lowest value of $\overline{C}_{D_{Rear}}$ coincides with the restoration of the symmetry in the vertical direction in the time averaged wake topology, confirming the conclusions drawn at the end of Chap. 4. This is achieved when the 12° taper is applied to the top trailing edge while leaving the bottom edge squared (Fig. 6.13). The downwash generated by the tapered surface counteracts the upwash produced the rear wheels, resulting in a more balanced wake. Strong similarities indeed

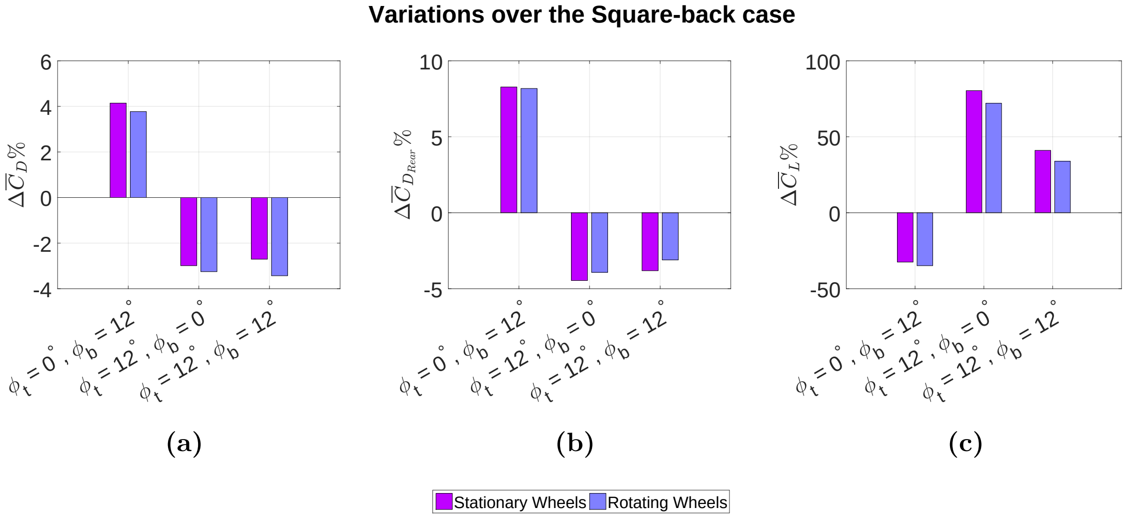

Figure 6.12: Effects produced by the application of 12° tapers to the horizontal trailing edges: overall drag **(a)**, rear drag **(b)** and lift **(c)** (variations over the square-back case). The aerodynamic forces refer to the main body only (see §2.1).

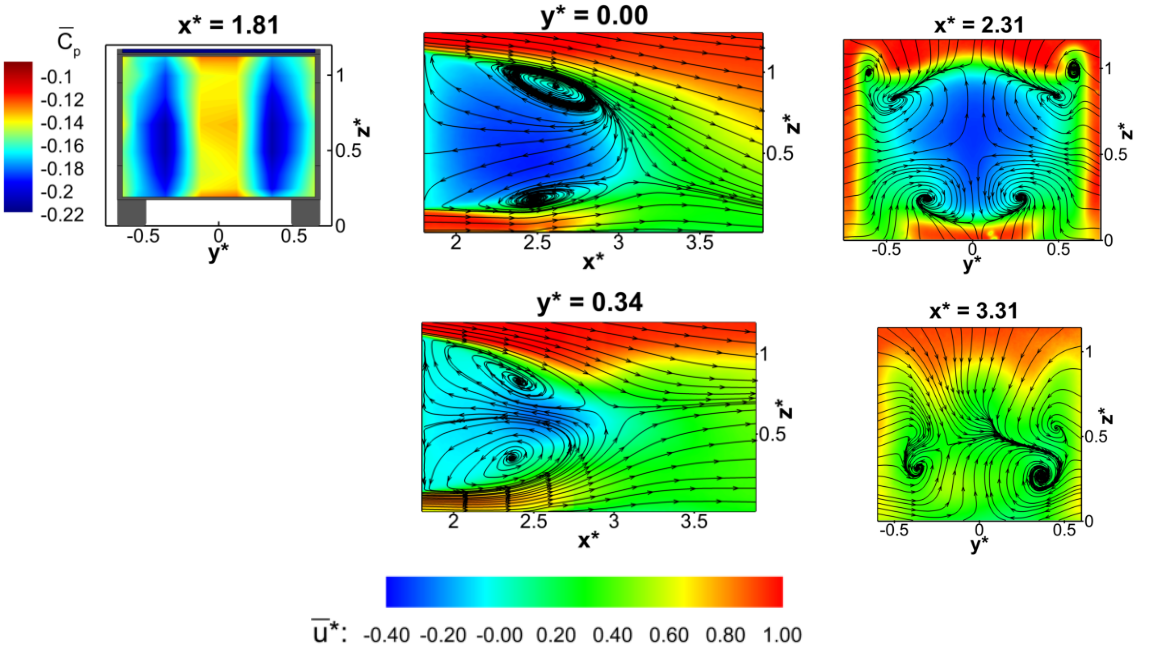

Figure 6.13: Time averaged fields for the configuration with $\phi_t = 12°$, $\phi_b = 0°$ and stationary wheels. Clockwise from top left: $\mathbf{x^* = 1.81}$, base pressure distribution; $\mathbf{y^* = 0.00}$, PIV vertical mid-plane; $\mathbf{x^* = 2.31}$ and $\mathbf{x^* = 3.31}$, PIV stereo cross-planes; $\mathbf{y^* = 0.34}$, PIV vertical off-centre plane. All PIV fields are coloured according to the values of the axial component of the velocity u^*; the streamlines refer to the in-plane components of the velocity.

are seen between this case and the low drag configuration investigated in Chap. 4, with the main difference being represented by the fact that the wake now features a slightly downwash dominated topology, unlike the slightly upwash dominated topology described in §4.1. This explains the lift increase recorded in this case over the square-back configuration tested with the same wheel setup (Fig. 6.12c). The symmetry in the vertical direction is lost again when a second taper, with the same chamfer angle ($\phi = 12°$) is added to the bottom trailing edge of the model. In these conditions, the effect of the wheels is amplified, leading to the formation of an upwash dominated wake (Fig. 6.14). The bottom recirculation starts to grow in size at the expenses of the top one. This becomes particularly visible when the PIV plane located at $y^* = 0.34$ is considered. The upwash generated by the bottom slant further increases the amount of low momentum flow (originating from the rear wheels' wake) entrained into the main body's wake. As a consequence, the lower vortex is seen to further increase in size compared to the square-back case (see §6.1) and it is pushed against the base, assuming an even more circular shape. On the plane at $x^* = 2.31$, the lower pair of vortices forming in the gap between the rear wheels is reduced in size compared to that seen in the case of the configuration with $\phi_t = 12°$, $\phi_b = 0°$. The wake topology on this plane presents some similarities with that reported by Huminic and Huminic (2017), when adding wheels to a modified Ahmed body featuring a

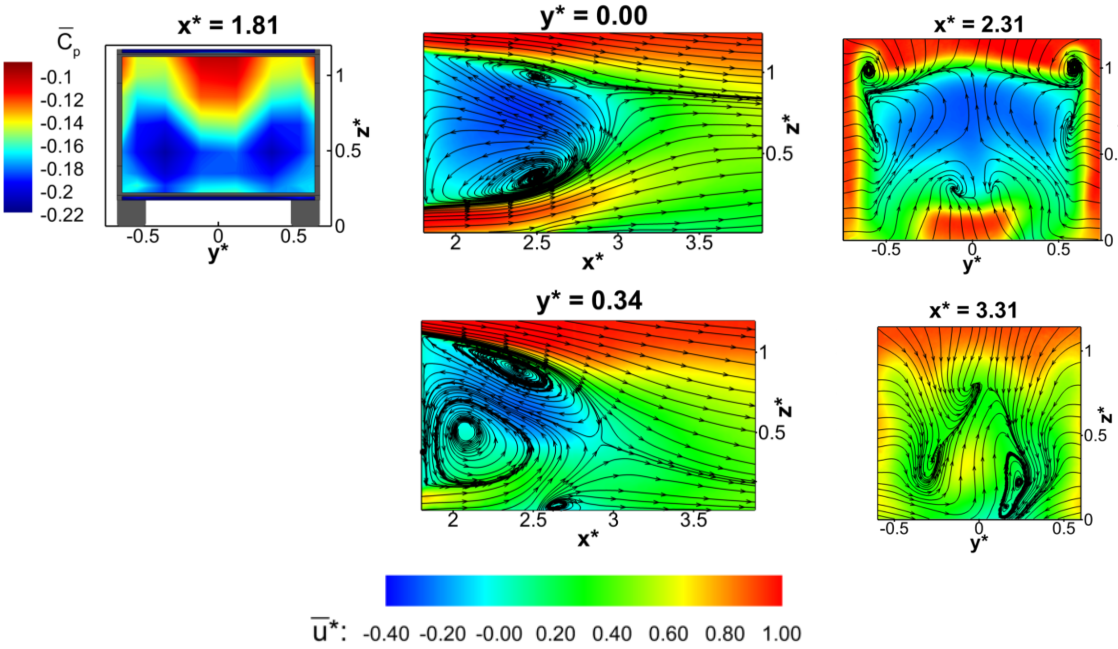

Figure 6.14: Time averaged fields for the configuration with $\phi_t = 12°$, $\phi_b = 12°$ and stationary wheels. Clockwise from top left: $\mathbf{x^* = 1.81}$, base pressure distribution; $\mathbf{y^* = 0.00}$, PIV vertical mid-plane; $\mathbf{x^* = 2.31}$ and $\mathbf{x^* = 3.31}$, PIV stereo cross-planes; $\mathbf{y^* = 0.34}$, PIV vertical off-centre plane. All PIV fields are coloured according to the values of the axial component of the velocity u^*; the streamlines refer to the in-plane components of the velocity.

35° roof slant and a 5° bottom diffuser, although with a lower aspect ratio than that considered in the present study. In such conditions, flow separation on the wind tunnel floor (due to the use of a stationary ground) is further accentuated and a small recirculation becomes visible on the plane at $y^* = 0.34$. The interactions between this recirculation and the vortical structures developing downstream of the main body may be the cause of the asymmetries observed on the cross-plane located at $x^* = 3.31$. As already pointed out in Chap. 4, the loss of symmetry in the vertical direction is found to have a direct impact on the pressure distribution behind the model. This is evident in the pressure maps presented in Fig. 6.13 and 6.14, where the low pressure region is seen to move from the sides to the lower portion of the base as a taper is added to the bottom trailing edge. In the same conditions, a ≈ 40 percentage point drop in the lift acting on the main body is also observed (Tab. 6.12 and Fig. 6.12c). The balance between the upper and lower recirculations becomes even worse when the top slant is removed (Fig. 6.15). In this case, the upper vortical structure seen on the planes at $y^* = 0.00$ and $y^* = 0.34$, is further reduced in size, until almost vanishing. A similar fate is faced by the streamwise vortices previously observed in the cross-plane at $x^* = 2.31$, close to the bottom trailing edge of the model. As a result, the bottom recirculation, and the low pressure region associated with it, expands until covering most of the base, thus explaining the drag rise reported in Fig.

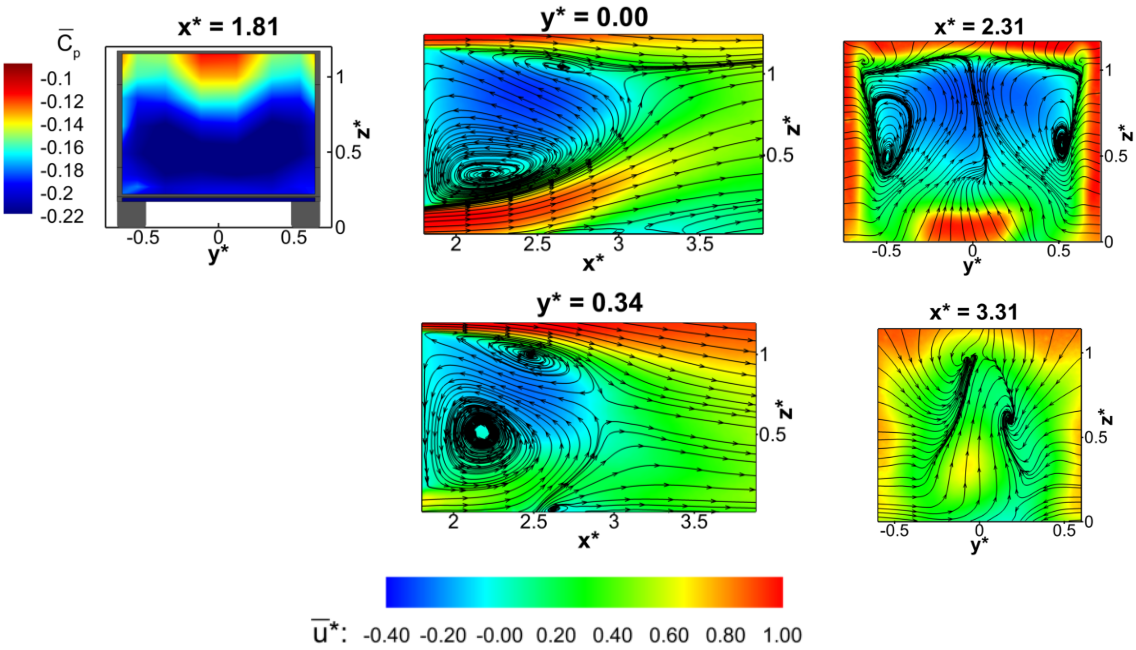

Figure 6.15: Time averaged fields for the configuration with $\phi_t = 0°$, $\phi_b = 12°$ and stationary wheels. Clockwise from top left: $\mathbf{x^* = 1.81}$, base pressure distribution; $\mathbf{y^* = 0.00}$, PIV vertical mid-plane; $\mathbf{x^* = 2.31}$ and $\mathbf{x^* = 3.31}$, PIV stereo cross-planes; $\mathbf{y^* = 0.34}$, PIV vertical off-centre plane. All PIV fields are coloured according to the values of the axial component of the velocity u^*; the streamlines refer to the in-plane components of the velocity.

6.12a and 6.12b. The increased level of upwash over the square-back configuration is found also to be at the origin of the $\approx 32\%$ reduction observed in the value of the lift over the same configuration.

The stabilising effect of the wheels on the long-time wake dynamics becomes clear when looking at the distribution of the pressure fluctuation over the model base as well as the lateral and vertical components of the normalised Reynolds stresses on the cross-plane at $x^* = 2.31$ (Fig. 6.17). Compared to the configuration with $\phi_t = 12°$, $\phi_b = 12°$ and no wheels (Fig. 6.16a), which is already a relatively stable configuration as discussed in Chap. 4, the addition of wheels yields a further reduction in the level of unsteadiness. A region of high pressure fluctuation is still visible when the 12° taper is applied to the top trailing edge only (Fig. 6.16b), although no bi-lobe distribution can be recognised. It is then shifted towards the top trailing edge and almost disappears when the symmetry in the vertical direction is broken by either adding a second chamfer to the bottom trailing edge (Fig. 6.17a), or removing the top slant while keeping the lower chamfer in place (Fig. 6.17b). A similar trend is seen in the distribution of the fluctuation of the lateral component of the velocity (T^*_{vv} in Fig. 6.17). The region of high unsteadiness seen in the flow reversal in the case of the model without wheels is reported to disappear when the wake (as seen on the plane at $x^* = 2.31$) transitions from a four-vortex

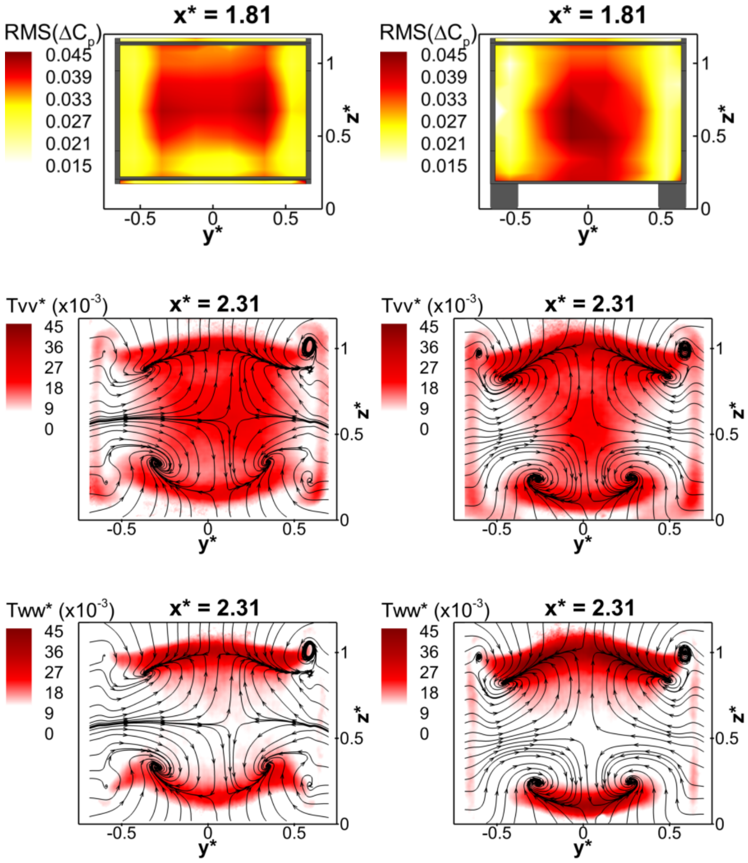

(a) $\phi_t = 12°$, $\phi_b = 12°$, no wheels

(b) $\phi_t = 12°$, $\phi_b = 0°$, stationary wheels

Figure 6.16: First row, distribution of the root mean square of the pressure fluctuation over the model rearward facing surfaces. Second and third rows, distribution of the lateral and vertical components of the normalised Reynolds stresses on the cross-plane at $x^* = 2.31$. From left to right: **a** $\phi_t = 12°$, $\phi_b = 12°$ with no wheels; **b** $\phi_t = 12°$, $\phi_b = 0°$ with stationary wheels. The streamlines refer to the time averaged in-plane components of the velocity.

structure to a two-vortex structure. The loss of symmetry in the vertical direction is also seen to affect the distribution of the vertical component of the Reynolds stresses (T^*_{ww} in Fig. 6.17). The switch from a balanced wake to an upwash dominated wake is accompanied with the stabilisation of the bottom shear layer, so that velocity fluctuations in the vertical direction are seen mainly close to the top trailing edge of the model. This agrees with that already discussed in §4.2.2 for the model without wheels, although here the trend is accentuated even further.

Additional insights on the impact of different wheel and taper configurations on the wake's unsteady behaviour can be obtained from the application of proper orthogonal decomposition (§2.4.1 and §2.5.3) to the pressure and velocity datasets. The weakening of the lateral instability is confirmed by the significant drop in the energy captured by the lateral symmetry breaking mode (Fig. 6.18a) as well as the narrowing of the PDF obtained for the values of the temporal

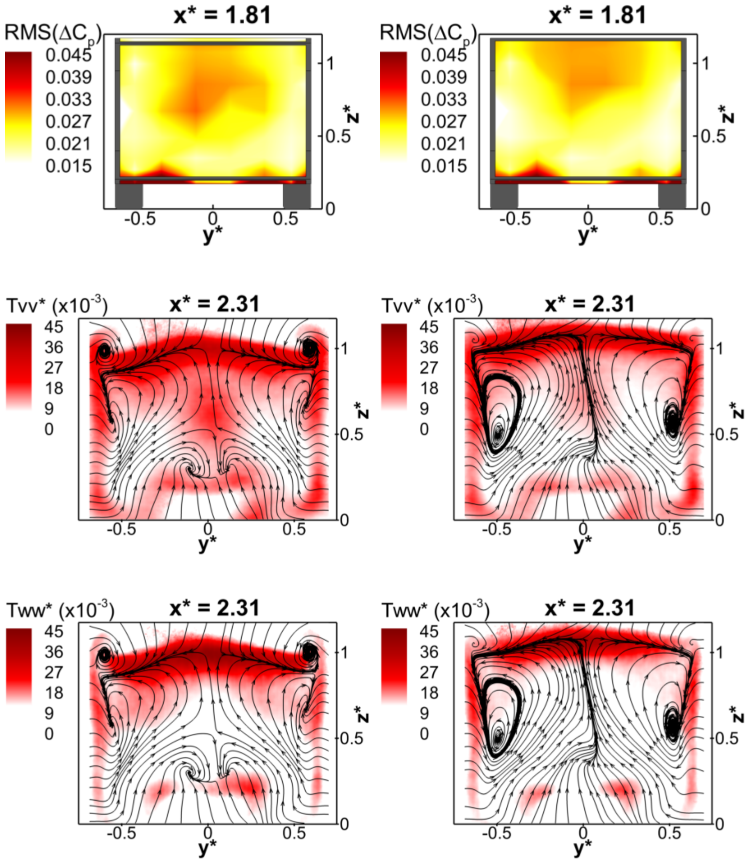

(a) $\phi_t = 12°$, $\phi_b = 12°$, stationary wheels

(b) $\phi_t = 0°$, $\phi_b = 12°$, stationary wheels

Figure 6.17: First row, distribution of the root mean square of the pressure fluctuation over the model rearward facing surfaces. Second and third rows, distribution of the lateral and vertical components of the normalised Reynolds stresses on the cross-plane at $x^* = 2.31$. From left to right: **a** $\phi_t = 12°$, $\phi_b = 12°$; **b** $\phi_t = 0°$, $\phi_b = 12°$. Both configurations are with stationary wheels. The streamlines refer to the time averaged in-plane components of the velocity.

coefficient related to the same mode. (Fig. 6.18b). Particularly interesting in this respect is the configuration with $\phi_t = 0°$, $\phi_b = 12°$. In this case, coherent motions are seen only in the region close to the top shear layer (Fig. 6.19). Nevertheless, spatial modes similar to those previously described can still be recognised, at least on the model base. Their impact on the global wake dynamics, however, is now much more limited. This becomes evident when the phase averaged low order model, built as in §3.2.5, is considered (Fig. 6.20). Indeed, no significant variations are observed in the evolution of the wake topology captured at $x^* = 2.31$ throughout the different values of the phase angle θ. Changes are only seen in proximity to the top shear layer, where a flapping motion, mostly in the lateral direction, is observed. This motion may be associated with the peak seen at $S_H = 0.035$ in the spectrum referring to the lateral symmetry breaking mode extracted from the pressure dataset and reported in Fig. 6.18c. Indeed, the

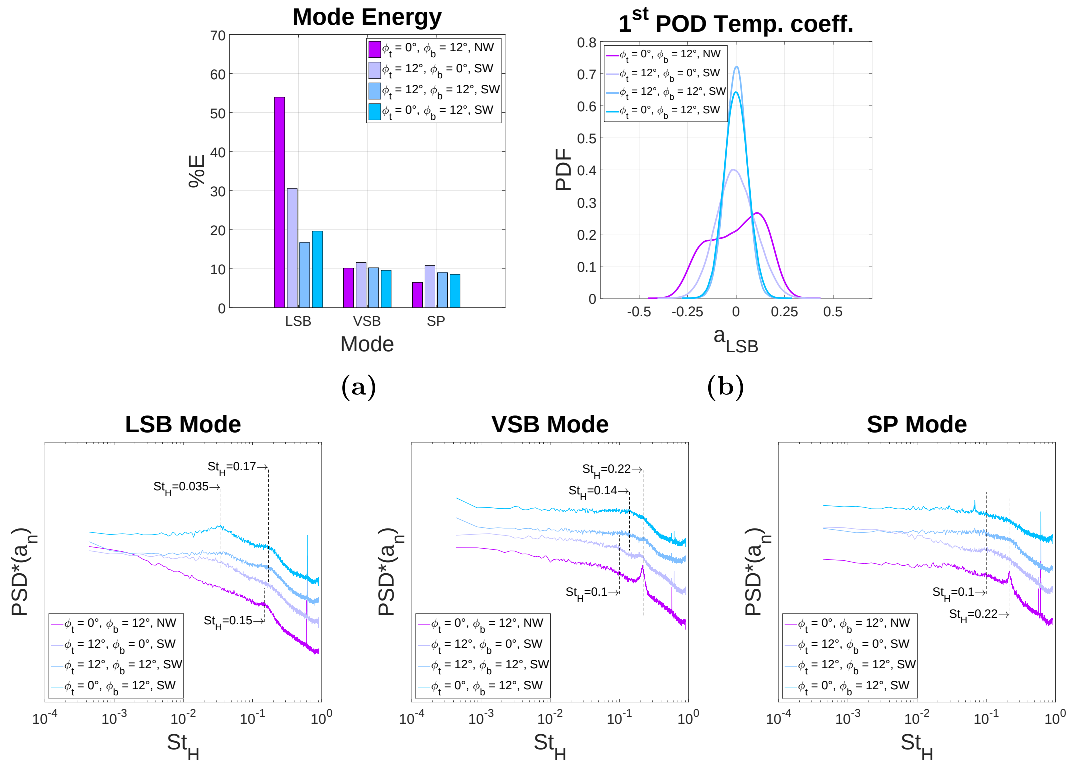

(a) **(b)**

(c) **(d)** **(e)**

Figure 6.18: Top row: **a** energy associated with the first three POD modes; **b** PDF of the values of first POD temporal coefficient. Bottom row, spectra of the POD temporal coefficients associated with: the lateral symmetry breaking mode (LSB, **c**), the vertical symmetry breaking mode (VSB, **d**), the symmetry preserving mode (SP, **e**). The curves have been shifted along the vertical axis. Base pressure data recorded for the configurations with 12° horizontal trailing edge tapers, with wheels (SW) and without wheels (NW).

trend described in §4.2.1 and §4.2.2, referring to the shortening of the characteristic time between switches as the separation between the top and bottom shear layers is reduced, seems to continue and to reach a 'limit' in this case. The lateral oscillations become slightly faster than those seen for the configuration with $\phi_t = 12°$, $\phi_b = 12°$ and no wheels (as the peak seen in the PSD of a_{LSB} shifts from ≈ 0.03 to 0.035 and becomes 'sharper', suggesting a more regular pattern). At the same time, however, the amplitude of these oscillations (in terms of deviation from the time averaged wake topology) is seen to decrease, until they become hardly visible. Additional changes are seen in the short-time wake dynamics. The characteristic frequency of the lateral flapping (Fig. 6.18c) is seen to slightly increase, from $St_H \approx 0.15$ to $St_H \approx 0.17$, whilst the sharp peak seen for the wake vertical flapping at $St_H = 0.24$, in the case of the model with $\phi_t = 12°$, $\phi_b = 12°$ and no wheels, is replaced by smaller humps spread between $St_H = 0.10$ and $St_H \approx 0.20$ (Fig. 6.18d), suggesting the existence of weaker coherent motions. Furthermore, in none of the cases considered here is the characteristic frequency reported in

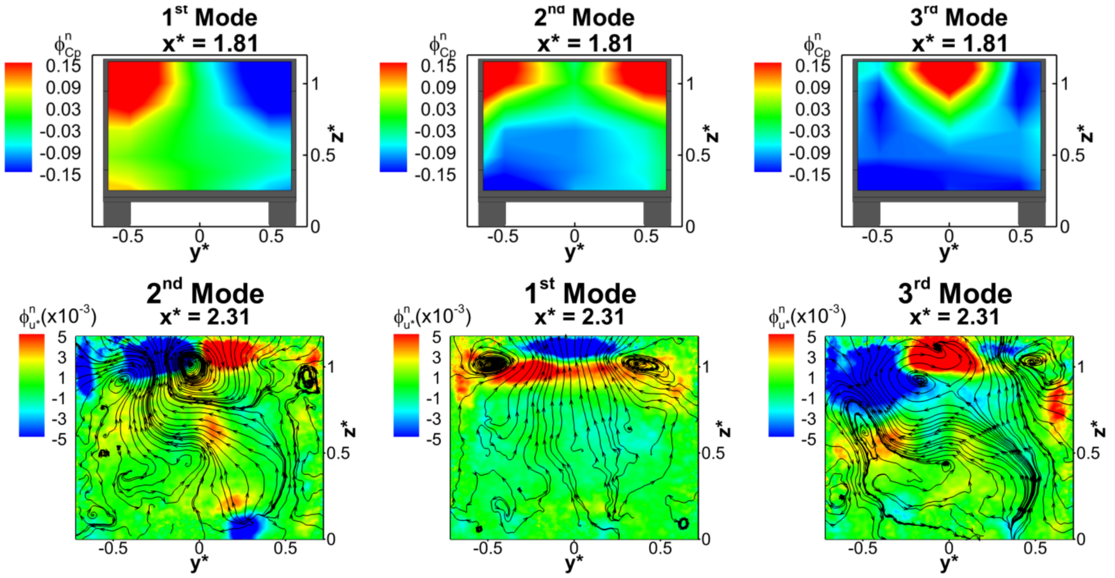

(a) LSB mode (b) VSB mode (c) SP mode

Figure 6.19: Spatial distribution of 3 of the most energetic POD modes extracted from the base pressure distribution (top row) and PIV cross-plane at $x^* = 2.31$ (bottom row) for the configuration with $\phi_t = 0°$, $\phi_b = 12°$ and stationary wheels. The modes are ordered according to their topology: **a** lateral symmetry breaking mode (LSB), **b** vertical symmetry breaking mode (VSB), **c** symmetry preserving mode (SP). $\phi^n_{C_p}$ refers to the magnitude of the spatial eigen-modes extracted from the field of the pressure fluctuation. The eigen-functions related to the velocity fluctuation are coloured according to the values of the through plane component ϕ^n_{u*} whereas the streamlines are drawn considering the in-plane components ϕ^n_{v*} and ϕ^n_{w*}.

Chap 3 for the wake pumping observed (Fig. 6.19c), suggesting a further stabilisation of the wake in the longitudinal direction.

In analogy with that observed in §6.1 for the square-back case, additional coherent motions are seen to develop downstream of the rear wheels. These motions are linked to the wheel wake flapping described by Croner et al (2013), as already discussed in §6.1, and are thought to be responsible for the localised pressure fluctuations isolated by the 6^{th} and 8^{th} POD modes (extracted from the pressure dataset) in the regions of the model base located close to the right and left rear wheel respectively (Fig. 6.21). They are also found to be at the origin of the high level of unsteadiness seen on either side of the bottom diffuser in the pressure maps and the Reynolds stress distributions reported in Fig. 6.17a and 6.17b. No peak however can be seen in the spectra obtained for the temporal coefficients related to these modes. This is likely to be a consequence of the limited frequency resolution of the pressure scanner employed in the experiment (§2.4).

The presence of a 'more stable' wake is also seen to produce effects on the unsteady aerodynamic forces acting on the main body. The application of wavelet analysis (see §2.3.1) to the dataset logged from the balance (having aligned the model with the onset flow, so that

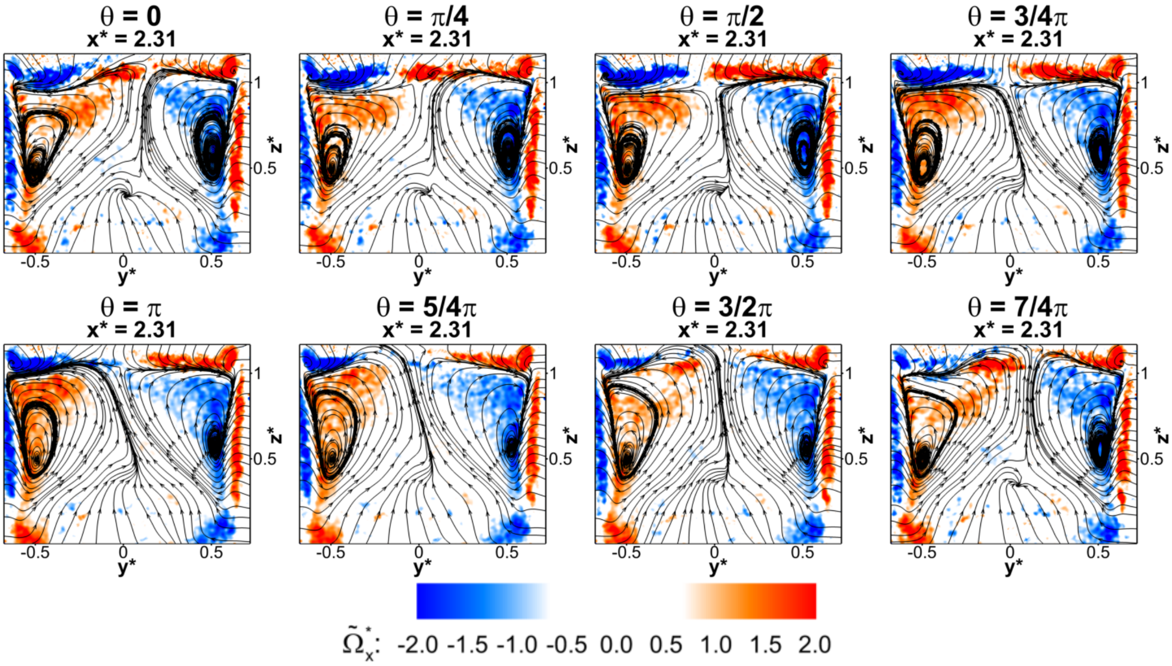

Figure 6.20: Low order phase averaged velocity field at $x^* = 2.31$ for the configuration with $\phi_t = 0°$, $\phi_b = 12°$ and stationary wheels. The plots are coloured according to the values of the normalised streamwise component of the vorticity $\tilde{\Omega}_x^*$; the streamlines are drawn considering the in-plane components of the velocity field.

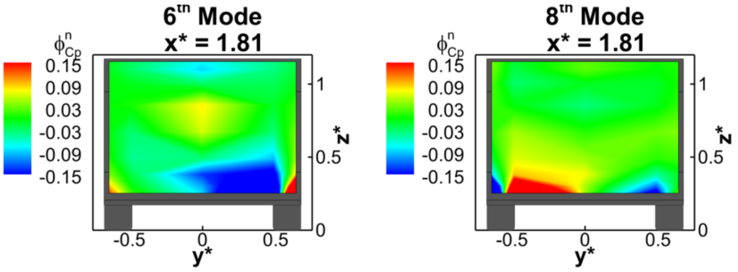

Figure 6.21: POD modes capturing the effects of the wheel wake flapping over the model base for the configuration with $\phi_t = 0°$, $\phi_b = 12°$ and stationary wheels.

$\Psi \approx 0°$), reveals a noticeable decrease in the level of activity observed in the signal recorded for the side force C_Y at very low frequency ($St_H <= 7.1 \cdot 10^{-4}$ in Fig. 6.22a), when compared to the square-back case with no wheels discussed in §3.2.1. This is found to directly affect the value of the standard deviation σ_{C_Y} associated with the same component of the aerodynamic force, as suggested by Grandemange et al (2015). The results are shown in the bar chart reported in Fig. 6.22b, referring to the standard deviation obtained after having resampled the side force signal at $5\,Hz$. A strong bi-stable mode is always characterised by high values of σ_{C_Y}. This is evident for the square-back model with no wheels as well as the same model with only the front axle in place, for which $\sigma_{C_Y} \approx 20\,counts$. The values of the standard deviation are seen to drop

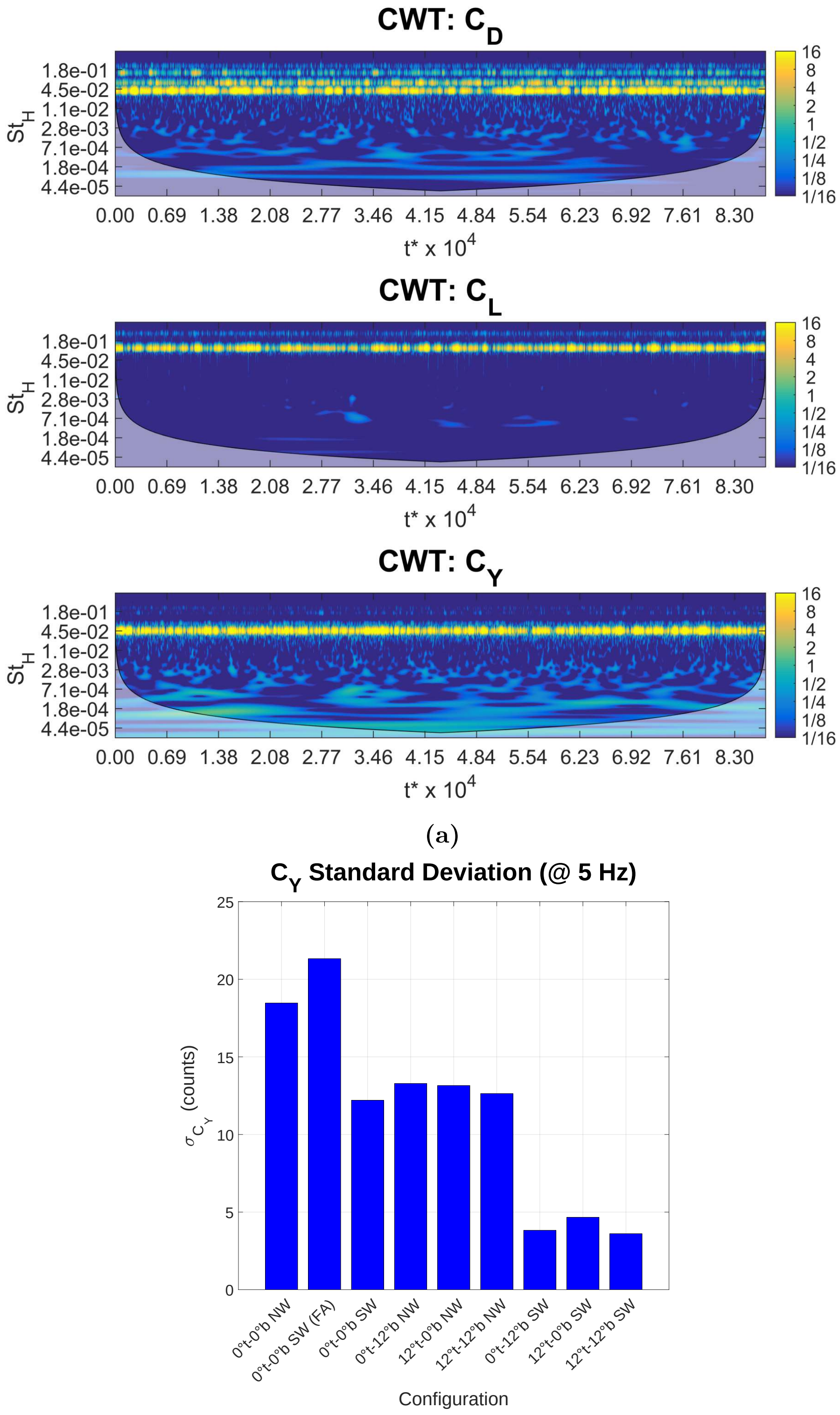

(a)

(b)

Figure 6.22: **a** continuous wavelet transform (CWT) of the three components of the aerodynamic force recorded for the configuration with with $\phi_t = 0°$, $\phi_b = 12°$ and stationary wheels. **b** standard deviation associated with the value of the side force C_Y, resampled at $5\,Hz$, for different tapered configurations, with wheels (SW) and without wheels (NW). In **a**, The colour scale is proportional to the wavelet power spectrum $|W^f(s,\tau)|^2$ (defined in §2.3.1) and is represented in octaves. The shaded region defines the cone of influence (COI) where the edge effects that might distort the results become predominant. For further information see Grinsted et al (2004).

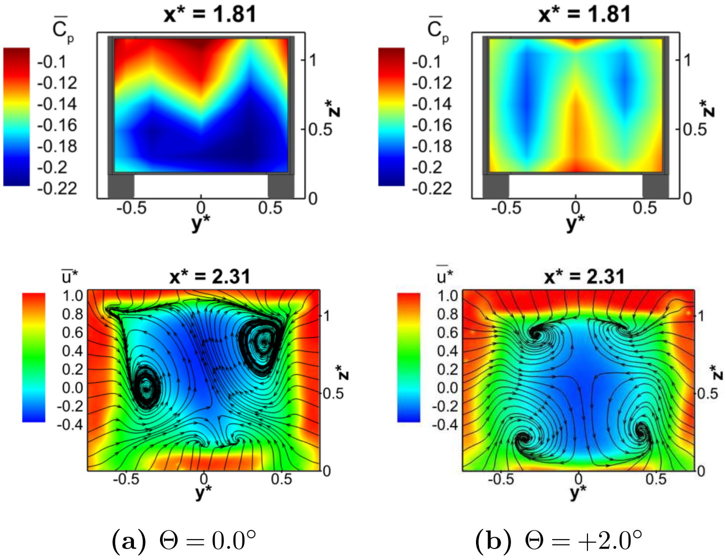

(a) $\Theta = 0.0°$ **(b)** $\Theta = +2.0°$

Figure 6.23: Time averaged fields for the configuration with $\phi_s = 12°$ and stationary wheels, tested at $\Theta = 0°$ **(a)** and $\Theta = +2°$ **(b)**. From top to bottom in each sub-figure: $\mathbf{x^* = 1.81}$ base pressure distribution; $\mathbf{x^* = 2.31}$ PIV stereo cross-planes. All PIV fields are coloured according to the values of the axial component of the velocity u^*; the streamlines refer to the in-plane components of the velocity.

to $\sigma_{C_Y} \approx 12\,counts$ when horizontal tapers are applied to the model without wheels, further confirming the weakening of the bi-stable mode already discussed in Chap. 4. Similar values of σ_{C_Y} are also reported when wheels are added to the square-back model, on both axles. The lowest level of uncertainty ($\sigma_{C_Y} < 5\,counts$) is obtained when the stabilising actions of both wheels and horizontal tapers are combined.

6.3 Vertical trailing edge tapering (model with wheels)

Unlike that seen in the case of horizontal trailing edge tapers, a strengthening of the long-time instability is observed when wheels are added to the configuration described in Chap. 5, featuring 12° chamfers applied to the vertical trailing edges. In this case, although the model was initially tested at 0° pitch, the increase in the level of underbody blockage caused by the addition of the wheels is enough to perturb the equilibrium between the top and bottom shear layers discussed in §5.1, leading to the formation of an upwash dominated wake. The topology of the wake, in fact, is more similar to that described in §5.3 for the no-wheel configuration tested at $\Theta = -2°$ (Fig. 6.23a).

Considering the cross-plane at $x^* = 2.31$, the time averaged wake appears dominated by two counter rotating vortical structures, covering most of the base. A region of low pressure is observed on the model rearward facing surfaces in proximity to the cores of these structures. Pressure recovery is seen to occur closer to the top trailing edge, where the rear stagnation point is located. As a result, a positive pressure gradient is observed in the vertical direction. Unlike that seen in Chap. 5, however, the lateral symmetry is not fully restored in the time averaged wake topology. An angle of ≈ 20° is indeed formed between the flow reversal on the plane at $x^* = 2.31$ and the model's vertical plane of symmetry. Nevertheless, the application of tapered surfaces to the vertical trailing edges, rather than the horizontal trailing edges, still appears to be a more effective way to reduce drag. In this case, $\overline{C}_{D_{Rear}}$ and $\overline{C}_D$ are seen to drop respectively by ≈ 13% and ≈ 8% over the square-back case discussed in §6.1 (Tab. 6.4). This represents a substantial gain when compared to the drag reduction reported in §6.2 when similar tapers are applied to the horizontal trailing edges only.

A further reduction, at least in terms of base drag ($\overline{C}_{D_{Base}}$), is found when the symmetry of the wake in the vertical direction is restored. Following the same approach described in §5.3, the time averaged wake was forced to switch from an upwash dominated topology to a more balanced structure by changing the pitch angle of the main body. Only positive variations of Θ were considered in this case (model pitched 'nose up'), due to the need to increase the amount of downwash. The results, in terms of time averaged base pressure distribution and velocity field recorded at $x^* = 2.31$, are presented in Fig. 6.23b. Strong analogies are seen between this case and the model tested using $\phi_t = 12°$, $\phi_b = 12°$ and no wheels (Chap. 4) as well as the configuration with $\phi_t = 12°$, $\phi_b = 0°$ and wheels discussed in §6.2. On the base, the restoration of the symmetry in the vertical direction yields a constant pressure distribution in the same direction ($\partial C_p / \partial z^* \to 0$). The low pressure region is seen to split in two parts and move towards either side of the base, allowing for a better pressure recovery at the centre of the base itself. This results in a 6.6% reduction in the value of $\overline{C}_{D_{Base}}$ over the same model tested at $\Theta = 0°$, which is even higher than that recorded when testing the configuration without wheels in similar conditions (see §5.3). This is arguably due to the presence of some residual asymmetries in the no-wheel case tested at $\Theta = -1°$, suggesting that there is still 'space' for further improvement. The pressure distribution presented in Fig. 6.23a resembles also that described for the lateral symmetry preserving state isolated in §3.2.5.1 for the simple square-back case. The similarities extend to the velocity field recorded at $x^* = 2.31$. In both cases, two pairs of counter rotating vortices are seen on the PIV cross-plane captured in this location.

From an unsteady point of view, the trends already discussed in §5.3 are still visible. As can be inferred from the distribution of the normal components of the Reynolds stresses on the

Config.	$\overline{C}_{D_{Rear}}$	$\overline{C}_D$	$\overline{C}_L$
$\phi_t = 0°$, $\phi_b = 0°$	0.175	0.306	0.173
$\phi_s = 12°$	0.153	0.282	0.174

Table 6.4: Time averaged values of the aerodynamic forces recorded for the configuration with 12° vertical trailing edge tapers and stationary wheels.

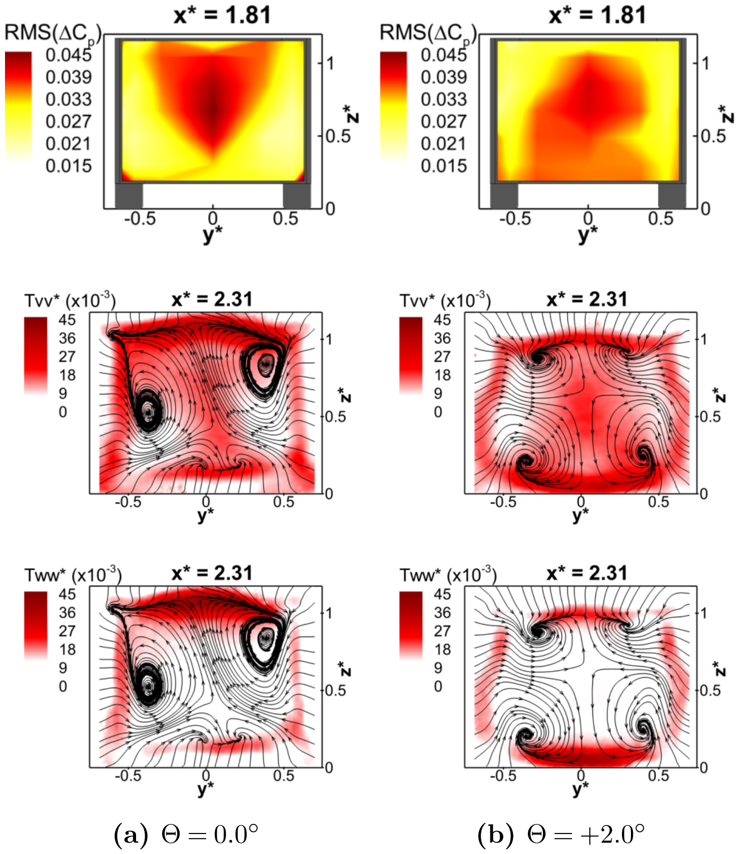

(a) $\Theta = 0.0°$ **(b)** $\Theta = +2.0°$

Figure 6.24: First row, distribution of the root mean square of the pressure fluctuation over the model rearward facing surfaces. Second and third rows, distribution of the lateral and vertical components of the normalised Reynolds stresses over the cross-plane at $x^* = 2.31$, for the configurations with $\phi_s = 12°$ and stationary wheels tested at $\Theta = 0°$ **(a)** and $\Theta = +2°$ **(b)**. The streamlines refer to the time averaged in-plane components of the velocity.

$y - z$ plane at $x^* = 2.31$, in the case of an upwash dominated wake (Fig. 6.24a), the velocity fluctuations in the lateral and vertical directions are mostly concentrated in the upper portion of the wake, with the bottom shear layer interrupted by the inwash generated by the rear wheels, feeding the stable recirculation described in §6.1. When the model is pitched 'nose up', the impact of the rear wheels' wake on the main body's wake is reduced because of the shielding effect of the model underbody. As such, a more uniform distribution is seen for both T^*_{vv} and T^*_{ww}. Nevertheless, in both cases high values of T^*_{vv} are visible at the core of the wake, and not just close to the shear layers as seen for some of the configurations discussed in §6.2. A similar trend is seen in the distribution of the pressure fluctuation recorded over the model base. This suggests that a certain level of 'mobility' is still present in the flow reversal, as also confirmed by the shape of the POD modes extracted from the velocity and pressure datasets.

In the first case, with the model tested at $\Theta = 0°$, the spatial functions associated with the first three POD modes strongly resemble those obtained for the square-back configuration

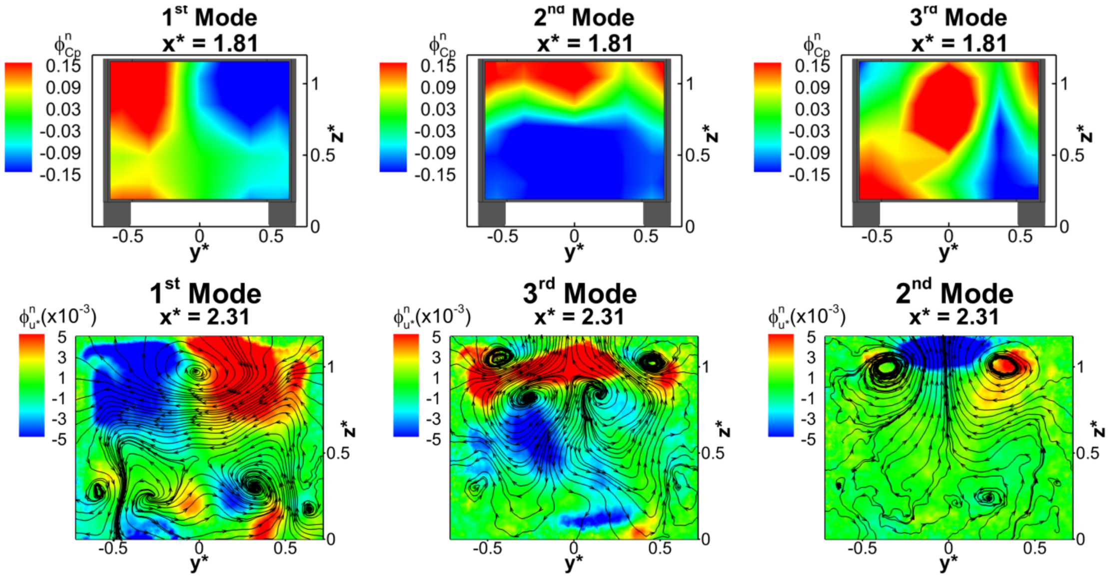

(a) LSB mode **(b)** VSB mode **(c)** SP mode

Figure 6.25: Spatial distribution of 3 of the most energetic POD modes extracted from the base pressure distribution (top row) and PIV cross-plane at $x^* = 2.31$ (bottom row) for the configuration with $\phi_s = 12°$, tested at $\Theta = 0°$ with stationary wheels. The modes are ordered according to their topology: **a** lateral symmetry breaking mode (LSB), **b** vertical symmetry breaking mode (VSB), **c** symmetry preserving mode (SP). $\phi^n_{C_p}$ refers to the magnitude of the spatial eigen-modes extracted from the field of the pressure fluctuation. The eigen-functions related to the velocity fluctuation are coloured according to the values of the through plane component $\phi^n_{u^*}$ whereas the streamlines are drawn considering the in-plane components $\phi^n_{v^*}$ and $\phi^n_{w^*}$.

investigated in §6.1 (Fig. 6.25). In analogy with that seen previously, the lower recirculation observed in the no-wheel case for the 1^{st} spatial mode (in the velocity dataset recorded at $x^* = 2.31$), is replaced by two pairs of counter rotating vortices (smaller in size), placed just behind the rear wheels (Fig. 6.25a). Vertical oscillations are seen mainly in the upper portion of the base (Fig. 6.25b), in the same region where the vertical component of the Reynolds stresses reaches its highest values, whilst a single plane of symmetry is reported for the symmetry preserving mode (Fig. 6.25c). The analogies with the case discussed in §6.1 extend also to the energy content of the same modes (Fig. 6.29a) as well as the wake evolution. This can be inferred by looking at the results of the phase averaged low order model presented in Fig. 6.27. The low frequency dynamics of the wake appear to be limited to swinging motions of the flow reversal, resulting in a continuous switching between a laterally symmetric state (seen at $\theta = 0\,rad$) and a non-symmetric state (visible for $\theta = \pi\,rad$). No 'radical changes' are seen in the wake topology throughout the entire phase domain. This is no longer the case when the model's pitch angle is brought to $\Theta = +2°$ and the symmetry of the time average wake in the vertical direction is restored. As can be inferred from the results presented in Fig. 6.28

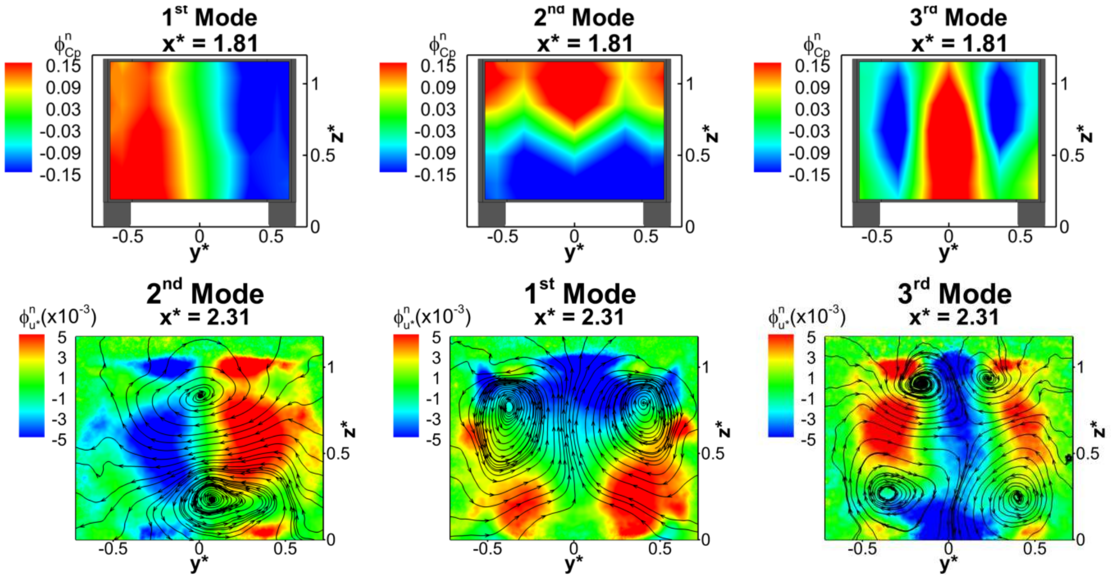

(a) LSB mode **(b)** VSB mode **(c)** SP mode

Figure 6.26: Spatial distribution of 3 of the most energetic POD modes extracted from the base pressure distribution (top row) and PIV cross-plane at $x^* = 2.31$ (bottom row) for the configuration with $\phi_s = 12°$, tested at $\Theta = +2°$ with stationary wheels. The modes are ordered according to their topology: **a** lateral symmetry breaking mode (LSB), **b** vertical symmetry breaking mode (VSB), **c** symmetry preserving mode (SP). $\phi^n_{C_p}$ refers to the magnitude of the spatial eigen-modes extracted from the field of the pressure fluctuation. The eigen-functions related to the velocity fluctuation are coloured according to the values of the through plane component $\phi^n_{u^*}$ whereas the streamlines are drawn considering the in-plane components $\phi^n_{v^*}$ and $\phi^n_{w^*}$.

for $x^* = 2.31$, the wake tends to switch between two laterally asymmetric states (at $\theta = 0\,rad$ and $\theta = \pi\,rad$). The transition between these two states is seen to occur through either the formation of a downwash dominated asymmetric state (at $\theta = \pi/2\,rad$) or the development of a symmetry preserving state (at $\theta = 3/2\pi\,rad$), where four different vortical structures seem to coexist. The fact that the latter state is visible for a wider range of phase angles suggests that it is also the most probable wake configuration, as also confirmed by its strong similarities with the time averaged flow field recorded on the same plane. This may also explain the higher reduction in base drag obtained in this case, when compared to that reported in §5.3. The higher level of variability seen in the wake is the result of the combination of coherent motions in both lateral and vertical directions that are not confined to a small region of the flow field (as seen for example in §6.2 for the configuration with $\phi_t = 0°$ and $\phi_t = 12°$), but extend over the entire cross-section of the rear recirculation. This becomes clear when the spatial functions related to the first three POD modes (the same used in the phase averaged low order model previously discussed) are considered (Fig. 6.26). The shapes obtained in these conditions are consistent with those reported for other unstable cases, such as the square-back model with

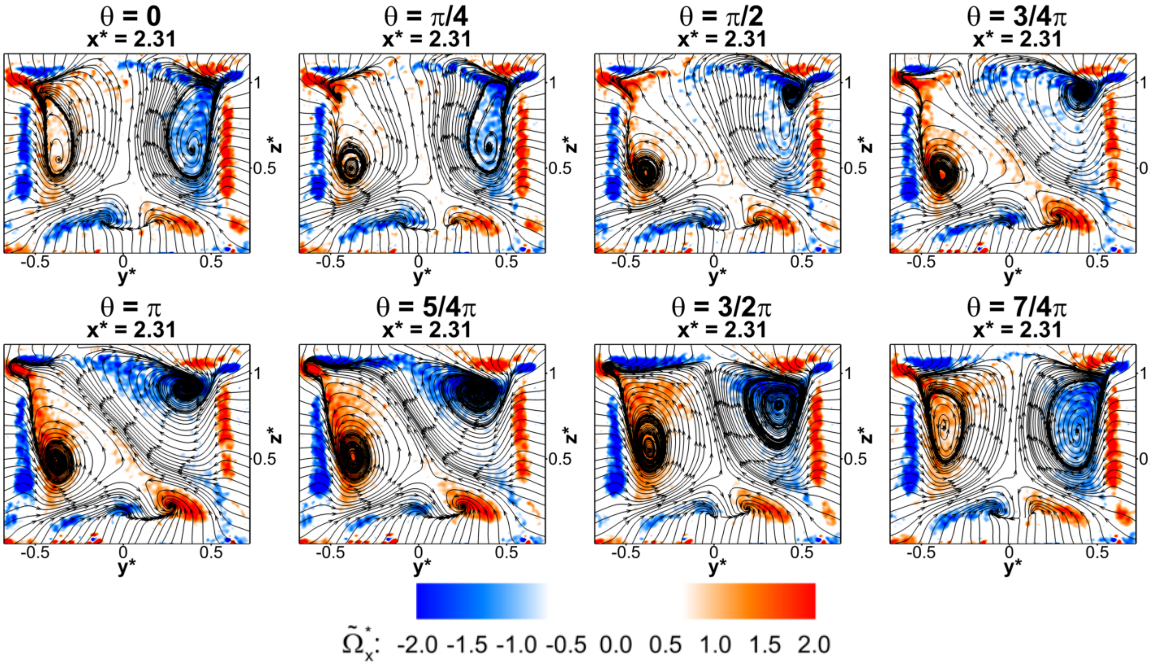

Figure 6.27: Low order phase averaged velocity field at $x^* = 2.31$ for the configuration with $\phi_s = 12°$ and stationary wheels, tested at $\Theta = 0.0°$. The plots are coloured according to the values of the normalised streamwise component of the vorticity $\tilde{\Omega}_x^*$; the streamlines are drawn considering the in-plane components of the velocity field.

no wheels (see §3.2.2) or the configuration with $\phi_s = 12°$ and no wheels tested at $-1°$ pitch (see§5.3). In analogy with those cases, both symmetry breaking modes are seen to extend over the entire base (Fig. 6.26a and 6.26b), matching the distribution of the lateral and vertical components of the Reynolds stresses reported in Fig. 6.24, whilst the small vortical structures previously observed in the 1^{st} POD mode behind the rear wheels are no longer visible (Fig. 6.26a). This is a consequence of the restoration of the 'continuity' in the bottom boundary layer (due to the shielding action of the model underbody on the rear wheels' wake) which, as pointed out by Morelli (2000), appears to be a necessary condition in order to achieve significant reductions in base drag. In the same conditions, two planes of symmetry are observed in the spatial function associated with the symmetry preserving mode (6.26c). Nevertheless, some differences can be noted in the energy content of these modes as well as the PDF of the related temporal coefficients. Compared to the symmetric configuration analysed in §5.3, for example, the recovery of the symmetry in the vertical direction in this case does not yield a significant rise in the energy associated with the *LSB* mode (Fig. 6.29a). On the contrary, an almost 100% increase, over the same configuration tested at 0° pitch, is seen in the amount of energy captured by the *VSB* mode. This trend is consistent with the establishment of a multi-stable condition, instead of the bi-stable condition seen for the simple square-back configuration, with some analogies with that described by Rigas et al (2014) and Gentile et al (2016) in the

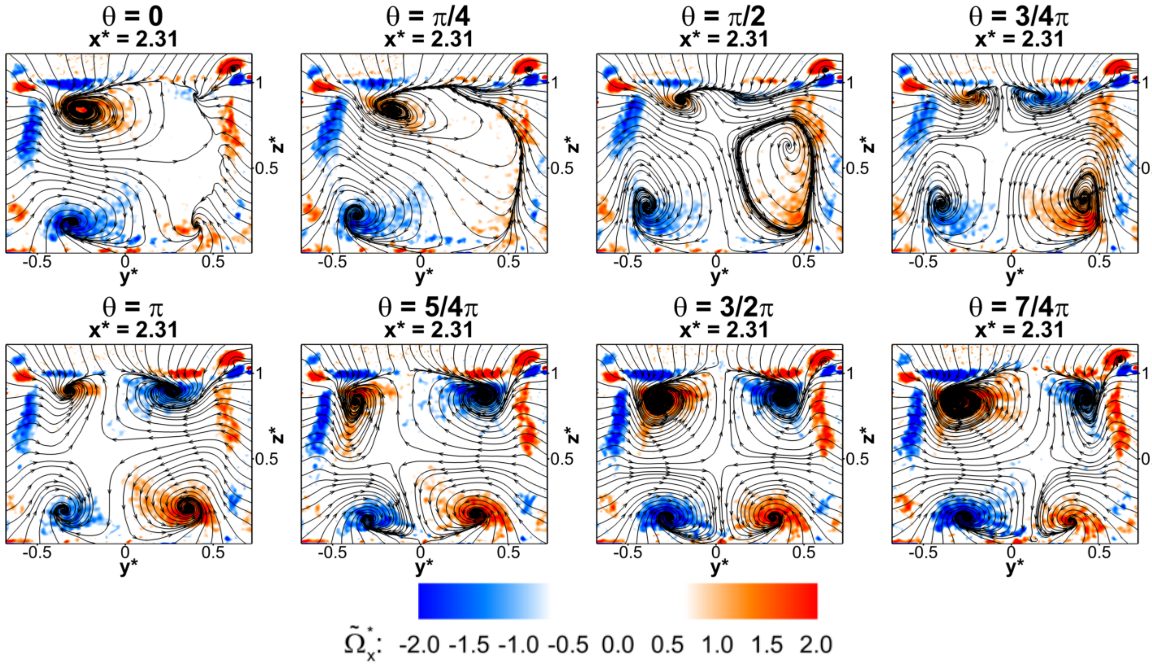

Figure 6.28: Low order phase averaged velocity field at $x^* = 2.31$ for the configuration with $\phi_s = 12°$ and stationary wheels, tested at $\Theta = +2.0°$. The plots are coloured according to the values of the normalised streamwise component of the vorticity $\tilde{\Omega}_x^*$; the streamlines are drawn considering the in-plane components of the velocity field.

case of axisymmetric bodies. A similar trend is observed in the PDFs of $a_{LSB}(t)$ and $a_{VSB}(t)$. Unlike the case studied in §5.3, hardly any difference can be discerned in the distribution of the value obtained for the first coefficient between $\Theta = 0°$ and $\Theta = +2°$ (Fig. 6.29b). The second coefficient, on the other hand, is seen to switch from a symmetric distribution to a non-symmetric distribution as the pitch angle is increased, although with still a limited range of variation in the values recorded for $a_{VSB}(t)$ (Fig. 6.29c). In the same conditions, a change in the characteristic frequency of the lateral flapping motion is also reported. When the pitch angle of the model is increased, the peak in the spectrum of the lateral symmetry breaking mode associated with this motion is seen to shift from $St_H = 0.17$ to $St_H = 0.12$ (Fig. 6.29d). The same peak is also observed for the vertical flapping motion (Fig. 6.29e). A similar behaviour has been reported in §5.3 when pitching the model in the opposite direction, although with a slightly higher frequency ($St_H = 0.17$). No additional peaks are noticed in the spectrum obtained for the temporal coefficient referring to the symmetry preserving mode (Fig. 6.29f), which seems to further confirm the link envisaged in §6.1, between the disappearing of the wake pumping and the tendency towards the selection of a four-vortex structure in the cross-plane at $x^* = 2.31$.

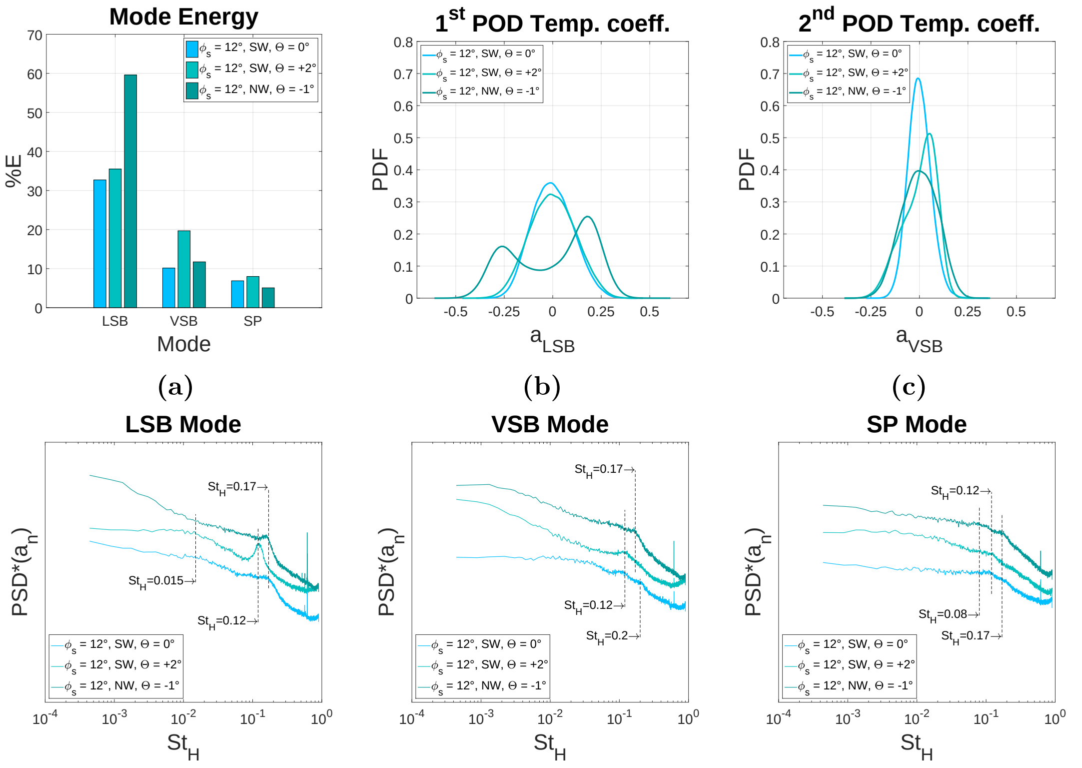

(a) (b) (c)

(d) (e) (f)

Figure 6.29: Top row: **a** energy associated with the three of the most energetic POD modes; **b** and **c**, PDFs of the values of first and second POD temporal coefficient. Bottom row, spectra of the POD temporal coefficients associated with: **d** the lateral symmetry breaking mode (LSB), **e** the vertical symmetry breaking mode (VSB), **f** the symmetry preserving mode (SP). The curves have been shifted along the vertical axis. Base pressure data recorded for the configurations with 12° vertical trailing edge tapers, with wheels (SW) and without wheels (NW).

6.4 Summary and conclusions

In this chapter the effects produced by wheels on the aerodynamic drag and the long-time instability have been investigated by means of pressure tappings, PIV and balance measurements. Both stationary and rotating wheels have been considered.

For the square-back model, an increase in base drag over the same configuration without wheels has been reported, accompanied with the loss of symmetry in the vertical direction. This has been found to be the result of an increase in size of the recirculating structures developing close to the bottom trailing edge of the base, downstream of each wheel. In these regions, the momentum deficit originating from the separations occurring in proximity to the wheel-arches as well as downstream of the wheels (Regert and Lajos (2007), Krajnovic et al (2011) and Aljure Osorio (2017)) yields an increase in size of the bottom recirculation, whose expansion come at the expenses of the upper vertical structure. As a result, the vertical symmetry seen in the time averaged wake topology for the no-wheel case at $y^* = 0.34$ (Chap. 3) is lost.

In analogy to that seen in Chap. 4 and 5, the loss of symmetry in the vertical direction is accompanied with the weakening of the lateral symmetry breaking mode described in Chap. 3. The wake appears indeed to lock into a lateral symmetry preserving state, characterised by the presence of two distinct pairs of vortices on the cross-plane located inside the near-wake recirculation (at $x^* = 2.31$). Only a swinging motion of the flow reversal is allowed, with a non-dimensional frequency of $St_H \approx 0.02$. This mode is reported to have a much more limited impact on the side force acting on the main body. Nevertheless, it may still affect other aspects, such as vehicle base soiling (Gaylard and Duncan, 2011). In the same conditions, the pumping motion is also seen to disappear.

A further confirmation of the stabilising effect of the rear wheels on the long-time wake dynamics is given by the fact that the bi-stable mode is seen to gain strength every time the interaction between the wheels' wake and the main body's wake is either limited, for example by increasing the model ground clearance, or prevented, by increasing the longitudinal distance between the wheels and the model base (achieved in this case by removing the rear axle from the model while keeping the front wheels in place).

The sensitivity of the wake to variations of the model's trailing edge geometry has also been investigated. In particular, a 'fully stable' wake has been reported when a bottom diffuser is added to the model, allowing for a higher amount of low momentum flow originating from the rear wheels' wake to be entrained into the main body's wake. In these conditions, the long-time instability is seen to vanish, replaced by an oscillating shear layer mode with a non-dimensional frequency of $St_H = 0.035$. As such, no low frequency activity is seen in the wavelet spectrum obtained from the signal recorded for the lateral component of the aerodynamic force, in contrast with that seen in Chap. 3 for the simple square-back configuration. This is found to be at the origin of the reduction in the standard deviation of the side force (resampled at $5\,Hz$) reported in this case, in agreement with the findings of Grandemange et al (2015).

In analogy with that described in Chap. 4 and Chap. 5, a decrease in drag is seen every time the symmetry in the vertical direction is restored. This, however, does not appear to be linked necessarily with the stabilisation of the wake. Indeed, the lowest base drag value is reported when the model equipped with 12° side edge tapers was tested at +2° pitch, in order to counteract the upwash seen for the same configuration at 0° pitch angle. In these conditions, the model underbody is seen to act as a 'shield', preventing the rear wheels' wake from interacting with the main body's wake, thus restoring the 'continuity' in the bottom boundary layer prior to separation (Morelli, 2000). In this case, the application of proper orthogonal decomposition to both the pressure dataset and the velocity fields recorded at $x^* = 2.31$, has revealed the existence of coherent motions of the wake, in the horizontal and vertical directions, spanning over the entire base. The combination of these modes has been shown to result in the development of a 'multi-stable' behaviour, as the wake is seen to switch between two laterally asymmetric states, a downwash dominated state and a symmetry preserving state. The fact that the latter state appears to be the most probable configuration of the wake may explain the slightly higher base drag reduction achieved in this case (over the same model tested at 0° pitch), when compared to that reported in §5.3 for the same configuration without wheels. This is line with that seen in §4.2.1 for the model with no wheels and 12° tapers applied to both horizontal trailing edges. In these two cases, the selection of the lateral symmetry preserving state and the concurrent disappearing of the peak at $St_H \approx 0.07$ in the spectrum extracted from the pressure dataset, also seems to suggest that the 'wake pumping' described in §3.2.4 may be a characteristic mode of the non-symmetric states only.

In all cases, no big differences have been seen in either the wake topology or the wake dynamics between having the wheels stationary or rotating, apart from a decrease in the values of the drag generated by the rearward facing surfaces in the latter case.

Chapter 7

Conclusions

The present work has focused on the experimental characterisation of the time averaged topology and unsteady features of the wake developing downstream of a simplified square-back ground vehicle. An extensive experimental campaign consisting of balance, pressure, particle image velocimetry and single point velocity measurements has been carried out, at a Reynolds number of $Re_H = 7.7 \times 10^5$ (based on the model height). The sensitivity of the wake topology and the main unsteady modes to small geometrical changes, such as the application of high aspect ratio tapers to either the horizontal or the vertical trailing edges, has been investigated, together with the effects produced by non geometry-related perturbations, such as changes in ground clearance, free-stream turbulence intensity, yaw and pitch angle. The impact of wheels, in either stationary or rotating conditions, on the same flow field has been assessed too.

For the square-back configuration without wheels, the existence of a long period bi-stable mode has been proven for the first time for a geometry with a more slanted front-end than the one considered in previous works (Grandemange et al (2012a), Grandemange et al (2013b)). This mode has been observed only for a limited range of yaw angles ($\Psi = \pm 0.5°$), in agreement with the findings of Volpe et al (2015) and Evrard et al (2016), although its presence has been documented for three different values of the ground clearance ($C^* = 0.138$, $C^* = 0.173$ and $C^* = 0.208$) and free-stream turbulence intensities up to 1.5%.

A quasi-steady correlation between the aerodynamic forces and the bi-stable mode has been demonstrated by applying wavelet and cross-wavelet transforms to the balance data. The nature of this relationship has been further investigated by applying proper orthogonal decomposition to the pressure and velocity datasets. A new structure has been proposed for each bi-stable state, consisting of a hairpin vortex that originates from one of the model's two vertical trailing edges and bends towards the opposite side as it merges into a single streamwise vortex downstream (Fig. 7.1a). In addition, two global oscillating modes, similar to those described in Grandemange et al (2013b) and Volpe et al (2015), have been identified. These modes have been shown to consist of lateral and vertical motions of the wake closure caused by the interactions between the hairpin vortex and the vertical and horizontal shear layers

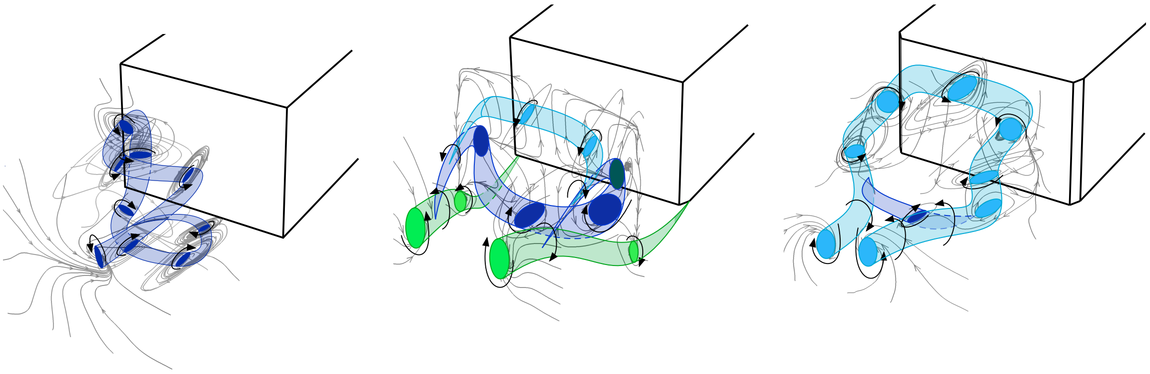

(a) *Square-back* **(b)** *Horizontal trailing edge tapering* **(c)** *Vertical trailing edge tapering*

Figure 7.1: Schematic representation of the different vortical structures identified in the present study.

originating from the opposite side of the model. The pumping mode reported in Duell and George (1999) has also been identified and, for the first time, linked to the motion of the bi-stable vortical structure in the streamwise direction.

Further insights on the long-time evolution of the wake have been obtained by building a phase averaged low order model, based on the three most energetic POD modes. This has provided a comprehensive description of the mechanisms of the switch between bi-stable states. It has been demonstrated that, during the switch, the wake becomes laterally symmetric and at this point the level of interaction between the recirculating structures and the base reaches a minimum, yielding a $\approx 7\%$ reduction of the base drag compared to the time averaged result.

The sensitivity of the wake downstream of such a model to small geometrical changes has then been studied. This follows the work of Littlewood and Passmore (2010) and Perry et al (2015). Short tapers ($\approx 4\%$ of the model length) have been applied to the top and bottom edges of the base, with the aim of replicating a shape optimisation process that is realistic for many modern mass-produced vehicles. The pressure drag associated with the rear facing surfaces has been calculated and correlated with the balance data. The results have highlighted the effectiveness of such small devices in modifying the time average wake topology. An increase in drag has been reported to occur when the application of the horizontal tapers leads to the creation of an upwash or downwash dominated wake, breaking symmetry seen in the vertical direction for the simple square-back configuration. In these conditions, the time averaged flow field has been shown to be dominated by the presence of a *'U'* shaped horseshoe vortex, acting in the region of the taper generating the strongest inflow, plus a second planar horseshoe vortex shed from the opposite trailing edge (Fig. 7.1b). As the *'U'* shaped vortex interacts with the surface of the base, a low pressure region (responsible for the drag increase) is formed.

The application of proper orthogonal decomposition to the pressure and velocity datasets, combined with the single point unsteady velocity measurements, has allowed some light to be shed on the impact of different levels of upwash and downwash on both the short-time and the long-time wake dynamics. An increase in the characteristic frequency of the vertical flapping has been reported as the gap between the top and bottom shear layers is reduced, in agreement with the trend observed for $2D$ bodies by Luo et al (1994). In the case of an upwash (or downwash) dominated wake, this mode has been shown to be the result of the interactions between a stable vortical structure forming in correspondence to the taper generating the highest amount of inflow and the shear layer emanating from the opposite side of the model. Indeed, it is the stabilisation of the former recirculation that has been found to be the cause of the loss of symmetry in the vertical direction that ultimately leads to a rise in the values of C_D. The reduced gap between the top and bottom shear layers has also been linked to the weakening of the bi-stable lateral symmetry breaking mode. Although the hairpin vortex described for the square-back case is still visible in the near-wake (when the two bi-stable states are isolated) it appears to be deformed by the upwash/downwash generated by the tapers and limited in size by the action of the counter-rotating vortices developing at the tips of each slant.

The weakening of the bi-stable mode, however, has been reported to yield a decrease in C_D over the square-back case only when accompanied with the restoration of the symmetry in the vertical direction. This has been obtained by applying 12° tapers on both horizontal trailing edges. In this case, the symmetry preserving state has been observed to become the most stable configuration, yielding a base drag reduction of $\approx 8\%$. This has been achieved by maximising the amount of reverse flow impinging on the base, as the *'U'* shaped vortex seen in the case of non symmetric wakes has been reported to be replaced by a horizontal horseshoe vortex, running parallel to the similar structure developing on the opposite side of the model, and a pair of transverse vortices acting in correspondence to the vertical trailing edges. The latter structures are seen to act very close to the base, suggesting that there may be still space for further improvements.

The increased distance between the base and the vortices developing in the near-wake, together with the stretching of the same structures, has been found to be the element driving the further reduction in base drag observed when similar tapers are applied to the vertical trailing edges, leaving the top and bottom trailing edges squared. In these conditions, the long-time bi-stable mode has been seen to evolve into multi-stable behaviour first (for $\phi_s = 6°$) and then vanish, for chamfer angles greater than 12°. The symmetry breaking state described in the square-back case has been reported to be now locked in a position rotated by 90° compared to that seen in the lateral bi-stable case. The fact that two distinct vortices are still visible downstream of the wake closure (unlike that described for the simple square-back configuration) has suggested the existence of a more horseshoe-like vortical structure, similar to that reported in Grandemange et al (2012b) (Fig. 7.1c).

POD filtered fields have shown that this vortex is not stationary but swings around the rear stagnation point, with a normalised frequency of $St_H \simeq 0.015$, without ever firmly changing side. Indeed, it appears to 'burst' (losing coherence) every time it deviates for more than $\approx 45°$

in the azimuthal direction from the time averaged (most probable) position. In these conditions, the interactions between the shear layers developing on either side of the model have also been shown to become stronger, so that the lateral flapping appears now to be the dominant global oscillating mode.

A multi-stable condition, similar to that seen for $\phi_s = 6°$, can be restored by dropping the model pitch angle by less than $-1°$, while keeping $\phi_s = 12°$. When this happens, the recovery of the symmetry in the vertical direction in the time averaged wake has been reported to coincide with a strengthening of the long-time instability. Nevertheless, a further reduction in the base drag recorded over the same model tested at zero degree pitch has been seen in this case, suggesting that a lower drag wake is not necessarily a more stable wake. On the other hand, a pitch angle variation of $\approx -1°$ has been found to be sufficient to force the time averaged wake to switch from a downwash dominated topology to an upwash dominated topology. This high level of sensitivity may explain the differences seen when comparing the time averaged results obtained in the present investigation with other results reported in the literature (Perry et al, 2015). It may also be the origin of the high level of variability seen in the wake topologies reported by Makihara et al (2016), when considering more realistic automotive shapes

Similar results have been reported when wheels, either stationary or rotating, are applied to the same model. In this case, a pitch variation in the opposite direction has been found to be needed in order to 'destabilise' the wake. When the model is brought to $\Theta = +2°$, the appearance of a multi-stable behaviour has been reported. The wake has been seen to switch between two laterally asymmetric states, a downwash dominated state and a symmetry preserving state. Indeed, the latter state has been observed to be the most probable wake configuration in these conditions, explaining the slightly better performance, in terms of base drag reduction over the same model tested at 0° pitch, achieved in this case compared to that obtained for the same configuration without wheels.

The establishment of a multi-stable condition however, appears to be an 'exception'. In all the other cases, in fact, the addition of wheels has been shown to yield a stabilisation of the wake. The reason for this has been found in the growth of the bottom recirculating structure developing close to the sides of the model base. The vortex acting in this region has been shown to increase in size when fed by the momentum deficit originating from the separations occurring at the rear wheel-arches as well as downstream of the rear wheels. This seems to prevent the development of the coherent motions in the lateral as well as vertical directions that are need to promote a switch. As a results, the wake has been seen to lock into a lateral symmetry preserving state, characterised by the presence of two distinct pairs of vortices in correspondence to the cross-plane located inside the near-wake recirculation (at $x^* = 2.31$). In these conditions, only a swinging motion of the flow reversal is allowed, with a non-dimensional frequency of $St_H \approx 0.02$. This mode is replaced by lateral flapping, limited mostly to the top shear layer and with a non-dimensional frequency of $St_H = 0.035$, when the symmetry in the vertical direction is disrupted further by adding a 12° taper to the bottom trailing edge of the model, increasing the amount of low momentum flow entrained into the lower recirculation of the main body's wake. In these conditions, the suppression of the long-time instability has been shown to yield a noticeable reduction in the standard deviation associated with the value of side force (when resampled at $5\,Hz$), in agreement with the findings of Grandemange et al (2015).

In terms of short-time wake dynamics, although variations in the characteristic frequency and/or strength are seen for both the vertical flapping and the lateral flapping, depending on the configuration considered, the most noticeable changes are reported for the pumping motion, which seems to disappear. In all cases, no big differences have been seen in either the wake topology or the wake dynamics between having the wheels stationary or rotating, apart from a decrease in the values of the drag generated by the rear facing surfaces in the latter case.

Overall, the present work has provided valuable insights on how the long-time instability past square-back automotive shapes develops as well as its impact on the aerodynamic drag. It has been shown that a drag reduction can be achieved every time the symmetry of the wake is restored, as a consequence of the increased amount of reverse flow impinging on the base of the model. This seems to be true regardless of the configuration considered (with or without wheels) and the type of optimisation strategy adopted. However, it does not necessarily imply the complete suppression of the long-time instability. In fact, a certain level of 'mobility' in the flow reversal seems to be inevitable every time the symmetry of the wake in the vertical direction is restored.

Several elements that can alter this behaviour have also been identified. It has been shown, for example, that the probability of the switches between bi-stable states can be increased (until eventually the long-time instability disappears, replaced by low frequency flapping or swinging motions) by changing the curvature of at least one of the four shear layers bounding the wake. This can be either on a 'global' scale (i.e. perturbing the shear layers over their entire span) or on a more 'local' scale (i.e. applying the perturbation only to a relatively limited portion of the shear layer, as seen when adding wheels to the model). This last aspect may help to 'bridge the gap' between simplified geometries and more realistic automotive shapes, when looking for long-time instabilities. In all cases, however, this type of instability has been observed to stem from the mutual interactions between all four shear layers rather than being the result of the state of perturbation of a single shear layer. This is proven by the fact that a wake asymmetric in the vertical direction, stabilised by increasing the curvature of the side shear layers, can become unstable if the model pitch angle is changed in such a way that the symmetry in the vertical direction is restored.

A good correlation has been found between the temporal scale of the instability and the level of change seen in the wake topology during each switch. Indeed, longer times between switches are usually associated with large deviations of the wake from the topology seen in the time averaged results. This aspect should be taken into account when setting up CFD simulations or comparing experimental and numerical results. In addition, some interesting connections between the long-time and the short time wake dynamics have been observed. In the case without wheels, the weakening of the long-time instability has been seen to coincide with the strengthening of either the vertical or the horizontal flapping. The pumping motion, on the other hand, has been reported to disappear as the symmetry preserving state becomes the most probable configuration of the wake. This suggests that this motion may be indeed a characteristic feature of the asymmetric state. However, only some of these trends are confirmed when wheels are added to the model. The suppression on the long-time instability in fact, is no longer accompanied with the strengthening of the flapping motions seen at $0.10 \lesssim St_H \lesssim 0.2$ which, although still visible, remain relatively weak. Even in this case, however, the establishment of a multi-stable condition has been seen to coincide with the convergence of the lateral and vertical flapping motions towards the same frequency, as seen in the case of bodies with $W/H \approx 1$, despite the fact that the lengths of the horizontal and vertical trailing edges still remain different.

References

Adrian RJ, Westerweel J (2011) Particle image velocimetry. Cambridge University Press

Ahmed S, Ramm G, Faltin G (1984) Some salient features of the time-averaged ground vehicle wake. Tech. rep., SAE Technical Paper

Ahmed SR (1981) Wake structure of typical automobile shapes. Journal of Fluids Engineering 103(1):162–169

Aider JL, Beaudoin JF, Wesfreid JE (2010) Drag and lift reduction of a 3d bluff-body using active vortex generators. Experiments in fluids 48(5):771–789

Al-Garni AM, Bernal LP, Khalighi B (2004) Experimental investigation of the flow around a generic suv. Tech. rep., SAE Technical Paper

Aljure Osorio DE (2017) Aerodynamic analysis of complex geometries using cfd. PhD thesis, Universitat Politècnica de Catalunya

Anderson JD (2009) Fundamentals of Aerodynamics. Tata McGraw-Hill Education

Ashton N, Revell A (2015) Comparison of rans and des methods for the drivaer automotive body. Tech. rep., SAE Technical Paper

Auguste F, Fabre D, Magnaudet J (2010) Bifurcations in the wake of a thick circular disk. Theoretical and Computational Fluid Dynamics 24(1):305–313

Axerio J, Iaccarino G, Issakhanian E, Elkins C, Eaton J (2009) Computational and experimental investigation of the flow structure and vortex dynamics in the wake of a formula 1 tire. SAE Technical Paper 2009-01-0775

Baden Fuller J (2012) The unsteady aerodynamics of static and oscillating simple automotive bodies. PhD thesis, Loughborough University

Balkanyi SR, Bernal LP, Khalighi B (2002) Analysis of the near wake of bluff bodies in ground proximity. In: ASME 2002 International Mechanical Engineering Congress and Exposition, American Society of Mechanical Engineers, pp 705–713

Barlow JB, Rae Jr WH, Pope A (1999) Low-Speed Wind Tunnel Testing. Wiley

Barros D, Borée J, Noack BR, Spohn A, Ruiz T (2016) Bluff body drag manipulation using pulsed jets and coanda effect. Journal of Fluid Mechanics 805:422–459

Barros D, Borée J, Cadot O, Spohn A, Noack BR (2017) Forcing symmetry exchanges and flow reversals in turbulent wakes. Journal of Fluid Mechanics 829

Batchelor GK (2000) An introduction to fluid dynamics. Cambridge university press

Bearman P (1965) Investigation of the flow behind a two-dimensional model with a blunt trailing edge and fitted with splitter plates. Journal of Fluid Mechanics 21(2):241–255

Bearman P (1969) On vortex shedding from a circular cylinder in the critical reynolds number regime. Journal of Fluid Mechanics 37(3):577–585

Bearman P (1997) Near wake flows behind two-and three-dimensional bluff bodies. Journal of Wind Engineering and Industrial Aerodynamics 69:33–54

Beaudoin JF, Aider JL (2008) Drag and lift reduction of a 3d bluff body using flaps. Experiments in fluids 44(4):491–501

Benedict L, Gould R (1996) Towards better uncertainty estimates for turbulence statistics. Experiments in fluids 22(2):129–136

Berger E, Scholz D, Schumm M (1990) Coherent vortex structures in the wake of a sphere and a circular disk at rest and under forced vibrations. Journal of Fluids and Structures 4(3):231–257

Bhattacharyya S, Maiti D (2004) Shear flow past a square cylinder near a wall. International Journal of Engineering Science 42(19):2119–2134

Bloor MS (1964) The transition to turbulence in the wake of a circular cylinder. Journal of Fluid Mechanics 19(2):290–304

Bohorquez P, Sanmiguel-Rojas E, Sevilla A, Jimenez-Gonzalez J, Martinez-Bazan C (2011) Stability and dynamics of the laminar wake past a slender blunt-based axisymmetric body. Journal of Fluid Mechanics 676:110–144

Bonnavion G, Cadot O, Évrard A, Herbert V, Parpais S, Vigneron R, Délery J (2017a) On multistabilities of real car's wake. Journal of Wind Engineering and Industrial Aerodynamics 164:22–33

Bonnavion G, Cadot O, Herbert V, Parpais S, Vigneron R, Délery J (2017b) Effect of a base cavity on the wake of the squareback ahmed body at various ground clearances and application to drag reduction. S18-Contrôle des écoulements

Brackston R, de la Cruz JG, Wynn A, Rigas G, Morrison J (2016) Stochastic modelling and feedback control of bistability in a turbulent bluff body wake. Journal of Fluid Mechanics 802:726–749

Bristol R, Ortega J, Marcus P, Savaş Ö (2004) On cooperative instabilities of parallel vortex pairs. Journal of Fluid Mechanics 517:331–358

Brown GL, Roshko A (1974) On density effects and large structure in turbulent mixing layers. Journal of Fluid Mechanics 64(4):775–816

Bruneau CH, Creusé E, Depeyras D, Gilliéron P, Mortazavi I (2010) Coupling active and passive techniques to control the flow past the square back ahmed body. Computers & Fluids 39(10):1875–1892

Bury Y, Jardin T (2012) Transitions to chaos in the wake of an axisymmetric bluff body. Physics letters A 376(45):3219–3222

Cabitza S (2014) Active control of the wake from a rectangular-sectioned body. PhD thesis, PhD thesis. Imperial College London

Cadot O (2016) Stochastic fluid structure interaction of three-dimensional plates facing a uniform flow. Journal of Fluid Mechanics 794

Cadot O, Evrard A, Pastur L (2015) Imperfect supercritical bifurcation in a three-dimensional turbulent wake. Physical Review E 91(6):063,005

Cantwell B, Coles D (1983) An experimental study of entrainment and transport in the turbulent near wake of a circular cylinder. Journal of fluid mechanics 136:321–374

Carr G (1971) Wind tunnel blockage corrections for road vehicles. Tech. Rep. 4, MIRA Report

Carr G (1983) Potential for aerodynamic drag reduction in car design. Int J Vehicle Design, 1983 pp 44–56

Castelain T, Michard M, Szmigiel M, Chacaton D, Juvé D (2018) Identification of flow classes in the wake of a simplified truck model depending on the underbody velocity. Journal of Wind Engineering and Industrial Aerodynamics 175:352–363

Chaligné S, Turner R, Gaylard A (2017) The aerodynamics development of the new land rover discovery 5. In: FKFS Conference, Springer, pp 145–159

Champagne F, Pao Y, Wygnanski I (1976) On the two-dimensional mixing region. Journal of Fluid Mechanics 74(02):209–250

Choi H, Lee J, Park H (2014) Aerodynamics of heavy vehicles. Annual Review of Fluid Mechanics 46:441–468

Chrust M, Goujon-Durand S, Wesfreid J (2013) Loss of a fixed plane of symmetry in the wake of a sphere. Journal of Fluids and Structures 41:51–56

Cogotti A (1983) Aerodynamic characteristics of car wheels. Int J Vehicle Design - Impact Aerodynamics on Vehicle Design, 1983, pp 173–196

Cogotti A (1998) A parametric study on the ground effect of a simplified car model. Tech. rep., SAE Technical Paper

Cooper KR, Bertenyi T, Dutil G, Syms J, Sovran G (1998) The aerodynamic performance of automotive underbody diffusers. Tech. rep., SAE Technical Paper

Corallo M, Sheridan J, Thompson M (2015) Effect of aspect ratio on the near-wake flow structure of an ahmed body. Journal of Wind Engineering and Industrial Aerodynamics 147:95–103

Coupland JM, Pickering CJ (1988) Particle image velocimetry: estimation of measurement confidence at low seeding densities. Optics and lasers in engineering 9(3-4):201–210

Croner E, Bézard H, Sicot C, Mothay G (2013) Aerodynamic characterization of the wake of an isolated rolling wheel. International Journal of Heat and Fluid Flow 43:233–243

Dassanayake P, Ramachandran D, Salati L, Barber T, Doig G (2012) Unsteady computational simulation of the flow structure of an isolated wheel in contact with the ground. In: Proceedings of the 18th Australasian Fluid Mechanics Conference, Launceston, Australia, pp 3–7

Davis JP (1982) Wind tunnel investigations of road vehicle wakes. PhD thesis, Imperial College London (University of London)

Diasinos S, Barber TJ, Doig G (2015) The effects of simplifications on isolated wheel aerodynamics. Journal of Wind Engineering and Industrial Aerodynamics 146:90–101

Dimotakis PE (1991) Turbulent free shear layer mixing and combustion. Tech. rep., Graduate Aeronautical Laboratories, California Institute of Technology

Duell EG, George A (1999) Experimental study of a ground vehicle body unsteady near wake. Tech. rep., SAE Technical Paper

EC-No-443/2009 R (2010) Regulation (ec) no 443/2009 setting emission performance standards for new passenger cars as part of the community's integrated approach to reduce co2 emissions from light-duty vehicles

Elofsson P, Bannister M (2002) Drag reduction mechanisms due to moving ground and wheel rotation in passenger cars. Tech. rep., SAE Technical Paper

Evrard A, Cadot O, Herbert V, Ricot D, Vigneron R, Délery J (2016) Fluid force and symmetry breaking modes of a 3d bluff body with a base cavity. Journal of Fluids and Structures 61:99–114

Evstafyeva O, Morgans A, Dalla Longa L (2017) Simulation and feedback control of the ahmed body flow exhibiting symmetry breaking behaviour. Journal of Fluid Mechanics 817

Fabijanic J (1996) An experimental investigation of wheel-well flows. Tech. rep., SAE Technical Paper

Fabre D, Auguste F, Magnaudet J (2008) Bifurcations and symmetry breaking in the wake of axisymmetric bodies. Physics of Fluids 20(5):051,702

Fackrell J, Harvey J (1975) The aerodynamics of an isolated road wheel. In: Proceedings of the Second AIAA Symposium of Aerodynamics of Sports and Competition Automobiles, Los Angleles, California, USA, vol 11, pp 119–125

Farge M (1992) Wavelet transforms and their applications to turbulence. Annual review of fluid mechanics 24(1):395–458

Forbes DC (2017) Coupling road vehicle aerodynamics and dynamics in simulation. PhD thesis, Loughborough University

Fuchs HV, Mercker E, Michel U (1979) Large-scale coherent structures in the wake of axisymmetric bodies. Journal of Fluid Mechanics 93(01):185–207

Fuller JB, Passmore M (2013) Unsteady aerodynamics of an oscillating fastback model. Tech. rep., SAE Technical Paper

Gaylard AP, Duncan B (2011) Simulation of rear glass and body side vehicle soiling by road sprays. SAE International Journal of Passenger Cars-Mechanical Systems 4(2011-01-0173):184–196

Gentile V, Schrijer F, Van Oudheusden B, Scarano F (2016) Low-frequency behavior of the turbulent axisymmetric near-wake. Physics of Fluids 28(6):065,102

Gentile V, Van Oudheusden B, Schrijer F, Scarano F (2017) The effect of angular misalignment on low-frequency axisymmetric wake instability. Journal of Fluid Mechanics 813

Gerrard J (1966) The mechanics of the formation region of vortices behind bluff bodies. Journal of Fluid Mechanics 25(02):401–413

Gilliéron P, Kourta A (2010) Aerodynamic drag reduction by vertical splitter plates. Experiments in fluids 48(1):1–16

Gilliéron P, Kourta A (2013) Aerodynamic drag control by pulsed jets on simplified car geometry. Experiments in fluids 54(2):1457

Graftieaux L, Michard M, Grosjean N (2001) Combining piv, pod and vortex identification algorithms for the study of unsteady turbulent swirling flows. Measurement Science and technology 12(9):1422

Grandemange M (2013) Analysis and control of three-dimensional turbulent wakes: from axisymmetric bodies to road vehicles. PhD thesis, Palaiseau, Ecole polytechnique

Grandemange M, Cadot O, Gohlke M (2012a) Reflectional symmetry breaking of the separated flow over three-dimensional bluff bodies. Physical review E 86(3):035,302

Grandemange M, Gohlke M, Parezanović V, Cadot O (2012b) On experimental sensitivity analysis of the turbulent wake from an axisymmetric blunt trailing edge. Physics of fluids 24(3):035,106

Grandemange M, Gohlke M, Cadot O (2013a) Bi-stability in the turbulent wake past parallelepiped bodies with various aspect ratios and wall effects. Physics of Fluids (1994-present) 25(9):095,103

Grandemange M, Gohlke M, Cadot O (2013b) Turbulent wake past a three-dimensional blunt body. part 1. global modes and bi-stability. Journal of Fluid Mechanics 722:51–84

Grandemange M, Mary A, Gohlke M, Cadot O (2013c) Effect on drag of the flow orientation at the base separation of a simplified blunt road vehicle. Experiments in fluids 54(5):1–10

Grandemange M, Gohlke M, Cadot O (2014a) Statistical axisymmetry of the turbulent sphere wake. Experiments in fluids 55(11):1838

Grandemange M, Gohlke M, Cadot O (2014b) Turbulent wake past a three-dimensional blunt body. part 2. experimental sensitivity analysis. Journal of Fluid Mechanics 752:439–461

Grandemange M, Cadot O, Courbois A, Herbert V, Ricot D, Ruiz T, Vigneron R (2015) A study of wake effects on the drag of ahmed's squareback model at the industrial scale. Journal of Wind Engineering and Industrial Aerodynamics 145:282–291

Grinsted A, Moore JC, Jevrejeva S (2004) Application of the cross wavelet transform and wavelet coherence to geophysical time series. Nonlinear processes in geophysics 11(5/6):561–566

Gulyás A, Bodor Á, Regert T, Jánosi IM (2013) Piv measurement of the flow past a generic car body with wheels at les applicable reynolds number. International Journal of Heat and Fluid Flow 43:220–232

Harris FJ (1978) On the use of windows for harmonic analysis with the discrete fourier transform. Proceedings of the IEEE 66(1):51–83

Heft AI, Indinger T, Adams NA (2012) Introduction of a new realistic generic car model for aerodynamic investigations. Tech. rep., SAE Technical Paper

Herry BB, Keirsbulck L, Labraga L, Paquet JB (2011) Flow bistability downstream of three-dimensional double backward facing steps at zero-degree sideslip. Journal of Fluids Engineering 133(5):054,501

Howell J (1994) The influence of ground simulation on the aerodynamics of simple car shapes with an underfoor diffuser. In: RAes Conference on Vehicle Aerodynamics, pp 36–1

Howell J, Le Good G (2004) Vortex drag for a simple car-like shape. In: 5th MIRA International Vehicle Aerodynamics Conference, 13th October

Howell J, Le Good G (2008) The effect of backlight aspect ratio on vortex and base drag for a simple car-like shape. Tech. rep., SAE Technical Paper

Howell JP (1993) Shape features which influence crosswind sensitivty. In: Vehicle Ride and Handling Conference (2nd Edition), IMechE, p C466/036/93

Huang R, Lin B, Yen S (2010) Time-averaged topological flow patterns and their influence on vortex shedding of a square cylinder in crossflow at incidence. Journal of Fluids and Structures 26(3):406–429

Hucho Wh, Sovran G (1993) Aerodynamics of road vehicles. Annual review of fluid mechanics 25(1):485–537

Huminic A, Huminic G (2017) Aerodynamic study of a generic car model with wheels and underbody diffuser. International Journal of Automotive Technology 18(3):397–404

Hussain A, Zaman K (1985) An experimental study of organized motions in the turbulent plane mixing layer. Journal of Fluid Mechanics 159:85–104

Instrumentation T (2011) Getting started-series 100 cobra probe. Victoria, Australia: Turbulent Flow

Ishima T, Takahashi Y, Okado H, Baba Y, Obokata T (2011) 3d-piv measurement and visualization of streamlines around a standard sae vehicle model. Tech. rep., SAE Technical Paper

Issakhanian E, Elkins CJ, Lo KP, Eaton JK (2010) An experimental study of the flow around a formula one racing car tire. Journal of Fluids Engineering 132(7):071,103

Jeong J, Hussain F (1995) On the identification of a vortex. Journal of fluid mechanics 285:69–94

Johl G (2010) The design and performance of a 1.9 mx 1.3 m indraft wind tunnel. PhD thesis, Loughborough University

Johl G, Passmore M, Render P (2004) Design methodology and performance of an indraft wind tunnel. The aeronautical journal 108(1087):465–473

Kähler C, Sammler B, Kompenhans J (2002) Generation and control of tracer particles for optical flow investigations in air. Experiments in fluids 33(6):736–742

Katz J (2006) Aerodynamics of race cars. Annu Rev Fluid Mech 38:27–63

Kawakami M, Murata O, Maeda K (2015) Improvement in vehicle motion performance by suppression of aerodynamic load fluctuations. SAE International Journal of Passenger Cars-Mechanical Systems 8(2015-01-1537):205–216

Khalighi B, Zhang S, Koromilas C, Balkanyi S, Bernal LP, Iaccarino G, Moin P (2001) Experimental and computational study of unsteady wake flow behind a bluff body with a drag reduction device. Tech. rep., SAE Technical Paper

Khalighi B, Chen KH, Iaccarino G (2012) Unsteady aerodynamic flow investigation around a simplified square-back road vehicle with drag reduction devices. Journal of fluids engineering 134(6):061,101

Kim TY, Lee Bs, Lee DH, Hwang Jh, Lee Dh (2003) A study on vortex shedding around a bluff body near the ground. Tech. rep., SAE Technical Paper

Kiya M, Abe Y (1999) Turbulent elliptic wakes. Journal of fluids and structures 13(7-8):1041–1067

Kiya M, Ishikawa H, Sakamoto H (2001) Near-wake instabilities and vortex structures of three-dimensional bluff bodies: a review. Journal of Wind Engineering and Industrial Aerodynamics 89(14):1219–1232

Knisely CW (1990) Strouhal numbers of rectangular cylinders at incidence: a review and new data. Journal of Fluids and Structures 4(4):371–393

Knowles R, Saddington A, Knowles K (2002) On the near wake of rotating, 40%-scale champ car wheels. Tech. rep., SAE Technical Paper

Kohri I, Yamanashi T, Nasu T, Hashizume Y, Katoh D (2014) Study on the transient behaviour of the vortex structure behind ahmed body. SAE International Journal of Passenger Cars-Mechanical Systems 7(2014-01-0597):586–602

Koitrand S, Lofdahl L, Rehnberg S, Gaylard A (2014) A computational investigation of ground simulation for a saloon car. SAE International Journal of Commercial Vehicles 7(2014-01-0615):111–123

Kolmogorov AN (1941) The local structure of turbulence in incompressible viscous fluid for very large reynolds numbers. In: Dokl. Akad. Nauk SSSR, vol 30-4, pp 299–303

Kowata S, Ha J, Yoshioka S, Kato T, Kohama Y (2008) Drag force reduction of a bluff-body with an underbody slant and rear flaps. SAE International Journal of Commercial Vehicles 1(2008-01-2599):230–236

Krajnovic S (2013) Les investigation of passive flow control around an ahmed body. In: ASME 2013 International Mechanical Engineering Congress and Exposition, American Society of Mechanical Engineers, pp V07AT08A010–V07AT08A010

Krajnovic S, Davidson L (2003) Numerical study of the flow around a bus-shaped body. Journal of Fluids Engineering 125(3):500–509

Krajnovic S, Davidson L (2005a) Flow around a simplified car, part 2: understanding the flow. Journal of Fluids Engineering 127(5):919–928

Krajnovic S, Davidson L (2005b) Influence of floor motions in wind tunnels on the aerodynamics of road vehicles. Journal of wind engineering and industrial aerodynamics 93(9):677–696

Krajnovic S, Sarmast S, Basara B (2011) Numerical investigation of the flow around a simplified wheel in a wheelhouse. Journal of Fluids Engineering 133(11):111,001

Landström C, Josefsson L, Walker T, Löfdahl L (2011a) An experimental investigation of wheel design parameters with respect to aerodynamic drag. In: 8th FKFS Conference

Landström C, Walker T, Christoffersen L, Löfdahl L (2011b) Influences of different front and rear wheel designs on aerodynamic drag of a sedan type passenger car. Tech. rep., SAE Technical Paper

LaVision G (2015) DaVis FlowMaster software manual for DaVis 8.3

Legrand M, Nogueira J, Lecuona A (2011) Flow temporal reconstruction from non-time-resolved data part i: mathematic fundamentals. Experiments in fluids 51(4):1047–1055

Lehmkuhl O, Rodríguez I, Borrell R, Chiva J, Oliva A (2014) Unsteady forces on a circular cylinder at critical reynolds numbers. Physics of Fluids 26(12):125,110

Lei B, Xia C, Shan X, Yang Z (2017) Numerical simulation of the bi-stable wake behind the square-back ahmed body. Tech. rep., Shanghai University

Lemons DS, Gythiel A (1997) Paul langevin's 1908 paper 'on the theory of brownian motion'['sur la théorie du mouvement brownien,' cr acad. sci.(paris) 146, 530–533 (1908)]. American Journal of Physics 65(11):1079–1081

Leśniewicz P, Kulak M, Karczewski M (2014) Aerodynamic analysis of an isolated vehicle wheel. In: Journal of Physics: Conference Series, IOP Publishing, vol 530-1, p 012064

Li R, Barros D, Borée J, Cadot O, Noack BR, Cordier L (2016) Feedback control of bimodal wake dynamics. Experiments in Fluids 57(10):158

Lienhart H, Becker S (2003) Flow and turbulence structure in the wake of a simplified car model. Tech. rep., SAE Technical Paper

Liou WW (1994) Linear instability of curved free shear layers. Physics of Fluids 6(2):541–549

Littlewood R (2013) Novel methods of drag reduction for squareback road vehicles. PhD thesis, Loughborough University

Littlewood R, Passmore M (2010) The optimization of roof trailing edge geometry of a simple square-back. Tech. rep., SAE Technical Paper

Littlewood R, Passmore M (2012) Aerodynamic drag reduction of a simplified squareback vehicle using steady blowing. Experiments in fluids 53(2):519–529

Littlewood R, Passmore M, Wood D (2011) An investigation into the wake structure of square back vehicles and the effect of structure modification on resultant vehicle forces. SAE International Journal of Engines 4(2011-37-0015):2629–2637

Lucas JM, Cadot O, Herbert V, Parpais S, Délery J (2017) A numerical investigation of the asymmetric wake mode of a squareback ahmed body–effect of a base cavity. Journal of Fluid Mechanics 831:675–697

Lumley JL (1967) The structure of inhomogeneous turbulent flows. Atmospheric turbulence and radio wave propagation pp 166–178

Luo S, Yazdani MG, Chew Y, Lee T (1994) Effects of incidence and afterbody shape on flow past bluff cylinders. Journal of Wind Engineering and Industrial Aerodynamics 53(3):375–399

Magarvey R, Bishop RL (1961) Transition ranges for three-dimensional wakes. Canadian Journal of Physics 39(10):1418–1422

Mair W (1978) Drag-reducing techniques for axi-symmetric bluff bodies. In: Aerodynamic drag mechanisms of bluff bodies and road vehicles, Springer, pp 161–187

Makihara T, Kitamura T, Yamashita T, Maeda K, Kato C, Takayama T, Yamamoto K, Yamade Y, Suzuki Y (2016) Identification of vortical structure that drastically worsens aerodynamic drag on a 2-box vehicle using large-scale simulations. SAE International Journal of Passenger Cars-Mechanical Systems 9(2016-01-1585):592–602

Mariotti A, Buresti G (2013) Experimental investigation on the influence of boundary layer thickness on the base pressure and near-wake flow features of an axisymmetric blunt-based body. Experiments in fluids 54(11):1612

Mariotti A, Buresti G, Salvetti M (2015) Connection between base drag, separating boundary layer characteristics and wake mean recirculation length of an axisymmetric blunt-based body. Journal of Fluids and Structures 55:191–203

Mariotti A, Buresti G, Gaggini G, Salvetti M (2017) Separation control and drag reduction for boat-tailed axisymmetric bodies through contoured transverse grooves. Journal of Fluid Mechanics 832:514–549

Marquet O, Larsson M (2015) Global wake instabilities of low aspect-ratio flat-plates. European Journal of Mechanics-B/Fluids 49:400–412

Martinuzzi R, Tropea C, et al (1993) The flow around surface-mounted, prismatic obstacles placed in a fully developed channel flow. Transaction-American Society of Mechanical Engineers Journal of Fluids Engineering 115:85–85

Mayer W, Wiedemann J (2007) The influence of rotating wheels on total road load. Tech. rep., SAE Technical Paper

McArthur D, Burton D, Thompson M, Sheridan J (2016) On the near wake of a simplified heavy vehicle. Journal of Fluids and Structures 66:293–314

McManus J, Zhang X (2006) A computational study of the flow around an isolated wheel in contact with the ground. Journal of Fluids Engineering 128(3):520–530

Mears A, Dominy RG, Sims-Williams D (2002) The air flow about an exposed racing wheel. Tech. rep., SAE Technical Paper

Meile W, Ladinek T, Brenn G, Reppenhagen A, Fuchs A (2016) Non-symmetric bi-stable flow around the ahmed body. International Journal of Heat and Fluid Flow 57:34–47

Mercker E, Berneburg H (1992) On the simulation of road driving of a passenger car in a wind tunnel using a moving belt and rotating wheels. In: Congresso ATA, Innovation and Reliability in Automotive Design and Testing, Firenze, Italy

Mercker E, Breuer N, Berneburg H, Emmelmann H (1991) On the aerodynamic interference due to the rolling wheels of passenger cars. Tech. rep., SAE Technical Paper

Miau J, Leu T, Liu T, Chou J (1997) On vortex shedding behind a circular disk. Experiments in Fluids 23(3):225–233

Minguez M, Pasquetti R, Serre E (2008) High-order large-eddy simulation of flow over the ahmed body car model. Physics of Fluids (1994-present) 20(9):095,101

Morelli A (1983) Aerodynamic basic bodies suitable for automobile applications. Int J Vehicle desgn - Impact Aerodynamics on Vehicle Design pp 70–98

Morelli A (2000) A new aerodynamic approach to advanced automobile basic shapes. Tech. rep., SAE technical paper

Newnham P (2007) The influence of turbulence on the aerodynamic optimisation of bluff body road vehicles. PhD thesis, © PS Newnham

Norberg C (1993) Flow around rectangular cylinders: pressure forces and wake frequencies. Journal of wind engineering and industrial aerodynamics 49(1):187–196

Norberg C (1994) An experimental investigation of the flow around a circular cylinder: influence of aspect ratio. Journal of Fluid Mechanics 258:287–316

Okajima A (1982) Strouhal numbers of rectangular cylinders. Journal of Fluid Mechanics 123:379–398

Onorato M, Costelli A, Garrone A (1984) Drag measurement through wake analysis. Tech. rep., SAE Technical Paper

Oxlade AR (2013) High-frequency pulsed jet forcing of an axi-symmetric bluff body wake. PhD thesis, PhD thesis. Imperial College London

Parezanović V, Cadot O (2012) Experimental sensitivity analysis of the global properties of a two-dimensional turbulent wake. Journal of Fluid Mechanics 693:115–149

Passmore MA, Spencer A, Wood D, Jowsey L, Newnham P (2010) The application of particle image velocimetry in automotive aerodynamics. Tech. rep., SAE Technical Paper

Pellerin S, Podvin B, Pastur L (2016) Characterization of the near-wake of an ahmed body profile. World Academy of Science, Engineering and Technology, International Journal of Mechanical, Aerospace, Industrial, Mechatronic and Manufacturing Engineering 10(5):926–931

Perry A, Chong M, Lim T (1982) The vortex-shedding process behind two-dimensional bluff bodies. Journal of Fluid Mechanics 116:77–90

Perry AK (2016a) private communication

Perry AK (2016b) An investigation into the base pressure of simplified automotive squareback geometries. PhD thesis, Loughborough University

Perry AK, Passmore M, Finney A (2015) Influence of short rear end tapers on the base pressure of a simplified vehicle. SAE International Journal of Passenger Cars-Mechanical Systems 8(2015-01-1560):317–327

Perry AK, Almond M, Passmore M, Littlewood R (2016) The study of a bi-stable wake region of a generic squareback vehicle using tomographic piv. SAE International Journal of Passenger Cars-Mechanical Systems 9(2016-01-1610):743–753

Pirozzoli S, Orlandi P, Bernardini M (2012) The fluid dynamics of rolling wheels at low reynolds number. Journal of Fluid Mechanics 706:496–533

Pitman J, Gaylard A (2017) An experimental investigation into the flow mechanisms around an suv in open and closed cooling air conditions. In: FKFS Conference, Springer, pp 61–79

Pope SB (2000) Turbulent flows. Cambridge university press

Prasad AK (2000a) Particle image velocimetry. Current Science 79(1):51–60

Prasad AK (2000b) Stereoscopic particle image velocimetry. Experiments in fluids 29(2):103–116

Provansal M, Mathis C, Boyer L (1987) Bénard-von kármán instability: transient and forced regimes. Journal of Fluid Mechanics 182:1–22

Pujals G, Depardon S, Cossu C (2010) Drag reduction of a 3d bluff body using coherent streamwise streaks. Experiments in fluids 49(5):1085–1094

Raffel M, Willert CE, Scarano F, Kähler CJ, Wereley ST, Kompenhans J (2018) Particle image velocimetry: a practical guide. Springer

Rao A, Minelli G, Basara B, Krajnovic S (2018) On the two flow states in the wake of a hatchback ahmed body. Journal of Wind Engineering and Industrial Aerodynamics 173:262–278

Regert T, Lajos T (2007) Description of flow field in the wheelhouses of cars. International Journal of Heat and Fluid Flow 28(4):616–629

Richardson LF (1922) Weather prediction by numerical process. Cambridge University Press

Rigas G, Oxlade A, Morgans A, Morrison J (2014) Low-dimensional dynamics of a turbulent axisymmetric wake. Journal of Fluid Mechanics 755:R5

Rigas G, Morgans A, Brackston R, Morrison J (2015) Diffusive dynamics and stochastic models of turbulent axisymmetric wakes. Journal of Fluid Mechanics 778

Roshko A (1954) On the drag and shedding frequency of two-dimensional bluff bodies. Tech. rep., DTIC Document

Roshko A (1961) Experiments on the flow past a circular cylinder at very high reynolds number. Journal of Fluid Mechanics 10(3):345–356

Roshko A (1993) Perspectives on bluff body aerodynamics. Journal of Wind Engineering and Industrial Aerodynamics 49(1):79–100

Rossitto G, Sicot C, Ferrand V, Borée J, Harambat F (2016) Influence of afterbody rounding on the pressure distribution over a fastback vehicle. Experiments in Fluids 57(3):43

Rouméas M, Gilliéron P, Kourta A (2009a) Analysis and control of the near-wake flow over a square-back geometry. Computers & Fluids 38(1):60–70

Rouméas M, Gilliéron P, Kourta A (2009b) Drag reduction by flow separation control on a car after body. International journal for numerical methods in fluids 60(11):1222–1240

Ryan K, Butler CJ, Sheard GJ (2012) Stability characteristics of a counter-rotating unequal-strength batchelor vortex pair. Journal of Fluid Mechanics 696:374–401

Saddington AJ, Knowles R, Knowles K (2007) Laser doppler anemometry measurements in the near-wake of an isolated formula one wheel. Experiments in fluids 42(5):671–681

SAE (1997) Testing of road vehicles in open jet wind tunnels. Tech. Rep. J2017, SAE International

SAE (2010) Surface vehicle recommended practice. Tech. Rep. J1594, SAE International

Saffman PG (1992) Vortex dynamics. Cambridge university press

Schewe G (1983) On the force fluctuations acting on a circular cylinder in crossflow from subcritical up to transcritical reynolds numbers. Journal of fluid mechanics 133:265–285

Schewe G (2013) Reynolds-number-effects in flow around a rectangular cylinder with aspect ratio 1: 5. Journal of Fluids and Structures 39:15–26

Schiwietz T, Westermann R (2004) Gpu-piv. In: VMV, pp 151–158

Schnepf B, Schütz T, Indinger T (2015) Further investigations on the flow around a rotating, isolated wheel with detailed tread pattern. SAE International Journal of Passenger Cars-Mechanical Systems 8(2015-01-1554):261–274

Schuetz T (2016) Aerodynamics of road vehicles 5th edition. SAE International

Schütz T, Klußmann S, Neuendorf R (2016) Automotive aerodynamics in 2020. ATZ worldwide 118(12):48–53

Schwarczkopf A, Régert T, Lajos T (2009) Investigation of simple possibilities for reduction of drag due to the wheels of road vehicles. Proceedings of the 4th European Automotive Simulation Conference

Sebben S (2004) Numerical simulations of a car underbody: effect of front-wheel deflectors. Tech. rep., SAE Technical Paper

Shi LL, Liu YZ, Wan JJ (2010) Influence of wall proximity on characteristics of wake behind a square cylinder: Piv measurements and pod analysis. Experimental Thermal and Fluid Science 34(1):28–36

Sims-Williams DB, Dominy R (1998) Experimental investigation into unsteadiness and instability in passenger car aerodynamics. Tech. rep., SAE Technical Paper

Sims-Williams DB, Kaye S, Watkins S (2006) Periodic structures within the formation region of trailing vortices. Tech. rep., SAE Technical Paper

Sirovich L (1987) Turbulence and the dynamics of coherent structures. i-coherent structures. ii-symmetries and transformations. iii-dynamics and scaling. Quarterly of applied mathematics 45:561–571

Sprot A, Minto J, Sims-Williams D, Dominy R (2011) Aerodynamic investigation on the effect of varying through-hub flow on a formula one front wheel assembly. SAE International journal of passenger cars Mechanical systems 4(1):929–944

Sprot A, Sims-Williams D, Dominy R (2012) The aerodynamic characteristics of a fully deformable formula one wind tunnel tyre. SAE International journal of passenger cars Mechanical systems 5(2):1026–1041

Strachan R, Knowles K, Lawson N (2007) The vortex structure behind an ahmed reference model in the presence of a moving ground plane. Experiments in fluids 42(5):659–669

Strangfeld C, Wieser D, Schmidt HJ, Woszidlo R, Nayeri C, Paschereit C (2013) Experimental study of baseline flow characteristics for the realistic car model drivaer. Tech. rep., SAE Technical Paper

Taira K, Brunton SL, Dawson ST, Rowley CW, Colonius T, McKeon BJ, Schmidt OT, Gordeyev S, Theofilis V, Ukeiley LS (2017) Modal analysis of fluid flows: An overview. AIAA Journal pp 1–29

Thacker A, Aubrun S, Leroy A, Devinant P (2010) Unsteady analyses of the flow separation on the rear window of a simplified ground vehicle model. AIAA paper 4569

Thacker A, Aubrun S, Leroy A, Devinant P (2012) Effects of suppressing the 3d separation on the rear slant on the flow structures around an ahmed body. Journal of Wind Engineering and Industrial Aerodynamics 107:237–243

Thivolle-Cazat E, Gilliéron P (2006) Flow analysis around a rotating wheel. In: 13th Int. Symposium on Applications of Laser Techniques to Fluid Mechanics, Lisbon, Portugal, Citeseer, pp 26–29

Torrence C, Compo GP (1998) A practical guide to wavelet analysis. Bulletin of the American Meteorological society 79(1):61–78

Townsend AA (1980) The structure of turbulent shear flow. Cambridge university press

Tunay T, Sahin B, Ozbolat V (2014) Effects of rear slant angles on the flow characteristics of ahmed body. Experimental Thermal and Fluid Science 57:165–176

Tunay T, Yaniktepe B, Sahin B (2016) Computational and experimental investigations of the vortical flow structures in the near wake region downstream of the ahmed vehicle model. Journal of Wind Engineering and Industrial Aerodynamics 159:48–64

Van Oudheusden B, Scarano F, Van Hinsberg N, Watt D (2005) Phase-resolved characterization of vortex shedding in the near wake of a square-section cylinder at incidence. Experiments in Fluids 39(1):86–98

Van Raemdonck G, Van Tooren M (2008) Time averaged phenomenological investigation of a wake behind a bluff body. In: Bluff Body Aerodynamics and Application VI Conference, Milan, Italy

Varney M, Passmore M, Gaylard A (2017) The effect of passive base ventilation on the aerodynamic drag of a generic suv vehicle. SAE International Journal of Passenger Cars-Mechanical Systems 10(2017-01-1548):345–357

Varon E, Eulalie Y, Edwige S, Gilotte P, Aider JL (2017a) Chaotic dynamics of large-scale structures in a turbulent wake. Physical Review Fluids 2(3):034,604

Varon E, Eulalie Y, Edwige S, Gilotte P, Aider JL (2017b) Control of the chaotic dynamics of a turbulent 3d wake. arXiv preprint arXiv:171200416

Vdovin A, Bonitz S, Landstrom C, Lofdahl L (2013) Investigation of wheel ventilation-drag using a modular wheel design concept. SAE International Journal of Passenger Cars-Mechanical Systems 6(2013-01-0953):308–315

Venning J, Jacono DL, Burton D, Thompson M, Sheridan J (2015) The effect of aspect ratio on the wake of the ahmed body. Experiments in Fluids 56(6):126

Venning J, Lo Jacono D, Burton D, Thompson MC, Sheridan J (2017) The nature of the vortical structures in the near wake of the ahmed body. Proceedings of the Institution of Mechanical Engineers, Part D: Journal of Automobile Engineering 231(9):1239–1244

Verzicco R, Fatica M, Iaccarino G, Moin P, Khalighi B (2002) Large eddy simulation of a road vehicle with drag-reduction devices. AIAA journal 40(12):2447–2455

Vino G, Watkins S, Mousley P, Watmuff J, Prasad S (2005) Flow structures in the near-wake of the ahmed model. Journal of fluids and structures 20(5):673–695

Volpe R, Devinant P, Kourta A (2015) Experimental characterization of the unsteady natural wake of the full-scale square back ahmed body: flow bi-stability and spectral analysis. Experiments in Fluids 56(5):1–22

Wang L, Sicot C, Boree J, Grandemange M (2018) Experimental study of wheel-vehicle aerodynamic interactions. In: Proceedings of the Third international conference in numerical and experimental aerodynamics of road vehicles and trains (Aerovehicles 3), Milan, Italy

Wang X, Zhou Y, Pin Y, Chan T (2013) Turbulent near wake of an ahmed vehicle model. Experiments in fluids 54(4):1490

Wäschle A (2007) The influence of rotating wheels on vehicle aerodynamics-numerical and experimental investigations. Tech. rep., SAE Technical Paper

Watkins S, Saunders JW (1995) Turbulence experienced by road vehicles under normal driving conditions. Tech. rep., SAE Technical Paper

Welch P (1967) The use of fast fourier transform for the estimation of power spectra: a method based on time averaging over short, modified periodograms. IEEE Transactions on audio and electroacoustics 15(2):70–73

Westerweel J (1994) Efficient detection of spurious vectors in particle image velocimetry data. Experiments in Fluids 16(3-4):236–247

Wickern G, Lindener N (2000) The audi aeroacoustic wind tunnel: Final design and first operational experience. Tech. rep., SAE Technical Paper

Wickern G, Zwicker K, Pfadenhauer M (1997) Rotating wheels-their impact on wind tunnel test techniques and on vehicle drag results. Tech. rep., SAE Technical Paper

Wieser D, Schmidt HJ, Müller S, Strangfeld C, Nayeri C, Paschereit C (2014) Experimental comparison of the aerodynamic behavior of fastback and notchback drivaer models. SAE International Journal of Passenger Cars-Mechanical Systems 7(2014-01-0613):682–691

Willert CE, Gharib M (1991) Digital particle image velocimetry. Experiments in fluids 10(4):181–193

Williamson CH (1996) Vortex dynamics in the cylinder wake. Annual review of fluid mechanics 28(1):477–539

Winant C, Browand F (1974) Vortex pairing: the mechanism of turbulent mixing-layer growth at moderate reynolds number. Journal of Fluid Mechanics 63(02):237–255

Wolf CC, Stumpf E (2014) The subsonic near wake of bluff bodies. PhD thesis, Lehrstuhl und Institut für Luft-und Raumfahrtsysteme (ILR)

Wood A, Passmore M, Forbes D, Wood D, Gaylard A (2015) Base pressure and flow-field measurements on a generic suv model. SAE International Journal of Passenger Cars-Mechanical Systems 8(2015-01-1546):233–241

Wood D (2015) The effect of rear geometry changes on the notchback flow field. PhD thesis, Loughborough University

Wordley S, Saunders J (2008) On-road turbulence. SAE International Journal of Passenger Cars-Mechanical Systems 1(2008-01-0475):341–360

Wygnanski I, Fiedler HE (1970) The two-dimensional mixing region. Journal of Fluid Mechanics 41(2):327–361

Yang J, Liu M, Wu G, Gu H, Yao M (2017) On the unsteady wake dynamics behind a circular disk using fully 3d proper orthogonal decomposition. Fluid Dynamics Research 49(1):015,510

Yi W (2007) Drag reduction of a three-dimensional car model using passive control device. PhD thesis, Seul National University

Zhang B, Zhou Y, To S (2015) Unsteady flow structures around a high-drag ahmed body. Journal of Fluid Mechanics 777:291–326